Mostafa Hoseini

On the Remote Sensing of the Atmosphere and Ocean Using Direct and Reflected GNSS Signals

Doctoral thesis

NTNU
Norwegian University of
Science and Technology

Mostafa Hoseini

On the Remote Sensing of the Atmosphere and Ocean Using Direct and Reflected GNSS Signals

Thesis for the Degree of Philosophiae Doctor

Trondheim, May 2022

Norwegian University of Science and Technology
Faculty of Engineering
Department of Civil and Environmental Engineering

NTNU
Norwegian University of
Science and Technology

To my parents,
the heavenly sources of
hope and unconditional love...

This page is intentionally left blank

Preface

This thesis is submitted in partial fulfillment of the *Philosophiae Doctor* (PhD) degree requirements at the Norwegian University of Science and Technology (NTNU). The research has been conducted for four years, between February 2018 to February 2022, from which three years were designated to the Ph.D. research and one year to non-curricular activities. The doctoral studies were performed predominantly at the Geomatics group of the Department of Civil and Environmental Engineering (IBM). A duration of about eight months was spent at the Department of Geodesy at the German Research Center for Geosciences (GFZ) in Potsdam, Germany. Most of the ground-based experimental data used in this thesis has been provided by GFZ.

The main supervisor of this thesis has been professor Hossein Nahavandchi at the Geomatics group at IBM. My co-supervisors have been professor Jens Wickert (GFZ-Potsdam), associate professor Egil Sverre Eide (Department of Electronic Systems at NTNU), and Professor Ole Baltazar Andersen (National Space Institute of the Technical University of Denmark). The NTNU Oceans has funded the PhD study.

This page is intentionally left blank

Abstract

The Global Navigation Satellite Systems (GNSS) signals have shown great potential for remote sensing applications. The ubiquitous GNSS signals in direct or reflected geometry can be processed to retrieve different geophysical parameters of the Earth system's components. This thesis presents several studies on the performance assessment and enhancement of GNSS-derived remote sensing data products and investigating possible new applications.

Exemplary datasets from three classes of GNSS data products are used. The first dataset belongs to GNSS meteorology, which is derived from the processing of direct GNSS signals. The data is among the established GNSS data products with about three decades of data archive. The thesis also presents studies based on reflected signals of Medium Earth Orbiting (MEO) GNSS satellites in bistatic radar configuration. The reflected signals can be received by ground-based receivers or spaceborne receivers onboard Low Earth Orbiting (LEOs) satellites. In this sense, the second part of the thesis focuses on ground-based GNSS-Reflectometry (GNSS-R) measurements with demonstrated applications for environmental monitoring. Finally, a new generation of observations from spaceborne GNSS-R technique is investigated.

The first study of this thesis focuses on Precipitable Water Vapor (PWV) time series. Although this data product has been produced for decades, its usage in climate applications depends on its homogeneity verification. This demand stems from the fact that the GNSS-derived PWV time series can have change points due to instrumentation upgrades or new settings in GNSS stations. Therefore, a data homogenization method is developed and tested on real and simulated PWV datasets. The method can identify and correct inhomogeneities in the GNSS tropospheric time series without affecting climate or meteorological signals within the time series.

A GNSS-R dataset from a coastal experiment has been used in four studies of this thesis to investigate possible quality improvements of sea surface characterization measurements. The dataset includes polarimetric observations recorded using a dedicated reflectometry receiver with multiple input antennas. The antennas have Right- and Left-Handed Circular Polarizations (RHCP and LHCP) and are installed at zenith and sea-looking orientations. The studies show that polarimetric observations can significantly improve the quality of the GNSS-R measurements. A clear improvement in the sensitivity and performance of GNSS-R sea surface roughness estimates is observed for combined polarimetric observations from

the RHCP and LHCP links. The sensitivity is even high-enough to discern the roughness change due to rainfall over a calm sea. The dataset is also used to assess GNSS-R sea-level monitoring under different scenarios. The effects of sea surface roughness, polarization and orientation of the antenna, and the frequency of the GNSS signal are studied. The results show that the roughness can degrade the accuracy of the GNSS-R sea-level measurements. The best GNSS-R altimetric performance is observed when combined multi-frequency measurements are used from a sea-looking antenna with an LHCP design.

Finally, two datasets from the new generation spaceborne GNSS-R observations are evaluated for novel applications of the GNSS remote sensing technique. In one of the studies, the feasibility of sensing mesoscale ocean eddies using spaceborne GNSS-R is demonstrated for the first time. A long dataset investigation in this thesis reveals the evidence of changes in GNSS-R Normalized Bistatic Radar Cross-Section (NBRCS) over the ocean eddies. The detected signatures are justified using different properties of the eddies, including the eddy-induced changes in Sea Surface Temperature (SST), the interaction of the eddy surface currents with overpass wind field, and accumulated surfactants brought to the surface by the turbulence associated with the eddies. The last study of the thesis evaluates the spaceborne GNSS-R observations for flood detection and mapping during heavy rainfalls. The study is conducted over an area with a high risk of flooding, requiring constant monitoring with timely observations. The results highlight the potential of the spaceborne GNSS-R for providing the observations with the required sensitivity and short revisit time to detect and map the inundated areas.

Acknowledgments

Mostafa Hoseini
Trondheim, January 2022

This page is intentionally left blank

Table of Contents

This page is intentionally left blank

List of Tables

This page is intentionally left blank

List of Figures

List of Abbreviations

ADC	Analog to Digital Converter
AGC	Automatic Gain Controller
BRCS	Bistatic Radar Cross Section
CME	Change Magnitude Estimator
CORS	Continuously Operating Reference Station
CS	Commercial Service
CYGNSS	Cyclone GNSS mission
DDM	Delay-Doppler Map
ECMWF	European Center for Medium-range Weather Forecast
EIRP	Equivalent Isotropically Radiated Power
GCOS	Global Climate Observing System
GEO	Geostationary orbit
GLONASS	GLObal NAvigation Satellite System
GNSS	Global Navigation Satellite Systems
GNSS-R	GNSS-Reflectometry
GNSS-RO	GNSS Radio Occultation
GORS	GNSS Occultation, Reflectometry, and Scatterometry receiver
GPS	Global Positioning System
GPT	Global Pressure and Temperature model
GRUAN	GCOS Reference Upper-Air Network
I/Q	In-phase/Quadrature
IF	Intermediate Frequency
IGS	International GNSS Service
IGSO	Inclined Geosynchronous Orbit
IRNSS	Indian Regional Navigation Satellite System

LEO	Low Earth Orbit
LHCP	Left-Handed Circular Polarization
LNA	Low-Noise Amplifier
LS-HE	Least-Squares Harmonics Estimation
MEO	Medium-altitude Earth Orbit
MSS	Mean Square Slopes
NBRCS	Normalized Bistatic Radar Cross Section
NWP	Numerical Weather Prediction model
OS	Open Service
PCO	Phase Center Offset
PCV	Phase Center Variation
PPS	Precise Positioning Service
PRN	PseudoRandom Noise
PRS	Public Regulated Service
PWV	Precipitable Water Vapor
QZSS	Quasi-Zenith Satellite System
RHCP	Right-Handed Circular Polarization
RMSE	Root Mean Squared Error
SAR	Synthetic Aperture Radar
SNR	Signal-to-Noise Ratio
SoOP	Signals of Opportunity
SP	Specular Point
SPS	Standard Positioning Service
SR	Surface Reflectivity
SSA	Singular Spectrum Analysis
SST	Sea Surface Temperature
SVD	Singular Value Decomposition
SWH	Significant Wave Height
VMF	Vienna Mapping Function
ZTD	Zenith Total Delay

Chapter 1

Introduction

1.1 Motivation

The privileged environment and ecosystem of our planet are affected by many different issues. It has been suffering from ever-growing anthropogenic effects, responsible for imposing climate change and its devastating consequences, including severe weather conditions. The situation needs special considerations for monitoring the environment, natural resources, and climate variability. Authorities at national or international levels have to be provided with timely and accurate information to plan effective measures and monitor the corresponding feedback.

The remote sensing technique has become the key approach to observing different climate variables within different Earth system components, i.e., atmosphere, hydrosphere, lithosphere, and biosphere. Numerous ground-based monitoring stations monitor various geophysical parameters connected with the Earth components. Moreover, spaceborne missions have provided crucial information for the Earth observations and are tracking the negative aspects of modern life on the environment. The observations can be made using active or passive sensors. The Global Navigation Satellite Systems (GNSS), primarily intended for positioning and navigation services, have opened up opportunities for ground-based or space-based remote sensing applications in a passive configuration. Multiple constellations of GNSS satellites in orbit provide full coverage anywhere on the Earth at any time of the day. The satellites transmit signals at L-band frequencies, providing reliable all-weather signals for the users on Earth and for Low Earth Orbiting (LEO) satellites.

There are different scenarios to utilize these signals for retrieving geophysical

parameters. The scenarios can be categorized based on the geometry of the signals, i.e., direct or reflected geometry, concerning a ground-based or spaceborne receiver. For example, propagation of direct GNSS signals through the atmosphere involves some changes in the characteristics of the signals. Although the atmosphere-induced changes can affect the high-precision positioning and navigation, they can be used to study the atmosphere in ground-based or spaceborne settings. As an exemplary case, one of the most successful and widely acknowledged remote sensing techniques, i.e., GNSS Radio Occultation (GNSS-RO), measures the atmospheric effects on the signals using receivers aboard LEO satellites to derive different parameters such as water vapor, vertical profiles of atmospheric temperature, and electron density [53]. Moreover, precise measurement of the atmospheric effects on the direct signals is possible using ground-based GNSS receivers. The reflection geometry can also be used to retrieve information about the physical or geometrical properties of the surface from which the signals are bounced off. For instance, the reflected signals can be used to measure sea surface height and estimate the sea state. Both the direct and reflected geometries are now being used by different GNSS-based remote sensing techniques to provide scientifically valuable data products.

The precise measurements made by GNSS-based observing systems provide high temporal resolution data that can be assimilated into the traditional observation resources within different disciplines for real time or near real-time applications. Besides, the time span of some of established GNSS-derived remote sensing data products have been growing in recent decades and soon they will be long enough to be used for the applications demanding long-term datasets. Studies are demonstrating such a feasibility [2] aiming to both facilitate and promote scientific use of the GNSS-derived data products.

The GNSS remote sensing data products can be classified into three classes based on their maturity and practical applications. The first group is a class of *traditional data products* that have been produced for decades and can be used in practice. For example, GNSS meteorology data products, e.g., measurements of water vapor content of the atmosphere, can be assimilated into Numerical Weather Prediction (NWP) models or can be used for monitoring climate variability [20].

Another class of GNSS measurements is still the scientific community's topic for possible performance improvement. The feasibility and usage of these measurements for different applications are demonstrated in numerous studies. This class of GNSS measurements can be considered as *developing data products* since there are ongoing efforts to apply them for different case studies and improve the quality of the products. For instance, ground-based GNSS-Reflectometry (GNSS-R) measurements, which are based on reflected Signals of Opportunity (SoOP) from
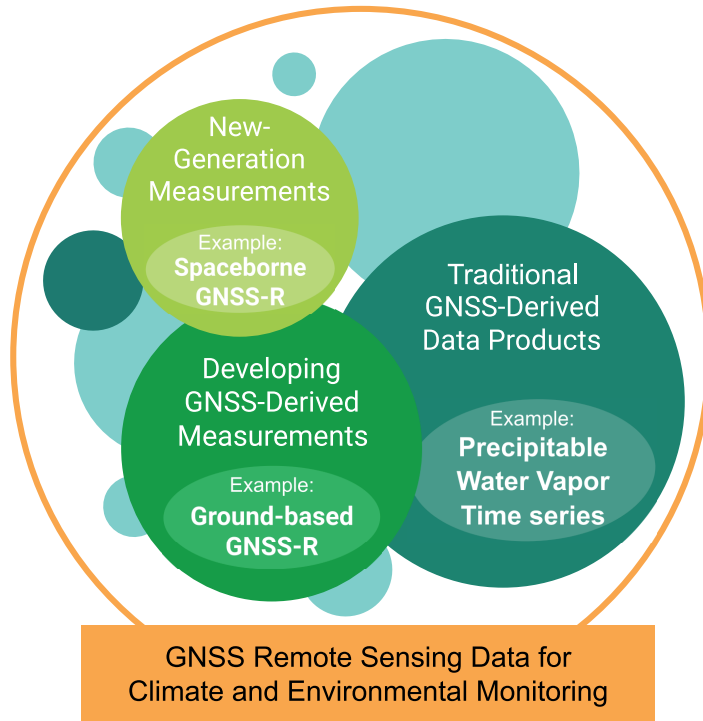
Figure 1.1: A schematic view of different classes of GNSS remote sensing data products for the monitoring of climate and environment.

GNSS satellites, are now being used for research in several applications such as sea surface characterization, soil moisture, vegetation growth, and snow depth retrieval. These measurements are still being enhanced, e.g. by novel data processing methods, utilizing modernized GNSS signals and multiple constellations, or by studying polarimetric aspects of the signals upon reflection.

Finally, a *new-generation GNSS-derived data products* class can also be found in the scientific community. For instance, several missions in recent years have demonstrated the possibility of utilizing reflected GNSS signals of opportunity in spaceborne configuration for monitoring different geophysical parameters of the Earth's surface. In addition, a substantial collection of spaceborne observations has been provided by pioneering GNSS-R missions, which have stimulated several novel applications of this new-generation of GNSS data products. Figure 1.1 shows an schematic view of this classification.

This thesis aims to contribute to promoting the exploitation of the GNSS-derived data products as well as improving the quality of the measurements for climate

and environmental monitoring applications. The contribution is different based on the introduced classes. The measurements at different levels, i.e., from raw observations to final scientific data products, have been processed, investigated, and evaluated in exemplary applications. Several issues have been highlighted and addressed to enhance GNSS-derived measurements. Moreover, some challenges worth further investigations have been discussed to stimulate future research in the community.

1.2   Problem Statement

The accuracy and reliability of the measurements and products from GNSS-based remote sensing systems could be affected by some of the inherent aspects of the systems. The satellites within different GNSS constellations have been modernized to offer new features and signals on top of the traditional services. This dynamic enhancement highlights the necessity of frequent instrumental or software changes in the observation equipment and data processing schemes every few years. In addition, it puts forward new demands for scientific research to utilize the new features to introduce new applications and improve the quality of the established data products.

One of the established products is the ground-based GNSS-derived atmospheric time series retrieved from the processing of direct GNSS signals. This product is based on the data streams from continuously operating permanent GNSS stations available from a worldwide network. Several processing centers of the International GNSS Service (IGS) process the data streams and produce, as a byproduct, zenith and slant atmospheric delays of the direct GNSS signals. Besides meteorological applications, this dataset with a time span of about three decades can gradually be considered for some climate applications. For climate applications, a fundamental issue associated with these time series is its homogeneity. A homogeneous time series for climate applications is considered to only contain the variations due to weather and climate [55]. Nevertheless, instrumental or other systematic changes can affect the homogeneity state of the GNSS-derived time series. On this basis, either verifying the homogeneity of the time series or finding and correcting inhomogeneities is a prerequisite step before approaching any climate applications.

The worldwide network of the permanent GNSS stations includes stations in coastal regions in the proximity of water bodies. These stations can receive the reflected GNSS signals from the sea surface. The signature of these reflections in the observations can transform such a station into a multi-purpose observation site for environmental monitoring purposes and natural hazard warning systems. However, the standard geodetic receivers used in these stations have not been specifically

designed to perform reflectometry observations. Exploring the potentials of reflectometry observations and introducing novel applications demands the utilization of a dedicated reflectometry receiver. The observations made by such a receiver can also give the flexibility of assessing the performance of GNSS-R sensors in different scenarios. The findings from such investigations could be used for spaceborne missions where low-cost, low-power, and low-mass GNSS-R sensors onboard small satellites can elucidate what can be expected from the new generation of Earth observation systems. As a bistatic Radar technique, spaceborne GNSS-R is particularly of interest since it utilizes L-band microwave signals that, unlike optical sensors, are not limited by cloud coverage or daytime and, compared to, e.g., Ku-band and C-band, provide better penetration through rain or even severe weather conditions. Moreover, relatively inexpensive small-satellite constellations that utilize GNSS-R signals or, in a broader view, L-band SoOP can provide a high temporal sampling of abrupt weather hazards.

1.3 Research Objectives and Research Questions

The availability of worldwide permanent GNSS stations for remote sensing applications, the brisk pace of the enhancements in the GNSS signal transmitters and receiving equipment, and the possibility of having low-cost high-competence GNSS-based Earth-observing small satellites, raise several research demands as well as data exploitation issues. This thesis focuses on some of the demands and issues. Regarding the data exploitation issues, the focus will be on well-recognized GNSS-derived tropospheric products from the analysis of direct GNSS signals in a ground-based setting. Concerning the relatively new GNSS-based remote sensing technique, i.e., GNSS-R, the thesis will focus on the assessment and quality improvement of GNSS-R observations, as well as introducing possible new applications based on the recent spaceborne observations. The objectives of this thesis can be briefly described as follows:

- **Objective 1: To contribute to promoting the exploitation of established GNSS-derived remote sensing data products**

  The estimates of Zenith Total Delays (ZTD) associated with the direct GNSS signals is a byproduct of GNSS data processing. The estimated ZTD includes information about the water vapor content of the troposphere. Water vapor is a major greenhouse gas with a significant impact on the earth's climate [26]. The retrieved water vapor content of the atmosphere from the observation of direct GNSS signals at ground-based stations has been identified as one of the reference data for GCOS (Global Climate Observing System) Reference Upper-Air Network (GRUAN) [38].

A simple way of evaluating the long-term behavior of water vapor content of the troposphere is to estimate the linear trend of the time series. The water vapor can be characterized by GNSS-derived Precipitable Water Vapor (PWV). The accuracy of the estimated PWV trends for climate analysis depends on the homogeneity of the PWV time series [2]. Hardware or software changes can impose some inhomogeneities to the GNSS PWV time series. Such inhomogeneities, sometimes discernible as abrupt jumps in the time series, have to be detected and eliminated. Since some climatic effects such as heat waves can also introduce abrupt changes, a delicate homogenization process should be developed to extract the artificial jumps without affecting climate-related changes. A widely used approach to find inhomogeneities in a GNSS time series is to use a reference time series for the comparison. Such reference time series are assumed to be homogeneous which could be a questionable assumption. Any robust homogenization approach should take into account these issues. Objective 1 of this thesis can be articulated through the following Research Questions (RQ):

- *RQ 1.1: In the presence of climate-related changes or possible inhomogeneities in the reference time series, how can we detect and correct inhomogeneities in GNSS-derived tropospheric products?*

- *RQ 1.2: What could be the impact of homogenization on inhomogeneous GNSS datasets for a climate application?*

- **Objective 2: To contribute to the enhancement of the developing class of GNSS-derived remote sensing data products**

In addition to the atmospheric time series, the worldwide network of permanent GNSS stations has enormous potential for producing remote sensing data products based on the observation of reflected signals. For instance, the stations in coastal regions with a possible field of view toward the sea can receive sea-reflected GNSS signals. Different pieces of information related to the sea surface, specifically the sea surface roughness and sea-level variations, can be retrieved from these stations. The stations utilize an almost uniform setup based on a standard geodetic receiver and a Right-Handed Circular Polarization (RHCP) zenith-looking antenna. However, reflectometry observations could have different performances in different scenarios based on the polarization and orientation of the antenna. Investigation of these scenarios provides insights both to enhance the measurements and introduce new applications in spaceborne configuration. Toward this goal, the thesis focuses on sea surface characterization with the following research questions:

- *RQ 2.1: How can we enhance the performance of the ground-based GNSS-R measurements for sea surface characterization?*

- *RQ 2.2: What could be the prospect for future ground-based GNSS-R stations?*

- **Objective 3: To demonstrate novel applications of the new-generation of spaceborne GNSS remote sensing measurements**

  The GNSS satellites are designed to provide the users with continuous navigation service on and near the Earth's surface, including LEO satellites. The ubiquitous GNSS signals with complete coverage of the Earth's surface offer the opportunity to build a passive Earth-observing system for all-weather, day and night operation. Unlike the traditional heavy and costly remote sensing satellites, GNSS-R sensors can be used with small satellites because of the low-demanding instrumentation. In a passive configuration, reflected GNSS signals from the Earth's surface together with their direct counterparts can be collected and processed by a GNSS-R sensor. This method can derive different geophysical parameters of the Earth's surface, which can be used in different scientific applications such as climate and environmental monitoring. Spaceborne GNSS-R can be implemented on a constellation of inexpensive CubeSats to provide high spatiotemporal resolution data with global coverage and a short revisit time. This new generation of observations can be used to study the atmosphere's interactions with the ocean or land. Such novel applications demand pioneering research to demonstrate their feasibility and draw further attention to the scientific community. Toward this ambition, the following research questions are considered to be addressed in this thesis:

  - *RQ 3.1: How can the new-generation of GNSS measurements from spaceborne reflectometry be used for climate and environmental monitoring?*

  - *RQ 3.2: What could be the prospect for future spaceborne GNSS-R missions and applications?*

1.4   Research Approach

This section provides an overview of the datasets, processing schemes, and data analysis used in this thesis.

Research questions RQ 1.1 and RQ 1.2 are investigated using a dataset including GNSS-derived PWV time series obtained from over 200 stations in Germany. This

dataset is accompanied by a reference dataset generated using a numerical weather model. To address RQ 1.1, a change detection method has to be developed to perform the offset detection task in the presence of seasonal components, high-frequency variations (noise), and data gaps. The performance of the detection method will be assessed using simulated time series with randomly inserted artificial offsets. The approach minimizes the impact of the reference time series to ensure that no inhomogeneity is transferred to the GNSS time series. To help the homogenization approach decide whether a detected change is an inhomogeneity or a false alarm, the GNSS time series, the reference time series, and their difference have to be investigated independently. The decision on each case can be made based on the presence of the change in the mentioned three time series. Regarding RQ 1.2, to check possible quality improvements made by applying the developed homogenization approach, the trends of PWV time series before and after homogenization are estimated and compared to those from the reference dataset.

To address the research questions RQ 2.1 and RQ 2.2, a one-year dataset from a coastal GNSS-R experiment at Onsala Space Observatory in Sweden is obtained. The dataset includes raw observations made by a dedicated GNSS-R receiver which concurrently collects reflected signals from three antennas with different polarizations and orientations. According to the focus of this thesis on sea surface characterization, the performance of the GNSS-R observations for retrieving sea surface roughness and sea level is assessed. The performance assessment is carried out based on different variables, e.g., polarization and orientation of the antenna, presence of wind, and precipitation. In response to RQ 2.2, the assessment results are then used to provide an outlook on future experiments and stimulate further research.

Regarding RQ 3.1, a dataset of spaceborne GNSS-R observations made by a constellation of micro-satellites launched by NASA is used. This thesis aims to utilize the new-generation GNSS-based observations for possible applications over the ocean and land. In doing so, the data is collocated with some match-up datasets for justification and verification purposes. In reply to RQ 3.2 and based on the findings from the investigation of both ground-based and spaceborne GNSS-R measurements, a possible design for future spaceborne GNSS-R sensors compatible with CubeSats specifications is introduced.

1.5   Structure of the Dissertation

This dissertation comprises five chapters. The introduction in the current chapter provided an overview of the topic and described the motivation, research questions, and research objectives. A short description of the research approach is also included in Chapter 1. In the second chapter, a brief explanation of the theoretical

background is provided. Chapter 3 presents an overview of the results and a summary of the papers included in this dissertation. Chapter 4 provides the concluding remarks together with an outlook for future research topics. A list of the references is provided after Chapter 4. The last chapter comprises the publications associated with this thesis.

This page is intentionally left blank

Chapter 2

Conceptual Foundations

2.1 A brief overview of the Global Navigation Satellite Systems (GNSS)

The Global Navigation Satellite Systems (GNSS) provide users on or near the Earth's surface with the services to determine the accurate position and time. The concept of satellite-based positioning is based on observing distant objects with known positions, similar to the traditional resection process that has been historically used for quite a long time. In this process, the distances of an object with an unknown position to some objects with known positions are measured and used to calculate the unknown position. For a thorough description of GNSS, the operation concepts and components, as well as an introduction on the applications, readers are referred to e.g., [33, 24, 54].

The distance measurement in the satellite-based positioning is carried out through electromagnetic waves or GNSS signals. The frequencies of the signals are in the part of the L-band spectrum, which resides between about 1.2 and 1.6 GHz, corresponding approximately to 25 and 19 cm wavelengths, respectively. The assigned frequency range provides an adequate setting for the signals to propagate through the atmosphere and reach the user at almost any weather condition. The coexistence of GNSS signals from several independent constellations, e.g. the US Global Positioning System (GPS), the Russian GLObal NAvigation Satellite System (GLONASS), European Galileo, Chinese Beidou, Japanese Quasi-Zenith Satellite System (QZSS), and Indian Regional Navigation Satellite System (IRNSS) increases the number of the observations. The high number of observations makes a positive contribution to the position accuracy, availability, integrity, and continuity of the GNSS services [24].

Most GNSS satellites use a near-circular Medium Earth Orbit (MEO) to provide global coverage. However, some of the satellites are in Inclined Geosynchronous Orbits (IGSO), or Geostationary Orbits (GEO) for regional applications [33]. The GPS satellites use L1 (1575.42MHz) and L2 (1227.6 MHz) frequencies as carrier signals. Different codes are modulated on the carrier signals for Standard and Precise Positioning Services (SPS and PPS). Authorized users can use PPS based on an encrypted Precise (P) code modulated on both L1 and L2. Civilian users have access to SPS by utilizing Coarse/Acquisition (C/A) code available only on L1. A new civil signal (L2C) on L2 and a new military signal (M) on L1 and L2 are implemented within the GPS modernization program. Additionally, the new L5 signal with the frequency of 1176.45 MHz has been implemented on some of the GPS satellites since May 2010 [33].

The GLONASS satellites transmit signals within two bands: Ll, 1602 - 1615.5 MHz, and L2, 1246 - 1256.5 MHz. A new generation of the satellites in this constellation has a new link, i.e., L3, with a frequency of 1202.025 MHz. Galileo satellites

Table 2.1: An overview of the operational constellations of Global Navigation Satellite Systems (GNSS) [33]. The orbit types of the satellites are Medium Earth Orbit (MEO), Geostationary orbit (GEO), and Inclined Geosynchronous Orbit (IGSO).

System	GPS	GLONASS	Galileo	BeiDou	QZSS	IRNSS/NavIC
Orbit	MEO	MEO	MEO	MEO, IGSO, GEO	GEO, IGSO	GEO, IGSO
Nominal satellites	24	24	30	27, 3, 5	1, 3	3, 4
Orbit inclination	56°	64.8°	56°	55°	43°	29°
Initial service	1993	1993	2016	2012	2018	2018
Origin	USA	Russia	Europe	China	Japan	India
Frequency (MHz)	L1 1575.42 L2 1227.60 L5 1176.45	L1 1602.00 L2 1246.00 L3 1202.025	E1 1575.42 E5a 1176.45 E5b 1207.14 E6 1278.75	B1 1561.098 B2 1207.14 B3 1268.52	L1 1575.42 L2 1227.60 L5 1176.45 LEX 1278.75	L5 1176.45 S 2492.028

utilize three frequency bands, i.e., E1 (centered on 1575.46 MHz), E6 (centered on 1278.75 MHz), and E5 (centered on 1191.795 MHz), to provide three levels of service called the Open Service (OS), the Public Regulated Service (PRS), and the Commercial Service (CS) [33]. BeiDou satellites provide open and authorized services using three frequency bands, including B1 (1561.098 MHz), B2 (1207.14 MHz), and B3 (1268.52 MHz). A new generation of this constellation called BeiDou-3 is designed to transmit modernized signals at the L1/E1 and L5/E5 bands as well as the BeiDou B3 frequency [33]. Table 2.1 provides an overview of the operational GNSS constellations. The studies conducted within this thesis are mainly based on the GPS L1 and L2 frequencies.

2.2 Signal specifications

The propagation of transmitted GNSS signals through space is described by Maxwell's theory. Using Maxwell equations (see e.g. [29]), the fundamental wave equations are as follows [36]:

$$\nabla^2 \mathbf{E} = \varepsilon\mu \frac{\partial^2 \mathbf{E}}{\partial t^2} \tag{2.1}$$

$$\nabla^2 \mathbf{B} = \varepsilon\mu \frac{\partial^2 \mathbf{B}}{\partial t^2} \tag{2.2}$$

where $\mathbf{E}$ and $\mathbf{B}$ are the electric and magnetic fields, respectively, the operator ∇^2 is vectorial Laplacean, t is time, and the constants ε and μ respectively denote the electrical permittivity and magnetic permeability of the medium through which the signals propagate. A solution to 2.1 can be described by the following equation [36]:

$$\mathbf{E}(\mathbf{r},t) = \mathbf{E_0} \cos{(\mathbf{k}.\mathbf{r} - kct + \phi_0)}, \quad \mathbf{k} = k\,\mathbf{n_0} \tag{2.3}$$

where $\mathbf{r} = (x,y,z)$ is the position vector, $\mathbf{E_0}$ identifies the strength of the electrical field, $\mathbf{k}$ denotes wave vector, $k = \frac{2\pi}{\lambda}$ is wave number, λ refers to the wavelength, $\mathbf{n_0}$ is a unit vector showing the direction of propagation, c is the speed of light, and ϕ_0 denotes zero-phase offset. If $\mathbf{E_0}$ and $\mathbf{k}$ are perpendicular, which is usually the case regarding the satellite navigation signals, then the wave is a transverse wave. Magnetic wave $\mathbf{B}$ follows similar considerations. The magnetic and electrical fields are both orthogonal to each other, as well as the propagation direction denoted by $\mathbf{n_0}$.

If the electric field or magnetic field oscillates within a plane along $\mathbf{k}$, the electromagnetic wave has linear polarization (Figure 2.1, left). The propagation of electromagnetic waves through the ionosphere or Earth magnetic field can alter
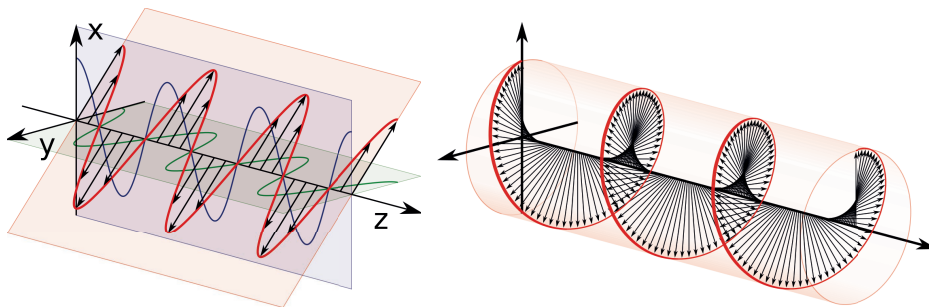
Figure 2.1: Linearly (left) and circularly (right) polarized waves.

linearly polarized waves to elliptically or circularly polarized waves [24]. This issue has been addressed for the navigation signals by using a circular polarization design.

To create a circularly polarized electromagnetic wave, two perpendicular electric waves with similar wave vectors ($\mathbf{k}$) and strengths ($||\mathbf{E_0}||$) can be superposed while the zero-phase offsets (ϕ_0) differ by $90°$ [36]. The strength of this electrical field at a given location $\mathbf{r}$ over time exhibits a circular variation (Figure 2.1, right). A clockwise rotation of the wave, when looking into the propagation direction, indicates a Right-Handed Circular Polarization (RHCP), and a counter-clockwise rotation is associated with a Left-Handed Circular Polarization (LHCP). All GNSS satellites transmit the navigation signals with RHCP. This setting avoids possible power losses due to orientation mismatch of the incoming electromagnetic field, and the receiving antenna [36].

All GNSS signals are transmitted with a modulated characteristic binary sequence called Pseudo-Random Noise (PRN) code at a typical rate of 1 to 10 MHz with a repetition period of a few milliseconds to seconds [33]. The modulation scheme used in GPS satellites is illustrated in Figure 2.2. The PRN code can be used as an identifier to separate the signals with the same frequency from different satellites. The modulated signals include the time of transmission and other required information encapsulated in the data messages to derive the satellites-receiver ranges and the position of the satellites.

Calculating the ranges is based on the estimation of the time delay between the received signal and the transmission time. To estimate the time delay, the receiver correlates the received signal with a local replica of the satellite's PRN code. Besides the time delay, another factor also influences the correlation, i.e., the Doppler effect. The effect is caused due to the relative satellite-receiver movement, which introduces a frequency shift in the GNSS signals known as Doppler frequency.
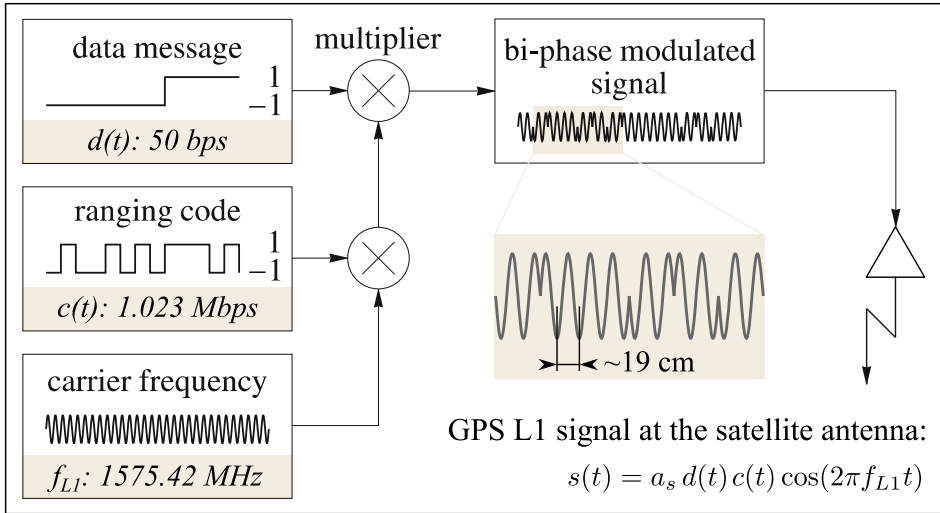
Figure 2.2: A schematic representation of phase modulation of data message and ranging code layers on GPS carrier signals, originally presented by [24]. The parameter a_s is the modulation amplitude.

Therefore, the correlation of the PRN replica with the received signal is a function of the code delay and Doppler shift. The receiver searches for the code delay and Doppler shift that produce the maximal correlation value. The detection can be done by producing a delay-Doppler Map (DDM) in the receiver. The DDM reveals the variation of correlation value at different code-delays and Doppler shifts (Figure 2.3).

GNSS receivers can make the following measurements using the received signals [33, 24]:

- *Code range or Pseudorange:* A measure of the delay between the signal reception and transmission time based on the receiver clock which can be scaled by the speed of light to yield the so-called Pseudorange. This measurement estimates the distance traveled by the signal from the satellite to the receiver.

- *Carrier phase:* Besides the PRN replica, a local oscillator in the receiver generates a signal with a frequency similar to the incoming carrier signal. Any deviation between the generated and incoming signals results in a beat frequency and a beat phase. A measure of the beat phase can be used to retrieve the phase of the satellite signal. Measurement of the carrier phase can precisely report on the change in the pseudorange.
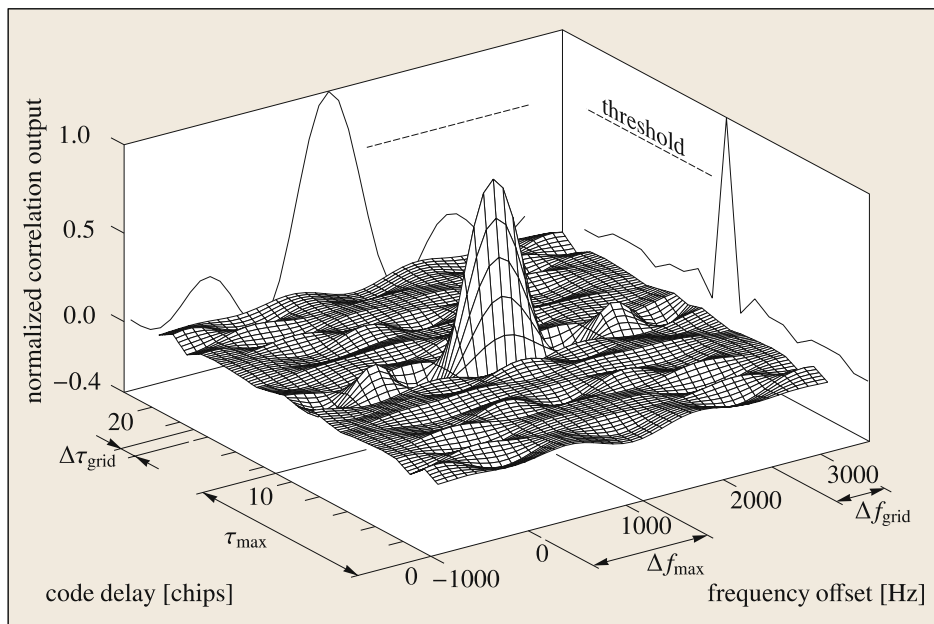
Figure 2.3: An exemplary Delay-Doppler Map (DDM), that is generated in typical GPS receivers (image source: [24]).

- *Doppler frequency:* A measure of the Doppler frequency provides information about the range-rate or line-of-sight velocity.

2.3   Receiver architecture

A conceptual block diagram of a typical GPS receiver architecture is shown in Figure 2.4. The components depicted in the figure are further elaborated in Figure 2.5 to Figure 2.7. The components perform the essential parts of the signal processing procedure on the user side. The variables used in the figures are as follows: a_r is the amplitude of the incoming signal at the receiver antenna, A is the amplitude of the received signal in the receiver, d and c are respectively the modulated data messages and PRN code as functions of time (t) and the path delay (τ), f_{L1} is the GPS L1 frequency, f_D is the Doppler frequency, and f_{IF} is the intermediate frequency. The hat symbol ($\hat{\bullet}$) is used to show an estimation of the respective parameter, e.g., $\hat{f}_D$ indicates an estimation of f_D. The variable φ_0 is the initial phase of the signal when it arrives at the receiver antenna, φ_{IF} is the initial phase of the intermediate frequency, $\Delta\varphi = \varphi_0 - \varphi_{IF}$ and $\delta\varphi = \Delta\varphi - \hat{\Delta\varphi}$ are used for the phase differences, and T_{CI} is the coherent integration time that can be from a few milliseconds usually up to 20 milliseconds.
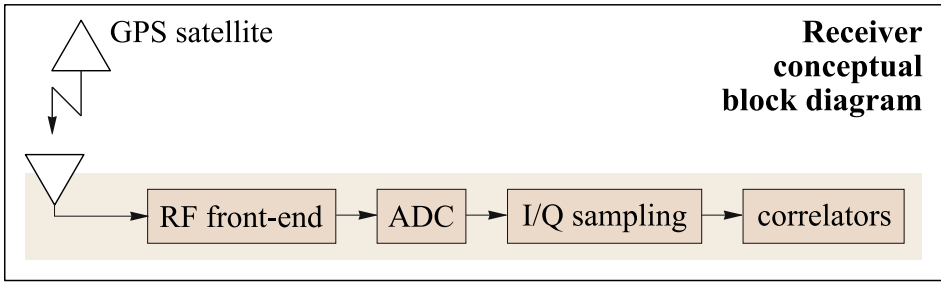
Figure 2.4: The fundamental components of a typical GPS receiver including the Radio Frequency (RF) front-end, Analog to Digital Converter (ADC), In-phase/Quadrature (I/Q) sampling unit, and correlators.

The antenna intercepts incoming signals from any GPS satellites in view and feeds the receiver with a mixture of all intercepted signals (Figure 2.5). Before starting the signal processing procedure, a Low-Noise Amplifier (LNA) increases the strength of the captured signals at the antenna. The receiver front-end shown in Figure 2.5 includes several band-pass filters, a local oscillator, and a mixer to provide a signal at a much lower frequency compared to the carrier frequency. The down-converted signal with a lower frequency is called Intermediate Frequency (IF) and has a frequency that is appropriate for the digitization of the signal in the Analog to Digital Converter (ADC).
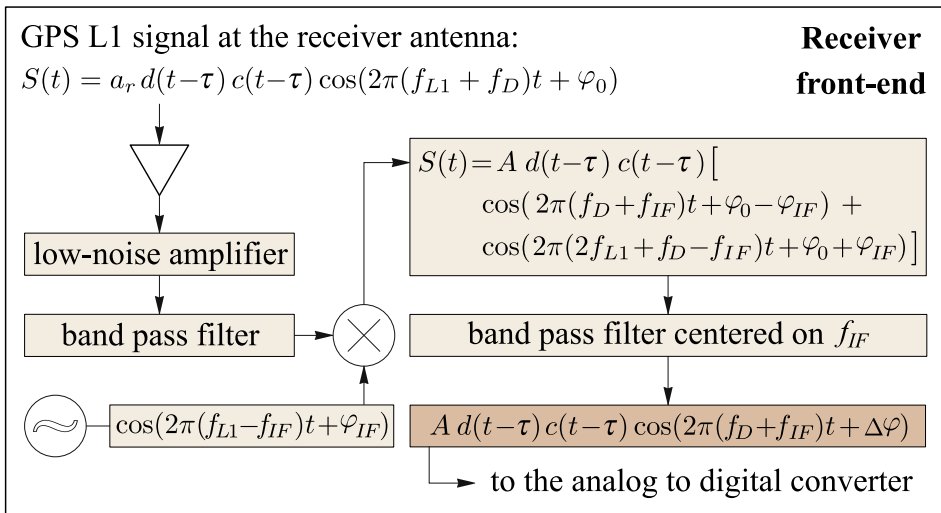
Figure 2.5: A block diagram of the signal processing steps in the receiver frond-end, produced based on the description presented in [54].

17

The digitized signal from the ADC contains the navigation data message, $d(t - \tau)$, and PRN codes, $c(t - \tau)$, of different GPS satellites. To retrieve PRN code delay and the navigation data, the trigonometric term of the signal, i.e., the cosine term, needs to be wiped off. For this purpose, the exact frequency and phase of the digitized signal are required. The frequency is slightly different from the IF frequency due to the Doppler effects, which are unknown and are different for different GPS satellites. Therefore, the receiver cannot completely eliminate the trigonometric term, which results in a remaining residual frequency. The residual frequency can introduce some slow-varying oscillation in the signal that can affect the correlation value between the PRN replicas and the digitized signal. The receiver uses an In-phase/Quadrature (I/Q) method (Figure 2.6) to address this issue. The method provides two outputs in separate I/Q channels to allow preserving correlation power through the following trigonometric equation:

$$[M\cos(\bullet)]^2 + [M\sin(\bullet)]^2 = M^2 \qquad (2.4)$$
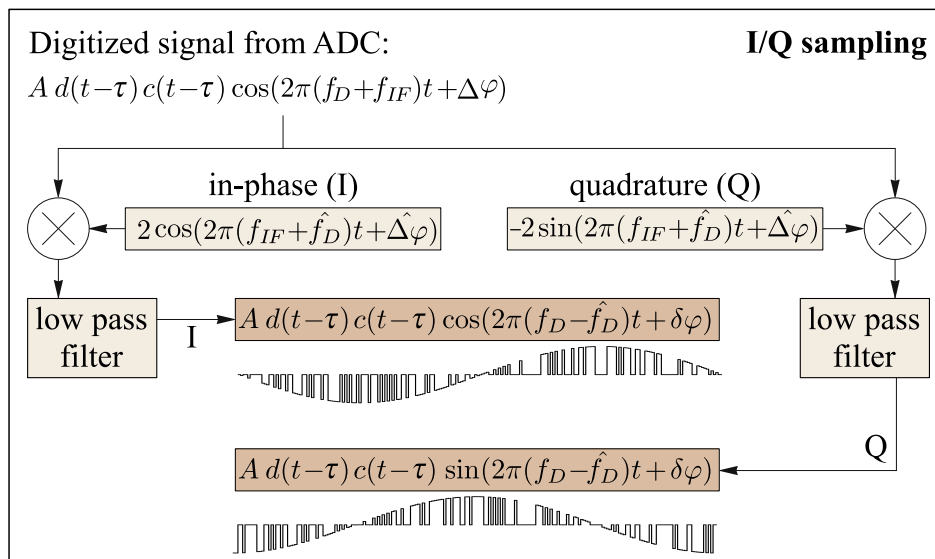
Figure 2.6: A block diagram of the signal processing steps during In-phase and Quadrature (I/Q) sampling. The ADC refers to the analog to digital converter, produced based on the description presented in [54].

The I/Q samples are duplicated to many channels to feed parallel correlators. Each channel can be dedicated to correlating the signal against one specific PRN code. An estimate of the code delay and Doppler shift is applied in each correlator before calculating the correlation between the replica and I/Q samples. For every pair of

the code-delay and Doppler shift estimates, one correlation output is produced. The correlation outputs for a range of different code-delays and Doppler shifts can form the DDM as shown in Figure 2.3. After forming the DDM, the peak value of the correlation in the DDM is detected by the receiver, and the corresponding delay and Doppler are retrieved. The retrieved delay and Doppler values are used to provide the fundamental GPS observables by the receiver, i.e., pseudorange, Doppler frequency, and carrier phase. The peak value of the correlation sum in the DDM can provide an estimate for the received signal strength. More details about the signal processing scheme in the receiver can be found in, e.g., [33, 24, 54].

Outputs from I/Q sampling: **Correlators**

in-phase channel: $A\,d(t-\tau)\,c(t-\tau)\cos(2\pi(f_D-\hat{f}_D)t+\delta\varphi)$

quadrature channel:
$A\,d(t-\tau)\,c(t-\tau)\sin(2\pi(f_D-\hat{f}_D)t+\delta\varphi)$

locally generated PRN replica: $c(t-\hat{\tau})$

$$\Sigma_Q = \frac{A\,d}{T_{CI}}\int_0^{T_{CI}} c(t-\hat{\tau})\,c(t-\hat{\tau})\sin(2\pi\Delta f_D t+\delta\varphi)dt$$

correlator output for each $\hat{\tau}$ and $\hat{f}_D$:
$\Sigma_I^2 + \Sigma_Q^2$

$$\Sigma_I = \frac{A\,d}{T_{CI}}\int_0^{T_{CI}} c(t-\hat{\tau})\,c(t-\hat{\tau})\cos(2\pi\Delta f_D t+\delta\varphi)dt$$
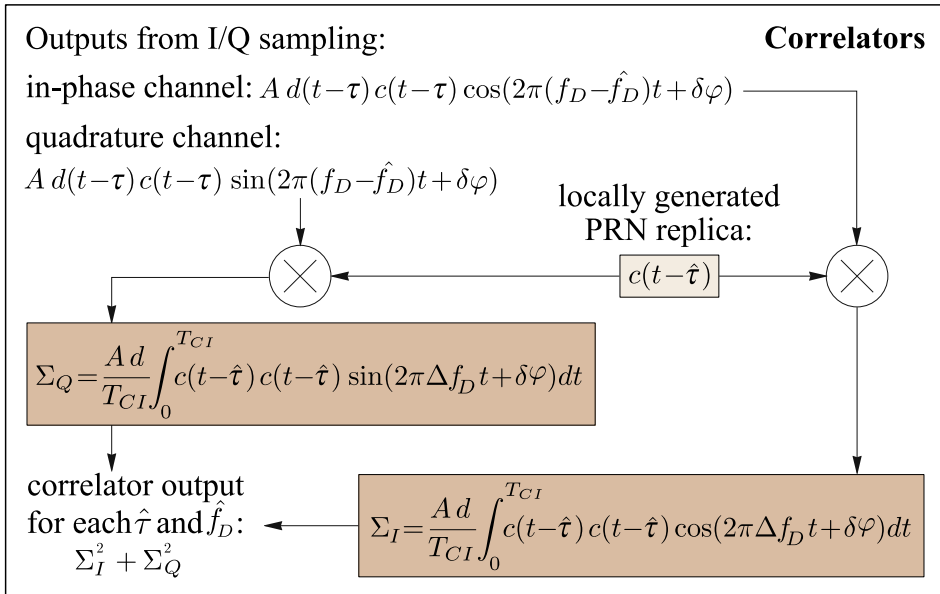
Figure 2.7: A block diagram of a correlator channel in the receiver, produced based on the description presented in [54].

2.4 Interference of the direct and reflected signals

The received signal in the receiver can be a compound signal generated by the interference of the direct signal and some reflections from nearby surfaces. In this case, the contribution of reflected signals can affect the peak correlation power in the DDM. The interference of the reflections with direct signals is considered as an error source in positioning and navigation applications. Nevertheless, this phenomenon is utilized in the GNSS-Reflectometry (GNSS-R) technique to characterize the surface the signals are reflected from. For instance, reflections from sea surface can be collected and processed to retrieve sea surface height or sea

state.

In this thesis, we use a dedicated reflectometry receiver with multiple antenna inputs. The details about this receiver and the experimental site can be found in [21, 28, 44]. The first antenna input of this receiver is called the master link. The master antenna is used for tracking direct signals similar to typical GPS receivers with the procedure described in section 2.3. The other antennas are called slave links and can be used to capture reflections from the target surfaces. In the following, we investigate the effect of reflected signals on the power of received signals in the master and slave antennas. We use the complex numbers system to simultaneously work with the outputs of I/Q channels in a unified formulation. The real part of the complex numbers is used for the in-phase channel and the imaginary part for the quadrature channel. In this sense, the symbol j indicates the imaginary unit ($j^2 = -1$).

As illustrated in Figure 2.8(a) and Figure 1 in [34], the intercepted direct and reflected signals in the master antenna can be expressed by:

$$\mathbf{A_c} = \mathbf{A_d} + \mathbf{A_r} \tag{2.5}$$

$$A_c e^{j\varphi_c} = A_d\, e^{j\varphi_d} + A_r\, e^{j(\varphi_d + \psi)} \tag{2.6}$$

where A_d, A_r, and A_c are respectively the amplitude of direct, reflected, and compound signals. Correspondingly, the phase values for these signals are φ_d, φ_r, and φ_c. The phase difference between the direct and reflected signals is represented by ψ. The phase of the direct signal comprises several components, i.e., the traveling path from the GNSS satellite to the receiver (including atmospheric refraction) denoted by φ_ρ, phase wind-up shown by φ_w, and Phase Center Variations (PCV) indicated by φ_{pcv}:

$$\varphi_d = \varphi_\rho + \varphi_w + \varphi_{pcv} \tag{2.7}$$

The receiver tracks the phase of the compound signal in the master channel. After tracking, the compound signal will have only an in-phase component as it is shown in Figure 2.8(b). In this case, the quadrature component which is expressed by the imaginary part in Equation 2.6 will be vanished, resulting in:

$$[A_c e^{j\varphi_c} = A_d e^{j\varphi_d} + A_r e^{j(\varphi_d + \psi)}].e^{-j\varphi_c} \tag{2.8}$$

$$A_c = A_d e^{j(\varphi_d - \varphi_c)} + A_r e^{j(\varphi_d + \psi - \varphi_c)} \tag{2.9}$$

$$= A_d e^{-j\delta\varphi} + A_r e^{j(\psi - \delta\varphi)} \tag{2.10}$$

$$= e^{-j\delta\varphi}.(A_d + A_r e^{j\psi}) \tag{2.11}$$
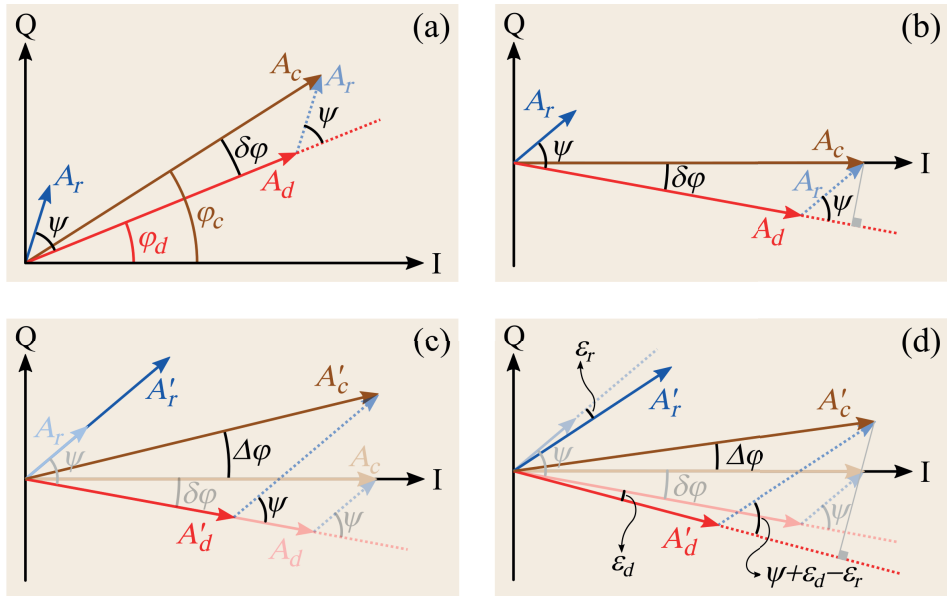
Figure 2.8: Phasor representation of the In-phase (I) and Quadrature (Q) components of the received direct and reflected GNSS signals at the receiver: (a) before tracking the phase of the compound signal (generated by the interference of the direct and reflected signals) in the master channel, (b) after tracking the phase of the compound signal in the master channel. The same value of the tracked phase in the master channel is applied to the slave channel and represented in (c) a simplified model and (d) a model including the phase contributions from other factors, e.g., possible baseline between the master and slave antennas. Panels (a) to (c) are reused from [44].

where the in-phase (I) and quadrature (Q) components of the master channel output are:

$$I_m = A_d \cos(\delta\varphi) + A_r \cos(\psi - \delta\varphi) = A_c \qquad (2.12)$$

$$Q_m = -A_d \sin(\delta\varphi) + A_r \sin(\psi - \delta\varphi) = 0 \qquad (2.13)$$

with subscript m referring to the master channel. From Figure 2.8(b), the value of the phase difference between the direct and compound signals ($\delta\varphi$) can be derived using:

$$\tan(\delta\varphi) = \frac{\sin(\delta\varphi)}{\cos(\delta\varphi)} = \frac{\frac{A_r \sin(\psi)}{A_c}}{\frac{A_d + A_r \cos(\psi)}{A_c}} = \frac{A_r \sin(\psi)}{A_d + A_r \cos(\psi)} \qquad (2.14)$$

The following equation can be used to calculate $e^{-j\delta\varphi}$:

$$e^{-j\delta\varphi} = \cos(\delta\varphi) - j\sin(\delta\varphi) \tag{2.15}$$

$$= \frac{A_d + A_r\cos(\psi) - jA_r\sin(\psi)}{A_c} = \frac{A_d + A_r e^{-j\psi}}{A_c} \tag{2.16}$$

The Signal-to-Noise Ratio (SNR) observations, similar to geodetic receivers' SNR, can be worked out by applying the law of cosines in Figure 2.8(b):

$$A_c^2 = I_m^2 = A_d^2 + A_r^2 + 2A_d A_r \cos\psi \tag{2.17}$$

As can be seen from the latter formula, the SNR value does not depend on $\delta\varphi$. In contrast, the in-phase component of the master channel, before squaring, depends on $\delta\varphi$ and should be accounted for in the analysis.

The phase rotation applied to the master channel to track the phase of the compound signal is concurrently applied to the slave channels. A tilted orientation would be favorable for the slave antennas since they are usually utilized to capture reflections from land or sea surfaces. Such an orientation can amplify the received reflections by assigning higher antenna gains to the reflected signals. Depending on the polarization of the tilted antenna, the intercepted direct and reflected signals would have different magnitudes. The effect of polarization of the reflected signals in association with the polarization design of the slave antenna is discussed in section 2.4.1. Figure 2.8(c) depicts the phasor diagrams for the slave channel. The amplitudes of the direct and reflected signals are changed due to the antenna gain factor. For simplicity, this panel does not show the other affecting factors, including the baseline effects between master and slave antennas, the effect of different phase wind-ups, and the phase center offset and variation. These effects are summarized by ε_d and ε_r for the direct and reflected signals, respectively (see Figure 2.8(d)). Therefore, the compound signal in the slave channels can be expressed in the following form:

$$A_c' e^{j\Delta\varphi} = A_d' e^{-j(\delta\varphi + \varepsilon_d)} + A_r' e^{j(\psi - \delta\varphi - \varepsilon_r)} \tag{2.18}$$

$$A_c' e^{j\Delta\varphi} = e^{-j\delta\varphi}.(A_d' e^{-j\varepsilon_d} + A_r' e^{j(\psi - \varepsilon_r)}) \tag{2.19}$$

$$A_c'^2 = I_s^2 + Q_s^2 \tag{2.20}$$

$$= A_d'^2 + A_r'^2 + 2A_d' A_r' \cos(\psi + \varepsilon_d - \varepsilon_r) \tag{2.21}$$

where the prime symbol $'$ is used to distinguish the amplitudes in the slave channel from those in the master channel. The formulation introduced in this section only accounts for RHCP reflected signals. A possible contribution from LHCP reflected signals is discussed and formulated in the following section.

2.4.1 Ellipticity and polarization of the reflected signals

Here, the direct signals are considered to be pure RHCP signals. However, the polarization of direct GPS signals can be slightly elliptical. According to the GPS documentation (IS-GPS-200M), the ellipticity of GPS L1 signal is below 1.2 dB for Block IIA satellites and 1.8 dB for Block IIR/IIR-M/IIF/III/IIIF satellites. Regarding the L2 signal, the ellipticity shall be no worse than 3.2 dB for Block II/IIA satellites and 2.2 dB for Block IIR/IIR-M/IIF and GPS III/IIIF satellites. These ellipticity limits are considered to be valid over the angular range of ± 13.8 degrees from the GPS satellite's nadir.

The nearly circular polarization of direct GPS signals can significantly change upon reflection. Consequently, reflected GPS signals can generally be regarded as elliptically polarized signals with RHCP and LHCP components. Common geodetic antennas have an RHCP design. These antennas are configured in a way that the possible LHCP component of the incoming signal is suppressed. For reflectometry receivers with multiple antenna inputs, an RHCP design with upward orientation (or slightly tilted from the zenith) is usually considered for the master antenna, similar to that of geodetic antennas. This setting assigns higher antenna gains to the incoming direct signals and facilitates the signal tracking processes. However, while an RHCP antenna almost mitigates the possible LHCP component of the direct signals, the signature of the LHCP component of reflected signals can be clearly visible at certain incoming angles for some of the geodetic antennas. Figure 2.9 shows the gain patterns of an RHCP antenna used in this thesis in two different orientations. The left panel is related to the zenith-looking orientation used as the master antenna, and the right panel shows the side-looking orientation, i.e., a tilt of 90 degrees with respect to the zenith, used as a slave antenna. The co-polarization gain of the antenna, which indicates reception performance for RHCP signals, is shown by blue color, and the cross-polarization reception, i.e., LHCP signal, is shown by red color. Dashed lines show the gain values associated with reflected signals.

As can be seen from Figure 2.9, the cross-talk gain of the antenna, i.e., the LHCP reception gain, can be significant for angles below -20° with respect to the zenith-looking antenna's ground plane. To account for the cross-talk component in the received signal at the receiver, Equation 2.6, which follows the simplified repres-
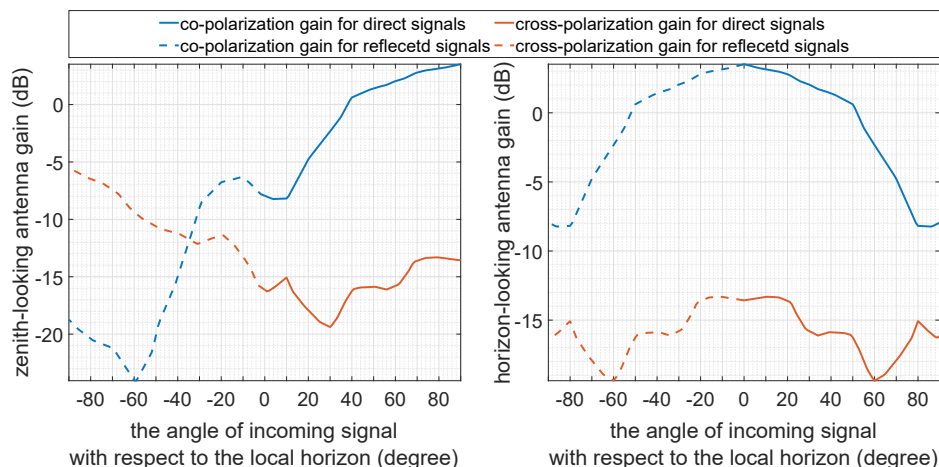
Figure 2.9: An exemplary antenna gain pattern for Righ- and Left-Handed Circular Polarization signals (RHCP and LHCP) referred respectively here as co- and cross-polarization receptions with respect to the RHCP design of the direct signals. Left panel is related to a zenith-looking orientation for the antenna and right panel shows a horizon-looking orientation. The gain values are retrieved from [39].

entation of the reflected signal in Figure 2.8(c), can be elaborated as:

$$A_c e^{j\varphi_c} = A_d \, e^{j\varphi_d} + A_{r_+} \, e^{j(\varphi_d + \psi_+)} + A_{r_-} \, e^{j(\varphi_d + \psi_-)} \tag{2.22}$$

where A_{r_+} and A_{r_-} are the amplitudes of the co-polarization (RHCP) and cross-polarization (LHCP) components of the reflected signal, respectively. Different factors contribute to the phase of the reflected signals. The direct-reflected signals phase difference for the co- (ψ_+) and cross-polarization (ψ_-) components of the reflected signal can have the following elements:

$$\psi_+ = \psi_{\delta\rho} + \psi_{w_+} + \psi_{R_+} + \psi_{\delta pcv_+} \tag{2.23}$$

$$\psi_- = \psi_{\delta\rho} + \psi_{w_-} + \psi_{R_-} + \psi_{\delta pcv_-} \tag{2.24}$$

with $\psi_{\delta\rho}$ being the phase due to the extra path traveled by the reflected signal as shown in Figure 2.10(a). ψ_{w_+} and ψ_{w_-} are the phase wind-up effects (see e.g., [8]) for co- and cross-polarization reflected signals, respectively. ψ_{R_+} and ψ_{R_-} are the phase changes due to the Fresnel reflection coefficients for co- and cross-polarization reflected signals, respectively. The formulas do not include any phase changes due to the sea surface roughness. Similar to the PCV parameter for the direct signal, the reflected signals at the antenna would manifest different phase delays based on the angle of reception. The corresponding effect, which is shown

in Figure 2.10(b), is denoted by $\psi_{\delta pcv_+}$ and $\psi_{\delta pcv_-}$ for the RHCP and LHCP components of the reflected signal, respectively. An exemplary PCV pattern for GPS L1 signal in an RHCP antenna is depicted in Figure 2.11.
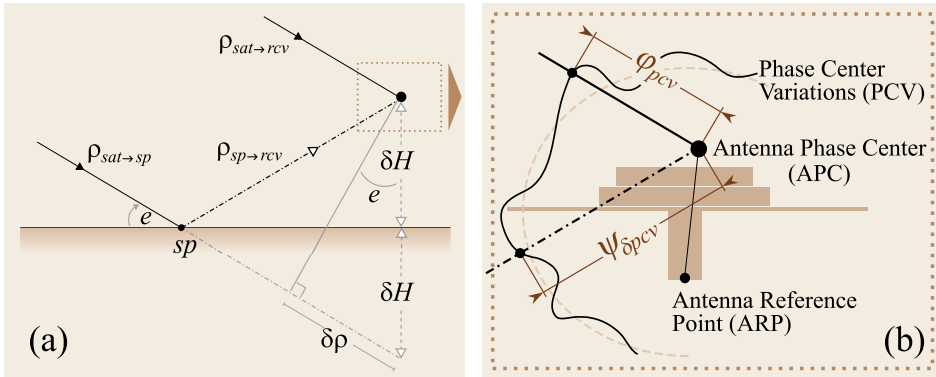
Figure 2.10: (a) The extra path traveled by the reflected signal in a ground-based GNSS-Reflectometry setting, (b) the Phase Center Variations (PCV) of the antenna for the direct and reflected signals. The parameter ρ is used for the signal path with subscript sat, sp, and rcv respectively denoting the satellite, reflection point, and receiver. δH is the height difference between the reflecting surface and the receiver antenna, and e refers to the elevation angle of the satellite. The variables φ_{pcv} and $\psi_{\delta pcv}$ are the phase residuals due to the PCV for the direct and reflected signals, respectively.
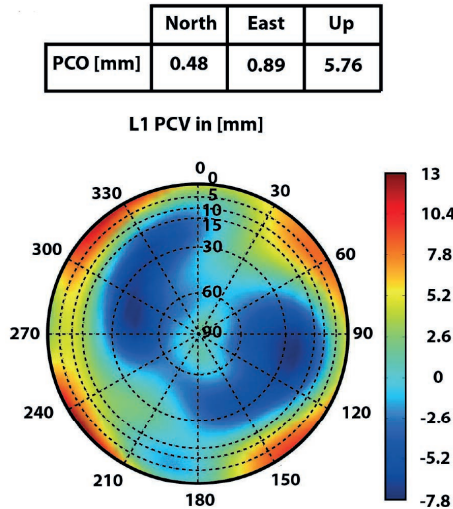
Figure 2.11: An example of the antenna Phase Center Offset and Variation (PCO and PCV) for GPS L1 signal in millimeter (image source: [35]).

An analysis of the parameters in Equation 2.22 is given as follows, starting with the amplitudes A_d, A_r. The amplitudes of the received direct and reflected signals in the receiver from the master antenna vary due to several factors, one of which is the antenna gain factor. Moreover, the receiver applies an Automatic Gain Controller (AGC) factor to adjust the received signal power. The AGC factor would be similar for each antenna input. These two factors, i.e., the antenna gain and AGC, will be indicated by F and k, respectively. The factor k is applied to the compound signal; therefore, it is the same for the direct and reflected signals. We keep using the subscript d and r to refer to the direct and reflected signals and the symbols $_+$ and $_-$ to denote the co- and cross-polarization components, respectively. Based on this:

$$A_d = k\, F_d\, U_d \tag{2.25}$$

$$A_{r_+} = k\, F_{r_+}\, U_{r_+} \tag{2.26}$$

$$A_{r_-} = k\, F_{r_-}\, U_{r_-} \tag{2.27}$$

where U_d and U_r are respectively the amplitudes of the direct and reflected signals immediately before reaching the antenna. Assuming that the gain and AGC values are available, the only unknown parameters will be U_d and U_r.

For ground-based GNSS-R with low reflector heights, one can assume that the amplitude of the direct signal before reaching the reflection point and before being intercepted by the antenna is almost the same. In this case, the amplitude of signal before and after reflection can be related through the following equation:

$$U_{r_+} = S(e, \sigma, \lambda)\, R_+(e, \varepsilon)\, U_d \tag{2.28}$$

$$U_{r_-} = S(e, \sigma, \lambda)\, R_-(e, \varepsilon)\, U_d \tag{2.29}$$

where S is a function that translates the random surface roughness to a dampening coefficient between 0 and 1. Here, the effect of roughness is assumed to be independent from the polarization. The standard deviation of the reflecting surface is considered as a measure of surface roughness and is indicated by σ. The elevation angle of the satellite with respect to the reflecting surface is denoted by e. The function S also depends on the wavelength of the carrier signal (λ) and reads [37]:

$$S(e, \sigma, \lambda) = exp(-\frac{1}{2}\frac{(2\pi)^2}{\lambda^2}\sigma^2 \sin^2 e) \tag{2.30}$$

In Equation 2.28 and Equation 2.29, reflectivity of the surface and polarization change due to reflection are described by Fresnel reflection coefficients denoted by R. This factor is a function of the permittivity (ε) and elevation angle (e) and

has the following forms [11]:

$$R_{\parallel} = \frac{\varepsilon_r \sin e - \sqrt{\varepsilon_{air}\varepsilon_r - (\varepsilon_{air}\cos e)^2}}{\varepsilon_r \sin e + \sqrt{\varepsilon_{air}\varepsilon_r - (\varepsilon_{air}\cos e)^2}} \tag{2.31}$$

$$R_{\perp} = \frac{\varepsilon_{air} \sin e - \sqrt{\varepsilon_{air}\varepsilon_r - (\varepsilon_{air}\cos e)^2}}{\varepsilon_{air} \sin e + \sqrt{\varepsilon_{air}\varepsilon_r - (\varepsilon_{air}\cos e)^2}} \tag{2.32}$$

with ε_r being the permittivity of the reflecting medium, $R_{\parallel}$ denoting the reflection with the polarization parallel to incidence plane, and $R_{\perp}$ indicating the reflection polarization perpendicular to the plane. The incidence plane, shown in Figure 2.12, is defined as a plane that contains the surface normal and the propagation vector of the incoming wave (wavevector). The coefficients $R_{\parallel}$ and $R_{\perp}$ (see Figure 2.13)
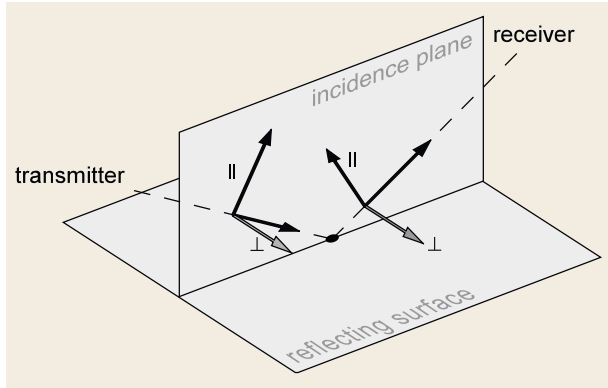
Figure 2.12: A sketch showing the incidence plane as well as the parallel and perpendicular components of the incoming and reflected waves. The figure is reused from [8].

can be combined to yield co- (R_+) and cross-polarization (R_-) forms of the Fresnel coefficients with respect to the incoming RHCP signals [11]:

$$R_+ = \tfrac{1}{2}(R_{\parallel} + R_{\perp}) \tag{2.33}$$
$$R_- = \tfrac{1}{2}(R_{\parallel} - R_{\perp}) \tag{2.34}$$

Figure 2.14 shows the variation of the co- and cross-polarization coefficients (left panel) and amount of power losses due to reflection (right panel) over different elevation angles for three reflecting surfaces. Among the three surfaces, the power loss in the RCHP component of the reflected signal from water (solid blue line in Figure 2.14) is the highest, and from dry soil is the lowest (solid brown line in the figure). This pattern is the opposite of the LHCP component (the dotted lines). Figure 2.15 and Figure 2.16 show the power loss variations due to the RHCP and LHCP Fresnel coefficients as a function of seawater salinity and temperature.
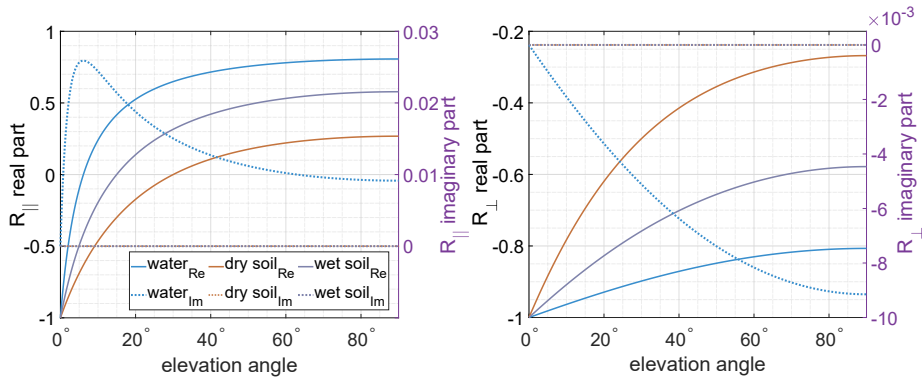
Figure 2.13: Real (*Re*) and imaginary (*Im*) parts of the parallel (left) and perpendicular (right) components of the Fresnel reflection coefficients for water, wet and dry soil. The imaginary parts of the permittivity for wet and dry soil are not considered here.
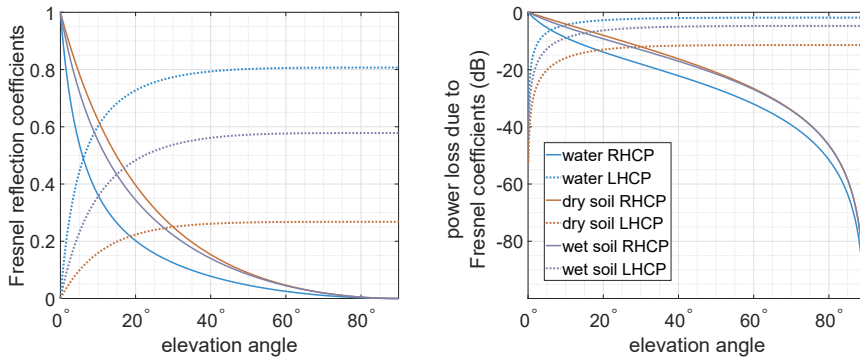
Figure 2.14: The RHCP and LHCP components of the Fresnel reflection coefficients with values ranging from 0 to 1 (left) and corresponding power losses in decibel (dB) (right) for water, wet and dry soil.

Now that all the elements of Equation 2.22 are described, we can use the formula for forward modeling of SNR observations. For this purpose, each term in Equation 2.22 is constructed separately and is shown in Figure 2.17. The actual SNR observations are taken from a ground-based GNSS-R setup at Onsala, Sweden, using a dedicated GNSS-R receiver [28]. An estimated sea surface roughness of $\sigma = 6\ cm$ for the whole observation interval is used in the simulation. For the calculation of $\psi_{\delta\rho}$ sea level measurements from the nearest tide gauge are used. The amplitude of the direct signal before reaching the antenna (U_d) is considered to be almost constant over the interval.
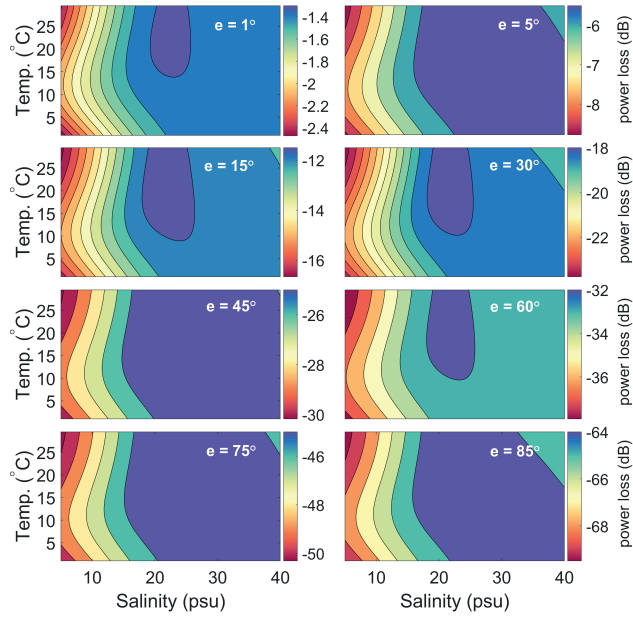
Figure 2.15: Power loss due to the co-polarization (RHCP) Fresnel reflection coefficient as a function of seawater salinity and temperature for different elevation angles.
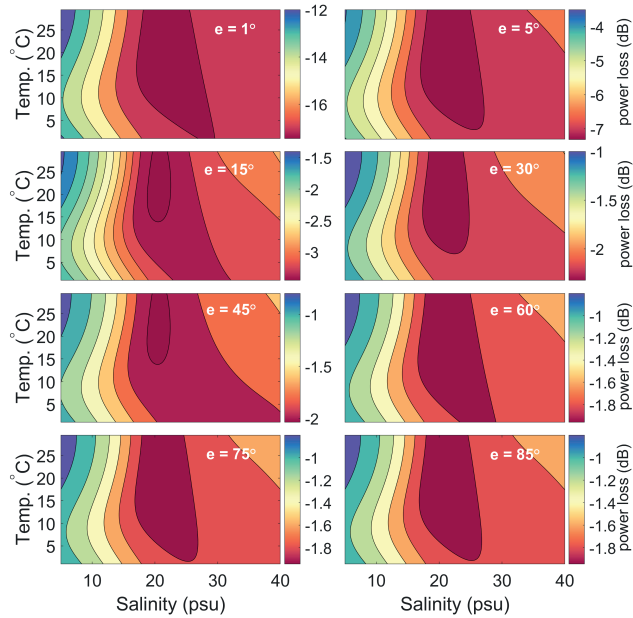
Figure 2.16: Power loss due to the cross-polarization (LHCP) Fresnel reflection coefficient as a function of seawater salinity and temperature for different elevation angles.
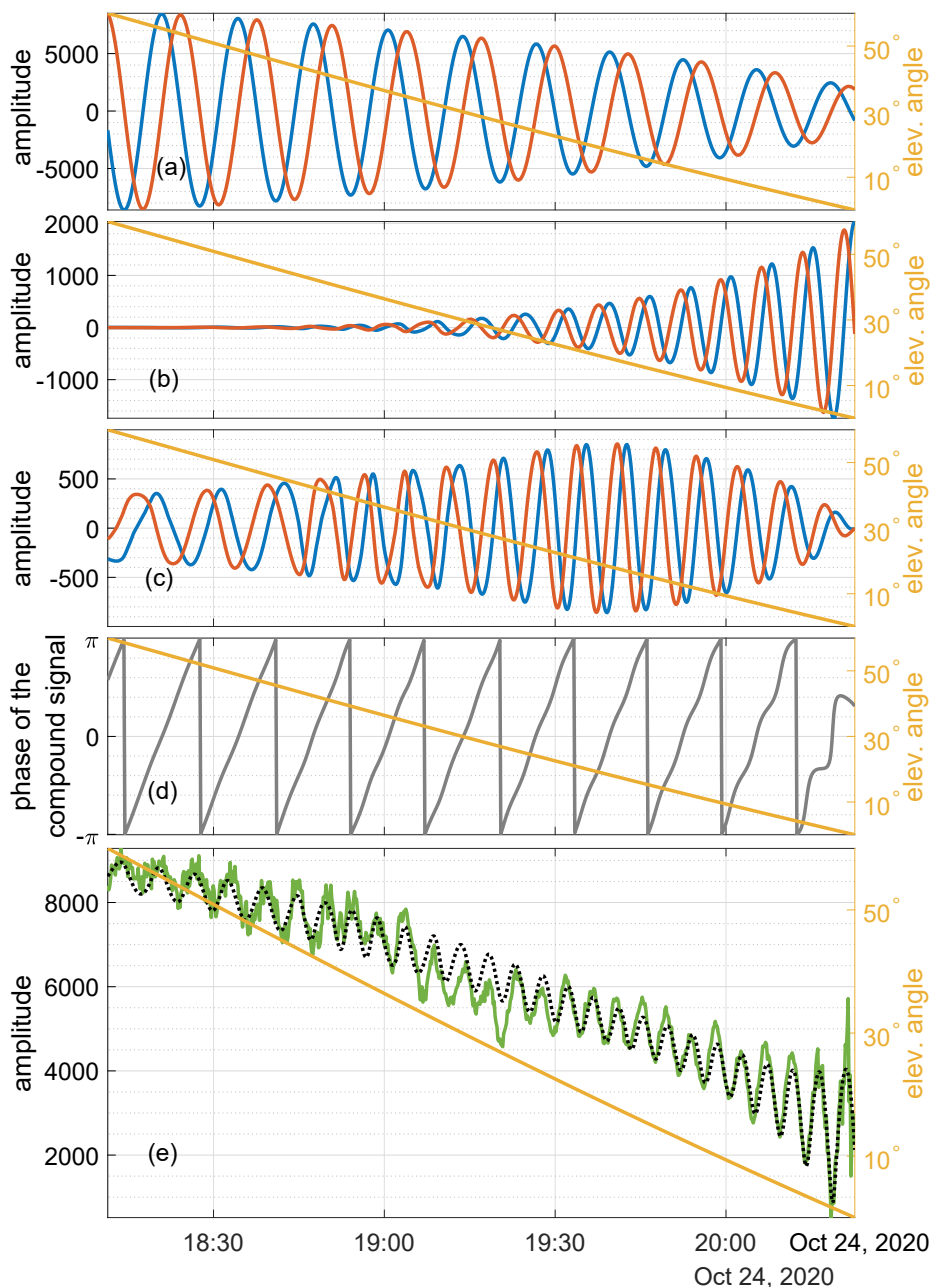
Figure 2.17: Reconstruction of different components of SNR observations from a zenith-looking antenna based on Equation 2.22: (a) contribution of the direct signal, (b) the RHCP component of the reflected signal, (c) the LHCP component of the reflected signal, (d) the phase of the compound signal, and (e) combination of the components (dotted line) overlaid on the actual observations (green line). The blue and red lines in panel (a) to (c) refer to the in-phase and quadrature components of the signals.

2.5 Direct and reflected GNSS signals for remote sensing

GNSS signals as sources of opportunity are being utilized for several remote sensing applications. The general concept behind the GNSS remote sensing is based on investigating the effects of geophysical phenomena that alter the signal characteristics. The remote sensing observations used in this thesis are basically made by investigating the following phenomena:

- the excess path due to the refraction of direct GNSS signals in the troposphere,

- the variation in the strength of reflected GNSS signal due to sea surface roughness, and

- the change of polarization, phase and frequency of GNSS signals in connection to the reflection geometry.

This section describes some of the relevant conceptual foundations for the specified remote sensing applications.

2.5.1 Monitoring the troposphere using GNSS signals

The troposphere is the lowest layer of Earth's atmosphere with the highest density. It is part of the neutral atmosphere that, in contrast to the ionosphere, comprises electrically neural gases [49], including water vapor and dry gases. The neutral atmosphere induces some changes in the propagation of the GNSS signals by altering the speed and bending the signal [30]. Also, this effect introduces an adverse impact on some GNSS applications, e.g., positioning, navigation, and reflectometry; it can be utilized for the remote sensing of the atmosphere. Since the delay caused by the neutral atmosphere is mainly due to the troposphere, the delay is usually referred to as GNSS tropospheric delay [30].

Troposphere modeling and mapping functions

A commonly used expression for the total GNSS tropospheric delay has hydrostatic (due to dry gases) and wet components and reads [14, 32]:

$$\Delta\rho_t(e) = \Delta\rho_h^z M_h(e) + \Delta\rho_w^z M_w(e) \tag{2.35}$$

This formula estimates the total delay ($\Delta\rho_t$) at elevation angle (e) based on the hydrostatic and wet delay in the zenith direction. The delays are respectively denoted by $\Delta\rho_h^z$ and $\Delta\rho_w^z$. To map the zenith delays to the elevation angle direction, two separate mapping functions for the dry (M_h) and wet (M_w) parts are used. The

mapping functions are elevation angle dependent and each one can be distinctly formed by their corresponding coefficients a, b, and c in the following equation [22, 32]:

$$M(e) = \frac{1 + \dfrac{a}{1 + \dfrac{b}{1 + c}}}{sin(e) + \dfrac{a}{sin(e) + \dfrac{b}{sin(e) + c}}} \tag{2.36}$$

Two types of tropospheric delay models with their corresponding mapping functions are mainly in use. The first type includes empirical models. For instance, the following two equations can be used to estimate the hydrostatic [47, 14, 32] and wet [6, 32] components of the delay:

$$\Delta\rho_h^z = \frac{0.0022768\, p}{1 - 0.00266\, cos(2\phi) - 0.28 \times 10^{-6}\, h} \tag{2.37}$$

$$\Delta\rho_w^z = 10^{-6}\, (k_2' + \frac{k_3}{T_m})\, \frac{R_d\, \omega}{g_m\, (\kappa + 1)} \tag{2.38}$$

with p being the pressure, ϕ the latitude, and h the ellipsoidal height of the observation point. The parameters k_2' and k_3 are refractivity constants estimated from laboratory experiments [7]. ω is water vapor pressure, T_m is weighted average of temperature based on water vapor pressure weights, κ is water vapor decrease factor, R_d is the specific gas constant for dry constituents, and g_m is the mean gravity of Earth [32].

The tropospheric delay for any observation point can be estimated using empirical models with few input parameters. However, despite the high-precision estimation of hydrostatic zenith delays in the above approach, the zenith wet delay values would be less precise. Higher precision can be achieved by using the second type of tropospheric models, which are based on the ray-tracing approach using data from Numerical Weather Models (NWMs) [52, 32]. Ray tracing can be defined as the reconstruction of the signal path through different media [53].

The parameters of mapping functions can be derived from climatological models, or NWMs [53]. In the empirical tropospheric models, the parameters a, b, and c are based on empirical functions, while in the models based on NWMs, the parameter a is estimated based on the information from NWMs [32].

GNSS-derived tropospheric data product

The tropospheric effect on GNSS signals can be used to monitor the highly-variable component of the neutral atmosphere, i.e., water vapor. First, the Zenith Total Delay (ZTD, $\Delta\rho_t^z$) is calculated through data processing of GNSS stations along with other unknowns, such as the station coordinates. Then, by having a precise model of the Zenith Hydrostatic Delay (ZHD, $\Delta\rho_h^z$), e.g., from Equation 2.37, the Zenith Wet Delay (ZWD, $\Delta\rho_w^z$) can be estimated:

$$\Delta\rho_w^z = \Delta\rho_t^z - \Delta\rho_h^z \qquad (2.39)$$

The ZWD estimates can be translated to Precipitable Water Vapor (PWV) using a conversion factor, Q [6]:

$$PWV = \frac{\Delta\rho_w^z}{Q} \qquad (2.40)$$

$$Q = 10^{-6} \, D_w \, R_w \, (k_2' + \frac{k_3}{T_m}) \qquad (2.41)$$

with D_w being the density of liquid water and R_w the specific gas constant for water vapor. The parameters k_2' and k_3 are laboratory-estimated constants [7]. T_m is the water vapor weighted mean temperature in Kelvin. An example of GNSS-derived PWV time series for a permanent station in Germany is shown in Figure 2.18.
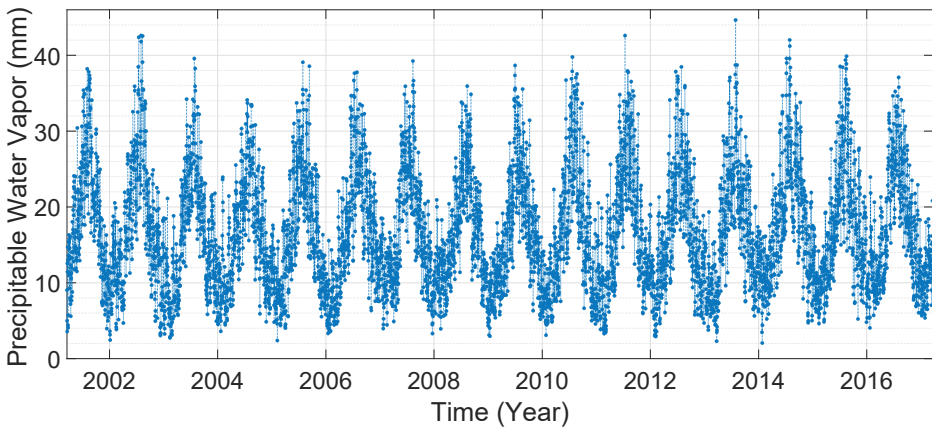
Figure 2.18: An example of Precipitable Water Vapor time series from a permanent GNSS station in the southeast of Berlin (latitude: 52.4097, longitude: 13.6022).

Homogeneity of GNSS-derived tropospheric time series

GNSS-derived PWV data provide accurate and high temporal resolution measurements even in severe weather conditions [26]. This has made the GNSS PWV data

one of the reference data for GCOS (Global Climate Observing System) Reference Upper-Air Network (GRUAN) [38]. However, the GNSS-derived PWV time series can include abrupt changes and inhomogeneities due to different reasons, primarily associated with upgrading or modifying the hardware or software in GNSS stations. Since not all the hardware or software changes are well-documented in the stations' log files, a homogenization method for detecting and correcting undocumented changes is necessary.

The GNSS-derived PWV time series, $F = (f_1, f_2, ..., f_N), f_i \in \mathbb{R}, i = 1, 2, ..., N$, can be considered as a linear combination of different components:

$$F = \overbrace{F_t + F_i + F_c + F_s}^{F_{SSA}+\varepsilon} + F_n \tag{2.42}$$

where F_t, F_i, F_c, F_s, and F_n are secular trend, inhomogeneities (mean shifts), cyclic, seasonal, and noise components, respectively. The goal of homogenization is to detect and correct F_i. The workflow of the homogenization method developed in this thesis is shown in Figure 2.19.
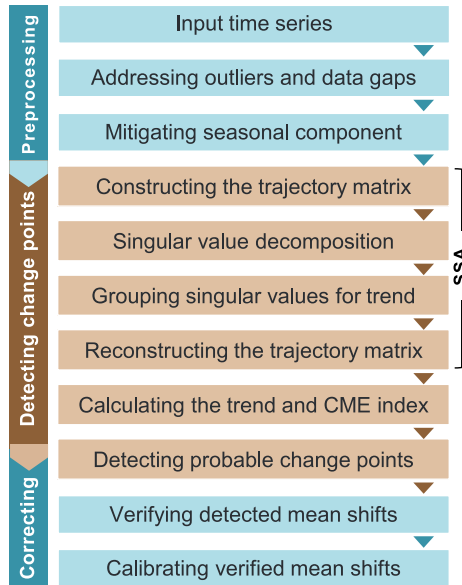
Figure 2.19: homogenization workflow (reused from [26])

This method utilizes Singular Spectrum Analysis (SSA) for retrieving the trend and inspecting the PWV time series for possible abrupt changes. In Equation 2.42, F_{SSA} is the extracted SSA trend, and ε is the residuals after subtracting the trend from the PWV time series. SSA is also used for gap-filling purpose within the data

preprocessing stage. The following section provides a brief description of SSA. More details on the theory and applications of SSA can be found in [19] and [18].

Singular spectrum analysis for inspection of GNSS time series

SSA is a time series analysis tool with a wide range of applications such as extracting time series trend, noise mitigation, forecasting, and change-point detection [1]. Here, we use SSA to model temporal variations of PWV time series and extract a representative trend from the time series. The representative trend is a smoothed, slowly-varying version of the time series with long-term variations and periodicities.

The first step in SSA is to construct a trajectory matrix. The matrix is formed using the elements of the time series. In the following steps, the matrix is decomposed into its principal components and is reconstructed back using the most important principal components of the matrix. Finally, SSA rebuilds the time series using the reconstructed trajectory matrix. These steps are elaborated in the following:

A) Forming the trajectory matrix: By moving a window with the length of L over the entries of the time series (f_i), the trajectory matrix ($\mathbf{X}$) is constructed:

$$\overbrace{f_1, f_2, ..., f_L}^{window \rightarrow}, f_{L+1}, f_{L+2}, ..., f_N$$

$$\mathbf{X} = (x_{ij})_{i,j=1}^{L,K} = \begin{bmatrix} f_1 & f_2 & f_3 & \cdots & f_K \\ f_2 & f_3 & f_4 & \cdots & f_{K+1} \\ f_3 & f_4 & f_5 & \cdots & f_{K+2} \\ \vdots & \vdots & \vdots & \ddots & \vdots \\ f_L & f_{L+1} & f_{L+2} & \cdots & f_N \end{bmatrix} \quad (2.43)$$

with $K = N - L + 1$ and $1 < L < K$.

B) Decomposition of the trajectory matrix: Singular Value Decomposition (SVD)[56] of $\mathbf{X}$ can be written as:

$$\mathbf{X} = \mathbf{U\Sigma V^T} \quad (2.44)$$

with the superscript ^{T} being the transpose operator. $\mathbf{U}$ and $\mathbf{V}$ contain left and right singular vectors, respectively, and Σ is a diagonal matrix containing the singular values (σ_i) of $\mathbf{X}$. Now, the trajectory matrix can be expressed as the sum of its uncorrelated components ($\mathbf{X_i}$):

$$\mathbf{X} = \mathbf{X_1 + X_2 + ... + X_d}, \quad \mathbf{X_i} = \sigma_i \mathbf{U_i V_i^T} \quad (2.45)$$

where d is the index of the smallest non-zero singular value.

C) Grouping components of the trajectory matrix: In the grouping step a group or subset of $\{\mathbf{X_1}, \mathbf{X_2}, ..., \mathbf{X_d}\}$ is selected in order to create a representative estimation of the original trajectory matrix ($\mathbf{X}$). The selected subset defines the smoothness of the final reconstructed time series. If the time series is not dominated by noise, the first few singular values can generally reflect a significant part of the total information within the time series. Details about the specific grouping approach chosen in our homogenization method can be found in [26].

D) Reconstruction of the time series: The selected group of trajectory matrix components, denoted by $\{\mathbf{X_1}, \mathbf{X_2}, ..., \mathbf{X_I}\}$, are added to reconstruct a matrix associated with the time series trend.

$$\mathbf{X_{trend}} = \mathbf{X_1} + \mathbf{X_2} + ... + \mathbf{X_I} = (\hat{x}_{ij})_{i,j=1}^{L,K} \tag{2.46}$$

Now, we retrieve the time series trend using the anti-diagonal elements of the trend matrix ($\mathbf{X_{trend}}$). Let $L < K$, then the trend of the time series $G = (g_1, g_2, ..., g_N)$ is:

$$g_i = \begin{cases} \frac{1}{i} \sum\limits_{m=1}^{i} \hat{x}_{m,i-m+1} & 1 \leq i < L \\ \frac{1}{L} \sum\limits_{m=1}^{L} \hat{x}_{m,i-m+1} & L \leq i \leq K \\ \frac{1}{N-i+1} \sum\limits_{m=i-K+1}^{N-K+1} \hat{x}_{m,i-m+1} & K \leq i \leq N \end{cases} \tag{2.47}$$

where $\hat{x}_{i,j}$ is an entry of the reconstructed trajectory matrix, which estimates the original element of the time series f_{i+j-1}. Therefore, the SSA-estimation of the element f_k can be calculated by averaging all $\hat{x}_{i,j}$ satisfying: $k = i + j - 1$.

We define an index called the Change Magnitude Estimator (CME) or symbolically ξ, to measure the amount of change around every single epoch of the time series. Having ξ values, we can detect all the local maxima of the CME diagram, which indicate the change points and their significance. Figure 2.20 shows the behavior of the CME index in the presence or absence of a change (mean shift) in a simulated time series. The CME index can be calculated through:

$$\xi^2 = \begin{cases} 0 & i \in \{1, N\} \\ \frac{1}{i-1} \sum\limits_{m=1}^{i} (\hat{x}_{m,i-m+1} - g_i)^2 & 1 < i < L \\ \frac{1}{L-1} \sum\limits_{m=1}^{L} (\hat{x}_{m,i-m+1} - g_i)^2 & L \leq i \leq K \\ \frac{1}{N-i} \sum\limits_{m=i-K+1}^{N-K+1} (\hat{x}_{m,i-m+1} - g_i)^2 & K < i < N \end{cases} \tag{2.48}$$
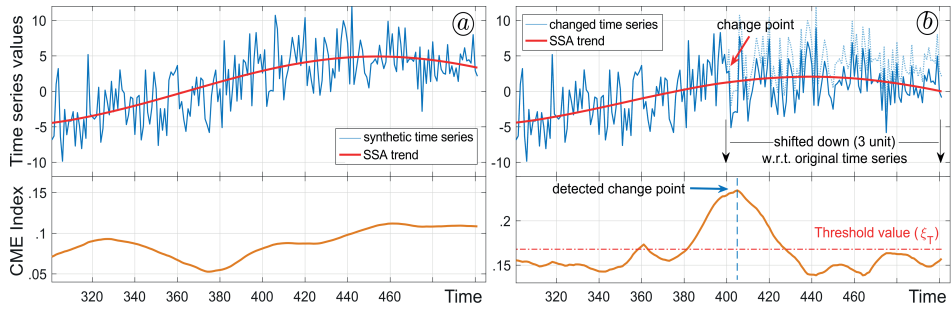
Figure 2.20: The application of Change Magnitude Estimator (CME) index based on Singular Spectrum Analysis (SSA) to a synthetic time series (reused from [26])

The developed SSA-based change detection tool can be applied to PWV time series or other tropospheric data products. It should be noted that homogenization is a delicate process and requires sensitive and careful handling. A mistakenly corrected time series for a fake change point introduces an inhomogeneity to the time series. To avoid such an issue, we apply a zero-difference homogenization approach. In this approach, we independently apply the developed change detection method to three time series: 1) the GNSS-derived time series, 2) a reference time series, 3) the difference time series produced by subtracting the GNSS-derived measurements from the reference time series. Then the detected change points are compared for verification, decision-making, and correcting the time series.

A reference data would be necessary in any robust homogenization approach. The reference time series provides the required information for distinguishing between inhomogeneities and the changes induced by climate or meteorological effects. Moreover, the robustness also demands that the homogenization approach cannot focus only on detecting changes in the difference time series. This is because the reference data might also contain inhomogeneities which would be misassigned to the GNSS data product. An available reference dataset for the PWV time series can be obtained from the NWMs that are released by the European Center for Medium-range Weather Forecast (ECMWF) [15].

2.5.2 Sea surface characterization using ground-based GNSS-R

A significant portion of the global population inhabits coastal regions where many economic and transportation activities are hosted. These regions have been prone to several natural disasters. In the era of climate change consequences, the necessity of monitoring these regions becomes more vital. Along with previous research on GNSS-R usage for monitoring coastal waters, this thesis contributes to two essential aspects of sea surface characterization, i.e., sea-level monitoring and

sea surface roughness estimation. Different factors affecting the performance of GNSS-R coastal altimetry and surface roughness estimation have been investigated. The formulation and the theoretical background used in these assessments are described as follows.

The phase variation due to extra path traveled by the reflected signal, $\psi_{\delta\rho}$, in Equation 2.23 and Equation 2.24 is:

$$\psi_{\delta\rho} = (\frac{2\pi}{\lambda})\delta\rho \qquad (2.49)$$

$$= (\frac{2\pi}{\lambda})(\rho_r - \rho_d) \qquad (2.50)$$

where λ is the carrier wavelength, ρ_r and ρ_d are the path lengths for the reflected and direct signals, respectively. Figure 2.10(a) shows a simple reflection geometry. In a ground-based setup with low reflector heights, i.e., the height difference between the antenna phase center and the reflecting surface, the GNSS signals reaching the antenna and the reflecting surface can be approximately considered to be parallel. In this case, the extra path traveled by the reflected signal ($\delta\rho$) can be approximated by the geometric paths as:

$$\delta\rho_g = 2 \, \delta H_g \sin e \qquad (2.51)$$

where $\delta\rho_g$ is the difference between the geometric paths of the direct and reflected signals, e is the elevation angle of satellite, and δH_g is the reflector height based on assuming the geometric paths shown by dotted lines in Figure 2.21. However, the actual path difference, $\delta\rho_a$, differs from $\delta\rho_g$ due to tropospheric refraction. The refraction induces a bending effect on the signals, which changes the elevation angles at the antenna and reflection points. Moreover, the refraction prolongs the path, leading to an excess phase.

Different approaches can be used for estimating the tropospheric effect in ground-based GNSS-R altimetry. For instance, Equation 2.51 can be modified to account for the bending of the signals [48]:

$$\delta\rho_a = 2 \, \delta H_a \sin(e + \delta e) \qquad (2.52)$$
$$\Delta_{tro} = \delta\rho_a - \delta\rho_g$$
$$\approx 2 \, \delta H_g \cos e \, \sin \delta e \qquad (2.53)$$

with δH_a being the actual reflector height, δe the excess of elevation angle due to the angular effect of the refraction, and Δ_{tro} the tropospheric bending effect on the interferometric path difference. As can be seen from the formula, the tropospheric effect is a function of the reflector height and elevation angle and is always
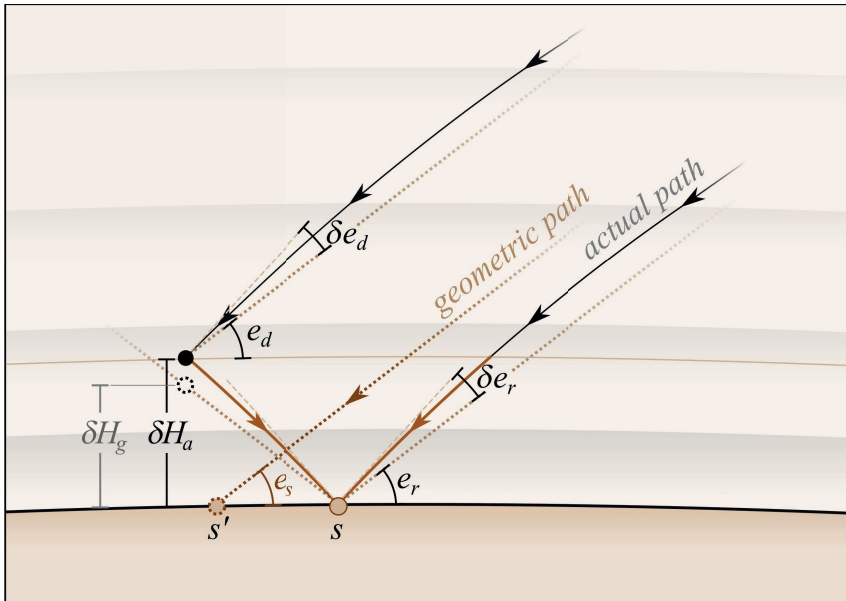
Figure 2.21: The effect of tropospheric refraction on ground-based GNSS-R altimetry.

positive. This means geometric approach in calculation of reflector height, i.e., δH_g, underestimates the actual reflector height δH_a (Figure 2.21). The effect is larger for low elevation angles and decreases at higher elevation angles. Moreover, a larger reflector height results in a larger tropospheric effect. The dashed lines in Figure 2.21 show the tangents to the actual rays. The estimated correction provided by Equation 2.53 corresponds to considering the dashed lines (the tangents) instead of the actual rays (solid lines), which can lead to overestimation of the actual reflector height. Moreover, this correction neglects linear refraction along the propagation path [57]. In contrast, another approach presented by [57] only considers the linear refraction and ignores the angular effect (the bending) on the elevation angle. The latter study utilizes Vienna Mapping Function (VMF1) [9] together with the Global Pressure and Temperature (GPT2w) model [10] to estimate total tropospheric delay at the antenna and reflection point using Equation 2.35. The difference between the two delays is multiplied by two to yield the total tropospheric correction. According to [57], GPS-derived sea levels show a scale error of 13 mm/m and 15 mm/m respectively for L1 and L2 signals due to the tropospheric refraction. This correction is added to the calculated geometric height, δH_g.

A widely used approach for estimating δH_g is based on the spectral analysis of SNR observations. To this end, the Doppler frequency shift caused by the inter-

ference of direct and reflected signals is estimated. This frequency describes the oscillation pattern observed in the SNR observations, otherwise known as the interferometric fringes. The following formulation relates the frequency of interference oscillations to the reflector height:

$$f = \frac{1}{\lambda} \frac{d(\delta\rho)}{dt} \tag{2.54}$$

where f is the interferometric Doppler shift. For simplicity, we introduce and use the variable $x = 2\sin e/\lambda$ in the calculations. The new interferometric frequency, f_x, can be retrieved by [45]:

$$
\begin{aligned}
\delta\rho &= \lambda\, \delta H_g\, x \\
f_x &= \frac{1}{\lambda} \frac{d(\delta\rho)}{dx} = \delta H_g + x \frac{d}{dx}(\delta H_g) = \delta H_g + x\, \delta\dot{H}_g \frac{dt}{dx} \tag{2.55} \\
\delta\dot{H}_g &= \frac{d(\delta H_g)}{dt} \tag{2.56}
\end{aligned}
$$

where $\delta\dot{H}_g$ is the height rate. The sea level retrieval starts with detecting the predominant interferometric frequency (f_{int}) in a power spectrum produced by any spectral analysis. Let us denote the spectral analysis operator as $\mathcal{L}$, then:

$$
\begin{aligned}
P(f_x) &= \mathcal{L}(x, Y) \tag{2.57} \\
\{P_{max}, f_{int}\} &= max[P(f_x)] \tag{2.58}
\end{aligned}
$$

where $P(f_x)$ is the power spectrum retrieved from the spectral analysis, Y is the SNR observation time series after removing the secular trend, and max is the function of detecting the maximum value in the spectrum. The frequency corresponding to the detected P_{max}, i.e., the maximum power within the power spectrum, estimates the reflector height:

$$\delta H_g \approx f_{int} \tag{2.59}$$

The approximation sign in the formula is based on the fact that the contribution of the height-rate, i.e., the second term of Equation 2.55, is not considered in the height estimation. Equation 2.59 is based on the assumption of $\delta\dot{H}_g = 0$. To account for the height-rate effect on the interferometric oscillation, the estimated height from Equation 2.59 can be used as an initial value in an iterative solution. An example of this approach is provided in the following.

Performance assessment of sea surface altimetry

Various setups have been used in GNSS-R experiments for altimetry purposes. Most of the experiments use a zenith-looking geodetic antenna and geodetic receiver. This thesis utilizes ground-based GNSS-R observations from a dedicated

reflectometry receiver called the Occultation, Reflectometry, and Scatterometry (GORS) receiver [21, 51]. The receiver outputs data streams from multiple antennas at I/Q levels with a 200 Hz sampling rate for GPS L1 and L2 signals. We use these simultaneous observations for the performance assessment of GNSS-R sea level measurements in different scenarios.

Within separate studies [40, 45], we applied two different mathematical method for the spectral analysis (Equation 2.57). The first method, i.e., SSA, was used in the first study for the performance assessment in the presence of sea surface roughness. In the second study, we utilized a multivariate spectral analysis tool for different combinations of the GNSS-R I/Q observations. The method is called Least-Squares Harmonics Estimation (LS-HE) and can be applied to datasets with data gaps or unevenly-spaced time series [45]. Besides the harmonic terms with different periods, LS-HE can include some terms to capture the deterministic trend, e.g., linear trend. LS-HE has a multivariate formulation, which effectively detects common-mode signals in a group of time series. This feature enhances the retrieval of the common interferometric signal in I/Q observations. More details about LS-HE method can be found in [4, 3, 42, 17].

The dataset used in the two performance assessment studies is acquired from a receiver with three antennas: one up-looking RHCP antenna as the master link and two sea-looking antennas with RHCP and LHCP designs as the slave links. Based on this setup, four sets of observations are formed in the following scenarios:

- A: The I component of the up-looking RHCP antenna (one time series)

- B: I/Q outputs of the sea-looking RHCP antenna (two time series)

- C: I/Q outputs of the sea-looking LHCP antenna (two time series)

- D: The I/Q components of both sea-looking antennas (four time series)

The observation matrices associated with each scenario include the following columns:

$$
\begin{aligned}
\text{A:} \quad Y &= [I_{m_+}^2] \\
\text{B:} \quad Y &= [I_{s_+}, Q_{s_+}] \\
\text{C:} \quad Y &= [I_{s_-}, Q_{s_-}] \\
\text{D:} \quad Y &= [I_{s_+}, Q_{s_+}, I_{s_-}, Q_{s_-}]
\end{aligned}
\tag{2.60}
$$

with subscripts $+$ and $-$ denoting the RHCP and LHCP, respectively. The subscripts m and s refer to the master and slave channels, respectively. For each

scenario, the analysis is independently done on L1 and L2 observations. The observation matrices introduced in Equation 2.60 are separately analyzed by LS-HE method to retrieve the initial estimations of the reflector height. Then, the following cost function is iteratively minimized to reach a more precise estimation of the sea-level by accounting for the height rate [45]:

$$\min_{\delta H_g, \delta \dot{H}_g} \sum_i^N \|\hat{Y}_i - a_i \sin(\frac{4\pi[\delta H_g + \eta]\sin e}{\lambda} + \phi_i)\| \tag{2.61}$$

$$\eta = \frac{\delta \dot{H}_g \tan e}{\dot{e}} \tag{2.62}$$

where η is a correction term to compensate the height rate effect, $\dot{e}$ is the elevation angle rate ($\dot{e} = de/dt$), $\hat{Y}_i$ is the i-th time series in the observation matrix after removing the linear trend, N is the number of observations processed by LS-HE, which is one in scenario A, two in scenarios B and C, and four in scenario D, a_i and ϕ_i are the amplitude and phase offset of the interferometric signal in the i-th observation time series that are estimated by a least-squares analysis.

Sea surface roughness estimation using polarimetric observations

The effect of random sea surface roughness on the reflection power loss can be described by the model presented in Equation 2.30. One of the studies included in this thesis [28] utilizes this model to estimate the roughness using the I/Q observations from an RHCP and an LHCP sea-looking antennas. The model uses the standard deviation of sea surface height, i.e., σ in Equation 2.30, as an indicator of the sea state. In our study, first the power of direct and reflected signals are estimated through an approach described by [50]. These estimates ($\hat{P}_\bullet$) can be calculated by the following equations [28]:

$$\hat{P}_d = G_d P_0 \tag{2.63}$$
$$\hat{P}_r = G_r |R|^2 S^2 P_0 \tag{2.64}$$

where P_0 is the power of the incoming signal at the antenna and at the reflection point, G is the antenna gain, R is the Fresnel reflection coefficient (Equation 2.33 or Equation 2.34), and S is the surface roughness dampening factor (e.g., Equation 2.30). The subscripts d and r refer to the direct and reflected signals, respectively. Since P_0 is unknown, the power estimates retrieved from the sea-looking RHCP and LHCP antennas can be converted into power ratio forms [28]:

$$L_+ = \frac{\hat{P}_{r_+}}{\hat{P}_{d_+}} = \frac{G_{r_+}}{G_{d_+}} |R_+|^2 S_+^2 \approx |R_+|^2 S_+^2 \tag{2.65}$$

$$L_- = \frac{\hat{P}_{r_-}}{\hat{P}_{d_+}} = \frac{G_{r_-}}{G_{d_+}} |R_-|^2 S_-^2 \approx |R_-|^2 S_-^2 \tag{2.66}$$

The signs $+$ and $-$ are used to refer to the RHCP and LHCP antennas, respectively. The final values of the two power ratios only depend on the Fresnel coefficients and roughness. This approximation is made since the boresights of the antennas are toward the local horizon, i.e., a tilt angle of about 90 degrees with respect to the zenith. Therefore the direct and reflected signals are intercepted with approximately similar gain factors. It should also be noted that in Equation 2.66, the estimated power of the direct signal comes from the RHCP sea-looking link. This is because the LHCP antenna, by design, suppresses the direct RHCP signals. Finally, it is worth noting that taking the direct signal from different channels can raise the issue of different AGC values. This issue is not considered in our study since the AGC values were not recorded during the experiment.

The Fresnel coefficients can be calculated based on the available information about the permittivity of seawater and satellite elevation angle. Based on this, the standard deviation of sea surface height (σ) can be retrieved using the calculated power ratios from different satellites over a temporal window, e.g., 6 hours. The retrieval is independently done for L_+, and L_- through minimization of the following cost function:

$$\min_{\sigma} \sum_i (L_i - |R_i|^2 \, S^2 \,)^2 \tag{2.67}$$

with *min* being the minimum function and the index *i* referring to all of the observations falling in the common temporal window.

2.5.3 Spaceborne GNSS-R scatterometry for the study of mesoscale ocean eddies

Spaceborne GNSS-R can provide a new source of observations for the study of the ocean. High-temporal resolution observations can be made using low-cost small satellites based on low-power GNSS-R sensors. A relatively large dataset from the NASA Cyclone GNSS (CYGNSS) mission is obtained and used in this thesis for a feasibility study of detecting mesoscale ocean eddies in GNSS-R observations [27]. The study seeks possible signatures of change in the ocean surface roughness due to the interaction of the eddies with the atmosphere. The main observation used in our investigation is the Normalized Bistatic Radar Cross Section (NBRCS) denoted by σ_0. This observation is retrieved from the primary observable of GNSS-R, i.e., the Delay Doppler Map (DDM). A brief description of the DDM and NBRCS is as follows.

Ordinary GNSS receivers utilize a close-loop scheme [30] for the acquisition and tracking of direct signals. These receivers find the time delay and Doppler frequency that produce the maximum correlation sum within the generated DDM
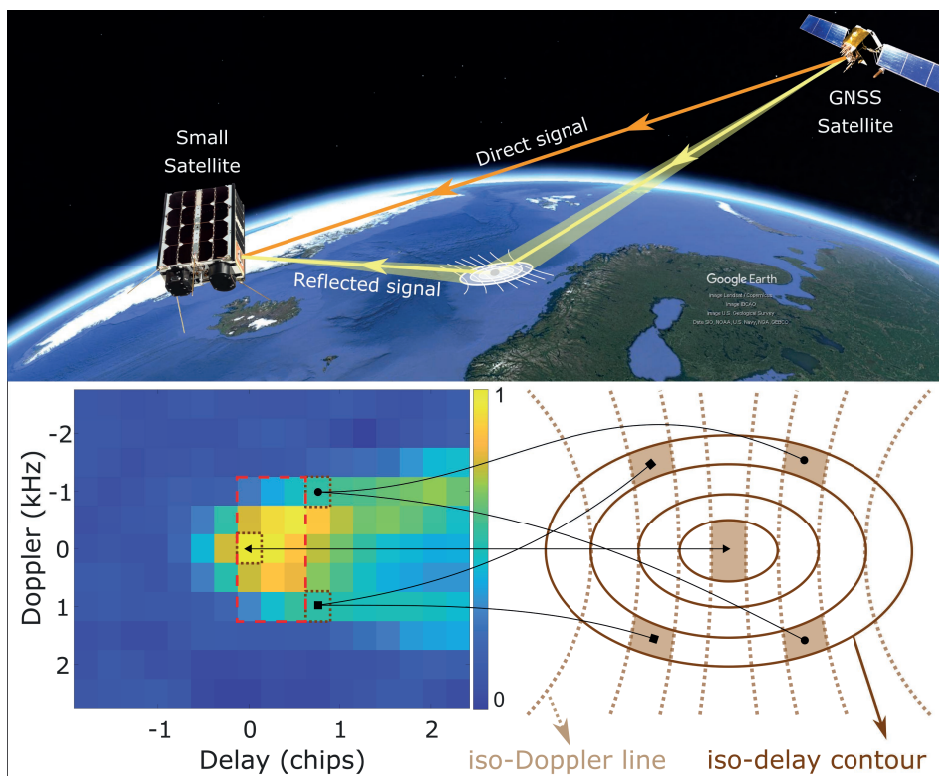
Figure 2.22: (Top) the concept of spaceborne GNSS-R using small satellites, (bottom) an illustration of a Delay Doppler Map (DDM) and corresponding patches on the ocean surface.

(Figure 2.3). In contrast, GNSS-R receivers can apply an open-loop scheme [30] in which predicted values of time delay and Doppler shift are used. The prediction is based on the available information of the geometry and dynamics of the transmitter, receiver, and reflecting surface.

In a ground-based setup with low reflector height, the delay and Doppler values associated with the reflected signal are very close to those of the direct signals. Therefore, in our ground-based studies (see section 2.5.2), in which we used a reflectometry receiver with an open-loop feature, the time delay, and Doppler shift were set to a relative value of zero with respect to the direct signal [28, 45]. In spaceborne setup, however, the delay and Doppler values of the reflected signals are significantly different from those of the direct signals. The relative values, in this case, are with respect to the nominal Specular Point (SP). Such spaceborne receivers measure the power of scattered signals from the oceans or land, based on

a range of predicted time delays and Doppler shifts [46]. Figure 2.22 illustrates variation of the measured power in the delay and Doppler domains. The DDM bins with positive delays are related to the corresponding patches on the reflecting surface.

As can be seen from Figure 2.22, the DDM is a function of the relative delay and Doppler. Negative values of the relative delay correspond to the locations above the surface, from which there is no significant scattered signal [46]. Longer delays are mapped to iso-delay contours on the surface surrounding the SP. The iso-Doppler lines intersecting the iso-Delay contours illustrate the variation of the Doppler frequency shift around the SP. The specular region at the center of the iso-delay contours has a one-to-one connection to the DDM. For the regions outside the specular region, there is an ambiguity due to mapping multiple spatial locations to the same DDM bin [46]. An schematics representation of this ambiguity is shown in Figure 2.22. The process of generating NBRCS values from the raw power measurements shown in the DDM in Figure 2.22 is as follows [46]:

According to [58], the power of GPS scattered signals, as represented by [46], is:

$$P_{g,\hat{\tau},\hat{f}} = \frac{P^T \lambda^2}{(4\pi)^3} \iint\limits_{A} \frac{G^T_{x,y} \; \sigma_{0\,x,y} \; G^R_{x,y}}{(R^T_{x,y})^2 \; (R^R_{x,y})^2 \; L_{a1} \; L_{a2}} \Lambda^2_{\hat{\tau};x,y} \; S^2_{\hat{f};x,y} \; dx \, dy \qquad (2.68)$$

with $P_{g,\hat{\tau},\hat{f}}$ being the coherently processed scattered signal power, in watts; P^T is the transmitted power, $G^T_{x,y}$, and $G^R_{x,y}$ are the antenna gains for the transmitter and receiver, σ_0 is the NBRCS, $R^T_{x,y}$ and $R^R_{x,y}$ are the path lengths from the transmitter to the reflecting surface and from the reflecting surface to the receiver, respectively. L_{a1} and L_{a2} are atmospheric losses to and from the reflecting surface. $\Lambda_{\hat{\tau};x,y}$ is the GPS signal spreading function, $S_{\hat{f};x,y}$ is the frequency response of the GPS signal; and A is the surface integration area, covering the region of diffuse scattering for each delay Doppler bin. Equation 2.68 provides a forward model that relates the factors influencing the power of GPS signals to the received signal at the GNSS-R receiver. Performing the integration expressed in Equation 2.68 over the patches corresponding to each DDM bin will provide a relationship between the affecting factors and the power at that specific bin:

$$P_{g,\hat{\tau},\hat{f}} = \frac{P^T \lambda^2 \bar{G}^T_{\hat{\tau},\hat{f}} \; \sigma_{0\,\hat{\tau},\hat{f}} \; \bar{G}^R_{\hat{\tau},\hat{f}} \bar{A}_{\hat{\tau},\hat{f}}}{(4\pi)^3 \; (\bar{R}^T_{\hat{\tau},\hat{f}})^2 \; (\bar{R}^R_{\hat{\tau},\hat{f}})^2 \; \bar{L}_{a1} \; \bar{L}_{a2}} \qquad (2.69)$$

with the overbar symbol ($\bar{\bullet}$) denoting the effective values corresponding to each DDM bin. For each DDM bin, the effective scattering area on the reflecting surface is represented by $\bar{A}_{\hat{\tau},\hat{f}}$. Equation 2.69 can be used to calibrate the estimated

power values for each DDM bin in the receiver for non-geophysical effects. The CYGNSS dataset used in this thesis offers two separate parameters, which are used in the calculation of σ_0. The parameters, which are in the form of 11×17 matrices, include the Bistatic Radar Cross Section (BRCS, σ), (unnormalized for the effect of the scattering area), and the estimation of effective scattering area ($\bar{A}_{\hat{\tau},\hat{f}}$)[46]. The NBRCS values can then be calculated from near specular DDM bins, e.g., a matrix of 3 delay bins $\times$ 5 Doppler bins (dashed red line in Figure 2.22):

$$\bar{\sigma}_0 = \frac{\bar{\sigma}_{total}}{\bar{A}_{total}} = \frac{\sum_{i=1}^{N} \sum_{j=1}^{M} \bar{\sigma}_{\tau_i,f_j}}{\sum_{i=1}^{N} \sum_{j=1}^{M} \bar{A}_{\tau_i,f_j}}, \qquad N = 3, M = 5 \tag{2.70}$$

where $\bar{\sigma}_{\tau_i,f_j}$ are the bin-by-bin estimation of BRCS values and $\bar{A}_{\tau_i,f_j}$ are corresponding effective scattering areas. For more detailed explanation about the CYGNSS data products and the calibration procedure, we may refer to [46].

The values of NBRCS are mainly governed by three parameters: permittivity of ocean water (a function of ocean surface salinity and temperature), incidence angle of GPS signals (or the elevation angle of the transmitter) at the reflection point, and the ocean surface roughness. The effects of the incidence angle (θ) and permittivity are packed into the Fresnel reflection coefficients which are discussed in the previous section. The surface roughness or sea state can be expressed through different parameters, e.g. Significant Wave Height (SWH), or Mean Square Slopes (MSS). The following simplified formula makes the connection between the NBRCS (σ_0) and MSS (ξ) values [46]:

$$\sigma_0(\theta) = \frac{|R(\theta)|^2}{\xi} \tag{2.71}$$

In our studies [25, 27], we assume that the incidence angle of the signals at the reflection point change gradually for successive NBRCS measurements. Therefore, any sudden change appearing between successive σ_0 values can be designated to parameters other than the incidence angle.

To investigate possible signatures of the oceanic eddies in the σ_0 measurements, we first retrieve the location and radius of the eddies (R) using an ancillary dataset. Then, a long-enough segment of the σ_0 track passing over the eddy is retrieved from the CYGNSS dataset. Figure 2.23 shows an eddy with an overpass σ_0 profile. To analyze and justify the variation of σ_0 profile over the eddies, the CYGNSS measurements are collocated with some ancillary datasets. Possible signatures of the eddies can mainly stem from the following phenomena:

- **Eddy surface current** can interact with the overpass wind field and change surface stress (Figure 2.24). At high-enough wind speeds (e.g., $\approx$5 m/s or
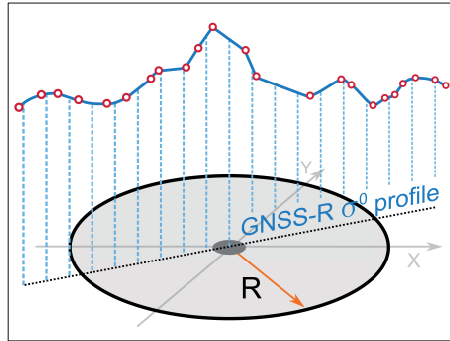
Figure 2.23: An illustration of the CYGNSS GNSS-R σ_0 profile over a mesoscale ocean eddy with the radius of *R*. The figure is reused from [27].

more), the intensity of GNSS reflections is controlled by two main mechanisms: the varying surface stress exerted by wind and the interaction of surface currents with short waves [27]. At low wind speeds, GNSS-R measurements become more sensitive to the surface state, even to small-scale roughness modifications. Under favorable conditions, i.e., low-enough wind speeds, such modifications from eddy surface currents can be detected in GNSS-R σ_0 variations.
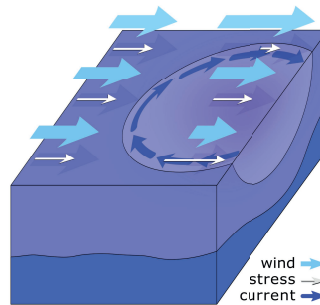
Figure 2.24: Variation of surface stress over an eddy due to the interaction of an overpass wind field with the eddy-induced surface current. The figure is reused from [27].

- **Eddy-induced anomalies in Sea Surface Temperature (SST)** can result in a varying wind field owing to the change in atmospheric boundary layer [31]. GNSS-R σ_0 responds to the modified local surface wind under the influence of marine boundary layer dynamics [27]. Warm-core eddies (Figure 2.25, left) can enhance the local wind leading to an increase in the surface roughness and an abrupt decrease in the GNSS-R NBRCS values. Cold-core ed-

dies (Figure 2.25, right) can introduce a dampening effect on wind intensity due to downward transport of wind momentum. This effect can decelerate the local wind and create a sharp peak in the σ_0 profile over the core region of the cold-core eddy [27].
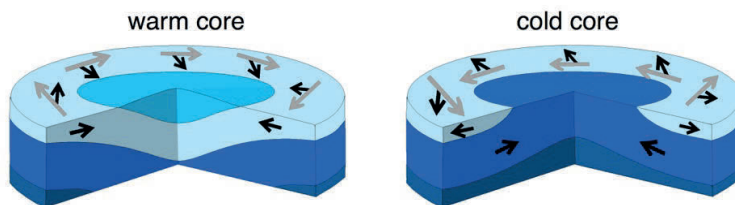
Figure 2.25: Schematic representations of warm-core and cold-core eddies (image source: railsback.org/Oceanography.html.)

- **Concentrated surfactants** can also enhance the power of reflected GNSS signals. Biogenic films from natural life (e.g., released from plankton and fishes) in the ocean can be brought to the surface by the turbulence associated with the eddies. Where surfactants are concentrated on the surface, the surfactant molecules can generate a surface tension that inhibits the development of Bragg waves [16, 27]. This leads to a suppressed surface roughness, visible on Synthetic Aperture Radar (SAR) images as dark regions (see Figure 2.26). This is because almost no back-scattering happens for the Radar signals and they are mainly forward scattered over these regions. For the GNSS-R concept in bistatic configuration, a boosted forward scattering over these regions strengthens the power of GNSS reflections, and a sharp increase in the σ_0 values can be seen.
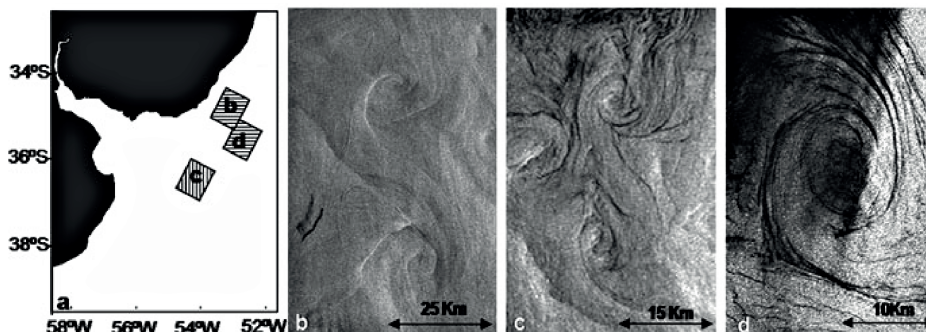
Figure 2.26: (a) A map showing the locations of the SAR images, (b) to (d) three examples of eddies signature in SAR images from ERS-2 mission (image source: [16]).

2.5.4 Flood detection and mapping using GNSS reflections

In recent years, the frequency of heavy precipitation and consequently flooding has significantly increased in many regions all over the world. Figure 2.27 shows a global prediction for the return period of flooding for the 21st century [23]. Detection and mapping of flooding events are of particular importance for two phases, i.e., during flood for emergency management, and after flood, for the assessments of damages and destruction, land use planning, as well as re-construction standards [43]. Therefore, providing accurate and timely information about the extent of floods and destruction is crucial.
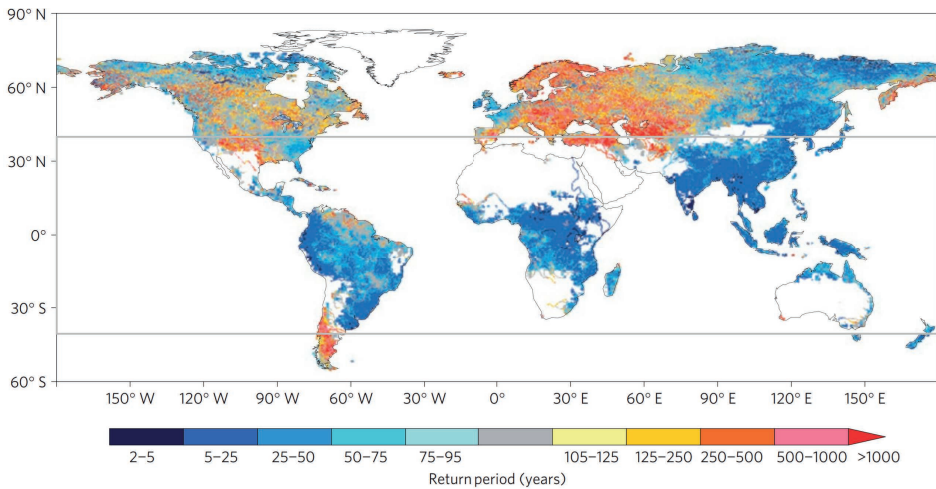
Figure 2.27: Global prediction map of flooding return period for 21st century. The gray lines show the coverage limits of the CYGNSS GNSS-R mission (image source: [23]).

Spaceborne GNSS-R as an emerging remote sensing technique has the potential to be used for flood detection and mapping. This technique has specific features that can provide a robust solution for flooding applications. The L-band frequency used for the satellite navigation systems creates a measuring tool, which is almost insensitive to severe weather conditions or heavy precipitation. The instrumentation used for the GNSS-R sensors is relatively low-cost and low-power. This makes the GNSS-R sensors to be a suitable choice for small satellite technology. Therefore, an inexpensive constellation of small satellites with GNSS-R payloads can make a spaceborne global Earth monitoring system with high temporal resolution. Since 2017, the NASA CYGNSS mission has provided spaceborne GNSS-R observations over tropical regions. The coverage of this mission is marked in Figure 2.27 by gray lines. With the constellation of eight satellites, the mission delivers an average revisit time of about seven hours. This thesis includes the application of

the CYGNSS dataset to flood detection and mapping during torrential rain in 2020 in the southeastern part of Iran, mainly over Sistan and Baluchestan province [43].

As discussed in the previous section, the peak power of each DDM generated by the GNSS-R receiver, includes several non-geophysical factors which should be accounted for. The following equation relates the factors to the coherent component of the power for the received GNSS reflected signals [13]:

$$P^R = \frac{P^T G^T}{4\pi (R^T + R^R)^2} \frac{G^R \lambda^2}{4\pi} \Gamma \tag{2.72}$$

where P^T is the transmitted RHCP power, G^T is the gain of the transmitter antenna, R^T and R^R are the lengths of the transmitter to reflection point and reflection point to receiver paths, respectively, G^R is the gain of the receiver antenna, λ is the GPS wavelength (≈ 0.19 m), and Γ is the Surface Reflectivity (SR).

For the simplicity of calculation, we can work in decibel (dB) scale. For conversion to dB scale, e.g., for a power value of P, the following formula can be used:

$$P_{dB} = 10 \log_{10}(P) \tag{2.73}$$

Then, the surface reflectivity in dB scale can be calculated by [13]:

$$\Gamma_{dB} = P_{dB}^R - P_{dB}^T - G_{dB}^T - G_{dB}^R - 20 \log \lambda + 20 \log(R^T + R^R) + 20 \log(4\pi) \tag{2.74}$$

There are following variables in the CYGNSS Level-1 (L1) data that can be used for the calculation of SR:

- **ddm_snr** is the SNR value in dB scale, which is the ratio of DDM peak power to the noise floor. SNR value is proportional to P_{dB}^R.

- **gps_tx_power_db_w** (P_{dB}^T)

- **gps_ant_gain_db_i** (G_{dB}^T)

- **sp_rx_gain** (G_{dB}^R)

- **tx_to_sp_range** (R^T)

- **rx_to_sp_range** (R^R)

By retrieving the above-mentioned variables from the CYGNSS L1 data, we can calculate a value that in magnitude is not equal to SR but it is directly proportional to Γ [13]:

$$\Gamma_{dB} \propto SNR_{dB} - P_{dB}^T - G_{dB}^T - G_{dB}^R - 20 \log \lambda + 20 \log(R^T + R^R) + 20 \log(4\pi) \tag{2.75}$$

Detection of flooded areas is done by applying a certain threshold to the calculated Γ values. This means the SR-proportional values (right side of Equation 2.75) above a specific limit are considered to be associated with inundated or partially inundated areas [13, 43]. This approach stems from the fact that the presence of water significantly changes the permittivity of the reflecting surface. The difference in reflection power losses due to different permittivities of dry soil and water are depicted in Figure 2.14, right panel.

Several issues can affect the accuracy of flood detection using GNSS-R measurements. The transmitting power of GPS satellites (P^T) can be different for different GPS blocks and can also decay due to aging. Inaccurate information about the transmitter antenna gain or the attitude of the satellite can be another error source. The issue of attitude determination is also valid for the receiver satellite. The attitude determination errors can be translated to incorrect gain value for the receiving antenna and misinterpreted as a geophysical effect. Another issue is related to the combined effect of incidence angle and topography of the reflecting surface. We apply a data preparation procedure to reduce some of the impacts of the mentioned issues. The key items of the data preparation procedure are as follows:

- *Calibration of transmitting power biases:* GPS satellites in different blocks or with different ages might have different transmission powers. This variation introduces some biases compared to the approximated values of the transmitter power and should be taken into account during the analysis. Different GPS PseudoRandom Noise (PRN) codes also contribute to the biases [43]. To address this issue, we calibrate the SNR values of different GPS satellites (SNR_{dB}) using empirically estimated biases, which can be found in [43].

- *Filtering high incidence angles:* high incidence angles can influence the coherent reflection from the surface. Therefore, we have removed all the observations with incidence angles above 65 degrees in our study [43].

- *Removing poor quality observations:* each observation made by CYGNSS satellites is accompanied with a quality control flag, which is a number indicating possible issues related to that specific observation. We eliminate all the observations with quality flags indicating the following issues: S-band transmitter powered up, spacecraft attitude error, black body DDM, DDM is a test pattern, the direct signal in DDM, and low confidence in the GPS Equivalent Isotropically Radiated Power (EIRP) estimate [43].

- *Additional filtering:* the CYGNSS observations with SNR_{dB} below 2 dB or with receiving antenna gains beyond the range of 0 to 13 dB are removed

from the analysis after [12].

Chapter 3

Results

This chapter briefly presents the main results of this dissertation. In addition, the connections of the papers of this dissertation with the raised research questions in Section 1.3 are also explained.

3.1   Overview

The thesis aims to contribute to quality improvement of the GNSS data products and investigate novel applications of the GNSS remote sensing measurements for climate and environmental monitoring. Towards this goal, the following papers are delivered to address the referred research questions:

Paper A presents a new approach for homogenizing GNSS-derived tropospheric products. The homogenization approach is successfully applied to simulated and real datasets ($\rightarrow$RQ 1.1). The process of water vapor trend retrieval is shown to be significantly improved after applying the homogenization approach ($\rightarrow$RQ 1.2).

Paper B describes the results of estimating sea surface roughness based on the GNSS-R observations in different polarizations. In this paper, the polarization-dependent results are verified against the local wind. Moreover, the effect of nearby coastlines on the measurements is also investigated. The results of this paper suggest that using fully-polarimetric GNSS-R observations can enhance the sea surface roughness estimation ($\rightarrow$RQ 2.1). In *paper C*, the possible impact of precipitation on GNSS-R observations in terms of seawater permittivity and sea surface roughness is investigated. This study investigates the effect using polarimetric GNSS-R observations and shows that the effect of rain is discernible in the roughness measurements ($\rightarrow$RQ 2.1). Similar reflectometry observations are analyzed for sea-level monitoring in *paper D*. This paper investigates the possible

effects of sea surface roughness on sea-level measurements. The results confirm that the surface roughness, or sea state, has a degrading impact on the sea surface height estimation (→RQ 2.1). *Paper E* describes the roles of polarization and orientation of the antenna as well as using signals with different wavelengths for sea level measurements. This study elucidates which configuration can improve the performance of GNSS-R sea-level measurements (→RQ 2.1). Based on these studies, a favorable setup for a coastal GNSS-R station is suggested to use a tilted antenna towards the reflection zone to assign the maximal gain to the reflected signals (→RQ 2.2). Using two antennas with different polarization and combining the results can enhance the quality of measurements (→RQ 2.2). The multi-frequency feature should be considered for a GNSS-R station since it significantly increases the number of observations leading to more robust sea surface characterization (→RQ 2.2).

Paper F for the first time reports on a possible application of spaceborne GNSS-R for observing mesoscale ocean eddies. The signatures of these oceanic features in the Normalized Bi-static Radar Cross Section (NBRCS) observations are investigated in this study. The results show that under certain conditions, spaceborne GNSS-R can observe the eddy-induced roughness change caused by the interaction between the atmosphere and ocean over the eddies (→RQ 3.1). In *Paper G* the spaceborne observations of surface reflectivity are used to detect and map a flooding event during torrential rain. The observations have a revisit time of about 7 hours, making the technique a suitable candidate for natural hazard monitoring purposes. The results of this study confirm the successful detection of inundated areas (→RQ 3.1). Based on the results achieved from the studies mentioned above, a GNSS-R CubeSat concept is proposed to perform high-resolution observations over selected regions (→RQ 3.2). A description of the proposed CubeSat concept is included in Chapter 4.

3.2   Papers of the dissertation

This section provides a short description of the content, methodology, results and the contribution of the authors in each paper of this dissertation.

3.2.1   Paper A: Towards a Zero-difference Approach for Homogenizing GNSS Tropospheric Products

Content

Long-term GNSS-derived tropospheric products, e.g., Precipitable Water Vapor (PWV) time series, are among the established GNSS remote sensing data products. However, the data might contain some inhomogeneities that challenge its validity for climate or meteorological applications. The origin of the inhomogeneities

could be related to hardware or software changes in the GNSS station. This paper presents a novel homogenization approach. The approach is equipped with an off-set detection method based on Singular Spectrum Analysis (SSA) to detect abrupt changes as the indicator of possible inhomogeneities. Since some climatic or meteorological effects can also introduce similar sudden changes, any homogenization approach needs some ancillary data or a reference time series, e.g., from numerical weather models, to prevent the miscorrection of these effects. The reference time series, however, can also have some inhomogeneities. The proposed approach in this study can distinguish the origin of the detected changes and safely correct the GNSS-derived tropospheric time series. The performance of the offset detection method developed in this study is assessed using simulations. The impact of homogenization is also demonstrated by applying the approach to a nationwide GNSS dataset consisting of 214 stations over Germany.

Research Method

The methodology of this paper includes detection of offsets (mean shifts), verification of the origin of the offsets, and correction of the verified inhomogeneities. The offset detection method developed in this study is based on the SSA technique. This technique creates a vector subspace using the elements of the time series. In doing so, SSA uses a sliding window to gradually role over the time series elements and form a matrix called trajectory matrix. The principal components of this matrix are used to retrieve a representative trend of the time series. The issue of data gaps is also addressed using the SSA technique. A change estimator parameter is defined to measure the distribution of the time series around the representative trend. The possible candidates for the change points exhibit themselves by large values of the change estimator parameter. Finally, the validity of this detection is checked using a statistical test.

The study uses reference time series from the European Centre for Medium-Range Weather Forecasts (ECMWF) ERA-Interim reanalysis dataset to distinguish the origin of a detected offset. For each GNSS station, the developed offset detection method is independently applied to three time series, and the results are used to verify the origin of the offsets. The three time series are the GNSS PWV time series, ERA-Interim PWV time series, and the difference. The detected changes in the difference time series can be connected to inconsistencies in the GNSS time series, ERA-Interim time series, or abrupt changes due to climatic effects. The decision about correcting the detected change for each case is made based on: 1) the appearance of the offsets in the three time series, 2) their time index, and 3) the values of the mean shifts.
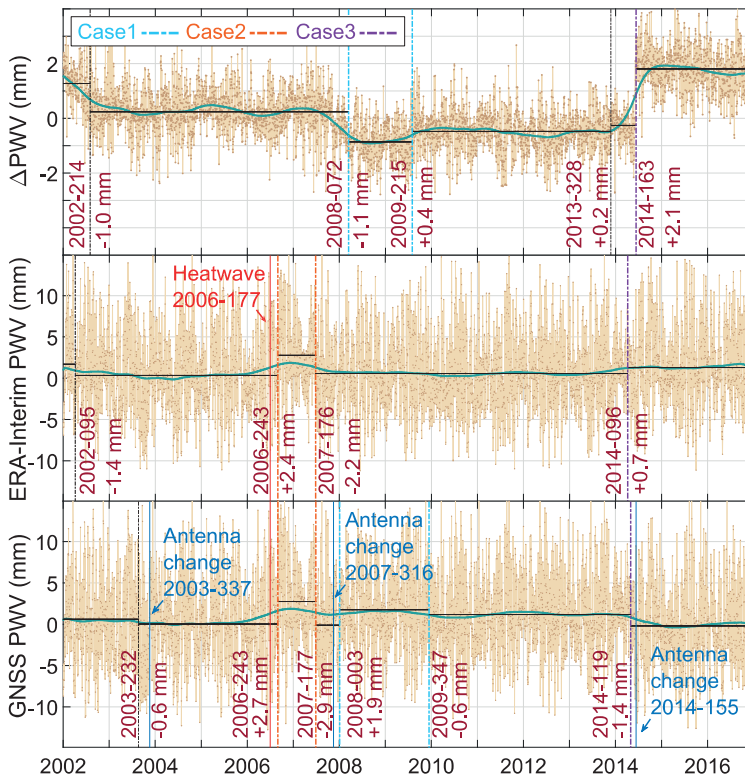
Figure 3.1: An exemplary inspection of inhomogeneities by applying the detection method to the difference (top), ERA-Interim (middle) and GNSS (bottom) PWV time series. The data is related to Saarbrücken GNSS station in Germany (49.22°N, 7.01°E) (reused from [26]).

Results

The performance of the offset detection method for PWV time series is assessed using a Monte Carlo simulation. The assessment results reports on a success rate of 81.1% for detecting mean shifts with values between 0.5 and 3 mm. The GNSS-derived PWV dataset over Germany is investigated for possible inhomogeneities and systematic changes. The dataset is homogenized by identifying and correcting 96 inhomogeneous time series containing 134 detected and verified mean shifts. In total, 45 changes out of 134 accounting for approximately 34% of the offsets are undocumented in the log files of the GNSS stations. The process of detection and classification of the detected change for each case is demonstrated for an exemplary GNSS station in Figure 3.1.
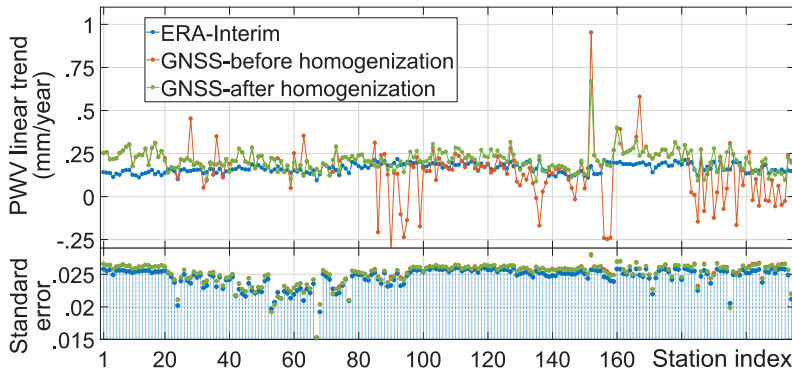
Figure 3.2: The impact of applying the proposed homogenization approach to a GNSS PWV dataset consist of 214 stations in Germany. A comparison of the fitting linear trends of the ERA-Interim and the GNSS PWV time series show significant improvements after the homogenization (reused from [26]).

The figure shows different cases in which the origin of the offsets are different. As can be seen from the figure, possible changes induced by climatic or meteorological effects can be identified using the developed method. To show the possible impact of homogenization on a GNSS dataset, the linear trends from the GNSS and ERA-Interim PWV datasets are estimated and compared. The result of this analysis is summarized in Figure 3.2 which highlights significant improvements after the homogenization process. The correlation between the two sets of the trends is increased by 39% after correcting the mean shifts in the GNSS data.

Authors Contributions

Conceptualization, M.H., F.A; Data curation, M.H., G.D.; Formal analysis, M.H., F.A., H.N. and J.W.; Funding acquisition, H.N., J.W.; Investigation, M.H. and F.A.; Methodology, M.H.; Software, M.H., G.D., F.A.; Supervision, H.N. and J.W.; Validation, M.H. and F.A.; Visualization, M.H.; Writing–original draft, M.H. and H.N.; Writing–review and editing, M.H., F.A., H.N., and J.W. All authors have read and agreed to the published version of the manuscript.

3.2.2 Paper B: On the Response of Polarimetric GNSS-Reflectometry to Sea Surface Roughness

Content

The paper describes the remote sensing of sea surface roughness using a coastal GNSS-R station over a period of one year from January to December 2016. The station is equipped with three antennas which are connected to a dedicated reflec-

tometry receiver. Besides an up-looking RHCP antenna which tracks the satellites, the station uses two side-looking antennas with RHCP and LHCP design to collect sea-reflected GNSS signals. The study estimates the power of direct and reflected signals at each epoch from interferometric observations of the sea-looking antennas. The power estimates are analyzed to infer the surface roughness as an indicator of sea state. The methodolgy used in this study precisely calculates the power by accounting for the impact of the reflection geometry. To this end, the sea level information from the nearest tide gauge is obtained and the elevation angle of the satellite is estimated using a ray tracing algorithm. The roughness estimates based on RHCP (co-polarization), and LHCP (cross-polarization) antennas are verified against wind speeds obtained from the nearest meteorological station. The effect of using observations with different polarization as well as combination of the RHCP and LHCP observations is also discussed in the paper. The analysis reveals the impact of wind direction and surrounding coastlines on the GNSS-R measurements.

Research Method

The study investigates the response of GNSS-R observations at different polarizations to the sea surface roughness during different wind conditions. The interference of the direct and sea-reflected GNSS signals is intercepted by two antennas with RHCP and LHCP designs. The captured compound electromagnetic signal is processed by the receiver to produce interferometric patterns at In-phase and Quadrature (I/Q) levels. The I/Q output streams are used to estimate the power of direct and reflected signals. These power estimates are converted to power ratios and are inverted to sea surface roughness measurements using a geophysical model function. To enhance the quality of roughness retrieval, information about the permittivity of seawater and sea level is needed. The required information is provided by collocating the main dataset with sea surface temperature, salinity, and tide gauge data. The inversion process is individually applied to RHCP, LHCP, and the combined dual-polarization observations. The roughness estimates are validated against the wind data which is obtained from the nearest meteorological station.

Results

The results of sea surface roughness estimation from both RHCP (Figure 3.3 (a)) and LHCP (Figure 3.3 (b)) antennas show successful retrievals over the one-year period of the analyzed dataset. However, the cross-polarization observations show more sensitivity to the roughness variations. The retrievals from the cross-polarization link can detect wind speeds as low as about 1 m/s, while co-polarization observations are mainly insensitive to wind speeds below 2 m/s. The dependency of cross-to-co-polarization power ratios to sea state variations (Figure 3.3 (c)) reveal
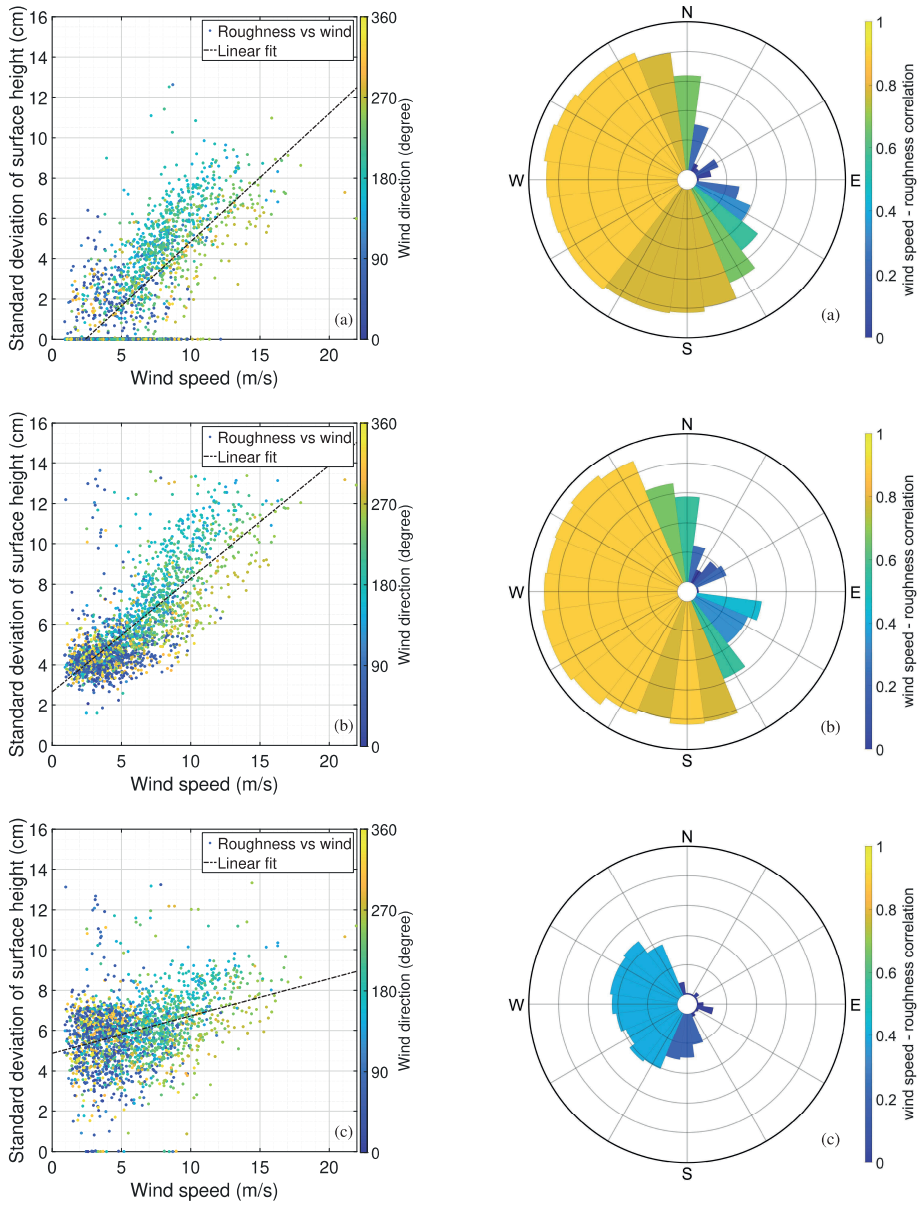
Figure 3.3: Left column shows the results of the roughness retrievals from: (a) co-polarization, (b) cross-polarization, and (c) cross-to-co-polarization power ratios calculated using one-year coastal GNSS-R observations at Onsala, Sweden. Right column highlights the Sensitivity of roughness measurements to wind directions. The correlation of wind speeds with (a) co-polarization, (b) cross-polarization, and (c) cross-to-co-polarization roughness retrievals is shown as a function of wind direction (reused from [28]).
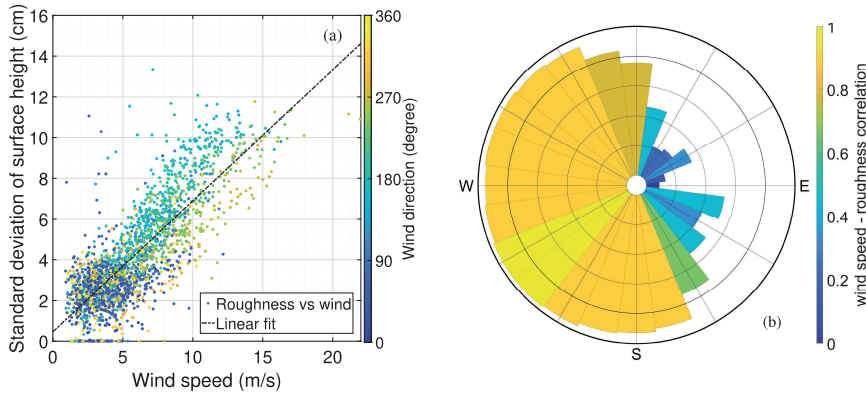
Figure 3.4: Results of a fully polarimetric solution for the estimation of sea surface roughness at a coastal GNSS-R station in Onsala, Sweden. The results are related to a time span of one-year from January to December 2016. (a) Roughness estimates against different wind speeds overlaid with the first-order polynomial. (b) Dependence of the roughness retrievals on the direction of wind fields (reused from [28]).

that the state-of-the-art model need an enhancement. The roughness measurement exhibit a clear dependence on the wind direction (Figure 3.3, right column). This effect is associated with different fetch lengths and the nearby complex coastlines. This justifies the observed maximal impact of sea-breeze on the GNSS-R measurements compared to the offshore winds. A full-polarimetric solution for roughness retrieval is presented in this study (Figure 3.4), which reports noticeable enhancements with respect to both co- and cross-polarization results.

Authors Contributions

Conceptualization, M.H., M.S; Data curation, M.H., E.R.; Formal analysis, M.H., M.S., H.N. and J.W.; Funding acquisition, H.N.; Investigation, M.H. and M.S.; Methodology, M.H. and M.S.; Software, M.H., M.S. and E. R.; Supervision, H.N. and J.W.; Validation, M.H., R.H. and J.S.; Visualization, M.H.; Writing–original draft, M.H.; Writing–review and editing, M.H., M.S., H.N., E.R., R.H., J.S. and J.W. All authors have read and agreed to the published version of the manuscript.

3.2.3 Paper C: Remote Sensing of Precipitation using Reflected GNSS Signals: Response Analysis of Polarimetric Observations

Content

This paper investigates the effect of precipitation on ground-based GNSS-R obser-

vations with different polarizations. The analysis first examines possible variation of reflection power loss due to precipitation based on theoretical models. This follows with an empirical assessment based on a long-term coastal GNSS-R dataset. The dataset is collocated with ancillary information about water temperature, salinity, wind conditions, rain rate and rain duration. Power estimates from RHCP and LHCP observations are sought to find the evidence of theoretically anticipated signatures. The detected variations of sea surface roughness and salinity at different rain rate are discussed in the study and an exemplary case is also demonstrated.

Research Method

The methodology of this research includes a theoretical evaluation of permittivity change during different rain rates. The evaluation uses available models to predict the salinity change due to the accumulation of fresh water on the sea surface at different rain rates and over different time spans. The simulated salinity changes together with a selected range of temperature values are used to estimate the amount of power loss associated with the sea-reflected GNSS signals. The simulation is followed by processing of a real GNSS-R dataset which is collected by a dedicated reflectometry receiver with dual-polarization antenna support. The observations from either of the two links, i.e. RHCP and LHCP antennas, are processed to estimate the power of direct and reflected signals. The power estimates are converted to power ratios and are used within an inversion process to calculate the surface roughness and salinity in the presence of rainfall. To exclude the impact of wind, the study selects periods during which the wind was blowing from the land side with the speed of less than 5 m/s. Using this setup, the fetch limitation of coastal waters helps to mitigate the wind effect.

Results

The results of power analysis during rainfall over a calm sea shows that noticeable drops can happen in both RHCP and LHCP reflections (Figure 3.5). These power drops become larger at higher elevation angles suggesting the presence of roughness change due to precipitation. For instance, at an elevation angle of $45°$, the average LHCP power drops by about 5 dB (Figure 3.5(c)). This power loss can also be discerned through the change of I/Q correlation sums amplitude in visual inspection. A comparison of the retrieved average power from the RHCP (Figure 3.5(a)) and LHCP (Figure 3.5(c)) observations suggests that the cross-polarization observations exhibit higher sensitivity to rainfall compared to the RHCP observations. Analysis of standard deviation of surface heights as a measure of roughness reports on a steady increase with the rain rate (Figure 3.6(a)). At rain rates higher than 10 mm/h a decline is observed in the derived surface salinity (Figure 3.6(b)).
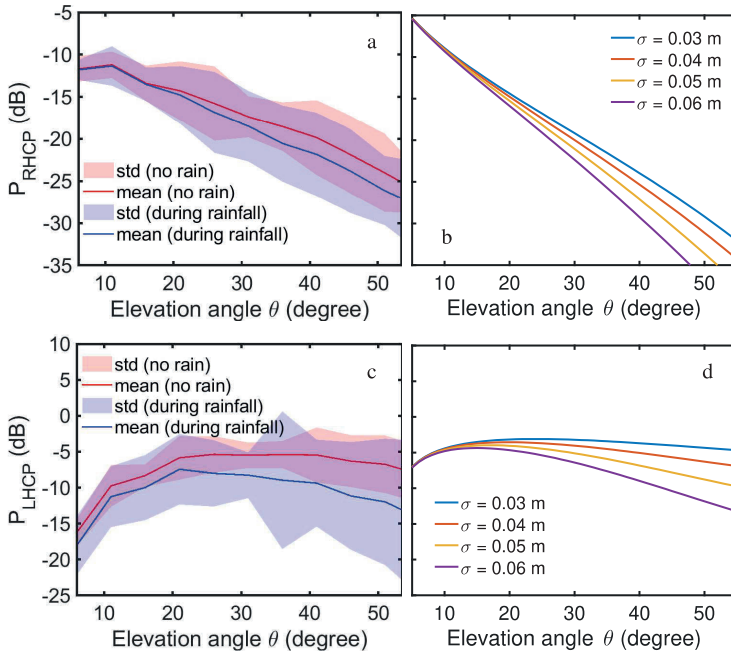
Figure 3.5: (a) RHCP and (c) LHCP power ratios and in different cases, during rain events, at rates higher than 0.2 mm/h, and at no rain along with model-simulated (b) RHCP and (d) LHCP power ratios at different standard deviations of surface heights σ. Average and maximum rain rates of the data during rainfall are 1.5 and 23.0 mm/h, respectively (reused from [5]).
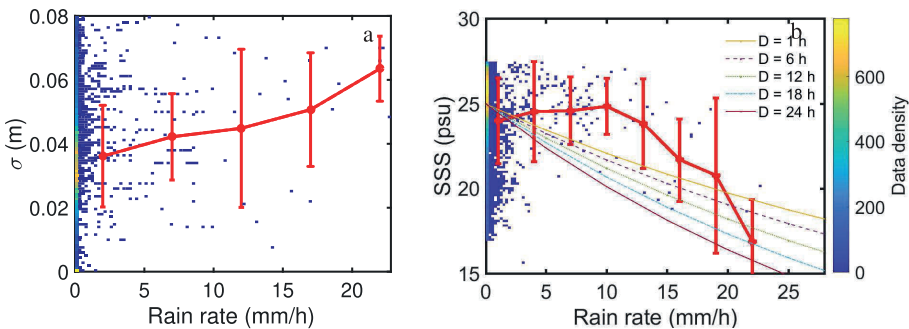
Figure 3.6: Obtained values of (a) standard deviation of sea surface heights σ and (b) SSS along with simulated SSS at different rain duration D versus rain rate. The average values and standard deviations are shown in red (reused from [5]).

Authors Contributions

Conceptualization, M.A. ; Data curation, M.A., M.H.; Formal analysis, M.A., M.H.; Funding acquisition, J.W., H.N.; Investigation, M.A., M.H.; Methodology, M.A., M.H., M.S.; Software, M.A, M.H., M.S.; Validation, M.A., M.H.; Visualization, M.A, M.H.; Writing–original draft, M.A., M.H.; Writing–review and editing, M.A., M.H., M.R., M.S., A.C., R.H.. All authors have read and agreed to the published version of the manuscript.

3.2.4 Paper D: A Performance Assessment of Polarimetric GNSS-R Sea Level Monitoring in the Presence of Sea Surface Roughness

Content

This paper appraises the performance of sea level measurements derived from ground-based GNSS-Reflectometry observations during different sea states. The GNSS-R observations which are used to retrieve sea surface height are obtained from a dedicated GNSS-R receiver with three links. The master links uses an up-looking RHCP antenna and two slave links use RHCP and LHCP antennas. The tilted seaward antennas are meant to capture the sea reflections with the highest gain value while the up-looking antenna is simulating the antenna orientation in an ordinary geodetic GNSS station. To analyze the effect of wind, the GNSS-R dataset is collocated with wind measurements from a nearby meteorological station. The study validates the GNSS-R derived sea surface heights against the tide gauge measurements which is about 300 meters away. The Root Mean Squared Error (RMSE) and bias of the measured sea level with respect to the tide gauge is then evaluated based on different wind speed ranges.

Research Method

The ground-based sea level measurements is based on the analysis of interferometric fringes which are results of the interference of direct and reflected GNSS signals. To extract these fringes, the study utilizes SSA technique. This technique can effectively separate different components of the GNSS-R observations and provide a clean retrieval of interferometric pattern. The periods of these patterns are then calculated using a peak detection algorithm. The periods is accompanied with satellite orbit information to estimate the sea level at each epoch. The epochs are classified based on sea states using the wind speed information. The GNSS-R derived sea level anomalies are compared to tide gauge measurements for evaluating the results at different sea states.
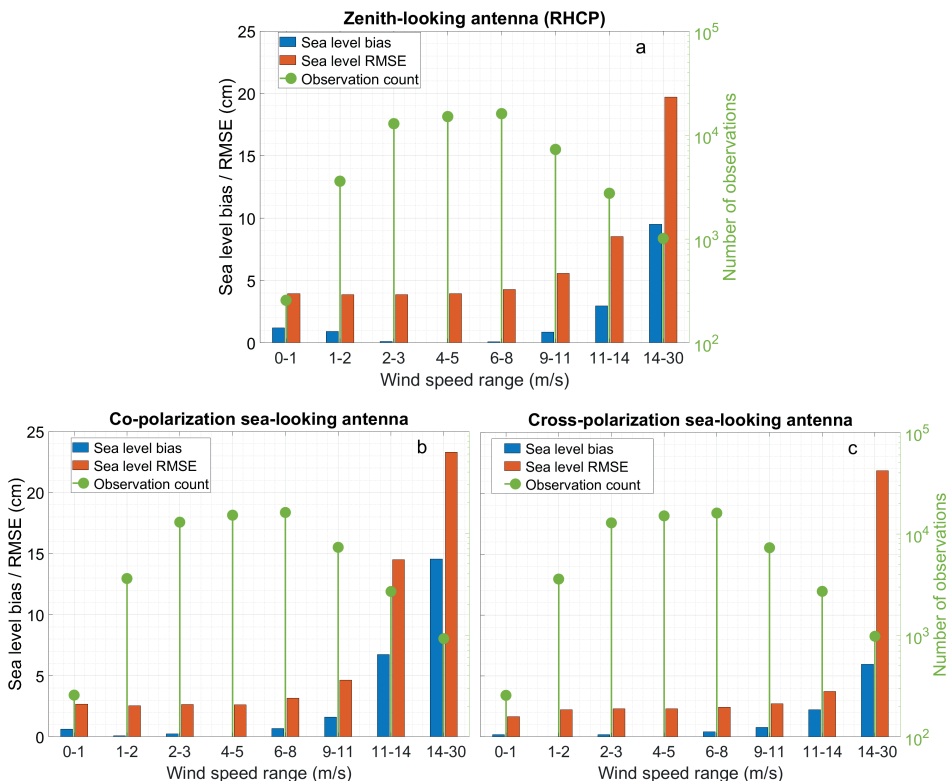
Figure 3.7: An evaluation of the performance of GNSS-R sea level measurements at different sea state based on the observations from RHCP and LHCP antennas with zenith-looking and sea-looking orientations. The panels show the results from the zenith-looking RHCP (a), sea-looking RHCP (b), and sea-looking LHCP (c) antennas. The blue bars show the bias of the GNSS-R measurements with respect to the tide gauge over each wind speed range. The red bars are the associated RMSE values (reused from [41]).

Results

This study suggests that the height estimates from the sea-looking LHCP antenna provide higher level of accuracy compared to both up- and sea-looking RHCP antennas. The RMSE of GNSS-R water levels compared to the nearest tide gauge measurements are 2.8 and 3.9 cm for the sea-looking LHCP and RHCP antennas, respectively, and 4.7 cm for the zenith-looking RHCP antenna. The corresponding correlation coefficients of the measurements pairs are 97.63, 95.02, 95.35 percent, respectively. The paper reports on a degrading impact of sea surface roughness on all types of the GNSS-R observations. The impact is prominent both in the bias and RMSE of the measurements with respect to the tide gauge data (Figure 3.7).

It is noteworthy that the estimated biases in this experiment could be different from other similar setups. This stems from the fact that the wind effect on coastal regions depends on the location of the station and wind direction. Therefore, different directions of wind can induce different impact on a coastal GNSS-R experiment.

Authors Contributions

Conceptualization, M.R. and M.H.; GNSS-R experiment and data, M.Ram., J.W.; Match-up wind data: R.H.; Data curation, M.R. and M.H.; Formal analysis, M.R., M.H., M.S.; Funding acquisition, M.R. and H.N.; Investigation, M.R. and M.H.; Methodology, M.R. and M.H.; Software, M.R., M.H. and M.S.; Supervision, H.N. and J.W.; Validation, M.R., M.H.; Visualization, M.R., M.H.; Writing—original draft, M.R., M.H.; Writing—review and editing, M.H., H.N., M.S., R.H. and J.W. All authors have read and agreed to the published version of the manuscript.

3.2.5   Paper E: Polarimetric GNSS-R Sea Level Monitoring using I/Q Interference Patterns at Different Antenna Configurations and Carrier Frequencies

Content

In this paper, the performance of GNSS-R monitoring of sea surface height based on different scenarios is evaluated. The flexible setup used in the GNSS-R experiment allows a multi-parameter evaluation in terms of frequency of the signals, polarization and orientation of the antennas, as well as the impact of temporal averaging. The quality of final sea level products based on each satellite Pseudorandom Noise (PRN) is determined for either of L1 and L2 GPS frequencies. The study also includes quality assessment of multi-frequency, dual-polarization GNSS-R data products. The evaluation uses an ancillary dataset including tide gauge measurements. The ancillary dataset also provides wind data which is used to examine the impact of wind on each GNSS-R data product.

Research Method

The methodology of sea level retrieval in this study is based on the estimation of interferometric frequency in the ground-based GNSS-R observations. To this end, the Least-Squares Harmonic Estimation (LS-HE) method is applied to a dataset of one year over 2016 for retrieving the interferometric frequency and calculating the height of reflecting surface. The LS-HE method can be simultaneously applied to estimate the frequency of interest in multiple sets of observations in the presence of data gaps or unevenly spaced data. The GNSS-R dataset includes I/Q output streams from each antenna. This gives the opportunity of using multiple series in the LS-HE analysis to boost the spectral analysis process. Using a sliding window,

the LS-HE spectral analysis is partially applied to the time series of the reflection events from each GPS PRN. The size of this window is set to a minimum of 15-min but it is flexibly extended to 30-min to include at least two interferometric periods. The estimated heights from different satellites are combined by calculating the median value of the estimations.

Results

The results show that the combination of observations from L1 and L2 frequencies (L12) from a sea-looking LHCP antenna provides the best performance. Regarding the comparison of the products based on L1 and L2 frequencies, the L2 observations generally provides a lower degree of accuracy most likely suffering from fewer observations. In terms of antenna orientation, a seaward tilting with the angle of 90 degrees with respect to the zenith, optimizes the antenna again for capturing the sea-reflected signals and magnifies interferometric patterns. Concerning the polarization, the analysis confirms that while the RHCP antenna can be readily used for grazing angles altimetry, using an antenna with LHCP design is the right choice for capturing the reflections at higher elevation angles.
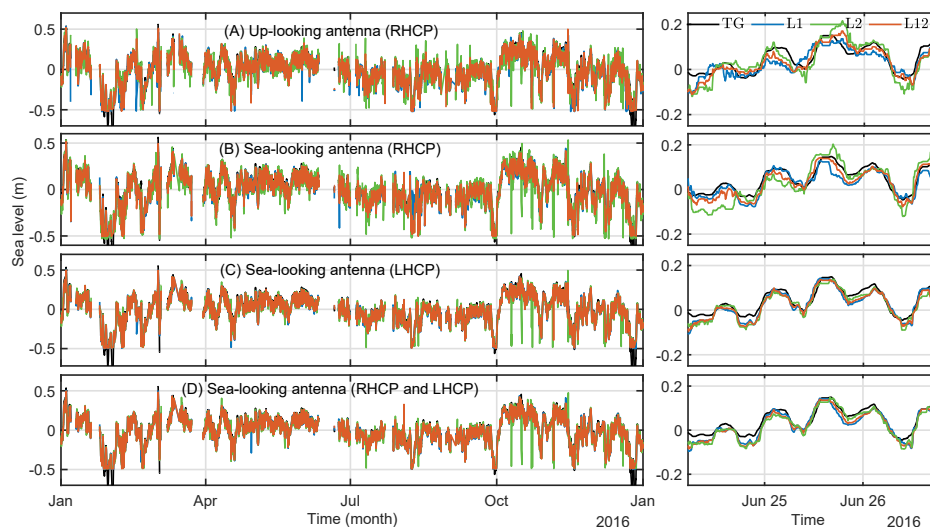
Figure 3.8: Time series of sea level anomalies derived from a one-year GNSS-R dataset (left panels), and zoomed views of a 2-day window (right panels), overlaid on the tide gauge (TG) measurements. The antennas used for the measurements are: (A) up-looking RHCP, (B) sea-looking RHCP, (C) sea-looking LHCP, and (D) sea-looking RHCP and LHCP. The lines with different colors show the estimates from different frequencies, i.e., L1 (blue), L2 (green), and combined L1 and L2 or L12 (red) (reused from [44]).

Figure 3.8 compares the sea level retrievals based on four different scenarios. Us-

66

Table 3.1: The root mean square deviation (ε) and correlation coefficient (ρ) based on one-year GNSS-R sea level measurements compared to nearby tide gauge measurements. The values are based on different averaging windows for four measurement scenarios. *Scenario A* is based on observations from a zenith-looking RHCP antenna, *scenario B* includes observations from a seaward-oriented RHCP antenna, *scenario C* shows the results from a sea-looking LHCP antenna, and *scenario D* combines the observations from the RHCP and LHCP antennas. For each scenario, the columns L1, L2, and L12 respectively indicate the sea level measurements using the GPS L1, L2 carrier frequencies as well as their combined solution in the averaging step. The table is reused from [44].

Win = 6 h	L1	L2	L12
ε_A (cm)	4.6	5.7	4.1
ρ_A	0.963	0.943	0.969
ε_B (cm)	4.2	5.7	3.1
ρ_B	0.968	0.948	0.982
ε_C (cm)	2.4	3.6	2.4
ρ_C	0.990	0.977	0.990
ε_D (cm)	2.4	3.8	2.3
ρ_D	0.990	0.973	0.990
Win = 3 h			
ε_A (cm)	6.1	7.8	5.7
ρ_A	0.940	0.901	0.946
ε_B (cm)	5.3	7.1	4.4
ρ_B	0.951	0.923	0.967
ε_C (cm)	3.2	4.0	3.0
ρ_C	0.982	0.972	0.984
ε_D (cm)	3.1	4.2	3.0
ρ_D	0.983	0.970	0.984
Win = 1 h			
ε_A (cm)	8.6	10.4	8.14
ρ_A	0.893	0.847	0.901
ε_B (cm)	7.4	9.1	6.6
ρ_B	0.912	0.884	0.930
ε_C (cm)	4.7	5.3	4.5
ρ_C	0.964	0.954	0.967
ε_D (cm)	4.6	5.4	4.5
ρ_D	0.965	0.952	0.967
Win = 15 min			
ε_A (cm)	11.7	12.1	10.3
ρ_A	0.827	0.811	0.854
ε_B (cm)	9.3	10.9	8.7
ρ_B	0.870	0.846	0.886
ε_C (cm)	5.8	6.4	5.6
ρ_C	0.946	0.935	0.949
ε_D (cm)	5.6	6.3	5.6
ρ_D	0.948	0.837	0.949

age of different averaging windows can also affect the quality of final products. The RMSE values of GNSS-R sea levels from the LHCP sea-looking antenna compared to collocated tide gauge measurements are 2.4, 3.0, 4.5, 5.6 cm for 6, 3, 1, and 0.25-hour window size, respectively. The performance assessments of the measurement scenarios based on different averaging windows are summarized in Table 3.1. The investigation of wind effect on the accuracy of GNSS-R sea level measurements reports lower degree of accuracy during higher wind speeds. The RMSE value of the products can be more than 2 times larger in wind speeds above 14 m/s compared to calm sea surface, i.e., during wind speeds below 2 m/s. However, the final L12 sea level estimates show a better tolerance against the degrading effect of wind speeds.

Authors Contributions

Conceptualization, M.R. and M.H.; GNSS-R experiment and data, M.Ram., J.W.; Match-up wind data: R.H.; Data curation, M.R. and M.H.; Formal analysis, M.R., M.H., M.S.; Funding acquisition, M.R., M.G. and H.N.; Investigation, M.R. and M.H.; Methodology, M.R. and M.H.; Software, M.R., M.H. and M.S.; Supervision, H.N. and J.W.; Validation, M.R., M.H.; Visualization, M.R., M.H.; Writing—original draft, M.R., M.H.; Writing—review and editing, M.H., H.N., M.S., M.G., R.H. and J.W. All authors have read and agreed to the published version of the manuscript.

3.2.6 Paper F: First Evidence of Mesoscale Ocean Eddies Signature in GNSS Reflectometry Measurements

Content

This paper demonstrates the feasibility of detecting mesoscale ocean eddies in spaceborne GNSS-R measurements of ocean surface roughness. The Normalized Bi-static Radar Cross Section, or NBRCS (σ_0) measurement, is considered as the indicator of ocean roughness. The σ_0 measurements is obtained from NASA Cyclone GNSS (CYGNSS) mission, which has eigth micro-satellites in orbit. Several match-up datasets from the Aviso eddy trajectory atlas, Ocean Surface Current Analysis Real-time (OSCAR) data, and ECMWF Reanalysis-5 (ERA-5) products are collocated with the main dataset for verification and justification purposes. The study analyzes the variations of σ_0 over the eddies and looks for possible responses to the eddy-induced roughness changes over the ocean surface. A statistical analysis is applied to the CYGNSS profiles in 2017 to detect repeatable patterns in the profiles with prominent signatures of these oceanic features. The observed patterns are discussed based on the potential contributing factors.

Research Method

The initiation of this research is based on visual inspections of the spaceborne roughness measurements over the prominent eddies. The eddies leave strong signatures on Sea Surface Temperature (SST) and surface current. The visually observed behaviors of the NBRCS profiles show noticeable changes over the central region or the edges of the eddies. The repeatability of the observed patterns are investigated through the following approach.

The Aviso trajectory atlas is first used to retrieve the dynamic position and radius of the documented eddies. The CYGNSS track passing over the eddies are extracted from the level-1 data product of the CYGNSS. The extracted parameters are position of the specular points, time of the observations, and the NBRCS values. All the match-up datasets are spatio-temporally interpolated according to the position and epoch of the specular points. The interpolated match-up parameters include near-surface ocean current from OSCAR dataset, as well as surface windfield, SST, Sensible Heat Flux (SHF), and turbulent surface stress field from ERA-5. These data products offer a possibility to discuss potential interactions of the geophysical parameters with the GNSS-R σ_0. The CYGNSS σ_0 profiles over the ocean eddies can exhibit different types of fluctuations, i.e., linear and non-linear variations in different scales. The Principal Component Analysis (PCA) method is applied to the CYGNSS profiles to reduce the dimensionality of the dataset and extract the main nonlinear σ_0 anomalies over the eddies. The PCA-reconstructed σ_0 profiles are then correlated with the observed patterns to check the similarities.

Results

Based on the findings of this study, under certain circumstances, two types of prominent anomalies can be observed in the GNSS-R σ_0 profiles in response to the eddies. The observed anomalies are single-jump pattern at the eddy center or double-jump at the eddy edges. The sudden increase of σ_0 in both of the patterns is significant enough to be easily discerned in the GNSS-R measurements.

Figure 3.9 shows a CYGNSS track overpassing three eddies. The σ_0 profile includes successive single-peak patterns. The track at the core regions of the first two eddies show a sudden increase in σ_0, which again drops to its initial level once the track moves off the center. The third eddy however exhibits a peak at the boundary regions.

Figure 3.10 shows a CYGNSS track that covers three cyclonic eddies. The track passes over the edge of the first eddy at which the profile keeps the high σ_0 values almost at the same level when moving over the eddy edges and again drops to lower values once it leaves the eddy's outer regions. The track sweeps the central region
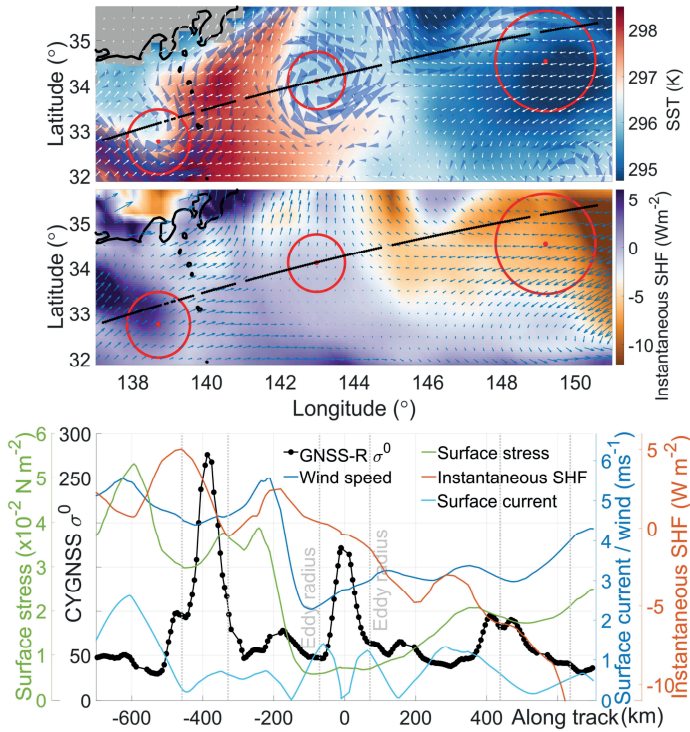
Figure 3.9: A CYGNSS track overpassing three mesoscale eddies on 29 June 2017, 20:45. The top panel displays SST, surface wind (white arrows) and current (blue cones). In the middle, instantaneous SHF as well as surface stress (blue arrows) are visualized. The profiles in the bottom panel include CYGNSS σ_0 along with the wind and current velocity, instantaneous SHF and surface stress magnitudes (reused from [27]).

of the second eddy and σ_0 responds with a low central values and two sharp peaks at the edges. A similar behavior can be observed over the third eddy, however with less prominent peaks. Besides the exemplary cases, the overall analysis of all profiles in 2017 reports on strong inverse correlations of σ_0 with the sensible heat flux and surface stress over mesoscale ocean eddies.

Authors Contributions

Conceptualization, M.H., H.N., M.A.; Data curation, M.H.; Formal analysis, M.H., M.A., V.Z. and C.R.; Funding acquisition, H.N.; Investigation, M.H. and M.A.; Methodology, M.H., M.A.; Software, M.H.; Supervision, H.N. and J.W.; Validation, M.H. and V.Z.; Visualization, M.H.; Writing–original draft, M.H. and M.A.; Writing–review and editing, M.H., M.A., V.Z., H.N., C.R. and J.W. All authors have read and agreed to the published version of the manuscript.
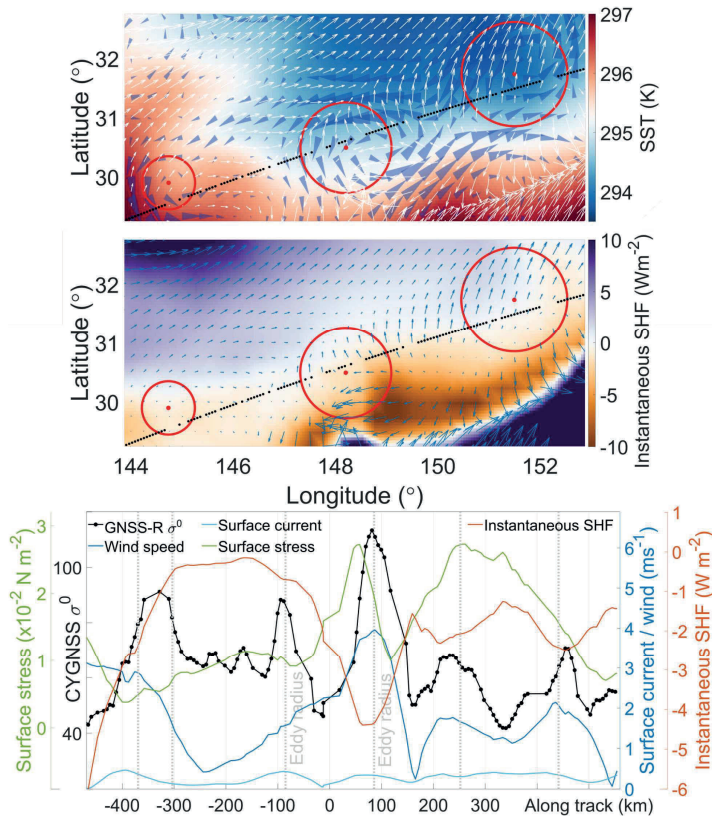
Figure 3.10: A CYGNSS track overpassing three mesoscale eddies on 4 June 2017, 08:11. The top panel displays SST, surface wind (white arrows) and current (blue cones). In the middle, instantaneous SHF as well as surface stress (blue arrows) are visualized. The profiles in the bottom panel include CYGNSS σ_0 along with the wind and current velocity, instantaneous SHF and surface stress magnitudes (reused from [27]).

3.2.7 Paper G: Evaluation of CYGNSS Observations for Flood Detection and Mapping during Sistan and Baluchestan Torrential Rain in 2020

Content

This paper evaluates a remote sensing application of spaceborne GNSS-R observations for the detection of a flooding event and mapping the affected areas. The main dataset used for the evaluation is obtained from the level-1 data product of NASA CYGNSS mission during a heavy rain in January 2020 over south-eastern part of Iran. The selected study area faces a high risk of flood, proven by similar events during recent years and needs continuous monitoring. The forward-

scattered GNSS signals are exploited to calculate the surface reflectivity using the bistatic radar equation. The flooded areas are detected based on the analysis of the derived reflectivity. For the verification purpose, the study uses Moderate-Resolution Imaging Spectroradiometer (MODIS) images.

Research Method

The main parameter of interest used in the analysis was the delay doppler map SNR, which was retrieved from the level-1 data product of NASA CYGNSS mission. First, a data preparation procedure was applied to remove outliers and discard low-quality data. In the next step, inverse bistatic radar formula was used to calculate the corrected SNR, which was closely related to surface reflectivity and hydrological conditions. The corrected SNR values were calibrated and interpolated to a regular grid over the study area. After calibration and gridding, the corrected SNR was verified with the MODIS optical image. A threshold of about 11 dB or more could be distinguished between the inundated and noninundated areas in the regions of interest. Finally, the flood-affected areas were mapped on Google Maps.

Results

This study demonstrated the potential of timely spaceborne GNSS-R observations over land for detecting and mapping floods. The investigation specifically focuses on a flood occurred in Sistan and Baluchestan province of Iran where a heavy rain in mid-January 2020 caused a destructive flood. The analysis estimates the inundated area to be about 19,644 km^2 (Figure 3.11). Many cities, roads, and other infrastructures were affected by the flood in these regions. The results indicate the regions close to depression, lakes, and coastal areas are at a high risk of flooding in this province (Figure 3.12). This study confirms that CYGNSS data is of value for hydrological investigations, particularly flood detection in the Sistan and Baluchestan province. Despite a relatively short revisit time of CYGNSS observations, the spatial resolution of the data products needs to be improved for mapping purposes. This issue could be addressed in future missions by, e.g., increasing the number of onboard processing channels, as well as by processing the reflected signals from other GNSS constellations such as GLONASS, Galileo, and BeiDou.

Authors Contributions
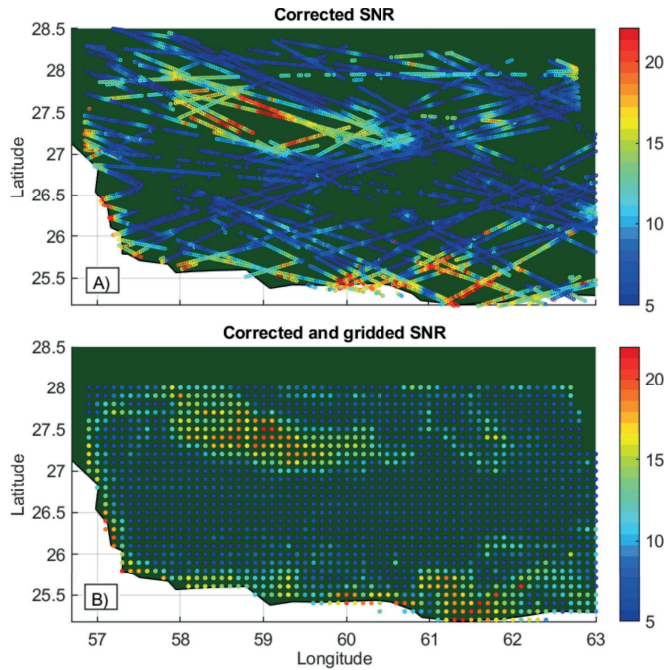
Figure 3.11: The outcome of interpolation process for the corrected SNR over the period of three days from 13 January to 15 January 2020. (A) Representation of the CYGNSS measurements along the satellite tracks, (B) the interpolated data at $0.1° \times 0.1°$ grid points using the natural neighbor interpolation method (reused from [43]).
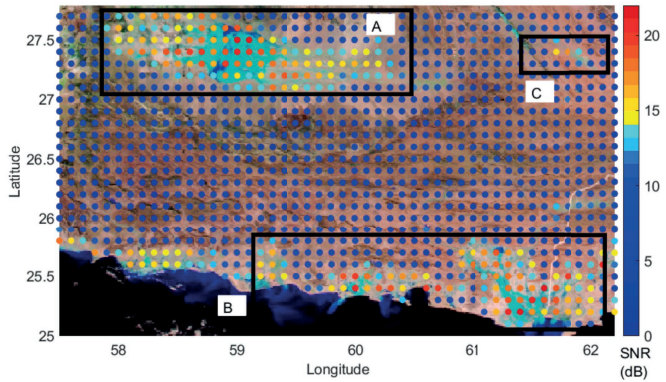
Figure 3.12: The georeferenced optical satellite imagery of the flood from MODIS (13 January 2020) overlaid by the corrected signal to noise ratio derived from CYGNSS observations (13 January to 15 January 2020). The regions labeled A, B, and C show significant SNR anomalies (reused from [43]).

This page is intentionally left blank

Chapter 4

Conclusions and Outlook for Future Research

This chapter provides a summary of conclusions based on the research conducted in this dissertation. The chapter also includes some insights about complementary future researches.

4.1 Practical Contribution

The remote sensing techniques based on the analysis of direct and reflected GNSS signals have been considered for several applications. The GNSS-derived remote sensing data products can be used for sounding the atmosphere, monitoring the earth surface and the interaction of the atmosphere with the ocean or land. For instance, the GNSS direct signals are utilized for monitoring the water vapor content of the troposphere as an essential climate variable. Moreover, the relatively new technique of utilizing GNSS reflected signals in a passive configuration has provided a new source of observations for different remote sensing applications. Ground-based GNSS-R stations have been exploited to provide measurements of different geophysical parameters, e.g. sea level, soil moisture, snow depth, ice coverage and concentration.

Although the GNSS-based observations provide a wide verity of remote sensing measurements, practical usage of the data have to be more promoted. In doing so, some of possible issues hindering practical utilization of these products were investigated in this thesis. Furthermore, the performance of some of the measurements were assessed within exemplary applications. The new-generation of GNSS-based observations from spaceborne GNSS-R technique were also demon-

strated to be useful for the study of atmospheric interactions with the ocean and land.

In the following, it is discussed how this thesis contributed to achieving the previously stated objectives and addressing the associated research questions:

- **Objective 1: To contribute to promoting the exploitation of established GNSS-derived remote sensing data products**

  The thesis has focused on a well-known GNSS-derived dataset, i.e. the ground-based tropospheric delays and precipitable water vapor, which could potentially be used for climate and meteorological applications (e.g. [2]). Homogeneity of the data products is an essential prerequisite for these applications. Therefore, detecting and correcting inhomogeneities specially those originating from undocumented hardware or software changes is inevitable. Since most of the available homogenization approaches utilize a reference data for detection, the homogenized GNSS data can be prone to the inhomogeneities in the reference data. Through one of the studies conducted in this thesis, a novel approach has been proposed which minimizes such cases of contamination from the reference data. The study also covers several other homogenization-related issues such as: avoiding any miscorrection of climate-related changes, dealing with possible data gaps, detecting changes in the presence of seasonality and high-frequency component of the time series, and addressing detected changes without any documentation in the stations log files.

  ✓ *RQ 1.1: In the presence of climate-related changes or possible inhomogeneities in the reference time series, how can we detect and correct inhomogeneities in GNSS-derived tropospheric products?*

  Concerning the detection of inhomogeneities which are characterized by mean shifts in the GNSS time series, a new data-driven offset detection method has been developed in this thesis. The method is based on Singular Spectrum Analysis (SSA) and can detect mean shifts ranging from 0.5 to 3 mm in PWV time series with 81.1% success rate. SSA is also adopted in this study to predict possible missing data in the presence of seasonality. Unlike most of the other homogenization methods, which subtract a reference time series from the GNSS PWV time series, the detection method can be directly applied to the original time series in the presence of high-frequency component of the time series. This feature helps to avoid any contamination from the reference PWV time series but raises the issue of miscorrection of climatic or meteorological changes. To distinguish any climate-induced

changes, the method is independently applied to the GNSS and the reference time series. Using the fact that the offsets associated with a climatic or meteorological effects happen at the same time and with similar magnitudes, the approach leaves such changes uncorrected.

✓ *RQ 1.2: What could be the impact of homogenization on inhomogeneous GNSS datasets for a climate application?*

The PWV time series can be used to estimate the trends of atmospheric water vapor, which is an indicator of warming climate. To demonstrate the impact of homogenization, the developed approach in this thesis was applied to a nation-wide GNSS-derived PWV dataset over Germany. Among 214 time series that were evaluated by the developed approach, 96 inhomogeneous time series with 134 detect and verified changes were identified. About one third of the changes could not be supported by any documented hardware or software changes in the stations log files. After homogenizing, the overall pair-wise correlation of the PWV trends from GNSS time series and the reference time series was significantly improved by 39%.

- **Objective 2: To contribute to the enhancement of the developing class of GNSS-derived remote sensing data products**

The remote sensing measurements based on ground-based GNSS-R observations have been developing in recent decades. The methodological improvement for observing different geophysical parameters of interest is still the topic of lots of undergoing research. Towards contributing enhancement of these measurements, this dissertation has devoted several studies to evaluate the performance of the measurements based on different scenarios. The studies are carried on based on a one-year dataset (January to December 2016) from a GNSS-R experiment conducted by German Research Center for Geosciences (GFZ) at Onsala, Sweden. The instrumentation setup at this station provides flexibility to investigate different potentials of ground-based GNSS-R observations.

✓ *RQ 2.1: How can we enhance the performance of the ground-based GNSS-R measurements for sea surface characterization?*

Regarding the characterization of sea surface using GNSS-R measurements, this dissertation has focused on three parameters: sea surface roughness, precipitation over the sea surface, and sea level anomalies. In one of the studies, the analysis of reflection power is used for the roughness retrieval. The results show that the sea surface roughness

measurements made by the GNSS-R station can measure the rough-ness associated with very low wind speeds with sensitivity to wind direction at a coastal setup. Using a Left-Handed Circular Polarization (LHCP) antenna (with a dedicated reflectometry receiver) can increase the sensitivity of the measurements compared to the Right-Handed Circular Polarization (RHCP) antennas. A fully-polarimetric solution, i.e. by utilization of both RHCP and LHCP observations can noticeably enhance the quality of the results.

Another investigation of this dissertation suggests that precipitation can leave its signature on the roughness or salinity of sea surface under certain conditions. This impact can influence the GNSS-R measure-ments and can reduce the observed reflection power by up to about 5 dB. Sensitivity of LHCP observations to the precipitation impact is found to be higher compared to RHCP observations. The analysis also shows that standard deviation of the surface height, as an indicator of roughness, monotonically increases with the rain rate. The GNSS-R estimated surface salinity can also sense a rain-induced decline at rain rates above 10 mm/h.

The performance of GNSS-R sea level measurements is also assessed through two studies. The first study investigated the behavior of the sea level measurements error and bias under different roughness con-ditions. Evaluation of the measurements obtained from an up-looking and two sea-looking antennas reports on an almost uniform quality for the measurements from each antenna at wind speeds from 0 to 8 m/s. At higher wind speeds all the three sets of measurements show a signi-ficant wind-dependent degradation in the quality of retrieved sea levels. This is manifested through both the Root Mean Squared Error (RMSE) and bias values of the measurements with respect to the nearest tide gauge. Overall, the seaward-tilted LHCP antenna shows the best per-formance with an RMSE of 1.7 to 2.7 cm for winds ranging from 0 to 11 m/s and 3.7 to 21.9 cm for higher winds up to 30 m/s.

Another performance assessment of sea level measurements has been conducted to investigate the role of observing system variables. These variables include the polarization and orientation of the antenna, as well as the frequency of the reflected signals. Moreover, possible improvements due to combination of different types of observations are evaluated. The results show that the combination of observations from L1 and L2 frequencies (L12) from a sea-looking LHCP antenna provides the best performance. Regarding the comparison of the products based on L1 and L2 frequencies, the L2 observations generally provides

a lower degree of accuracy most likely suffering from fewer observations. In terms of antenna orientation, a seaward tilting with the angle of 90 degrees with respect to the zenith, optimizes the antenna agains for capturing the sea-reflected signals and magnifies interferometric patterns. Concerning the polarization, the analysis confirms that while the RHCP antenna can be readily used for grazing angles altimetry, using an antenna with LHCP design is the right choice for capturing the reflections at higher elevation angles. Usage of different averaging windows can also affect the quality of final products. The RMSE values of GNSS-R sea levels from the LHCP sea-looking antenna compared to collocated tide gauge measurements are 2.4, 3.0, 4.5, 5.6 cm for 6, 3, 1, and 0.25-hour window size, respectively. The final L12 sea level estimates show an increased tolerance against high wind speeds.

✓ *RQ 2.2: What is the prospect for future ground-based GNSS-R stations?*

The ground-based GNSS-R technique can be used for real-time or near real-time monitoring of different geophysical parameters. Data streams are available from numerous permanent GNSS stations with possibility of receiving reflection from land or sea. These data stream can be used for e.g., monitoring soil moisture variations, and sea surface characterization. However, permanent GNSS stations use standard geodetic receivers with RHCP up-looking antenna. Based on the studies carried on in this dissertation, utilization of an LHCP antenna or tilting antenna towards the reflecting surface can enhance the performance of reflectometry measurements. Therefore, a potential future permanent station can be a combined geodetic and reflectometry station. Such stations can utilize several antennas for direct signals tracking as well as reflectometry purposes.

An exemplary configuration has been established by German Research Center for Geosciences (GFZ) at Onsala Space Observatory in Sweden, where a zenith-looking antenna simultaneously feeds a geodetic and a reflectometry receiver by an antenna splitter. Up to three antennas with RHCP or LHCP design can be installed at such station to capture and process reflections from the surrounding areas.

- **Objective 3: To demonstrate novel applications of a new-generation of GNSS remote sensing measurements**

In recent years, several spaceborne missions with dedicated GNSS-R payloads are designed and launched for Earth observations. The most famous missions are the UK TechDemoSat-1 (TDS-1) and NASA Cyclone GNSS

(CYGNSS). The availability of spaceborne GNSS-R observations has opened up the opportunity of exploring new possible applications within the scientific community. The applications introduced by the community are associated with different geophysical parameters over the ocean, land, and cryosphere.

✓ *RQ 3.1: How can the new-generation of GNSS measurements from spaceborne reflectometry be used for climate and environmental monitoring?*

Mesoscale ocean eddies are among the important features of the ocean that play an active role in ocean-atmosphere interactions. Spaceborne GNSS-R technique can provide a new source of observations to improve understanding of the dynamics of these oceanic features. A study of this dissertation demonstrated that the eddies can leave their signature on the spaceborne GNSS-R observations. The signature is characterized by the change in the ocean surface roughness due to the interaction of the eddies with atmosphere. The study reports on two detected patterns in the CYGNSS profiles of Normalized Bi-static Radar Cross Section (NBRCS) over the eddies. In addition, strong negative correlations between both surface heat flux, and surface stress with the NBRCS are observed over the eddies.

In addition to the remote sensing of the eddies, timely GNSS-R observations over the land can be used to monitor natural hazards and severe weather conditions due to climate variations. Another study included in this thesis is dedicated to evaluating the potential of spaceborne GNSS-R observations from NASA CYGNSS mission for flood detection and mapping. The study shows that the Signal to Noise Ratio (SNR) observations from CYGNSS can effectively detect the presence of flooding events and retrieve the associated inundated areas.

✓ *RQ 3.2: What is the prospect for future spaceborne GNSS-R missions and applications?*

The passive instrumentation used for spaceborne GNSS-R sensors are relatively low-cost, low-power, and low-mass. This feature makes GNSS-R a perfect match for CubeSats. The idea of using dedicated GNSS-R CubeSats is being pursued by several international research teams. However, several challenges have to be addressed to produce remote sensing data products based on the scientific demands. Recording reflected GNSS signals at rawest possible level in space creates several opportunities for improvements in, e.g., on-board processing scheme, calibration procedure, and spatial or temporal resolution of

the observations. Moreover, feasibility of some new applications could be investigated. Finally, dual-polarization observations are foreseen to be provided by some of future missions, which can initiate new applications and research topics in the community.

4.2   Future Research

On the basis of the research conducted in this dissertation, the following research topics are proposed for the enhancement of the GNSS-derived remote sensing data products and to introduce new applications:

- **Real-time ground-based GNSS-R measurements in practice:** Based on the availability of real-time observations from permanent geodetic GNSS stations, several GNSS-R data products related to land or sea can now be generated. Therefore, national authorities or private companies can initiate generating low-cost high-gain byproducts from the already available data streams. This can initiate the usage of the products and development of the processing algorithms. For instance, in the presence of multi-constellation multi-frequency observations, a *unified approach* for processing the concurrent reflectometry observations can be pursued to simultaneously retrieve any possible geophysical parameters of interest. This can turn the stations to *Multi-purpose GNSS stations* which can perform new remote sensing tasks in addition to serving several established applications including positioning and navigation, timing, and geodynamics.

- **New-generation of permanent GNSS stations:** This dissertation comprises several studies based on the dual-polarization GNSS-R observations. As the results elucidate the superior performance of polarimetric observations with tilted antennas, a new-generation of permanent stations can be considered for future networks of Continuously Operating Reference Stations (CORS). These stations can be equipped with both LHCP and RHCP antennas to maximize the outcome of the reflectometry observations. For this purpose, a new receiver design is needed to support multiple antennas and simultaneously provide both regular and reflectometry data streams.

- **Fully-polarimetric reconstruction of GNSS reflected signal:** The dataset used in this thesis for the analysis of ground-based GNSS-R observations can be used to improve the understanding of the ellipticity of GNSS reflected signals based on the variations of different geophysical parameters.

- **Multi-frequency Polarimetric observations from GNSS-R CubeSats:** Spaceborne GNSS-R is a novel remote sensing technique. Most of its applica-

tions are under development or need more research to be mature enough for practical implementation on CubeSats. Having raw-level signal recording in dual-polarization mode provides invaluable polarimetric dataset as a foundation for methodological improvements of the applications and for paving the way for routine operations. A promising improvement in the spatio-temporal resolution of the GNSS-R observations can be achieved by including other GNSS constellations, i.e. Russian GLONASS, European Galileo, and Chinese BeiDou systems.

References

[1] Theodore Alexandrov. A method of trend extraction using singular spectrum analysis. *arXiv preprint arXiv:0804.3367*, 2008.

[2] Fadwa Alshawaf, Florian Zus, K Balidakis, Z Deng, Mostafa Hoseini, G Dick, and J Wickert. On the statistical significance of climatic trends estimated from gps tropospheric time series. *Journal of Geophysical Research: Atmospheres*, 123(19):10–967, 2018.

[3] Ali Reza Amiri-Simkooei, Christian CJM Tiberius, and Peter JG Teunissen. Assessment of noise in GPS coordinate time series: methodology and results. *Journal of Geophysical Research: Solid Earth*, 112(B7), 2007.

[4] AR Amiri-Simkooei. On the nature of GPS draconitic year periodic pattern in multivariate position time series. *Journal of Geophysical Research: Solid Earth*, 118(5):2500–2511, 2013.

[5] Milad Asgarimehr, Mostafa Hoseini, Maximilian Semmling, Markus Ramatschi, Adriano Camps, Hossein Nahavandchi, Rüdiger Haas, and Jens Wickert. Remote sensing of precipitation using reflected gnss signals: Response analysis of polarimetric observations. *IEEE Transactions on Geoscience and Remote Sensing*, 60:1–12, 2021.

[6] J Askne and H Nordius. Estimation of tropospheric delay for microwaves from surface weather data. *Radio Science*, 22(03):379–386, 1987.

[7] Michael Bevis, Steven Businger, Steven Chiswell, Thomas A Herring, Richard A Anthes, Christian Rocken, and Randolph H Ware. Gps meteorology: Mapping zenith wet delays onto precipitable water. *Journal of applied meteorology*, 33(3):379–386, 1994.

[8] Georg Beyerle. Carrier phase wind-up in gps reflectometry. *GPS solutions*, 13(3):191, 2009.

[9] Johannes Boehm, Birgit Werl, and Harald Schuh. Troposphere mapping functions for gps and very long baseline interferometry from european centre for medium-range weather forecasts operational analysis data. *Journal of geophysical research: solid earth*, 111(B2), 2006.

[10] Johannes Böhm, Gregor Möller, Michael Schindelegger, Gregory Pain, and Robert Weber. Development of an improved empirical model for slant delays in the troposphere (gpt2w). *GPS solutions*, 19(3):433–441, 2015.

[11] Estel Cardellach, Fran Fabra, Antonio Rius, Simone Pettinato, and Salvatore D'Addio. Characterization of dry-snow sub-structure using GNSS reflected signals. *Remote Sensing of Environment*, 124:122 – 134, 2012. ISSN 0034-4257.

[12] CC Chew and EE Small. Soil moisture sensing using spaceborne gnss reflections: Comparison of cygnss reflectivity to smap soil moisture. *Geophysical Research Letters*, 45(9):4049–4057, 2018.

[13] Clara Chew, John T Reager, and Eric Small. Cygnss data map flood inundation during the 2017 atlantic hurricane season. *Scientific reports*, 8(1):1–8, 2018.

[14] JL Davis, TA Herring, II Shapiro, AEE Rogers, and Gunnar Elgered. Geodesy by radio interferometry: Effects of atmospheric modeling errors on estimates of baseline length. *Radio science*, 20(6):1593–1607, 1985.

[15] Dick P Dee, S M Uppala, Adrian J Simmons, Paul Berrisford, Paul Poli, Shinya Kobayashi, U Andrae, MA Balmaseda, G Balsamo, d P Bauer, et al. The era-interim reanalysis: Configuration and performance of the data assimilation system. *Quarterly Journal of the royal meteorological society*, 137(656):553–597, 2011.

[16] Domingo A. Gagliardini. *Medium Resolution Microwave, Thermal and Optical Satellite Sensors: Characterizing Coastal Environments Through the Observation of Dynamical Processes*, pages 251–277. Springer Berlin Heidelberg, Berlin, Heidelberg, 2011. ISBN 978-3-642-16541-2. doi: 10.1007/978-3-642-16541-2_13. URL https://doi.org/10.1007/978-3-642-16541-2_13.

[17] Yusof Ghiasi, Claude R Duguay, Justin Murfitt, Joost J van der Sanden, Aaron Thompson, Hugo Drouin, and Christian Prévost. Application of GNSS

Interferometric Reflectometry for the Estimation of Lake Ice Thickness. *Remote Sensing*, 12(17):2721, 2020.

[18] Michael Ghil, MR Allen, MD Dettinger, K Ide, D Kondrashov, ME Mann, Andrew W Robertson, A Saunders, Y Tian, F Varadi, et al. Advanced spectral methods for climatic time series. *Reviews of geophysics*, 40(1):3–1, 2002.

[19] Nina Golyandina, Vladimir Nekrutkin, and Anatoly A Zhigljavsky. *Analysis of time series structure: SSA and related techniques*. CRC press, 2001.

[20] LP Gradinarsky, JM Johansson, HR Bouma, H-G Scherneck, and G Elgered. Climate monitoring using gps. *Physics and Chemistry of the Earth, Parts A/B/C*, 27(4-5):335–340, 2002.

[21] Achim Helm, Oliver Montenbruck, Javad Ashjaee, Sergey Yudanov, Georg Beyerle, Ralf Stosius, and Markus Rothacher. Gors-a gnss occultation, reflectometry and scatterometry space receiver. In *Proceedings of the 20th International Technical Meeting of the Satellite Division of The Institute of Navigation (ION GNSS 2007)*, pages 2011–2021, 2007.

[22] TA Herring. Modeling atmospheric delays in the analysis of space geodetic data. *Proceedirws of Refraction of Transatmospheric simals in Geodesy, eds. JC De Munck and TA Spoelstra, Netherlands Geodetic Commission Publications on Geodesy*, 36(4), 1992.

[23] Yukiko Hirabayashi, Roobavannan Mahendran, Sujan Koirala, Lisako Konoshima, Dai Yamazaki, Satoshi Watanabe, Hyungjun Kim, and Shinjiro Kanae. Global flood risk under climate change. *Nature climate change*, 3 (9):816–821, 2013.

[24] Bernhard Hofmann-Wellenhof, Herbert Lichtenegger, and Elmar Wasle. *GNSS–global navigation satellite systems: GPS, GLONASS, Galileo, and more*. Springer Science & Business Media, 2007.

[25] Mostafa Hoseini, Milad Asgarimehr, Hossein Nahavandchi, and Jens Wickert. Spaceborne gnss-r observations of mesoscale ocean eddies; preliminary results from cygnss mission. In *IGARSS 2019-2019 IEEE International Geoscience and Remote Sensing Symposium*, pages 8696–8699. IEEE, 2019.

[26] Mostafa Hoseini, Fadwa Alshawaf, Hossein Nahavandchi, Galina Dick, and Jens Wickert. Towards a zero-difference approach for homogenizing gnss tropospheric products. *GPS Solutions*, 24(1):1–12, 2020.

[27] Mostafa Hoseini, Milad Asgarimehr, Valery Zavorotny, Hossein Nahavand-chi, Chris Ruf, and Jens Wickert. First evidence of mesoscale ocean eddies signature in gnss reflectometry measurements. *Remote Sensing*, 12(3):542, 2020.

[28] Mostafa Hoseini, Maximilian Semmling, Hossein Nahavandchi, Erik Rennspiess, Markus Ramatschi, Rüdiger Haas, Joakim Strandberg, and Jens Wickert. On the response of polarimetric gnss-reflectometry to sea surface roughness. *IEEE Transactions on Geoscience and Remote Sensing*, 2020.

[29] John David Jackson. Classical electrodynamics, 1999.

[30] Shuanggen Jin, Estel Cardellach, and Feiqin Xie. *GNSS remote sensing*, volume 16. Springer, 2014.

[31] J. A. Johannessen, V. Kudryavtsev, D. Akimov, T. Eldevik, N. Winther, and B. Chapron. On radar imaging of current features: 2. Mesoscale eddy and current front detection. *Journal of Geophysical Research: Oceans*, 110(C7), 2005. doi: 10.1029/2004JC002802. URL https://agupubs.onlinelibrary.wiley.com/doi/abs/10.1029/2004JC002802.

[32] Daniel Landskron and Johannes Böhm. Vmf3/gpt3: refined discrete and empirical troposphere mapping functions. *Journal of Geodesy*, 92(4):349–360, 2018.

[33] Richard B. Langley, Peter J.G. Teunissen, and Oliver Montenbruck. *Introduction to GNSS*, pages 3–23. Springer International Publishing, Cham, 2017. ISBN 978-3-319-42928-1. doi: 10.1007/978-3-319-42928-1_1.

[34] Kristine M Larson, Eric E Small, Ethan Gutmann, Andria Bilich, Penina Axelrad, and John Braun. Using gps multipath to measure soil moisture fluctuations: initial results. *GPS solutions*, 12(3):173–177, 2008.

[35] Wei Liu, Jamila Beckheinrich, Maximilian Semmling, Markus Ramatschi, Sibylle Vey, Jens Wickert, Thomas Hobiger, and Rüdiger Haas. Coastal sea-level measurements based on gnss-r phase altimetry: A case study at the onsala space observatory, sweden. *IEEE Transactions on Geoscience and Remote Sensing*, 55(10):5625–5636, 2017.

[36] Michael Meurer and Felix Antreich. *Signals and Modulation*, pages 91–119. Springer International Publishing, Cham, 2017. ISBN 978-3-319-42928-1. doi: 10.1007/978-3-319-42928-1_4.

[37] Felipe G Nievinski and Kristine M Larson. Forward modeling of GPS multipath for near-surface reflectometry and positioning applications. *GPS solutions*, 18(2):309–322, 2014.

[38] T Ning, J Wickert, Z Deng, Stefan Heise, G Dick, Sibylle Vey, and Tilo Schöne. Homogenized time series of the atmospheric water vapor content obtained from the gnss reprocessed data. *Journal of Climate*, 29(7):2443–2456, 2016.

[39] Kirill Palamartchouk, Peter J Clarke, Stuart J Edwards, and Rajesh Tiwari. Dual-polarization gnss observations for multipath mitigation and better high-precision positioning. In *Proceedings of the 28th International Technical Meeting of the Satellite Division of The Institute of Navigation (ION GNSS+ 2015)*, pages 2772–2779, 2015.

[40] M. Raiabi, M. Hoseini, H. Nahavandchi, M. Semmling, M. Ramatschi, M. Goli, R. Haas, and J. Wickert. A performance assessment of polarimetric gnss-r sea level monitoring in the presence of sea surface roughness. In *2021 IEEE International Geoscience and Remote Sensing Symposium IGARSS*, pages 8328–8331, 2021. doi: 10.1109/IGARSS47720.2021.9554562.

[41] M. Raiabi, M. Hoseini, H. Nahavandchi, M. Semmling, M. Ramatschi, M. Goli, R. Haas, and J. Wickert. A performance assessment of polarimetric gnss-r sea level monitoring in the presence of sea surface roughness. In *2021 IEEE International Geoscience and Remote Sensing Symposium IGARSS*, pages 8328–8331, 2021. doi: 10.1109/IGARSS47720.2021.9554562.

[42] Mahmoud Rajabi, Alireza Amiri-Simkooei, Hossein Nahavandchi, and Vahab Nafisi. Modeling and prediction of regular ionospheric variations and deterministic anomalies. *Remote Sensing*, 12(6):936, 2020.

[43] Mahmoud Rajabi, Hossein Nahavandchi, and Mostafa Hoseini. Evaluation of cygnss observations for flood detection and mapping during sistan and baluchestan torrential rain in 2020. *Water*, 12(7):2047, 2020.

[44] Mahmoud Rajabi, Mostafa Hoseini, Hossein Nahavandchi, Maximilian Semmling, Markus Ramatschi, Mehdi Goli, Rüdiger Haas, and Jens Wickert. Polarimetric gnss-r sea level monitoring using i/q interference patterns at different antenna configurations and carrier frequencies. *IEEE Transactions on Geoscience and Remote Sensing*, 2021.

[45] Mahmoud Rajabi, Mostafa Hoseini, Hossein Nahavandchi, Maximilian Semmling, Markus Ramatschi, Mehdi Goli, Rüdiger Haas, and Jens Wick-

ert. Polarimetric gnss-r sea level monitoring using i/q interference patterns at different antenna configurations and carrier frequencies. *IEEE Transactions on Geoscience and Remote Sensing*, pages 1–1, 2021. doi: 10.1109/TGRS.2021.3123146.

[46] C Ruf, Paul Chang, Maria-Paola Clarizia, Scott Gleason, Z Jelenak, J Murray, M Morris, S Musko, D Posselt, D Provost, et al. Cygnss handbook. *Ann Arbor, MI, Michigan Pub*, 154, 2016.

[47] J Saastamoinen. Atmospheric correction for the troposphere and stratosphere in radio ranging satellites. *The use of artificial satellites for geodesy*, 15:247–251, 1972.

[48] Alvaro Santamaría-Gómez and Christopher Watson. Remote leveling of tide gauges using gnss reflectometry: case study at spring bay, australia. *GPS solutions*, 21(2):451–459, 2017.

[49] Franck Selsis. *Neutral Atmosphere*, pages 1112–1112. Springer Berlin Heidelberg, Berlin, Heidelberg, 2011. ISBN 978-3-642-11274-4. doi: 10.1007/978-3-642-11274-4_1050. URL https://doi.org/10.1007/978-3-642-11274-4_1050.

[50] A Maximilian Semmling, Anja Rösel, Dmitry V Divine, Sebastian Gerland, Georges Stienne, Serge Reboul, Marcel Ludwig, Jens Wickert, and Harald Schuh. Sea-Ice Concentration Derived From GNSS Reflection Measurements in Fram Strait. *IEEE Transactions on Geoscience and Remote Sensing*, 57(12):10350–10361, 2019.

[51] Maximilian Semmling. *Altimetric monitoring of Disko Bay using interferometric GNSS observations on L1 and L2*. PhD thesis, Deutsches Geo-ForschungsZentrum GFZ Potsdam, 2012.

[52] Kamil Teke, Johannes Böhm, Tobias Nilsson, Harald Schuh, Peter Steigenberger, Rolf Dach, Robert Heinkelmann, Pascal Willis, Rüdiger Haas, Susana García-Espada, et al. Multi-technique comparison of troposphere zenith delays and gradients during cont08. *Journal of Geodesy*, 85(7):395–413, 2011.

[53] Peter Teunissen and Oliver Montenbruck. *Springer handbook of global navigation satellite systems*. Springer, 2017.

[54] Frank Van Diggelen and Per Enge. The world's first gps mooc and worldwide laboratory using smartphones. In *Proceedings of the 28th international technical meeting of the satellite division of the institute of navigation (ION*

GNSS+ 2015), pages 361–369, 2015. URL https://scpnt.stanford.edu/research/current-research/gps-mooc.

[55] Victor KC Venema, Olivier Mestre, Enric Aguilar, Ingeborg Auer, José Antonio Guijarro, Peter Domonkos, Gregor Vertacnik, Tamas Szentimrey, Petr Stepanek, P Zahradnicek, et al. Benchmarking homogenization algorithms for monthly data. In *AIP Conference Proceedings*, volume 1552, pages 1060–1065. American Institute of Physics, 2013.

[56] Michael E Wall, Andreas Rechtsteiner, and Luis M Rocha. Singular value decomposition and principal component analysis. In *A practical approach to microarray data analysis*, pages 91–109. Springer, 2003.

[57] SDP Williams and FG Nievinski. Tropospheric delays in ground-based gnss multipath reflectometry—experimental evidence from coastal sites. *Journal of Geophysical Research: Solid Earth*, 122(3):2310–2327, 2017.

[58] Valery U Zavorotny and Alexander G Voronovich. Scattering of gps signals from the ocean with wind remote sensing application. *IEEE Transactions on Geoscience and Remote Sensing*, 38(2):951–964, 2000.

This page is intentionally left blank

Chapter 5

Publications

This chapter includes some of the publications which present the main focus of the thesis:

- *Paper I:*

  Hoseini, Mostafa; Alshawaf, Fadwa; Nahavandchi, Hossein; Dick, Galina; Wickert, Jens. (2020) Towards a Zero-difference Approach for Homogenizing GNSS Tropospheric Products. GPS Solutions. vol. 24 (8). DOI: 10.1007/s10291-019-0915-2

- *Paper II:*

  Hoseini, Mostafa; Semmling, Maximilian; Nahavandchi, Hossein; Rennspiess, Erik; Ramatschi, Markus; Haas, Rüdiger; Strandberg, Joakim; Wickert, Jens. (2021) On the Response of Polarimetric GNSS-Reflectometry to Sea Surface Roughness, in IEEE Transactions on Geoscience and Remote Sensing, vol. 59, no. 9, pp. 7945-7956, Sep. 2021. DOI: 10.1109/TGRS.2020.3031396

- *Paper III:*

  Asgarimehr, Milad; **Hoseini, Mostafa**; Semmling, Maximilian; Ramatschi, Markus; Camps, Adriano; Nahavandchi, Hossein; Haas, Rüdiger; Wickert, Jens. (2021) Remote Sensing of Precipitation using Reflected GNSS Signals: Response Analysis of Polarimetric Observations. IEEE Transactions on Geoscience and Remote Sensing. DOI: 10.1109/TGRS.2021.3062492

- *Paper IV:*

  Rajabi, Mahmoud; **Hoseini, Mostafa**; Nahavandchi, Hossein; Semmling, Maximilian; Ramatschi, Markus; Goli, Mehdi; Haas, Rüdiger; Wickert, Jens. (2021) A Performance Assessment of Polarimetric GNSS-R Sea Level Monitoring in the Presence of Sea Surface Roughness. IEEE International Geoscience and Remote Sensing Symposium IGARSS, 2021, pp. 8328-8331. DOI: 10.1109/IGARSS47720.2021.9554562

- *Paper V:*

  Rajabi, Mahmoud; **Hoseini, Mostafa**; Nahavandchi, Hossein; Semmling, Maximilian; Ramatschi, Markus; Goli, Mehdi; Haas, Rüdiger; Wickert, Jens. (2021) Polarimetric GNSS-R Sea Level Monitoring using I/Q Interference Patterns at Different Antenna Configurations and Carrier Frequencies, in IEEE Transactions on Geoscience and Remote Sensing. DOI: 10.1109/TGRS.2021.3123146

- *Paper VI:*

  Hoseini, Mostafa; Asgarimehr, Milad; Nahavandchi, Hossein; Wickert, Jens. (2019) Spaceborne GNSS-R Observations of Mesoscale Ocean Eddies; Preliminary Results from Cygnss Mission. IEEE International Geoscience and Remote Sensing Symposium proceedings. DOI: 10.1109/IGARSS.2019.8898461

- *Paper VII:*

  Hoseini, Mostafa; Asgarimehr, Milad; Zavorotny, valery; Nahavandchi, Hossein; Ruf, chris; Wickert, Jens. (2020) First Evidence of Mesoscale Ocean Eddies Signature in GNSS Reflectometry Measurements. Remote Sensing. vol. 12 (542). DOI: 10.3390/rs12030542

- *Paper VIII:*

  Rajabi, Mahmoud; Nahavandchi, Hossein; **Hoseini, Mostafa**. (2020) Evaluation of CYGNSS Observations for Flood Detection and Mapping during Sistan and Baluchestan Torrential Rain in 2020. Water. vol. 12 (7). DOI: 10.3390/w12072047

The author has other following contributions which are not included in this thesis:

○ Modiri, Sadegh; Belda, Santiago; Heinkelmann, Robert; **Hoseini, Mostafa**; Ferrandiz, Jose M; Schuh, Harald. (2018) Polar motion prediction using the

combination of SSA and Copula-based analysis. Earth Planets and Space. vol. 70 (1). DOI: 10.1186/s40623-018-0888-3

○ Alshawaf, Fadwa; Zus, Florian; Balidakis, Kyriakos; Deng, Zhiguo; **Hoseini, Mostafa**; Dick, Galina; Wickert, Jens. (2018) On the Statistical Significance of Climatic Trends Estimated From GPS Tropospheric Time Series. Journal of Geophysical Research (JGR): Space Physics. vol. 123 (19). DOI: 10.1029/2018JD028703

○ Van Malderen, Roeland; Pottiaux, E.; Klos, A.; Domonkos, P.; Elias, M.; Ning, T.; Bock, O.; Guijarro, J.; Alshawaf, F.; **Hoseini, M.**; Quarello, A.; Lebarbier, E.; Chimani, B.; Tornatore, V.; Zengin Kazancı, S.; Bogusz, J.. (2020) Homogenizing GPS Integrated Water Vapor Time Series: Benchmarking Break Detection Methods on Synthetic Data Sets. Earth and Space Science. vol. 7 (5). DOI: 10.1029/2020EA001121

○ Shamshiri, Roghayeh; Motagh, Mahdi; Nahavandchi, Hossein; Haghshenas, Mahmud; **Hoseini, Mostafa**. (2020) Improving tropospheric corrections on large-scale Sentinel-1 interferograms using a machine learning approach for integration with GNSS-derived zenith total delay (ZTD). Remote Sensing of Environment. vol. 239 (111608). DOI: 10.1016/j.rse.2019.111608

○ Modiri, Sadegh; Belda, Santiago; **Hoseini, Mostafa**; Heinkelmann, Robert; Ferrandiz, Jose M; Schuh, Harald. (2020) A new hybrid method to improve the ultra-short-term prediction of LOD. Journal of Geodesy. vol. 94 (2). DOI: 10.1007/s00190-020-01354-y

○ Modiri, Sadegh; Heinkelmann, Robert; Belda, Santiago; Malkin, Zinovy; **Hoseini, Mostafa**; Korte, Monika; Ferrándiz, José M.; Schuh, Harald. (2021) Towards Understanding the Interconnection between Celestial Pole Motion and Earth's Magnetic Field Using Space Geodetic Techniques. Sensors 21, no. 22: 7555. DOI: 10.3390/s21227555

Paper I

Towards a zero-difference approach for homogenizing GNSS tropospheric products

Mostafa Hoseini[1] · Fadwa Alshawaf[2] · Hossein Nahavandchi[1] · Galina Dick[2] · Jens Wickert[2,3]

Abstract

A data homogenization method based on singular spectrum analysis (SSA) was developed and tested on real and simulated datasets. The method identifies abrupt changes in the atmospheric time series derived from Global Navigation Satellite System (GNSS) observations. For simulation and verification purposes, we used the ERA-Interim reanalysis data. Our method of change detection is independently applied to the precipitable water vapor (PWV) time series from GNSS, ERA-Interim and their difference. Then the detected offsets in the difference time series can be related to inconsistencies in the datasets or to abrupt changes due to climatic effects. The issue of missing data is also discussed and addressed using SSA. We appraised the performance of our method using a Monte Carlo simulation, which suggests a promising success rate of 81.1% for detecting mean shifts with values between 0.5 and 3 mm in PWV time series. A GNSS-derived PWV dataset, consisting of 214 stations in Germany, was investigated for possible inhomogeneities and systematic changes. We homogenized the dataset by identifying and correcting 96 inhomogeneous time series containing 134 detected and verified mean shifts from which 45 changes, accounting for approximately 34% of the offsets, were undocumented. The linear trends from the GNSS and ERA-Interim PWV datasets were estimated and compared, indicating a significant improvement after homogenization. The correlation between the trends was increased by 39% after correcting the mean shifts in the GNSS data. The method can be used to detect possible changes induced by climatic or meteorological effects.

Introduction

Global Navigation Satellite System (GNSS) signals are affected by the earth's atmosphere. The delayed signals limit the high-precision positioning and navigation applications, but the error can be exploited to study different parts of the atmosphere, including the water vapor. Monitoring the atmospheric water vapor is important since it is a major atmospheric greenhouse gas with significant impact on the earth's radiative balance (Sinha and Harries 1997). It can generally act as a warming amplifier so that the cycling rate of water vapor reduces with the warming climate (Schneider et al. 2010). High-temporal resolution observations and an increasing number of satellites have turned GNSS into a promising measuring tool for investigating the variability of the water vapor, especially in the presence of a dense network of permanent stations.

Owing to the high temporal resolution, the accuracy of products, and the capability of making measurements even in severe weather conditions, the retrieved water vapor content of the atmosphere from ground-based GNSS observations has been identified as one of the reference data for GCOS (Global Climate Observing System) Reference Upper Air Network (GRUAN, Ning et al. 2016). Precipitable water vapor (PWV) from GNSS has increasingly been

✉ Mostafa Hoseini
mostafa.hoseini@ntnu.no

1 Department of Civil and Environmental Engineering, Norwegian University of Science and Technology NTNU, Trondheim, Norway

2 German Research Centre for Geosciences GFZ, Potsdam, Germany

3 Institute of Geodesy and Geoinformation Science, Technische Universität Berlin, Berlin, Germany

used for climate research (Gradinarsky et al. 2002; Nilsson and Elgered 2008; Wang et al. 2016; Alshawaf et al. 2017). The accuracy of the estimated climatic trends using GNSS PWV depends on the homogeneity of the analyzed time series (Alshawaf et al. 2018; Klos et al. 2018). For different reasons such as hardware or software changes, the data might contain inhomogeneities (temporal jumps or offsets). Such artifacts should be detected and eliminated through a delicate homogenization process without affecting climatic abrupt changes.

By definition, a homogeneous climate time series can only contain the variations caused by weather and climate (Venema et al. 2012). The main sources of inhomogeneity in GNSS-derived PWV data are instrumental changes or software settings of the GNSS station, e.g., antenna change, radome installation or removal, and cut-off angle setting (Vey et al. 2009). Most of the changes stem from the technological advancements, which make it unavoidable to update the hardware in GNSS stations. Therefore, GNSS-derived PWV time series are likely to have inhomogeneities, especially in the longer time series that would be used for climate studies. The changes are usually documented in the stations' log files, but the documentation might be incomplete or missing for some of them. Change in the measurement conditions and the surrounding area of the station such as urbanization and growth or removal of vegetation might also affect the homogeneity of the time series. In the case of not using a reprocessed dataset, the change of processing software or procedure is another possible source of inhomogeneity. The external measurements that are used to obtain PWV from GNSS data processing, such as air pressure and temperature can pass their heterogeneity to the derived PWV time series. It should be noted that the mentioned reasons of inhomogeneity are generally not documented in the station's log file. Therefore, finding a pragmatic solution for detection and verification of undocumented changes during the homogenization process is inevitable.

Different approaches have been introduced to check the homogeneity of GNSS products. For instance, Rodionov (2004) proposed a sequential algorithm which introduced a statistic entitled the Regime Shift Index (RSI) coupled with the Student's *t* test to enhance detection of a regime shift. The Penalized maximal *t* test has widely been used for data homogenization (Jarušková 1996; Wang et al. 2007; Ning et al. 2016; Balidakis et al. 2018). Wang (2008), Ning et al. (2016), Klos et al. (2017), and Van Malderen et al. (2017), considered lag-1 autocorrelation in time series of first-order autoregressive noise. To support the detection of multiple change points in a time series, Wang (2008) proposed an empirical approach based on a stepwise testing algorithm. Ning et al. (2016) applied an iterative adapted version of penalized maximal *t* test to the monthly PWV time series, which helps in avoiding the difficulty of change

point detection in the presence of high temporal variations and noise in the daily PWV data.

The "Data homogenization" activity of the sub-working group WG3 of COST ES1206 Action has assessed various statistical tools for homogenization using a synthetic benchmark dataset. The simulated dataset was based on the difference between GNSS-derived PWV time series and the European Centre for Medium-Range Weather Forecasts (ECMWF) reanalysis data (ERA-Interim) (Van Malderen et al. 2017). Using the difference time series can facilitate the detection of slight changes, but it is difficult to interpret the origin of the detected changes. Ning et al. (2016) validated detected change points using more than one reference dataset (e.g., VLBI, DORIS). Therefore, the verification process is left inconclusive in the case of not having another reference data set for a station. The latter study shows the possibility of the presence of inhomogeneities in the ERA-Interim dataset. The study reveals the need for having an independent verification procedure of any reference data. Van Malderen et al. (2017) preferred not to consider absolute statistical homogenization methods as practical approaches, owing to the problem of reliability, even though they confirm that ERA-interim might have its own inhomogeneities.

We develop and apply an approach to detect abrupt changes in an undifferenced time series. GNSS-derived PWV time series, in addition to the probable inconsistencies, contain the effects of climate or meteorological variabilities. Therefore, at least one reference dataset is required, e.g., ERA-Interim, to distinguish whether the offsets are caused by climate or meteorological effects or by inhomogeneities. We developed a method of offset detection in PWV time series, which is independently applicable to GNSS and ERA-Interim PWV data as well as their difference. This is performed by analyzing the time series variations with respect to a representative model. For this purpose, we exploit the singular spectrum analysis (SSA) as a subspace-based technique, which makes use of empirical functions derived from the data to model the time series in a pre-specified level of details. SSA is a non-parametric method that does not need any statistical assumptions such as stationarity of the series or normality of the residuals (Hassani and Thomakos 2010). Even in the presence of periodicity and noise, SSA can offer an adequate estimation of the time series based on setting a few arguments (such as window length). It can be used for trend extraction and extrapolation (Alexandrov 2008; Modiri et al. 2018), periodicity detection, seasonal adjustment, smoothing, noise reduction (Ghil et al. 2001; Golyandina et al. 2001) as well as change point detection (Escott-Price and Zhigljavsky 2003).

After a brief description of the datasets in the next section, we sketch out the SSA technique at the beginning of the methodology section, which continues by introducing our approach for homogenization. That section also

comprises details of the offset detection method, as well as preprocessing and verification procedures. The performance assessment based on applying the method to simulated data is followed by a real GNSS dataset homogenization in the results section. A summary of the conclusions of this study is provided in the last section.

Dataset

We use a PWV near real-time dataset produced by the German Research Centre for Geosciences (GFZ). The dataset has a temporal resolution of 15 min with a delay of about 30 min and an accuracy of 1–2 mm (Li et al. 2014). The PWV time series are calculated from the Zenith Total Delay (ZTD) derived at GNSS stations of the German SAPOS network in PPP mode.

The GNSS-derived PWV can be obtained from the wet part of the ZTD, the Zenith Wet Delay (ZWD), via the conversion factor Q:

$$ZWD = ZTD - ZHD \tag{1}$$

$$PWV = \frac{ZWD}{Q} \tag{2}$$

where the ZHD is the Zenith Hydrostatic Delay (ZHD) estimated by the Saastamoinen model (Saastamoinen 1972) using measurements of surface pressure. The conversion factor is computed using (Askne and Nordius 1987):

$$Q = 10^{-6} \rho_w R_w \left(k_2' + \frac{k_3}{T_m} \right) \tag{3}$$

where ρ_w and R_w are the density of liquid water and the specific gas constant for water vapor. The k_2' and k_3 are constants estimated from laboratory experiments (Bevis et al. 1994) and T_m is the water vapor weighted mean temperature in Kelvin.

Near real-time GNSS tropospheric time series are likely to contain more cases of inconsistencies compared to the time series from a post-processed dataset that utilizes a consistent strategy and settings for the processing. Therefore, choosing the near real-time dataset gives us the opportunity of encountering and addressing more cases of inhomogeneities. We apply our homogenization approach to a selected dataset of near real-time GNSS-derived PWV time series at 214 permanent GNSS stations from 2010 to 2016. See Fig. 10 for the location of the stations.

The proposed homogenization method utilizes a reference dataset which contains a priori information about abrupt changes that are not inhomogeneities. Here we use ERA-Interim PWV time series as the reference to provide the required information about climatic and meteorological effects. The ERA-Interim dataset, released by ECMWF,

is a global atmospheric reanalysis product covering a time span of about 40 years from 1979 onwards. It provides gridded data products with a spatial resolution of approximately 79 km including a wealth of 3-hourly information of surface parameters describing weather, ocean-wave and land-surface conditions, as well as 6-hourly upper-air parameters covering the troposphere and stratosphere. The vertical resolution includes 60 model layers with the top of the atmosphere located at 0.1 hPa (Dee et al. 2011). For verification of the detected inhomogeneities as well as performance assessment of the proposed method, we will also simulate a test dataset based on the ERA-Interim time series.

The undifferenced PWV datasets, i.e. GNSS and ERA-Interim, compared to their difference exhibit different noise characteristics. Figure 1 depicts the pattern of natural variability of PWV from GNSS, ERA-Interim, and the difference time series at a station in Berlin, Germany. For each day of this annual pattern, the standard deviation of PWV is calculated using the values of the same day in 15 years of GNSS, ERA-Interim, and the difference time series. As expected, during hot months the variations reach the maxima while lowest variations happen in the cold season. We have higher variability in the undifferenced time series compared to significantly lower variability in the difference time series. We will consider these aspects of the time series for selecting appropriate sensitivity threshold during offset detection.

Singular spectrum analysis

In our homogenization approach, filling data gaps and method of change point detection are based on SSA. This technique is a general time series analysis tool, which has been used for a wide range of applications such as trend extraction, noise mitigation, forecasting and change-point detection (Alexandrov 2008). For more information about SSA and its main steps, readers are referred to, e.g., Golyandina et al. (2001) and Ghil et al. (2001).
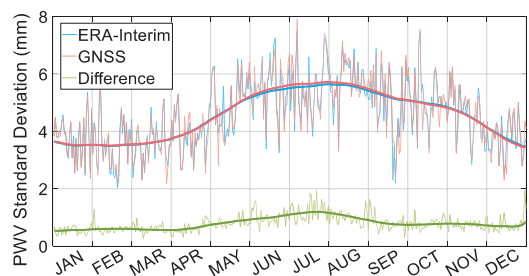

Fig. 1 PWV yearly variation pattern at a GNSS station in Berlin, Germany

To model the variations of a time series into a representative trend, we use the SSA technique. By the term trend, we mean a smoothed slowly-varying version of a time series that comprises long-term variations and periodicities. SSA builds a specific matrix using the time series entries, then decomposes the matrix to its principal components and finally reconstructs the time series using the most important principal components of the matrix.

Assuming the time series $F = (f_1, f_2, \ldots, f_N)$, $f_i \in \mathbb{R}$, $i = 1, 2, \ldots, N$, SSA at the first step which is called the embedding step forms a trajectory matrix ($\mathbf{X}$) by moving a window over the entries of the time series, as follows:

$$\overbrace{\boxed{f_1, f_2, \ldots, f_L}}^{window\rightarrow}, f_{L+1}, f_{L+2}, \ldots, f_N$$

$$\mathbf{X} = \left(x_{ij}\right)_{i,j=1}^{L,K} = \begin{bmatrix} f_1 & f_2 & f_3 & \cdots & f_K \\ f_2 & f_3 & f_4 & \cdots & f_{K+1} \\ f_3 & f_4 & f_5 & \cdots & f_{K+2} \\ \vdots & \vdots & \vdots & \ddots & \vdots \\ f_L & f_{L+1} & f_{L+2} & \cdots & f_N \end{bmatrix} \quad (4)$$

where L is the window length, $K = N - L + 1$ and $1 < L < K$. Next, the singular value decomposition (SVD) is applied to the trajectory matrix, i.e.,

$$\mathbf{X} = \mathbf{U}\Sigma\mathbf{V}^{\mathbf{T}} \quad (5)$$

with the superscript T being the transpose operator. $\mathbf{U}$ and $\mathbf{V}$ contain left and right singular vectors, respectively, and Σ is a diagonal matrix containing the singular values (σ_i) of $\mathbf{X}$. Now, the trajectory matrix can be written as the sum of its uncorrelated components ($\mathbf{X_i}$):

$$\mathbf{X} = \mathbf{X_1} + \mathbf{X_2} + \cdots + \mathbf{X_d}, \ \mathbf{X_i} = \sigma_i \mathbf{U_i} \mathbf{V_i^T} \quad (6)$$

By selecting a proper group of $\{\mathbf{X_1}, \mathbf{X_2}, \ldots, \mathbf{X_d}\}$, which is called the grouping step, we can create a representative estimation of the original trajectory matrix ($\mathbf{X}$) that will finally be used for the trend extraction:

$$\begin{cases} \mathbf{X_{trend}} = \mathbf{X_1} + \mathbf{X_2} + \cdots + \mathbf{X_I} = (\hat{x}_{ij})_{i,j=1}^{L,K} \\ \mathbf{X_{residual}} = \mathbf{X_{I+1}} + \mathbf{X_{I+2}} + \cdots + \mathbf{X_d} \end{cases} \quad (7)$$

The trend values are calculated by averaging the anti-diagonal entries of $\mathbf{X_{trend}}$. Let $L < K$, then the trend of time series $G = (g_1, g_2, \ldots, g_N)$ is:

$$g_i = \begin{cases} \dfrac{1}{i} \displaystyle\sum_{m=1}^{i} \hat{x}_{m,i-m+1} & 1 \le i < L \\ \dfrac{1}{L} \displaystyle\sum_{m=1}^{L} \hat{x}_{m,i-m+1} & L \le i \le K \\ \dfrac{1}{N-i+1} \displaystyle\sum_{m=i-K+1}^{N-K+1} \hat{x}_{m,i-m+1} & K \le i \le N \end{cases} \quad (8)$$

where $\hat{x}_{i,j}$ is an estimation of the element f_{i+j-1} of the original time series.

Homogeneity check

GNSS-derived tropospheric time series, e.g., PWV or ZTD, can generally be considered as a linear combination of different components. Assuming the time series $F = (f_1, f_2, \ldots, f_N)$, $f_i \in \mathbb{R}$, $i = 1, 2, \ldots, N$ is given by the sum of five components, i.e.

$$\begin{cases} F = F_t + F_i + F_c + F_s + F_n \\ \varepsilon = F_t + F_i + F_c + F_s - F_{SSA} \end{cases} \quad (9)$$

where F_t, F_i, F_c, F_s, and F_n represent the group of low to high-frequency components comprising secular trend, inhomogeneities (mean shifts), cyclic, seasonal, and noise components, respectively. The cyclic part involves fluctuations, e.g. due to extreme meteorological events, which might be repeated but cannot be called periodic. F_{SSA}, the extracted SSA trend, estimates the sum of the first four components and leaves the residuals ε. We focus on detecting mean shifts stored in F_i. Based on the occurrence rate of the documented changes in the log files of the GNSS stations, we consider F_i to be a non-periodic step function. Encountering periodic inhomogeneities with approximately similar magnitudes is considered as an unlikely situation and is not focused on in this study. The SSA trend, owing to its smoothing feature, would not perfectly model the step function in the immediate vicinity of jumps. We assume that by choosing an appropriate window length, singular values and corresponding singular vectors, the SSA can capture almost all the information stored in the first four components, except F_i in close proximity to the abrupt changes. We will use this assumption for detecting the position of change points.

Figure 2 shows a flowchart of the homogenization approach we have developed to detect change points and correct the GNSS tropospheric time series. It mainly comprises three stages. The first stage, the preprocessing, starts with identifying and eliminating outliers followed by applying SSA to fill the gaps, and modeling and removing the seasonal component. In the next stage, we use the SSA-based method to detect change points. The last stage is devoted to the verification of detected change points and correcting the GNSS time series.

Preprocessing

Addressing data gaps is also performed using the SSA technique. The first step in applying SSA is the choice of the window length. According to Golyandina and Zhigljavsky (2013), the largest window length that would provide the
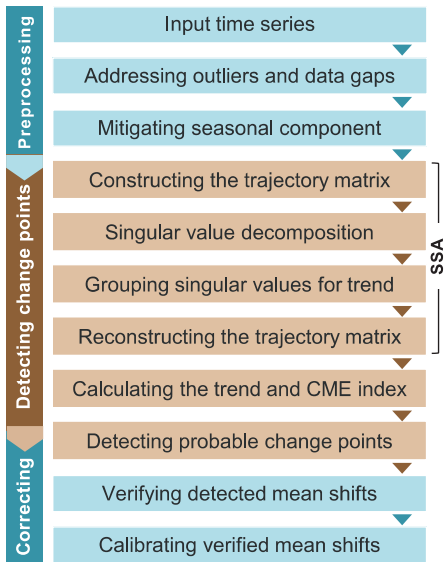
Fig. 2 Homogenization workflow

Fig. 3 Effect of data gaps on the SSA trend extraction. The trend extraction ignoring data gaps (top), trend extraction after applying gap filling (bottom). The black line shows the Fourier series estimation of the time series, which is used as initial values for iterative SSA gap filling

most detailed decomposition is $L \simeq N/2$. For periodic time series with a dominant period of T, the smallest choice for the window length would be $L = T$. Selecting such a window length would maximize the correlation between the columns of the trajectory matrix. This, in turn, leads to a more efficient decomposition. For the window lengths larger than T, they suggest to choose L so that it is close to $N/2$, and L/T is an integer, although it dramatically increases the processing time. In the PWV time series with a dominant annual component, we use a 365-day window length that produces the maximum average correlation between columns of the trajectory matrix.

Finding the change points is based on the assessment of variations with respect to the representative trend of the time series. Missing data might lead to an erroneous analysis of the variations. Figure 3, using a real PWV time series, gives an idea about how data gaps can make the estimated SSA trend unrepresentative. The time series shown in the figure contain a data gap of about 1 year. The top panel is produced just by taking out the missed values and applying SSA to the remaining data. It can clearly be seen that the trend of the time series around the gap area is wrong. The bottom panel is the result of filling the data gaps in the same PWV time series. To generate such a trend, we chose a 365-day window length in the embedding step and five singular values (and vectors) in the grouping step. The reasons for selecting this setting for the grouping step is discussed in the next section.

We apply SSA iteratively to predict missing values based on the temporal correlation present in the data. Kondrashov

and Ghil (2006) and Golyandina and Zhigljavsky (2013) provide more details about the application of SSA to gap filling. Before starting the iteration, the missing values are replaced by initial values calculated using a Fourier series containing bias, linear trend, annual and semi-annual terms which are shown in black line in Fig. 3 (bottom). Having the initial values calculated, we apply SSA to compute the trend from which new estimates of the missing values for the next iteration are extracted. In GNSS tropospheric products, the seasonal component dominates the behavior of the time series. Therefore, for detecting slight changes in the time series, dominant periodicities should be modeled and eliminated.

Detecting change points

The reconstructed trajectory matrix in the grouping step contains useful entries that can indicate abrupt changes in the time series. Considering the chosen window length, up to L-adjacent columns of the trajectory matrix directly contribute to the calculation of the trend values. Figure 4 (top) schematically highlights involving elements of $\mathbf{X_{trend}}$ in calculation of the i-th trend value.

The dispersion of the anti-diagonal elements of $\mathbf{X_{trend}}$ can reveal the fluctuations of the time series around the trend. Therefore, we define the change point as a point at which the original distribution of the time series with respect to the trend in its vicinity is being changed. For this reason, a quantity is needed by which we can observe how the spread of anti-diagonal elements is being squeezed or stretched. The impact of a change on the anti-diagonal elements can be seen in Fig. 4 (bottom). Each anti-diagonal element is an estimation for the trend values. Therefore, more dispersion corresponds to more error in the estimation of the trend by each column of $\mathbf{X_{trend}}$.
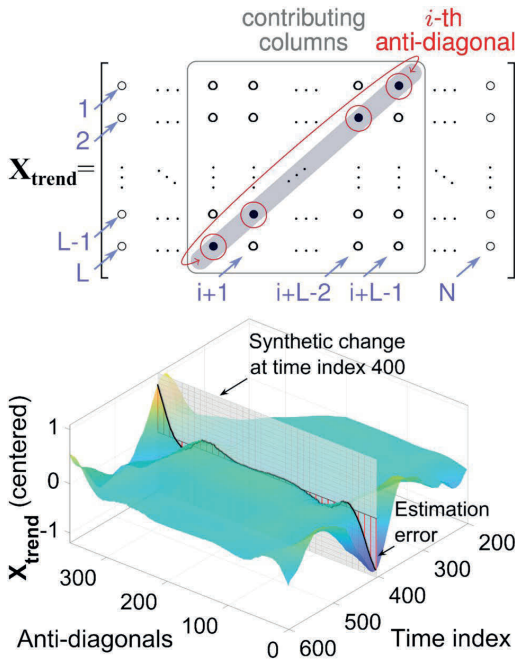
Fig. 4 Involving elements of the reconstructed trajectory matrix in the calculation of the i-th trend value (top) and worsening estimation precision of the anti-diagonals of $\mathbf{X_{trend}}$ in the vicinity of a change point at time index = 400 (bottom)

Consequently, while the averages of anti-diagonals produce the trend values, g_i in (8), their standard deviations quantify the perturbations of the time series with respect to the trend and could be used as an indicator of a change point.

We define the Change Magnitude Estimator (CME) index, represented by ξ, to evaluate the amount of change at every single epoch of the time series. Therefore, the local maxima of the CME diagram indicate the change points and their significance. The CME index is calculated using the entries of each anti-diagonal of $\mathbf{X_{trend}}$ as:

$$
\xi_i^2 = \begin{cases}
0 & i \in \{1, N\} \\
\frac{1}{i-1} \sum_{m=1}^{i} \left(\hat{x}_{m,i-m+1} - g_i \right)^2 & 1 < i < L \\
\frac{1}{L-1} \sum_{m=1}^{L} \left(\hat{x}_{m,i-m+1} - g_i \right)^2 & L \le i \le K \\
\frac{1}{N-i} \sum_{m=i-K+1}^{N-K+1} \left(\hat{x}_{m,i-m+1} - g_i \right)^2 & K < i < N
\end{cases}
\tag{10}
$$

To define a change point, we need the magnitude of change and the time index, i.e., the temporal location in the time series. Our first aim is to find the temporal location of the change points. It should be noted that properly timing the offsets is important. The timing uncertainty may affect the long-term linear trend determination. Particularly, shifts at the beginning and end of the time series will have more weight on the linear trend estimation (Williams 2003).

The grouping step or selecting proper singular values and vectors for trend extraction has a significant impact on the results of change point detection. Including more singular values and vectors in the reconstruction of the trajectory matrix corresponds to more sensitivity to slight local variations of the time series and will result in false alarms, i.e. a point is reported as a change point by mistake. Including fewer singular values, however, would reduce the accuracy of finding the temporal location of change points. Therefore, we complete the procedure of selecting singular values in two steps. The first step is finding the region of maximum curvature in the singular values spectrum and the second step is selecting the singular values with a minimum ξ_T value, defined as follows:

$$
\xi_T = \text{sd}(\mathbf{X_\Delta})
\tag{11}
$$

$$
\mathbf{X_\Delta} = \begin{bmatrix}
\hat{x}_{1,1} - g_1 & \hat{x}_{1,2} - g_2 & \cdots & \hat{x}_{1,K} - g_K \\
\hat{x}_{2,1} - g_2 & \hat{x}_{2,2} - g_3 & \cdots & \hat{x}_{2,K} - g_{K+1} \\
\hat{x}_{3,1} - g_3 & \hat{x}_{3,2} - g_4 & \cdots & \hat{x}_{3,K} - g_{K+2} \\
\vdots & \vdots & \ddots & \vdots \\
\hat{x}_{L,1} - g_L & \hat{x}_{L,2} - g_{L+1} & \cdots & \hat{x}_{L,K} - g_N
\end{bmatrix}
\tag{12}
$$

where ξ_T is the overall CME calculable using the residual trajectory matrix, $\mathbf{X_\Delta}$, and sd is the standard deviation of all entries of the matrix. The matrix $\mathbf{X_\Delta}$ is formed by subtracting trend values (g_i) from the corresponding anti-diagonals of $\mathbf{X_{trend}}$. We use ξ_T to select a proper set of singular values and vectors. Figure 5 illustrates the behavior of the CME index with and without having a change (mean shift) in a synthetic time series. Application of ξ_T as a threshold is shown in the figure. Its application in selecting singular values can be seen in Fig. 6.

The residuals after the trend estimation might contain autoregressive noise, which in turn might affect the CME values. False alarms induced by this effect can be reduced by setting ξ_T as a threshold. We then justify and enhance the estimated positions of our detected offsets by applying a t test to symmetric intervals around the time index of the candidate change points.
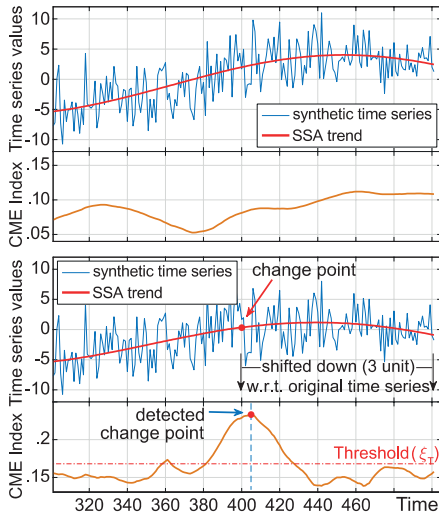
Fig. 5 Behavior of CME (ξ) index for a synthetic time series: without any mean shift (top), with an artificial offset at time index = 400 (bottom)

Verification and correction

After detecting the position of mean shifts (jumps), we estimate the magnitude of the offsets in the three time series of each station, i.e., ERA-Interim, GNSS, and the difference time series. The magnitude of each offset is calculated using the difference between the mean values of the left and right sides of the offset. After manual verification of the detected offsets, we correct the verified offsets within the GNSS time series by constructing and then subtracting the step function F_i in (9). It should be noted that the step function does not change the overall mean value of the GNSS time series after the correction.

The procedure of finding and verifying inhomogeneities is demonstrated using the real data of the station in Saarbrücken, Germany (Fig. 7). Data gaps, seasonality and outliers have been addressed in the three time series, and then we applied our SSA-based offset detection method to find the position of change points.

As can be seen in Fig. 7, the time series contain three different cases of change points. The first case consists of the offsets, which are seen in the GNSS and the difference time series within a six-month time window with almost the same magnitude. If there is no shift in the ERA-Interim time series; we correct the GNSS time series using the time index and mean shift obtained from the difference time series.

The second case includes the mean shifts, which are seen in GNSS and ERA-Interim with almost the same
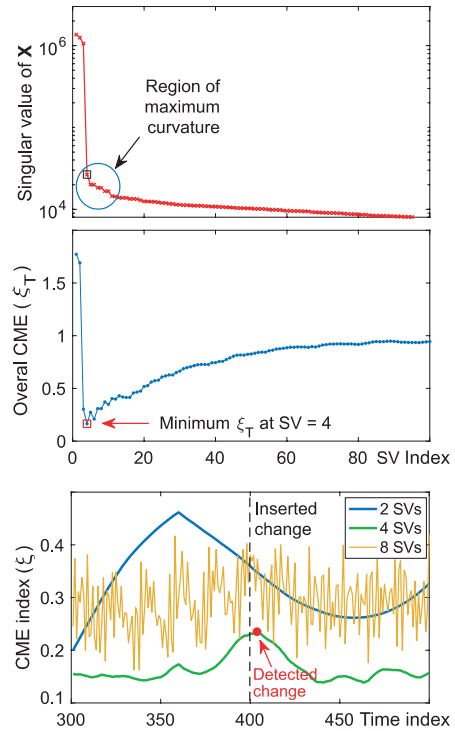
Fig. 6 Selecting singular values for change point detection using the synthetic time series from Fig. 5. Finding the maximum curvature region on the singular values spectrum (top), minimizing the overall CME that makes the extracted SSA trend representative (middle), the effect of selected singular values on the accuracy of detection and the number of false alarms (bottom)

time index and magnitude. These shifts might be due to a phenomenon sensed by both datasets, e.g., climatic or meteorological effects. In this case, even if due to different sensitivities some slight changes are transferred to the difference time series, the GNSS data are left uncorrected.

The third case is the changes which happen in all three time series (difference, GNSS and ERA-Interim) at approximately the same epochs with quite different mean shifts. If the sum of the mean shifts in the GNSS and ERA-Interim data equals to the shift in the difference time series, the GNSS time series is corrected using the mean shift obtained from the GNSS. As a special case in this station, we have an antenna and radome change and, at the same time, a non-systematic event (maybe a climatic signal) has happened. In this case, we search for the same signal in the nearby stations. If we find the same signal, we correct the GNSS data using the shift obtained from the difference time series.

Fig. 7 Sample result of change detection in the difference (top), ERA-Interim (middle) and real GNSS (bottom) PWV time series for the station in Saarbrücken, Germany (latitude = 49.22°, longitude = 7.01°). The range of vertical axis for the difference time series (ΔPWV) is reduced to improve the visibility
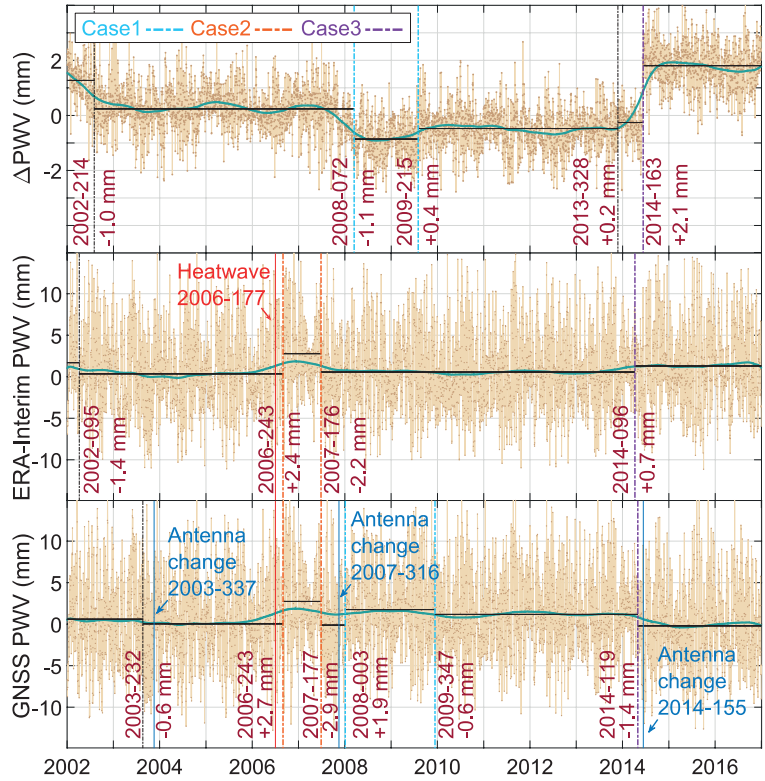
Results

We use a test and a real dataset to evaluate the developed method for detecting possible inconsistencies and homogenizing tropospheric products. The impact of homogenization of GNSS data is shown through a comparison of linear trends and internal consistency of datasets.

Test dataset

We performed a Monte Carlo simulation to evaluate the performance of our method. This simulation is based on the ERA-Interim dataset at 400 points distributed over Germany from 2002 to 2017. This choice assumed that the ERA-Interim time series are less likely to contain inhomogeneities. We randomly inserted 2.1×10^5 offsets in 7×10^4 time series. To create new cases in each iteration, the time series were altered by adding newly generated random offsets. However, these time series contain possible abrupt changes due to climatic or meteorological conditions. In every iteration process, about 200 time series out of 400 were randomly selected for imposing synthetic offsets and the remaining were left unchanged. We added in average 6 offsets with

a maximum of 10 offsets (upper limit) that randomly have different magnitudes between 0.5 and 3 mm with a negative or positive sign in every time series. The distribution of the inserted changes into the time series is done randomly such that separation between two successive changes is at least 1 year. Different classes are considered for summarizing the results. Based on these classes, the test results are arranged in Table 1. For each case, the Mean Absolute Error (MAE) of detection for the time index, MAE_τ, and the mean shift, MAE_δ, are estimated as follows:

$$
\begin{cases}
e_i^\tau = \hat{\tau}_i - \tau_i, & \text{MAE}_\tau = \frac{1}{n}\sum_{i=1}^{n}\left|e_i^\tau\right| \\
e_i^\delta = \hat{\delta}_i - \delta_i, & \text{MAE}_\delta = \frac{1}{n}\sum_{i=1}^{n}\left|e_i^\delta\right|
\end{cases}
\tag{13}
$$

where τ_i and δ_i are the true values, $\hat{\tau}_i$ and $\hat{\delta}_i$ are the estimated values of the time index and the magnitude of mean shift, respectively. e_i^τ and e_i^δ denote the detection errors in terms of the time index and the magnitude, respectively, and n is the total number of successfully detected offsets.

The left side of Table 1 explains how successful the method is in finding the time index of change points. Three

Table 1 Success rate of the proposed method based on different thresholds of detection

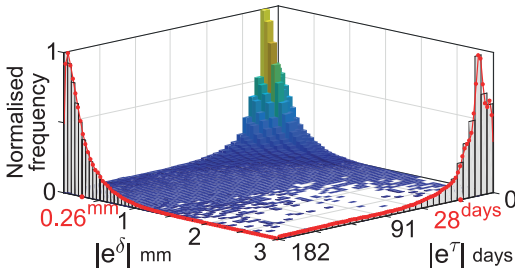| Detection criterion (day)	Success rate (%)	MAE_τ (day)	MAE_δ (mm)	Detection criterion (mm)	Success rate (%)	MAE_τ (day)	MAE_δ (mm)
$\lvert e^\tau \rvert \le 182$	81.1	27.9	0.26	$0.5 \le \lvert \delta_i \rvert \le 1$	45.9	51.5	0.23
$\lvert e^\tau \rvert \le 91$	74.6	18.8	0.25	$1 < \lvert \delta_i \rvert \le 2$	86.0	30.9	0.25
$\lvert e^\tau \rvert \le 30$	62.0	12.4	0.24	$2 < \lvert \delta_i \rvert \le 3$	97.4	18.7	0.27

Fig. 8 Overview of the detection performance of the SSA-based method for detecting change points in PWV time series based on a Monte Carlo simulation. The mean absolute errors of the time index and the magnitude of the detected offsets are marked with red dots on the axes and are associated with a success rate of 81.1%. The prominent peak of the histogram indicates the highest occurrence frequency of the simulation results with $\lvert e^\delta \rvert \approx 0.05$ mm and $\lvert e^\tau \rvert \approx 13$ days

criteria of 182, 91, and 30 days are chosen for the time index to calculate the number of successful detections. Beyond each chosen criterion, e.g. $\lvert e^\tau \rvert > 30^{days}$ for the detection criterion of 30 days, we define the method to be unsuccessful. It should be noted that the simulation study could not be carried out using the difference data. The difference time series contain much less background noise, which leads to higher accuracy in detecting mean shifts. Our goal for applying the method to the original dataset (ERA-Interim or GNSS) is to justify the detected mean shifts in the differenced time series. Table 1 shows a success rate of 81.1% with MAE of about 28 days in detecting time index and 0.26 mm for estimating mean shift.

The right side of Table 1 shows how successful the method performs in estimating the magnitude of offsets. The method successfully detected most of the offsets bigger than 1 mm while about half of the inserted changes with a magnitude of 0.5–1 mm are retrieved. Figure 8 depicts a performance overview of the change detection method in terms of the magnitude and the time index of offsets.

Real GNSS-derived PWV data

We applied our homogenization method to a GNSS PWV dataset consisting of 214 stations in Germany over a 7-year

timespan (2010–2016). We did not use a reprocessed dataset since we aimed to detect all possible different changes in the dataset. A sensitivity threshold for the detection procedure, which is the slightest change detectable by the method, can be chosen based on the time series characteristics discussed in the dataset section. The sensitivity of detection has been set to 0.2 mm for the difference PWV time series and 0.5 mm for both ERA-Interim and GNSS PWV time series.

We first applied the method to identify all possible mean shifts in the GNSS, ERA-Interim, and the difference time series (ERA-Interim minus GNSS) without considering stations log files. Then, the log files of the GNSS stations were checked to find any support for the detected changes. Next, we manually inspected the detected offsets and corrected GNSS time series using the verified offsets. As mentioned earlier, climatic or meteorological effects can also induce changes in the time series. This type of changes must be left uncorrected. If changes are detected at more than one station in the same sub-region, only those having a documented event in the log file, e.g., hardware change, are corrected.

The detected change points and corresponding mean shifts are listed in the supplementary material. In total, 140 change points were detected of which 134 were related to the mean shifts in the GNSS time series and 6 shifts were more likely to be originating from ERA-Interim data. Amongst all detected changes in the GNSS dataset, 45 of them (~34%) are not supported by the documented changes in the station log files. The detection accuracy, MAE_τ, based on the documented changes in the GNSS dataset is approximately 30 days.

Linear trends

We apply linear regression to PWV time series of GNSS stations to evaluate the impact of homogenization on the trend value. It should be noted that the scope of this research is not the trends themselves; therefore, the readers are referred to e.g. Alshawaf et al. (2018) and Klos et al. (2018) for detailed discussion about trend estimation in GPS tropospheric time series. Estimations of the linear trends were carried out for homogenized and not-homogenized GNSS time series. Figure 9 shows the trends before and after correction of mean shifts together with trends obtained from the ERA-Interim data. Note that no correction was implemented on the

Fig. 9 Impact of homogenization on the fitting linear trends of the ERA-Interim and the GNSS PWV time series (before and after homogenization)
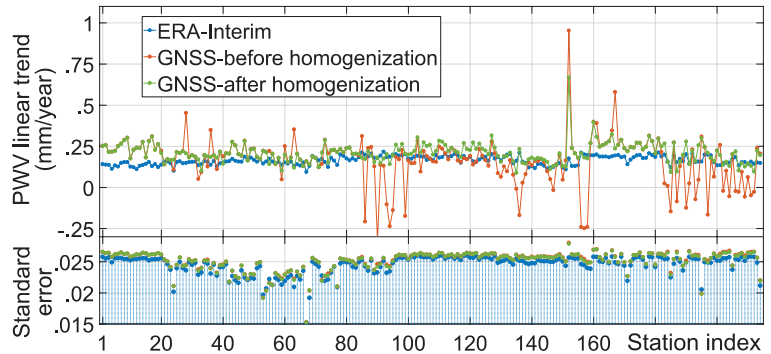
ERA-Interim dataset. The figure highlights a clear improvement in the consistency between the GNSS and ERA-Interim datasets after homogenization. The lower part of the figure shows the standard error of the linear regression. Lower improvements at some stations, e.g. station Hamburg with the index 154 (latitude = 53.55°, longitude = 9.98°), can be related to the remaining unverified changes specially at the beginning or the end of the time series or at vicinity of a gap interval. The unverified changes are the offsets that are detected in the difference time series but could not be attributed to either of the GNSS or the reference time series.

Regional correlations of the stations were defined and calculated to be used for evaluating the internal consistency of the GNSS dataset after homogenization. The value of the regional correlation for each station is a weighted average of all the correlations with other stations. We used Inverse Distance Weighting (IDW) for calculating the correlations. Figure 10 reflects an improved internal consistency after the GNSS data is corrected for the mean shifts. A noticeable regional improvement can be seen over the southwest of Germany (the right panel of Fig. 10). It should be noted that the upgrade or maintenance procedure of adjacent stations in a GNSS network might be scheduled and performed consecutively within a short period. Thus, similar inhomogeneities might be introduced to the time series of nearby stations

which could be misinterpreted as non-systematic events if they are not documented. The zero-difference approach introduced in this study can avoid such a misinterpretation.

Conclusion

A homogenization method based on singular spectrum analysis (SSA) for detecting and correcting temporal mean shifts (inhomogeneities) in GNSS-derived tropospheric time series was introduced. To assess the performance of the method, a Monte Carlo simulation was performed based on the ERA-Interim dataset. The result of the Monte Carlo process suggests an overall success rate of 81.1%. The simulation study estimates the precision of 28 days and 0.26 mm for detecting the position of changes and the mean shifts in the undifferenced time series, respectively.

We used the method to investigate the possible shifts in the precipitable water vapor (PWV) time series of 214 GNSS stations in Germany. The data was obtained from near real-time PPP processing over a 7-year timespan (2010–2016). The method was independently applied to the GNSS, ERA-Interim and the difference (ERA-Interim minus GNSS) daily time series of each station to find and verify inconsistencies. In total, 96 GNSS stations were identified as inhomogeneous

Fig. 10 Regional correlation of PWV time series for the ERA-Interim and the GNSS datasets before and after homogenization (left), regional correlation improvement for each GNSS station (right)
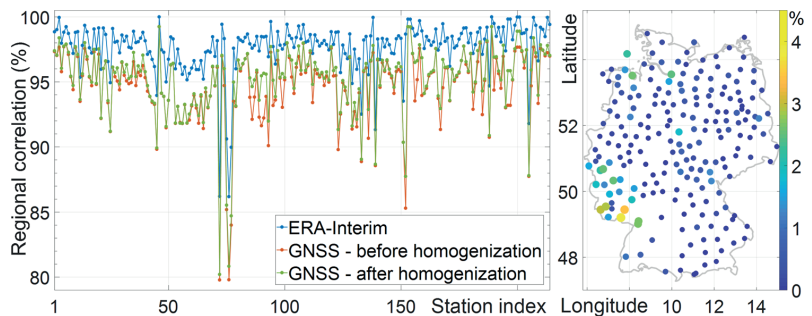
containing 134 mean shifts from which 45 changes (~34%) were undocumented in the stations' log files.

The comparison between the retrieved linear trends from GNSS and ERA-Interim dataset indicates a significant improvement after homogenization. An increase in correlation of 39% is seen for the trends after correcting the mean shifts in the GNSS time series.

The proposed method can successfully detect changes with and without reference dataset. Since using a reference dataset for homogeneity checking tries to make datasets look like each other, it might contaminate the target time series. Therefore, the homogenization approach discussed here would mitigate major inconsistencies and provide a more homogenized GNSS time series. The homogenized GNSS datasets would be a promising data source for climatic applications. The capability of the method to find changes in the undifferenced time series would also make it a useful tool to detect climatic and meteorological signals. The proposed method can be applied to other regions and for other meteorological parameters such as pressure, temperature as well as GNSS coordinate time series.

References

Alexandrov T (2008) A method of trend extraction using singular spectrum analysis. p 7. arXiv preprint arXiv:0804.3367

Alshawaf F, Balidakis K, Dick G, Heise S, Wickert J (2017) Estimating trends in atmospheric water vapor and temperature time series over Germany. Atmos Meas Tech 10:3117–3132. https://doi.org/10.5194/amt-10-3117-2017

Alshawaf F, Zus F, Balidakis K, Deng Z, Hoseini M, Dick G, Wickert J (2018) On the statistical significance of climatic trends estimated from GPS tropospheric time series. J Geophys Res Atmos. https://doi.org/10.1029/2018JD028703

Askne J, Nordius H (1987) Estimation of tropospheric delay for microwaves from surface weather data. Radio Sci 22(3):379–386. https://doi.org/10.1029/RS022i003p00379

Balidakis K, Nilsson T, Zus F, Glaser S, Heinkelmann R, Deng Z, Schuh H (2018) Estimating integrated water vapor trends from VLBI, GPS, and numerical weather models: sensitivity to tropospheric parameterization. J Geophys Res Atmos. https://doi.org/10.1029/2017JD028049

Bevis M, Businger S, Chiswell S, Herring TA, Anthes RA, Rocken C, Ware RH (1994) GPS meteorology: mapping zenith wet delays onto precipitable water. J Appl Meteorol 33(3):379–386. https://doi.org/10.1175/1520-0450(1994)033%3c0379:GMMZWD%3e2.0.CO;2

Dee DP, Uppala SM, Simmons A, Berrisford P, Poli P, Kobayashi S, Andrae U, Balmaseda M, Balsamo G, Bauer DP (2011) The

ERA-interim reanalysis: configuration and performance of the data assimilation system. Q J R Meteorol Soc 137(656):553–597. https://doi.org/10.1002/qj.828

Escott-Price V, Zhigljavsky A (2003) An algorithm based on singular spectrum analysis for change-point detection. Commun Stat Simul Comput 32:319–352. https://doi.org/10.1081/SAC-120017494

Ghil M, Allen MR, Dettinger M, Ide K, Kondrashov D, Mann M, Saunders A, Tian Y, Varadi F (2001) Advanced spectral methods for climatic time series. Rev Geophys. https://doi.org/10.1029/2000RG000092

Golyandina N, Zhigljavsky A (2013) Singular spectrum analysis for time series. Springer, Berlin

Golyandina N, Viktorovich Nekrutkin V, Zhigljavsky A (2001) Analysis of time series structure: SSA and related techniques. Monogr Stat Appl Probab. https://doi.org/10.1201/9781420035841

Gradinarsky LP, Johansson J, Bouma HR, Scherneck H-G, Elgered G (2002) Climate monitoring using GPS. Phys Chem Earth 27:335–340. https://doi.org/10.1016/S1474-7065(02)00009-8

Hassani H, Thomakos D (2010) A review on singular spectrum analysis for economic and financial time series. Stat Interface 3:377–397

Jarušková D (1996) Change-point detection in meteorological measurement. Mon Weather Rev 124(7):1535–1543. https://doi.org/10.1175/1520-0493(1996)124%3c1535:CPDIMM%3e2.0.CO;2

Klos A, Van Malderen R, Pottiaux E, Bock O, Bogusz J, Chimani B, Elias M, Gruszczynska M, Guijarro J, Zengin Kazanci S, Ning T (2017) Study on homogenization of synthetic GNSS-retrieved IWV time series and its impact on trend estimates with autoregressive noise. European Geosciences Union General Assembly 2017, Vienna, Austria

Klos A, Hunegnaw A, Teferle FN, Abraha KE, Ahmed F, Bogusz J (2018) Statistical significance of trends in Zenith wet delay from re-processed GPS solutions. GPS Solut 22(2):51. https://doi.org/10.1007/s10291-018-0717-y

Kondrashov D, Ghil M (2006) Spatio-temporal filling of missing points in geophysical data sets. Nonlinear Process Geophys 13(2):151–159. https://doi.org/10.5194/npg-13-151-2006

Li X, Dick G, Ge M, Heise S, Wickert J, Bender M (2014) Real-time GPS sensing of atmospheric water vapor: precise point positioning with orbit, clock, and phase delay corrections. Geophys Res Lett 41(10):3615–3621. https://doi.org/10.1002/2013GL058721

Modiri S, Belda S, Heinkelmann R, Hoseini M, Ferrándiz J, Schuh H (2018) Polar motion prediction using the combination of SSA and Copula-based analysis. Earth Planets Space 70:115. https://doi.org/10.1186/s40623-018-0888-3

Nilsson T, Elgered G (2008) Long-term trends in the atmospheric water vapor content estimated from ground-based GPS data. J Geophys Res Atmos. https://doi.org/10.1029/2008JD010110

Ning T, Wickert J, Deng Z, Heise S, Dick G, Vey S, Schöne T (2016) Homogenized time series of the atmospheric water vapor content obtained from the GNSS reprocessed data. J Clim 29:2443–2456. https://doi.org/10.1175/JCLI-D-15-0158.1

Rodionov S (2004) A sequential algorithm for testing climate regime shifts. Geophys Res Lett. https://doi.org/10.1029/2004GL019448

Saastamoinen J (1972) Atmospheric correction for the troposphere and stratosphere in radio ranging satellites. Use Artif Satell Geodesy 15:247–251

Schneider T, O'Gorman PA, Levine XJ (2010) Water vapor and the dynamics of climate changes. Rev Geophys. https://doi.org/10.1029/2009RG000302

Sinha A, Harries JE (1997) The earth's clear-sky radiation budget and water vapor absorption in the far infrared. J Clim 10(7):1601–1614. https://doi.org/10.1175/1520-0442(1997)010%3c1601:Tescsr%3e2.0.Co;2

Van Malderen R, Pottiaux E, Klos A, Bock O, Bogusz J, Chimani B, Elias M, Gruszczynska M, Guijarro J, Kazancı SZ, Ning T (2017) Homogenizing GPS integrated water vapour time series:

methodology and benchmarking the algorithms on synthetic datasets. In: Ninth seminar for homogenization and quality control in climatological databases and fourth conference on spatial interpolation techniques in climatology and meteorology, Budapest. pp 104–116

Venema VKC, Mestre O, Aguilar E, Auer I, Guijarro JA, Domonkos P, Vertacnik G, Szentimrey T, Stepanek P, Zahradnicek P, Viarre J, Müller-Westermeier G, Lakatos M, Williams CN, Menne MJ, Lindau R, Rasol D, Rustemeier E, Kolokythas K, Marinova T, Andresen L, Acquaotta F, Fratianni S, Cheval S, Klancar M, Brunetti M, Gruber C, Prohom Duran M, Likso T, Esteban P, Brandsma T (2012) Benchmarking monthly homogenization algorithms. Clim Past 8:89–115. https://doi.org/10.5194/cp-8-89-2012

Vey S, Dietrich R, Fritsche M, Rülke A, Steigenberger P, Rothacher M (2009) On the homogeneity and interpretation of precipitable water time series derived from global GPS observations. J Geophys Res Atmos. https://doi.org/10.1029/2008JD010415

Wang X (2008) Accounting for autocorrelation in detecting mean shifts in climate data series using the penalized maximal t or F test. J Appl Meteorol Climatol 47:2423–2444. https://doi.org/10.1175/2008JAMC1741.1

Wang X, Wen QH, Wu Y (2007) Penalized maximal t test for detecting undocumented mean change in climate data series. J Appl Meteorol Climatol 46:916–931. https://doi.org/10.1175/JAM2504.1

Wang J, Dai A, Mears C (2016) Global water vapor trend from 1988 to 2011 and its diurnal asymmetry based on GPS, radiosonde, and microwave satellite measurements. J Clim 29(14):5205–5222

Williams SDP (2003) Offsets in global positioning system time series. J Geophys Res 108(B6):2310. https://doi.org/10.1029/2002JB002156

quality of these maps by statistical data fusion, time series analyses, and data homogenization.

Hossein Nahavandchi is currently a professor of geodesy at the Norwegian University of Science and Technology (NTNU). His primary research interests are Earth-monitoring satellites and GPS. He has been Principal Investigator of several ocean and climate related research projects using the global geodetic observing system.

Galina Dick graduated in Mathematics from the University of Charkow, Ukraine, and received her Ph.D. in Mechanics from the Technical University in Tallinn, Estonia. In 1992, she started at the German Research Center for Geosciences GFZ at Potsdam working in the different fields of satellite geodesy. Since 2000, she is responsible for the ground-based GNSS atmospheric sounding at GFZ and is involved in many international projects, e.g., she is head of GFZ GNSS Analysis Center within European Project E-GVAP (''The EUMETNET GNSS Water Vapor Program'').

Mostafa Hoseini is a Ph.D. candidate at the Norwegian University of Science and Technology (NTNU). His research interest is GNSS remote sensing. He is working on the ocean monitoring using GNSS-Reflectometry concept onboard small satellites.

Jens Wickert received the graduate degree in physics from the Technische Universität Dresden, Germany, and the Ph.D. degree in geophysics/meteorology from the University of Graz, Austria, in 1989 and 2002, respectively. He worked for several institutions as AWI, DLR and DWD before he came to GFZ in 1999. Currently he is research topic director" Atmosphere in Global Change", deputy section head of the Space Geodetic Techniques and head of the research area GNSS Remote Sensing. Since 2016 he is also Professor for GNSS Remote Sensing and Positioning at Technische Universität Berlin. Wickert is involved in numerous interdisciplinary GNSS related research projects. He was Principal Investigator of the pioneering GPS Radio Occultation experiment aboard the German CHAMP satellite. Wickert was also coordinating the GEROS-ISS proposal to ESA and chairing the related Science Advisory Group. He was Co-PI of the G-TERN Earth Explorer 9 proposal and is author/coauthor of more than 230 ISI listed publications on GNSS Earth Observation.

Fadwa Alshawaf received the Ph.D. degree in remote sensing from Karlsruhe Institute of Technology (KIT), Karlsruhe, Germany, in 2013. Since 2015, she has been a Research Assistant at the GFZ German Research Centre for Geosciences. She works on remote sensing and analyses of atmospheric data for weather and climate research. Her research interests include water vapor mapping using interferometric synthetic aperture radar and GNSS, and improving the

Paper II

On the Response of Polarimetric GNSS-Reflectometry to Sea Surface Roughness

Mostafa Hoseini, Maximilian Semmling, Hossein Nahavandchi, Erik Rennspiess, Markus Ramatschi, Rüdiger Haas, Joakim Strandberg, and Jens Wickert

Abstract—Reflectometry of Global Navigation Satellite Systems (GNSS) signals from the ocean surface has provided a new source of observations to study the ocean–atmosphere interaction. We investigate the sensitivity and performance of GNSS-Reflectometry (GNSS-R) data to retrieve sea surface roughness (SSR) as an indicator of sea state. A data set of one-year observations in 2016 is acquired from a coastal GNSS-R experiment in Onsala, Sweden. The experiment exploits two sea-looking antennas with right- and left-hand circular polarizations (RHCP and LHCP). The interference of the direct and reflected signals captured by the antennas is used by a GNSS-R receiver to generate complex interferometric fringes. We process the interferometric observations to estimate the contributions of direct signals and reflections to the total power. The power estimates are inverted to the SSR using the state-of-the-art model. The roughness measurements from the RHCP and LHCP links are evaluated against match-up wind measurements obtained from the nearest meteorological station. The results report on successful roughness retrieval with overall correlations of 0.76 for both links. However, the roughness effect in LHCP observations is more pronounced. The influence of surrounding complex coastlines and the wind direction dependence are discussed. The analysis reveals that the winds blowing from land have minimal impact on the roughness due to limited fetch. A clear improvement of roughness estimates with an overall correlation of 0.82 is observed for combined polarimetric observations from the RHCP and LHCP links. The combined observations can also improve the sensitivity of GNSS-R measurements to the change of sea state.

Index Terms—Global Navigation Satellite Systems (GNSS)-Reflectometry, polarimetric observations, sea state, sea surface roughness (SSR).

I. INTRODUCTION

THE characterization and monitoring of sea surface roughness (SSR) are important for understanding air–sea interactions. This parameter is considered as one of the indicators of the sea state. The difficulty of making direct SSR measurements due to the complexity and random behavior of sea surface fluctuations has cleared the way for remote sensing techniques [1]. A robust observation resource of SSR can be acquired from the reflectometry of the Global Navigation Satellite Systems (GNSS) signals.

The GNSS-Reflectometry (GNSS-R) is an all-weather operating technique offering high temporal resolution observations based on low-cost passive instrumentation. Spaceborne observations of the surface roughness variations can be related to the near-surface wind stress [2] and used for the estimation of wind speed [3]. The anomalies of surface roughness over mesoscale ocean eddies can reveal the presence of these oceanic features and the ongoing air–sea interaction [4].

The ground-based GNSS-R setup has been used in several experimental campaigns for sea state observations. Different observables are proposed to retrieve SSR or Significant Wave Height (SWH) as descriptors of the sea state or predictors of wind speed. The complex delay Doppler Maps (DDMs) produced from the processing of GNSS reflected signals [5] can provide several observables. The waveforms extracted from the DDMs can be fit to a wind-dependent model to estimate the speed [2]. The volume of the DDMs can be normalized and directly connected to the sea state [6].

Interferometric observations of the superimposed direct and reflected signals can be utilized for the sea state estimation. The coherence time of the observed signal can be modeled and related to the ratio of SWH and mean wave period [7]. Variability of the sea state can be derived from the analysis of power loss due to the roughness. The latter approach is considered in this article for the SSR estimation.

The nature of GNSS signals at the reflection is subject to polarization change described by the Fresnel equations. Therefore, the incoming direct signals with right-hand circular polarization (RHCP) produce composite reflected signals, including left-hand circular polarization (LHCP) and RHCP components. This phenomenon offers the opportunity of making polarimetric observations. The reflectometry receivers can be fed by RHCP or LHCP antennas to perform the GNSS-R measurements. The use of polarimetric observations for different applications has been considered in several earlier studies [8]–[11].

This study aims at investigating the performance of GNSS-R observations with RHCP, LHCP, and a combination of them in the SSR estimations. To this end, we use a long-term data set from a coastal GNSS-R experiment equipped with RHCP and LHCP antennas. We analyze the impact of the surface roughness on the interferometric observations of the Global Positioning System (GPS) signals collected by each of the antennas during different sea states. The GNSS-R setup used in this study together with the data set is described in Section II. The processing flow from receiving signals at the antennas to deriving the surface roughness, i.e., the geophysical parameter of interest, is explained in Section III. The processing results are discussed in Section IV. Section V provides concluding remarks.

II. DATA

The data set used in this study includes one-year observations of a ground-based coastal GNSS-R experiment at the Onsala space observatory ($57.393°N, 11.914°E$) in Sweden. The station uses a metal structure that is placed on a cliff at about 3 m above the sea level to accommodate the antennas. A zenith-looking antenna is used for tracking direct signals. Sea surface reflections are intercepted by two sea-looking antennas with RHCP and LHCP designs. The sea-looking antennas have a tilt angle of about 98° with respect to the zenith, i.e., slightly down-looking. These antennas are, respectively, optimized for receiving copolarized (CPo) and cross-polarized (XPo) reflected signals by analogy with the incoming direct RHCP signals. The boresight of the reflectometry antennas is fixed at about 150° azimuth angle to overlook the sea. Fig. 1 shows the location of the station along the Sweden coastlines, as well as the top and side views of the setup.

A GNSS Occultation, Reflectometry, and Scatterometry (GORS) receiver [12] is used at the station providing up to four input links. The first link is connected to the master channel of the receiver to track the direct signals of the satellites. The other links are connected to slave channels for reflectometry purposes. The receiver can process GPS signals and delivers raw data streams at the sampling rate of 200 Hz.

Direct and reflected signals from the GPS satellites in view are captured by the antennas and fed to the master and slave channels of the receiver. The receiver tracks the satellites by cross-correlating a replica of their pseudorandom noise (PRN) codes with the signals received from the master link. Similar cross-correlations are computed within the slave channels. The receiver can be instructed to use different delay and Doppler values in the slave channels. These values are relative with respect to the master channel. The geometrical configuration of the setup at Onsala station demands negligible relative delay and Doppler values. Therefore, the relative delay and Doppler values for all of the tracked satellites are set to zero. The correlation sums are provided by the receiver at In-phase and Quadrature (I/Q) levels. The 200-Hz data stream is downsampled to 0.1 Hz by 10-second integration. The downsampled observations suffice the required temporal resolution for the

Fig. 1. (Top Left) Top view of the Onsala GNSS-R station located in southern Sweden. (Top Right) Nearby coastlines. (Bottom Left) Close eastward. (Bottom Right) Downward photographs from the antennas and the setup structure. The GNSS-R station is marked with a yellow diamond, and the yellow circle shows the location of the nearby tide gauge station. The orange arrow indicates the boresight of the reflectometry antennas.
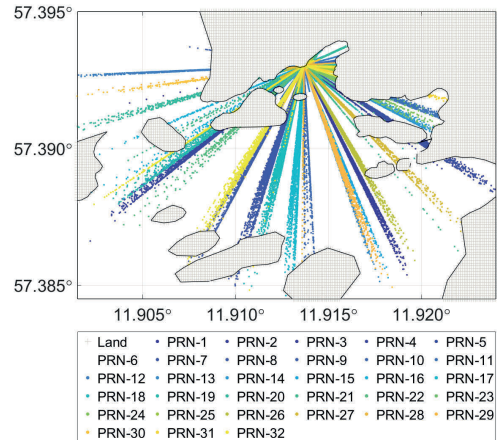
Fig. 2. Distribution of the reflection points of the GPS satellites over the sea surface.

processing, due to the small height difference between the reflectometry antennas and the sea surface [according to (4)].

The data set used in this study covers the period from January to December 2016. On average, about 44 reflection events per day from different GPS satellites were recorded and used for the analysis. Fig. 2 shows the spatial spread of the reflection tracks of the satellites over the sea surface. The selected region of the sea surface encompasses specular points with corresponding elevation angles of up to 55°.
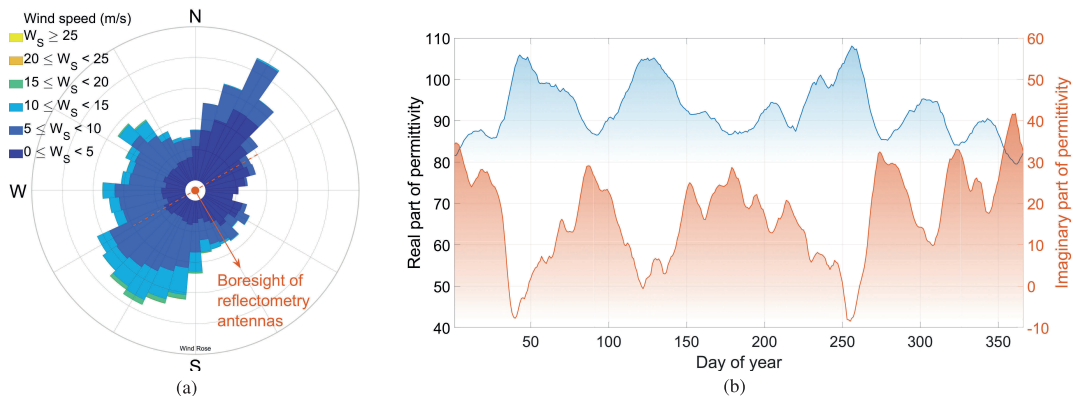
Fig. 3. Overview of the ancillary data at Onsala station in 2016. (a) Distribution of wind speeds with respect to wind directions (bin size for the speeds: 5 m/s and sector size for the directions: 10°). (b) Seawater relative permittivity.

The reflectometry observations in the main data set are coupled with available ancillary information. Hourly measurements of wind speed and direction are acquired from a nearby meteorological station. Distribution of wind direction and the range of wind speeds in 2016 are shown in Fig. 3(a). Sea level anomalies with a resolution of 1 min are also measured by a tide gauge station, which is marked with a yellow circle to the east of the reflectometry station in Fig. 1.

To improve the accuracy of the roughness estimates, relative permittivity values are calculated and used within the processing. To this end, we use a model developed by [13] to describe the dielectric constant of seawater at L-band frequency as a function of salinity and temperature. The model utilizes a third-order polynomial that is trained using a set of accurate measurements at the frequency of 1.413 GHz [14]. The required water temperature values are obtained from the meteorological station. Due to the lack of *in situ* salinity observations, we use daily averages based on nine years of historical records (2001–2009) from another station that is about 29 km away. The estimated seawater permittivity at the Onsala station in 2016 is shown in Fig. 3(b).

III. METHOD

The method used in this study is based on the analysis of interference fringes caused by the superposition of the direct and reflected GNSS signals. The superimposed signals generate a compound electromagnetic field. The field is intercepted by the antennas and processed by the receiver to generate output streams in the form of I/Q components. The receiver output can be represented by a complex time series as

$$E = I_{\text{int}} + i\,Q_{\text{int}} \tag{1}$$

where E denotes the complex vector form and I_{int} and Q_{int} are, respectively, the I and Q components of the interferometric signal from the receiver output. We process these I/Q correlation sums (data level 0) to extract the power of direct and reflected signals and combine them into three power ratios (data level 1). The estimated power ratios are then inverted to
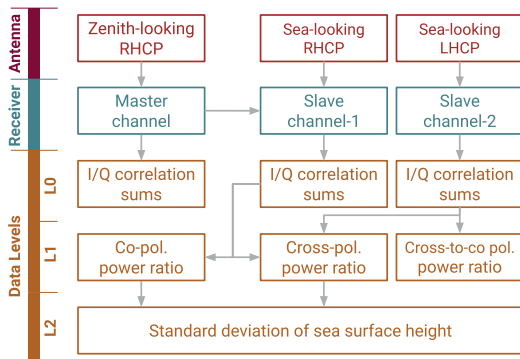
Fig. 4. Procedure of data processing from the raw interferometric observations at in-phase and quadrature (I/Q) levels to the final data product of SSR.

SSR (data level 2) using a geophysical model function. The following description provides detailed information about the processing procedure shown in Fig. 4.

The observed signal contains contributions from the direct and reflected signals and can be written, cf. [15], as

$$I_{\text{int}} + i\,Q_{\text{int}} = (I_{\text{dir}} + i\,Q_{\text{dir}}) + (I_{\text{ref}} + i\,Q_{\text{ref}}) \tag{2}$$

with the subscript dir and ref denoting the components of the direct and reflected signals, respectively. Fig. 5 demonstrates an example of the receiver output from the two slave antennas. As can be seen in the figure, both the I and Q components exhibit long- and short-term variations that originated from different contributors. The long-term slowly varying trend is governed by variations of the direct signal amplitude, antenna gain pattern, and the baseline between the master and slave antennas. The prominent high-frequency oscillations at the beginning and the end of the time series shown in the figure are the interferometric fringes. These fringes are extracted from the compound signal and are investigated in our analysis. The amplitude of the interferometric oscillations is
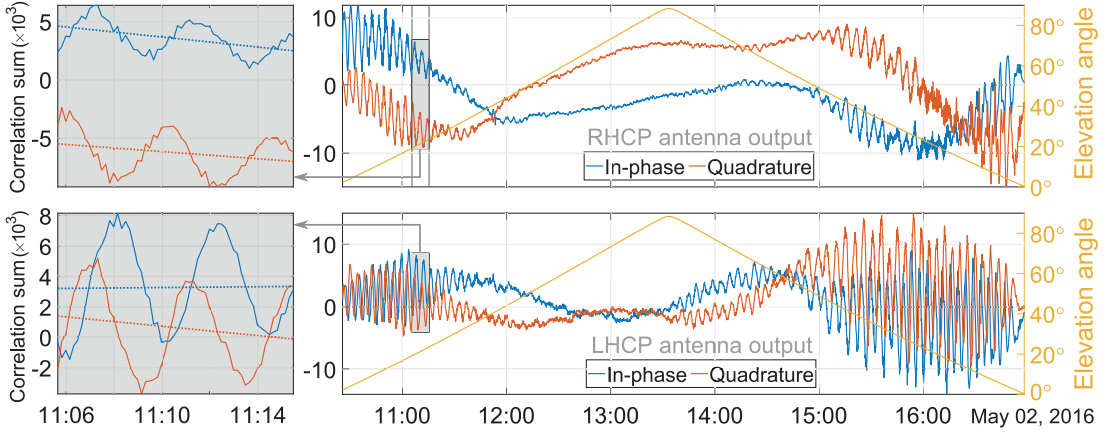
Fig. 5. Examples of in-phase (I) and quadrature (Q) correlation sums of GPS PRN 12 from the two sea-looking antennas used for the reflectometry. The top figures are related to the copolarization link (RHCP antenna), and the bottom figures show the data from the cross-polarization link (LHCP antenna). The selected segments shown on the left figures are used for estimating the power of direct and reflected signals. The first-order order polynomial fits in these segments (dotted lines) indicate the contribution of the direct signals.

the main parameter of interest in the analysis. This parameter is controlled by several factors. The main factors are the strength of the incoming direct signal, antenna gain, satellite elevation angle, dielectric constant of seawater, and SSR. The methodology of this study is focused on estimating the effect of the SSR. Therefore, the effects of the other factors are either modeled or mitigated within the processing flow.

To decompose the compound signal, we estimate and utilize the frequency of the interference fringes. This frequency is the Doppler shift caused by the different traveling paths of the direct and reflected signals and can be calculated, cf. [15], by

$$\delta f = \frac{1}{\lambda} \frac{d(\delta\rho)}{dt}, \quad \delta\rho = \rho_{\text{ref}} - \rho_{\text{dir}} \quad (3)$$

where δf is the Doppler shift, ρ_{dir} and ρ_{ref} are lengths of the paths traveled by the direct and reflected signals, respectively, and λ is the wavelength of the signal carrier. It should be noted that another Doppler shift could also be found in the observations due to the baseline [16]. However, the frequency of the latter shift in the Onsala setup is much lower compared to the interferometric frequency and would not noticeably affect the power retrievals. We use the period of interferometric oscillations to split the I/Q time series into successive segments from which the power of direct and reflected signals can be estimated [15]. The reciprocal value of this period, i.e., the frequency δf, is related to the geometry of reflection (see Fig. 6) by

$$\delta\rho = 2\, \delta H\, \sin(e)$$
$$\delta f = \frac{2\, \delta H\, \cos(e)}{\lambda} \frac{de}{dt} \quad (4)$$

where e is the elevation angle of the tracked satellite and δH is the height difference between the phase center of the slave antennas and sea level. From a fast Fourier transform (FFT)
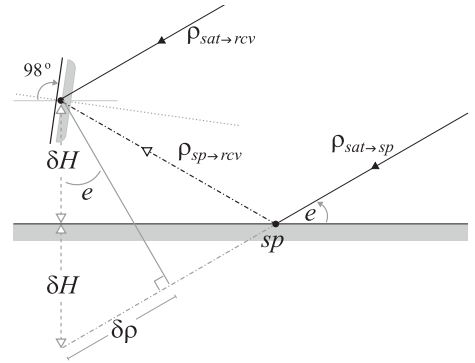
Fig. 6. Geometry of specular reflection and the path difference between the direct and reflected signals.

analysis, the dominant interferometric period in the observations is estimated to be around 5 min. Therefore, we use a time interval of 10 min for the segmentation to include two complete interferometric periods in each segment.

The separated segments of I/Q samples from the slave channels are independently processed to retrieve the contributions of the direct and reflected signals. The first-order polynomial is used to model the long term variations [see Fig. 5 (Left)]. These variations are attributed to the direct signal and can be used to estimate the corresponding power

$$\hat{P}_{\text{dir}} = \text{avg}(\,|\hat{I}_{\text{dir}} + i\, \hat{Q}_{\text{dir}}|^2) \quad (5)$$

where avg denotes the average function and $\hat{P}_{\text{dir}}$ is the estimate of the direct signal power over the segment. The variables $\hat{I}_{\text{dir}}$ and $\hat{Q}_{\text{dir}}$ are, respectively, the modeled I and Q amplitudes using the first-order polynomial and can be used to retrieve

the contribution of the reflected signal ($\hat{I}_{\text{ref}}$ and $\hat{Q}_{\text{ref}}$) by

$$\hat{I}_{\text{ref}} = \hat{I}_{\text{int}} - \hat{I}_{\text{dir}}$$
$$\hat{Q}_{\text{ref}} = \hat{Q}_{\text{int}} - \hat{Q}_{\text{dir}}. \tag{6}$$

The retrieved I/Q contributions of the reflected signal over each segment are processed using a Lomb–Scargle periodogram (LSP) to estimate the power of reflected signals in a similar approach used by [17] and [15]. According to (4), a change in the height difference (δH) results in a change in the interferometric frequency. The height difference between the antennas and the sea level over each segment is obtained from the tide gauge measurements. Therefore, with the knowledge of the satellite elevation angle from orbit information, we can precisely extract the power of reflected signals ($\hat{P}_{\text{ref}}$) from the periodogram. The estimated powers of the direct and reflected signals from the described procedure can be now related to the main involving factors through [18]

$$\hat{P}_{\text{dir}} = G_{\text{dir}} \, P_0$$
$$\hat{P}_{\text{ref}} = G_{\text{ref}} \, |R|^2 \, S^2 \, P_0 \tag{7}$$

with P_0 being the power of the incoming signal at the antenna (and at the specular point), G the antenna gain factor, R the complex-valued Fresnel reflection coefficient, and S a dampening factor due to the reflecting surface roughness. The power loss due to insufficient delay-Doppler tracking of reflected signal [15] is ignored since the difference of the delay/Doppler values for the reflected and direct signals are negligible in the Onsala configuration.

The Fresnel reflection coefficient describes polarization states of the reflected signals. The RHCP polarization of the incoming signal is altered during the reflection. The reflected signal includes both RHCP and LHCP polarizations. The proportion of each part in the reflected signal is estimated using Fresnel copolarization and cross-polarization coefficients. Both of the two coefficients are functions of elevation angle of the incoming signal and the permittivity of the reflecting medium [15], [19]

$$R_\parallel = \frac{\epsilon_{\text{sea}} \, \sin e - \sqrt{\epsilon_{\text{air}} \, \epsilon_{\text{sea}} - (\epsilon_{\text{air}} \, \cos e)^2}}{\epsilon_{\text{sea}} \, \sin e + \sqrt{\epsilon_{\text{air}} \, \epsilon_{\text{sea}} - (\epsilon_{\text{air}} \, \cos e)^2}}$$
$$R_\perp = \frac{\epsilon_{\text{air}} \, \sin e - \sqrt{\epsilon_{\text{air}} \, \epsilon_{\text{sea}} - (\epsilon_{\text{air}} \, \cos e)^2}}{\epsilon_{\text{air}} \, \sin e + \sqrt{\epsilon_{\text{air}} \, \epsilon_{\text{sea}} - (\epsilon_{\text{air}} \, \cos e)^2}} \tag{8}$$

where $R_\parallel$ and $R_\perp$ denote, respectively, the reflections with the polarization parallel to incidence plane and perpendicular to it. These coefficients can be combined to yield copolarization (R^{co}) and cross-polarization (R^{cross}) forms of the Fresnel coefficients [19]

$$R^{\text{co}} = \frac{1}{2}(R_\parallel + R_\perp)$$
$$R^{\text{cross}} = \frac{1}{2}(R_\parallel - R_\perp). \tag{9}$$

Fig. 7 depicts the Fresnel coefficients using the estimated permittivity of seawater at the Onsala station. The shaded areas show the slight variations of the coefficients based on variations of the permittivity on different days of the year.
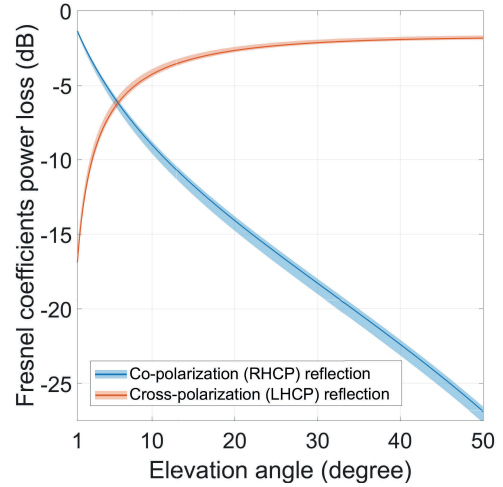
Fig. 7. Fresnel reflection coefficients calculated using the permittivity of seawater at the Onsala GNSS-R station. Based on the average permittivity, the blue and orange lines denote the magnitude of the copolarization and cross-polarization reflection coefficients in decibels (dB), respectively. The spread of the shaded areas shows the distribution of the coefficients based on the variations of local seawater permittivity shown in Fig. 3(b).

The factor S in (7) is a model that relates the standard deviation of sea surface height (σ) as a measure of surface roughness to the resultant power loss. The model is independent of the polarization and reads [18]

$$S = \exp\left(-\frac{1}{2}\frac{(2\pi)^2}{\lambda^2}\sigma^2 \sin^2 e\right). \tag{10}$$

We use the introduced Fresnel equations and the roughness model to invert the observed powers to the SSR measurements. The unknown parameter P_0 can be canceled out by forming the following power ratios:

$$L^c = \frac{\hat{P}_{\text{ref}}^{\text{co}}}{\hat{P}_{\text{dir}}^{\text{co}}} = \frac{G_{\text{ref}}}{G_{\text{dir}}} \, |R^{\text{co}}|^2 \, S_c^2$$
$$L^x = \frac{\hat{P}_{\text{ref}}^{\text{cross}}}{\hat{P}_{\text{dir}}^{\text{co}}} = \frac{G_{\text{ref}}}{G_{\text{dir}}} \, |R^{\text{cross}}|^2 \, S_x^2. \tag{11}$$

The variables L^c and L^x are, respectively, copolarization and cross-polarization power ratios that are our level-1 observables through which we estimate the SSR. L^c and L^x are estimated using the power of reflected signals, i.e. $\hat{P}_{\text{ref}}^{\text{co}}$ and $\hat{P}_{\text{ref}}^{\text{cross}}$, which are derived from the RHCP and LHCP slave antennas, respectively. Note that, for both of the ratios, the reference power in (11), $\hat{P}_{\text{dir}}^{\text{co}}$, is retrieved from the sea-looking RHCP antenna. Besides, cross-to-copolarization power ratio L^{x2c} that is the ratio of L^x to L^c reads

$$L^{x2c} = \frac{\hat{P}_{\text{ref}}^{\text{cross}}}{\hat{P}_{\text{ref}}^{\text{co}}} = \frac{|R^{\text{cross}}|^2 \, S_x^2}{|R^{\text{co}}|^2 \, S_c^2}. \tag{12}$$

We invert the calculated power ratios to the standard deviation of sea surface height. The inversion is independently done for L^c, L^x, and L^{x2c} through solving an optimization problem. For this purpose, all the power ratios from different
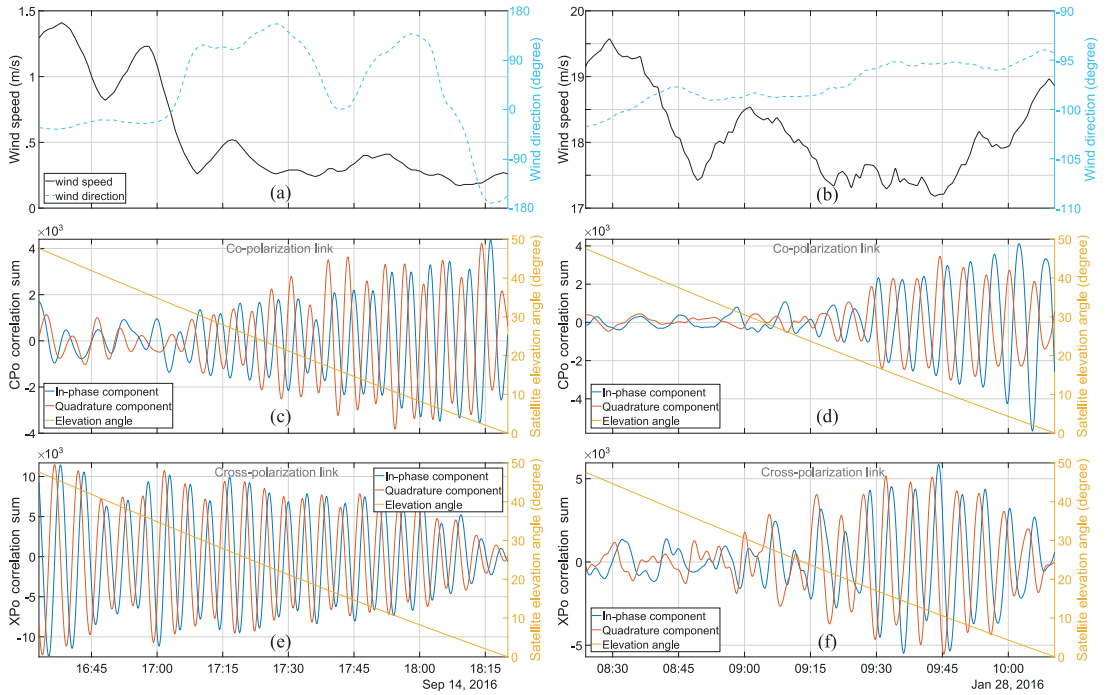
Fig. 8. Exemplary case of the impact of wind speed on the amplitude of copolarization (CPo) and cross-polarization (XPo) reflectometry observations from the GPS satellite PRN 1. The observations are associated with a similar range of the satellite elevation angles on two different days. The left and right columns are associated with periods of low and high wind speeds, respectively. (a) and (b) Direction and speed of the wind. Figures (c) and (d) In-phase and quadrature components of the copolarization observations that are recorded from the RHCP sea-looking antenna. (e) and (f) In-phase and quadrature components of the cross-polarization observations that are recorded from the LHCP sea-looking antenna. The reduced intensity of signals on the right figures (d) and (f) during wind speed of about 18 m/s is remarkable compared with the significantly higher signal amplitudes shown in (c) and (e) during the wind speed of about 1 m/s.

satellites over a common time interval are grouped and used to minimize the following cost function:

$$\min_{\sigma} \sum_i (L_i - |R_i|^2 \, S^2)^2 \qquad (13)$$

with min being the minimum function and the index i referring to all of the observations falling in a common time interval.

IV. RESULTS AND DISCUSSION

We apply the described method to the observed amplitude anomalies of interferometric signals to measure SSR variations. In the absence of *in situ* roughness estimates, we use the wind speed and wind direction for the analysis.

An exemplary case of the amplitude anomaly is shown in Fig. 8. The figure demonstrates the copolarization and cross-polarization reflection amplitudes at two different wind speeds during the setting period of the GPS satellite PRN 1. The left column in the figure shows the I/Q components of the reflected signal during a low wind speed period. A drastic reduction of the signal amplitude due to a significantly higher wind speed can be seen in the right column graphs.

The comparison of the amplitudes from the two links in Fig. 8(c) and (d) with those in Fig. 8(e) and (f) reports

much more powerful cross-polarization reflections. Moreover, the magnitudes of the in-phase and quadrature components in the cross-polarization link are varying consistently over time. On the contrary, the relatively weaker copolarization reflections exhibit inconsistencies between the magnitudes of the I and Q components. A prominent case of the inconsistency occurs at about 17:40 in Fig. 8(c) where the wind field shows an abrupt direction change. Such inconsistency between I and Q magnitudes appears in a fading of signal amplitude linked with a short-term loss of phase coherence. Hence, abrupt changes in the wind field could result in a loss of phase coherence.

The results of processing for about 7×10^4 segments of 10-min intervals in 2016 are summarized in Fig. 9. The figure shows the distribution of the observed power ratios against the elevation angle of the satellite. The estimates of power ratios are overlaid with the roughness model, i.e., (10), with different σ values. A comparison of the distributions with the model predictions suggests an overall agreement for all of the power ratios.

The distribution of the copolarization power ratios in Fig. 9(a) is mainly scattered around the lowest roughness models, i.e., $\sigma \leq 10$ cm. This can be an indicator of
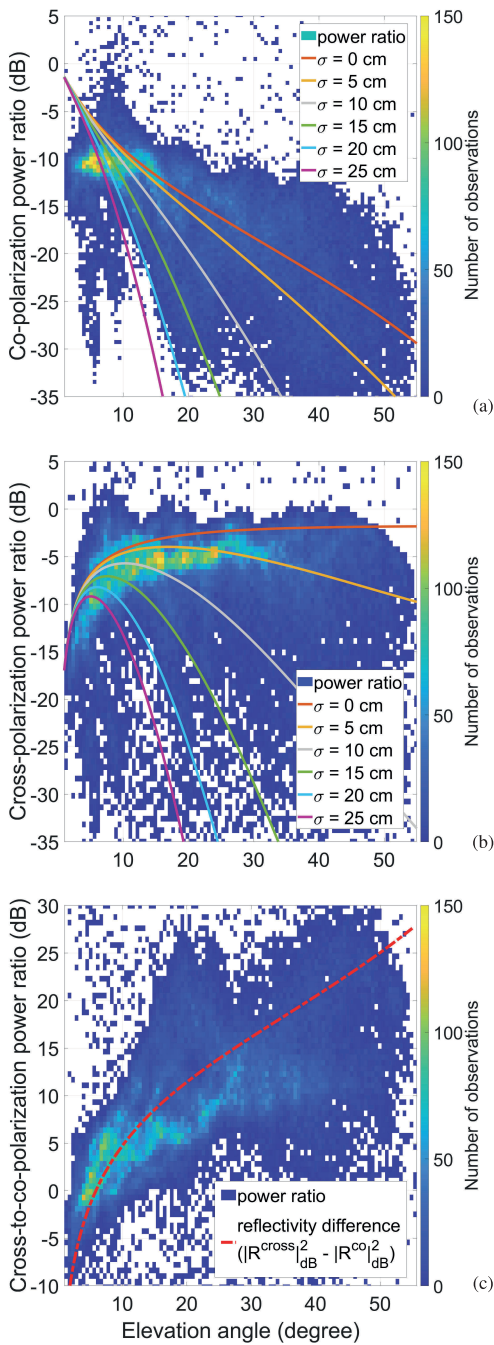
Fig. 9. Distribution of the estimated power ratios from the sea-looking antennas. (a) Copolarization (RHCP). (b) Cross-polarization (LHCP). (c) Cross-to-copolarization. The solid lines are model predictions based on different values of standard deviation of sea surface height (σ). The dashed–dotted line is the ratio of cross-to-copolarization reflectivity.
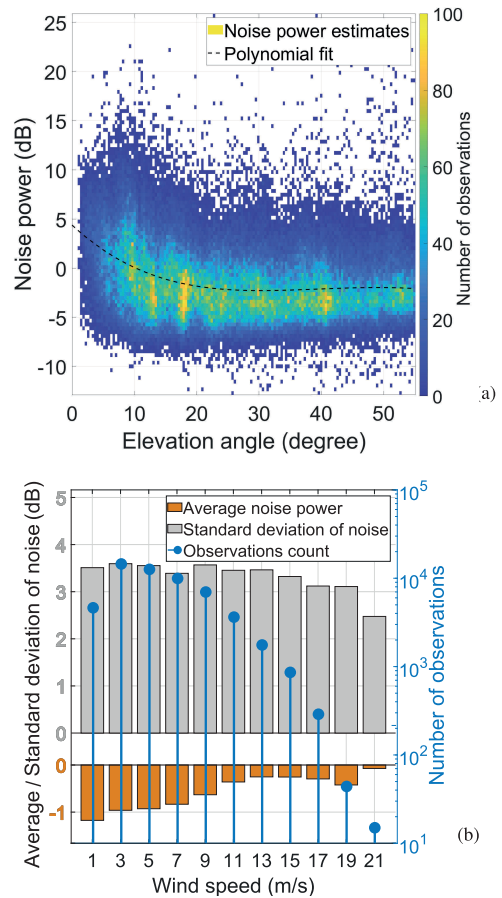
Fig. 10. (a) Distribution of noise power estimates against the elevation angle of incoming signals. (b) Average and standard deviation of the noise power in different wind speeds.

less sensitivity of copolarization observations to the SSR. Moreover, two noticeable biases with respect to the model predictions can be observed for the ratios in Fig. 9(a). The first bias occurs at very low elevation angles. This bias could be related to the performance of the roughness model, i.e., over these angles, the model underestimates the impact of the roughness for copolarization power ratios. Interestingly, at the elevation angles below 5° where the impact of roughness is expected to almost disappear, the ratios still reflect the impact of high sea states.

The estimated power ratios from the cross-polarization link are shown in Fig. 9(b). These ratios manifest a wider spread around the models with different values of σ compared to the copolarization power ratios. The presence of positive power ratios at elevation angles about 8° for both copolarization and cross-polarization power ratios can be related to the antenna gain. The antenna gain pattern used in our processing is
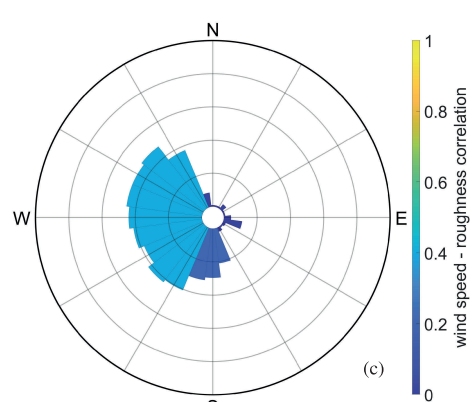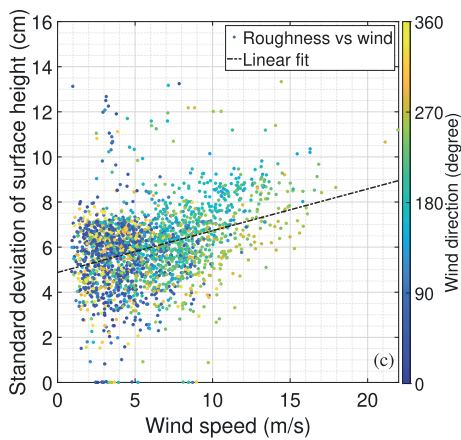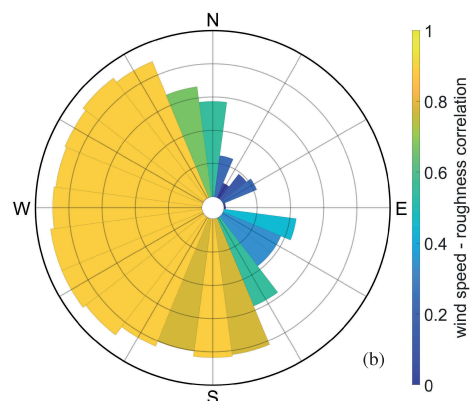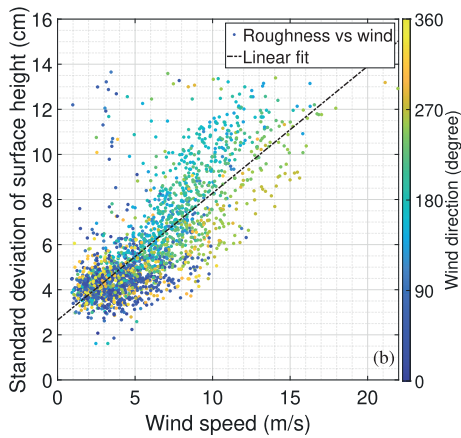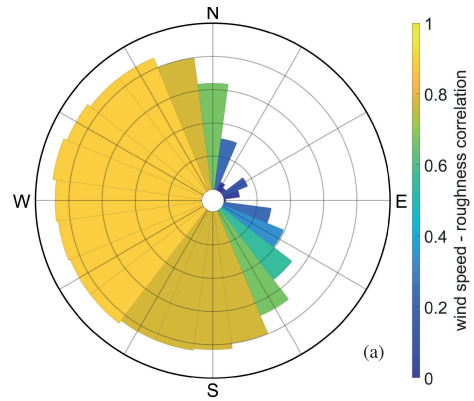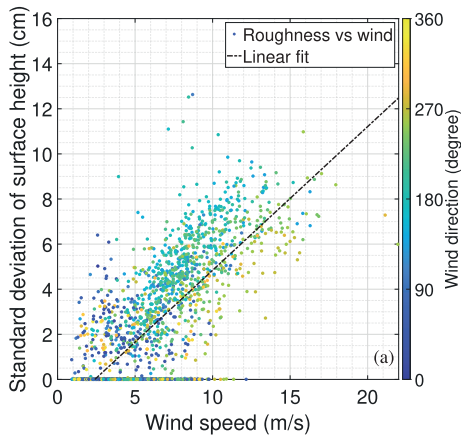
Fig. 11. Results of the roughness retrievals based on the one-year GNSS-R measurements in 2016 estimated from: (a) copolarization, (b) cross-polarization, and (c) cross-to-copolarization power ratios.

Fig. 12. Sensitivity of roughness measurements to wind direction. The correlation of wind speeds with (a) copolarization, (b) cross-polarization, and (c) cross-to-copolarization roughness retrievals is shown as a function of wind direction.

Fig. 13. Demonstration of the impact of wind direction and the complex coastlines on the SSR over different areas nearby the Onsala GNSS-R station. The station is shown by a yellow diamond symbol.

estimated based on the interpolation of a few discrete gain values provided by the antenna datasheet. The gain pattern is assumed to be symmetric in terms of the azimuth angle. At the boresight of the tilted antennas, the specularly reflected signals from the satellites at elevation angles around 8° (the dotted gray line in Fig. 6) are collected at the highest possible gain. At this configuration, the gain can dramatically change with the change of the satellite azimuth angle. Therefore, possible uncertainties within the interpolated gain pattern could produce positive power ratios.

Fig. 9(c) shows the distribution of cross-to-copolarization power ratios with respect to the reflectivity difference calculated from the Fresnel equations. Having the polarization-independent roughness model described by (10), we expect to have a roughness-free power distribution from (12). The power distributions, however, indicate wide variations around the dashed line in Fig. 9(c), i.e., the line of the reflectivity difference. This indicates the polarization-dependence of the roughness effect.

The plots of Fig. 10 show the estimates of noise power calculated from the quadrature component of the zenith-looking antenna [15]. As can be seen in Fig. 10(a), higher noise powers occur at lower elevation angles where the power of copolarization reflection is prominently high. This makes the tracking of the direct signals more difficult compared to higher elevation angles where both the reflectivity power loss (see Fig. 7) and roughness effect suppress the reflection power. Fig. 10(b) presents the statistics of noise power estimates against different wind speeds. No prominent dependence on sea state can be observed in the variations of noise power described by the standard deviation values. The unaffected noise power here in a coastal setup is in contrast to sea-
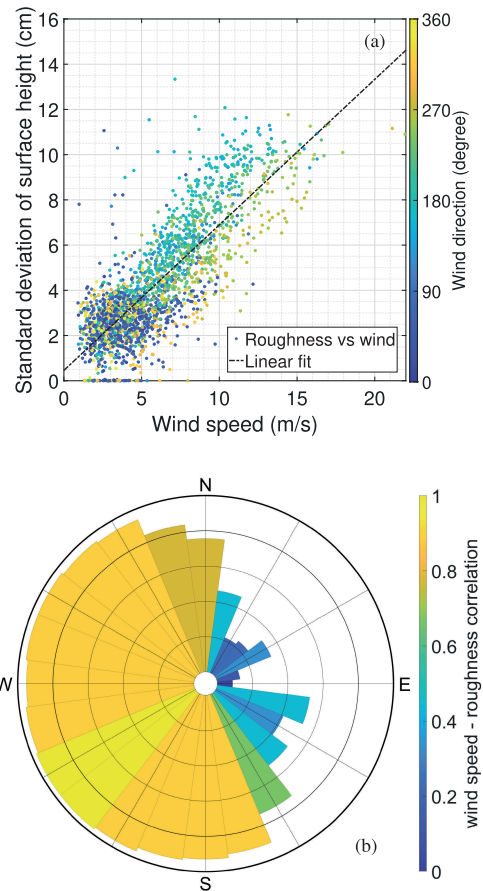
Fig. 14. Results of the full polarimetric roughness retrievals based on the one-year GNSS-R measurements in 2016. (a) Roughness estimates against different wind speeds overlaid with the first-order polynomial. (b) Dependence of the roughness retrievals on the direction of wind fields.

state-dependent noise from the ship measurements described in [15]. However, an insignificant rise of noise power with the increasing wind speed can be seen in our measurements.

The level-2 product of SSR measurements against different wind speeds and wind directions is depicted in Fig. 11. The standard deviation of surface height is the measured parameter describing the SSR. In general, the anomalies of the roughness estimates derived from the copolarization and cross-polarization observations are well connected to the variations of wind speed. The overall correlations of the roughness products with wind speed are about 0.76 for the copolarization and cross-polarization links. However, an analogy between the behavior of the results in Fig. 11(a) and (b) reveals noticeable discrepancies.

Fig. 11(a) includes observations that are mapped to zero-roughness. This is particularly the case for most of the winds blowing from 0° to 90° azimuth angles. Besides, the roughness measurements in the figure exhibit wind direction dependence
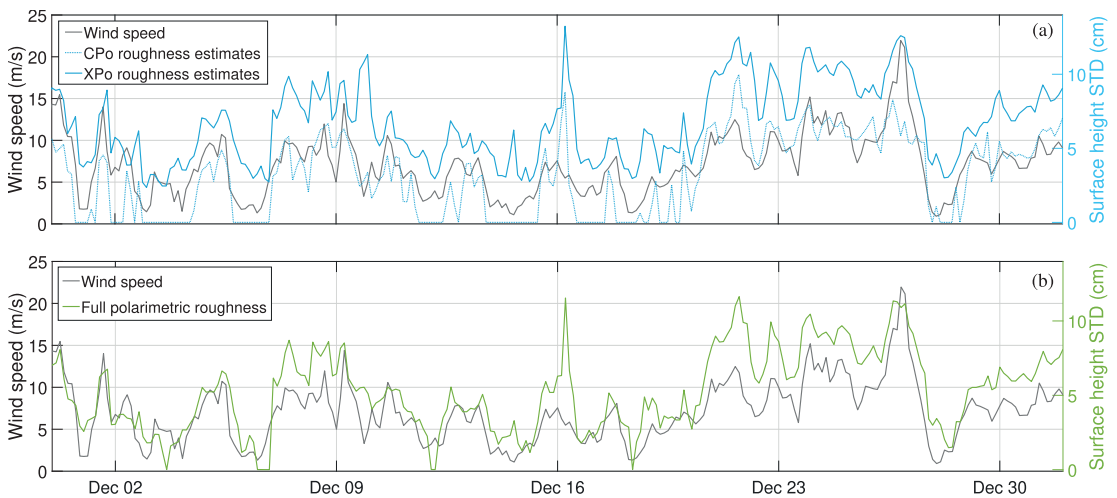
Fig. 15. Exemplary time series of SSR estimates from GNSS-R measurements in December 2016. (a) Roughness retrievals from the copolarization (CPo) and cross-polarization (XPo) measurements. (b) Roughness retrievals from a full polarimetric solution, i.e., combination of CPo and XPo measurements.

patterns. A bias can be seen in the copolarization measurements, which indicates that the corresponding observations are mostly not responsive to the wind speeds below 2 m/s. The values of σ derived from the copolarization link are mainly below 9 cm.

The roughness estimates from the cross-polarization antenna present better performance compared to the copolarization link. The distribution of the roughness retrievals against different wind speeds shows a higher sensitivity of cross-polarization measurements to the sea state.

The dependence of the roughness retrievals to the wind direction can be distinguished from the clustered pattern in Fig. 11(b). The lowest dependence can be seen for the north to the east winds. In contrast, south and west winds have triggered clearer responses in the results. As can be seen in the figure, the linear fit to the data reveals a bias in the roughness retrievals, which could be partly attributed to the signal processing procedure in the receiver. The signals received by the two sea-looking antennas are processed within two separate channels. Therefore, different Automatic Gain Controller (AGC) factors are applied to the received signals. In the calculation of cross-polarization ratios (11), the reference power of the direct signal is estimated from the copolarization link. Therefore, the cross-polarization power ratios could be affected by different AGC values. This bias is shown more clearly in the cross-to-copolarization roughness measurements [see Fig. 11(c)]. The retrievals shown in Fig. 11(c) present an overall correlation of about 0.35 with wind speeds despite the expectation of having almost no correlation. This implies that the effect of roughness in the cross-polarization observations is more pronounced.

The mean absolute errors associated with the roughness retrievals are listed in Table I. The error estimates are calculated based on the residuals of the optimized solution for (13). The retrievals from the cross-polarization link are associated

TABLE I
MEAN ABSOLUTE ERROR VALUES ASSOCIATED WITH THE ROUGHNESS RETRIEVALS SHOWN IN FIG. 11

		wind speed range (m/s)			
	power ratios	0-5	5-10	10-15	>15
mean	co-polarization	3.9	3.7	4.2	5.6
absolute	cross-polarization	3.1	3.1	3.9	5.7
error (dB)	cross to co-polarization	3.7	3.8	3.9	3.8

with smaller error values. However, the errors increase with the rise of wind speed for the copolarization and cross-polarization roughness retrievals.

The impact of wind direction on the roughness retrievals is shown in Fig. 12. The correlation of the retrieved SSR with the direction at which the wind is blowing is shown in a polar coordinate system. The copolarization and cross-polarization roughness estimates are highly correlated with the winds blowing from the range of south-southeast to north, i.e., from 150° to 360°. The winds with the directions falling in the range of 10°–90° are almost ineffectual to produce strong responses in the observations.

The different performance of the roughness retrievals with respect to the wind direction can be related to the location of the station. From the wind distribution shown in Fig. 3(a), it can be recognized that the north–northeast wind is a major direction of the wind in this area. However, this direction and the wind fields with the direction from 15° to 135° do not stimulate prominent roughness in the sea surface. When the wind is blowing from land, i.e., during the "offshore or land breeze," there is no fetch for wind-driven waves at the coast. Thus, the roughness will not increase. Using wind speed ancillary data as a proxy for roughness may be difficult in fetch-limited areas. Roughness and wave spectrum are also constrained by shallow water in coastal areas. The coastal effect on roughness is observed in synthetic aperture

radar (SAR) data [20] and is well known in the ocean wave modeling community [21]. Conditions change when the wind is blowing from the sea (south, west, and north–west). Winds from these directions, i.e., the "onshore or sea breeze," can produce developed sea states and, thus, maximal roughness. However, even the roughness developed by these winds could be suppressed by the complex coastlines surrounding the station and nearby small islands. Fig. 13 shows three regions with different sea states. The developed sea state in region C is partly transferred to region B, and a calmer condition can be seen in region A compared to the regions B and C.

We combine the observations from the two sea-looking antennas to assess the performance of a full polarimetric solution to (13). The results are presented in Fig. 14. The full polarimetric roughness estimates have an overall correlation of about 0.82 with wind speeds. The results manifest almost no bias compared to Fig. 11(a) and (b). Fig. 14(b) reports on the improved sensitivity to wind-driven roughness for all wind directions. The figure shows that the roughness responses to the wind fields from the azimuth of 165° to 345° are almost entirely identified by the polarimetric GNSS-R observations.

Fig. 15 demonstrates exemplary time series of the reflectometry-derived SSR from the copolarization and cross-polarization power ratios in December 2016. Both the time series in Fig. 15(a) represent high correlations with the wind speed variations. Fig. 15(b) illustrates the time series of full polarimetric roughness estimates with enhancements compared to the copolarization and cross-polarization time series.

V. CONCLUSION

We have investigated the response of GNSS reflectometry observations to the SSR during different wind conditions. A coastal GNSS-R experiment has been used to assess the performance of polarimetric observations for estimating the roughness. Two sea-looking antennas with copolarization and cross-polarization designs with respect to the polarization of incoming direct signals are used in the experiment. The processing results from both antennas show successful roughness retrievals over the one-year period of the analyzed data set. However, stronger manifestations of the SSR can be seen in the cross-polarization measurements. The left- and right-handed polarized components of reflected signals are affected differently by SSR. Wind speeds as low as about 1 m/s are detected in cross-polarization retrievals, whereas significant copolarization retrievals occur mainly for wind speeds above 2 m/s. The effect of sea state can be seen in the cross-to-copolarization power ratios, which is not expected. This reveals the need for an enhancement in the state-of-the-art model. A clear dependence on the wind direction, due to different fetch lengths and the nearby complex coastlines, is observed in the roughness estimates. The winds blowing from the open-sea areas have shown the maximal impact on the roughness values compared with the winds blowing from land. A full-polarimetric solution has been also tested for roughness retrieval. The results show noticeable improvements compared to the copolarization or cross-polarization results.

The full-polarimetric retrievals show an increased sensitivity to wind speeds from all directions.

REFERENCES

[1] H. Zhang *et al.*, "Observation of sea surface roughness at a pixel scale using multi-angle sun glitter images acquired by the ASTER sensor," *Remote Sens. Environ.*, vol. 208, pp. 97–108, Apr. 2018.

[2] V. U. Zavorotny and A. G. Voronovich, "Scattering of GPS signals from the ocean with wind remote sensing application," *IEEE Trans. Geosci. Remote Sens.*, vol. 38, no. 2, pp. 951–964, Mar. 2000.

[3] C. S. Ruf *et al.*, "A new paradigm in Earth environmental monitoring with the CYGNSS small satellite constellation," *Sci. Rep.*, vol. 8, no. 1, pp. 1–13, Dec. 2018.

[4] M. Hoseini, M. Asgarimehr, V. Zavorotny, H. Nahavandchi, C. Ruf, and J. Wickert, "First evidence of mesoscale ocean eddies signature in GNSS reflectometry measurements," *Remote Sens.*, vol. 12, no. 3, p. 542, Feb. 2020.

[5] A. Camps, X. Bosch-Lluis, I. Ramos-Perez, J. F. Marchan-Hernandez, B. Izquierdo, and N. Rodriguez-Alvarez, "New instrument concepts for ocean sensing: Analysis of the PAU-radiometer," *IEEE Trans. Geosci. Remote Sens.*, vol. 45, no. 10, pp. 3180–3192, Oct. 2007.

[6] J. F. Marchan-Hernandez *et al.*, "Sea-state determination using GNSS-R data," *IEEE Geosci. Remote Sens. Lett.*, vol. 7, no. 4, pp. 621–625, Oct. 2010.

[7] F. Soulat, M. Caparrini, O. Germain, P. Lopez-Dekker, M. Taani, and G. Ruffini, "Sea state monitoring using coastal GNSS-R," *Geophys. Res. Lett.*, vol. 31, pp. 1–4, 2004, Art. no. L21303, doi: 10.1029/2004GL020680.

[8] E. Cardellach, S. Ribó, and A. Rius, "Technical note on Polarimetric phase interferometry (POPI)," 2006, *arXiv:physics/0606099*. [Online]. Available: https://arxiv.org/abs/physics/0606099

[9] A. Egido *et al.*, "Airborne GNSS-R polarimetric measurements for soil moisture and above-ground biomass estimation," *IEEE J. Sel. Topics Appl. Earth Observ. Remote Sens.*, vol. 7, no. 5, pp. 1522–1532, May 2014.

[10] D. Schiavulli, A. Ghavidel, A. Camps, and M. Migliaccio, "GNSS-R wind-dependent polarimetric signature over the ocean," *IEEE Geosci. Remote Sens. Lett.*, vol. 12, no. 12, pp. 2374–2378, Dec. 2015.

[11] E. Motte *et al.*, "GLORI: A GNSS-R dual polarization airborne instrument for land surface monitoring," *Sensors*, vol. 16, no. 5, p. 732, May 2016.

[12] A. M. Semmling *et al.*, "A zeppelin experiment to study airborne altimetry using specular global navigation satellite system reflections," *Radio Sci.*, vol. 48, no. 4, pp. 427–440, Jul. 2013.

[13] Y. Zhou, R. H. Lang, E. P. Dinnat, and D. M. Le Vine, "L-band model function of the dielectric constant of seawater," *IEEE Trans. Geosci. Remote Sens.*, vol. 55, no. 12, pp. 6964–6974, Dec. 2017.

[14] R. Lang, Y. Zhou, C. Utku, and D. Le Vine, "Accurate measurements of the dielectric constant of seawater at L band," *Radio Sci.*, vol. 51, no. 1, pp. 2–24, Jan. 2016.

[15] A. M. Semmling *et al.*, "Sea-ice concentration derived from GNSS reflection measurements in Fram Strait," *IEEE Trans. Geosci. Remote Sens.*, vol. 57, no. 12, pp. 10350–10361, Dec. 2019.

[16] W. Liu *et al.*, "Coastal sea-level measurements based on GNSS-R phase altimetry: A case study at the Onsala space observatory, Sweden," *IEEE Trans. Geosci. Remote Sens.*, vol. 55, no. 10, pp. 5625–5636, Oct. 2017.

[17] K. M. Larson, E. E. Small, E. Gutmann, A. Bilich, P. Axelrad, and J. Braun, "Using GPS multipath to measure soil moisture fluctuations: Initial results," *GPS Solutions*, vol. 12, no. 3, pp. 173–177, Jul. 2008.

[18] F. G. Nievinski and K. M. Larson, "Forward modeling of GPS multipath for near-surface reflectometry and positioning applications," *GPS Solutions*, vol. 18, no. 2, pp. 309–322, Apr. 2014.

[19] E. Cardellach, F. Fabra, A. Rius, S. Pettinato, and S. D'Addio, "Characterization of dry-snow sub-structure using GNSS reflected signals," *Remote Sens. Environ.*, vol. 124, pp. 122–134, Sep. 2012.

[20] M. A. Sletten and P. A. Hwang, "The effect of wind-wave growth on SAR-based waterline maps," *IEEE Trans. Geosci. Remote Sens.*, vol. 49, no. 12, pp. 5140–5149, Dec. 2011.

[21] *Shore Protection Manual*, Dept. Army, Waterways Exp. Station, Corps Eng., CERC. (US), Vicksburg, MS, USA, 1984.

Mostafa Hoseini graduated in geodesy from the University of Tehran, Tehran, Iran. He is pursuing the Ph.D. degree with the Norwegian University of Science and Technology (NTNU), Trondheim, Norway.

He worked for several institutions as a GNSS Engineer in the field of positioning and navigation. He worked on the analysis of GNSS atmospheric products with the German Research Center for Geosciences (GFZ), Potsdam, Germany. His research interests include GNSS-based remote sensing techniques and sensors. His research focuses on the monitoring of the ocean and Arctic using the GNSS-reflectometry sensor onboard small satellites.

Maximilian Semmling graduated in physics from Leipzig University, Leipzig, Germany, in 2007, and the Ph.D. degree from Technische Universität Berlin, Berlin, Germany, in 2012.

For his doctoral and post-doctoral studies, he was with the German Research Center for Geosciences (GFZ), Potsdam, Germany, the Institute for Space Studies of Catalonia (IEEC), Catalonia, Spain, and the University of the Littoral Opal Coast (ULCO), Dunkirk, France. In 2020 he joined the Observation Department, German Aerospace Center (DLR), Institute for Solar-Terrestrial Physics, Neustrelitz, Germany. He is experienced in GNSS for Earth Observation with a research focus on ocean altimetry and sea ice remote sensing. His work concentrates on signal propagation effects for application in atmosphere sounding. Corresponding methods cover a wide range from ground-based measurements over maritime, airborne to satellite platforms.

Hossein Nahavandchi received the Ph.D. degree from the Royal Institute of Technology (KTH), Stockholm, Sweden, in 1998.

He is a Professor of Geodesy and Geophysics with the Norwegian University of Science and Technology (NTNU), Trondheim, Norway. His research interests involve global geodetic observations system (GGOS) including satellite gravimetry, satellite altimetry, satellite radar interferometry, and GNSS to understand the dynamic Earth system by quantifying Earth's change in space and time.
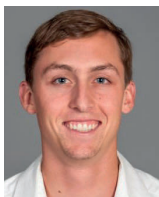
Erik Rennspiess was born in Pittsfield, MA, USA. He received the B.S. degree in environmental design with an emphasis on the built environment from the University of Massachusetts, Amherst, MA, USA, in 2013. He is pursuing the master's degree in geodesy and geoinformation science with the Technische Universität Berlin, Berlin, Germany.

His research interest includes GNSS remote sensing with a focus on ground-based GNSS-Reflectometry technique for monitoring coastal sea surface characteristics.

Markus Ramatschi received the Dipl.rer.nat. degree in geophysics and the Ph.D. degree in geophysics from the Technical University of Clausthal, Clausthal-Zellerfeld, Germany, in 1992 and 1998, respectively.

He is a Senior Scientist with the German Research Center for Geosciences (GFZ), Potsdam, Germany. His research interests include the operation of a global GNSS sensor station network.

Rüdiger Haas received the M.Sc. and Ph.D. degrees in geodesy from Bonn University, Bonn, Germany.

He is a Full Professor of space geodesy with the Department of Space, Earth and Environment, Chalmers University of Technology, Gothenburg, Sweden. He is the Head of the Research Group for Space Geodesy at Chalmers and responsible for the geoscience activities at the Onsala Space Observatory, Onsala, Sweden. His research interests focus primarily on space geodetic techniques, such as Global Navigation Satellite Systems (GNSS), including GNSS-reflectometry, and Very Long Baseline Interferometry (VLBI).

Joakim Strandberg received the M.Sc.Eng. degree in physics and the Ph.D. degree in radio and space science from the Chalmers University of Technology, Gothenburg, Sweden, in 2015 and 2020, respectively.

His research focuses on using reflected GNSS signals for remote sensing, especially for maritime purposes.

Jens Wickert received the Diploma degree in physics from Technical University Dresden, Dresden, Germany, in 1989, and the Ph.D. degree in geophysics/meteorology from Karl-Franzens-University Graz, Graz, Austria, in 2002.

He was the Principal Investigator of the pioneering GPS radio occultation experiment aboard the German CHAllenging Minisatellite Payload (CHAMP) Satellite and coordinates numerous research projects on GNSS remote sensing. He holds a joint professorship of GFZ with the Technical University of Berlin on Global Navigation Satellite Systems (GNSS) remote sensing, navigation, and positioning. He is also the Deputy GFZ Section Head Space Geodetic Techniques and the GFZ Research Topic Director of The Atmosphere in Global Change. He has authored or coauthored more than 250 Web of Science indexed publications on GNSS Earth observation.

Paper III

Paper IV

A PERFORMANCE ASSESSMENT OF POLARIMETRIC GNSS-R SEA LEVEL MONITORING IN THE PRESENCE OF SEA SURFACE ROUGHNESS

M. Rajabi[1], M. Hoseini[1], H. Nahavandchi[1], M. Semmling[2], M. Ramatschi[3],
M. Goli[4], R. Haas[5] and J. Wickert[3,6]

[1] Norwegian University of Science and Technology NTNU, Trondheim, Norway
[2] Institute for Solar-Terrestrial Physics, German Aerospace Center (DLR-SO), Neustrelitz, Germany.
[3] German Research Centre for Geosciences GFZ, Potsdam, Germany
[4] Faculty of Civil & Architectural Engineering, Shahrood University of Technology, Iran
[5] Department of Space, Earth and Environment, Chalmers University of Technology, Gothenburg, Sweden
[6] Technische Universität Berlin, Berlin, Germany

ABSTRACT

Monitoring coastal sea level has gained a large socio-economic and environmental significance. Ground-based Global Navigation Satellite System Reflectometry (GNSS-R) offers various geophysical parameters including sea surface height. We investigate a one-year dataset from January to December 2016 to evaluate the performance of GNSS-R coastal sea levels during different sea states. Our experiment setup uses three types of antenna in terms of polarization and orientation. A zenith-looking antenna tracks Right-Handed Circular Polarization (RHCP) direct signals and two sea-looking antennas capture both Left-Handed Circular Polarization (LHCP) and RHCP reflections. The Singular Spectrum Analysis (SSA) is used for extracting interferometric frequency from the data and calculating the heights. The results indicate that the height estimates from the sea-looking antennas have better accuracy compared to the zenith-looking orientation. The LHCP antenna delivers the best performance. The yearly Root Mean Square Errors (RMSE) of 5-min GNSS-R L1 water levels compared to the nearest tide gauge are 2.8 and 3.9 cm for the sea-looking antennas and 4.7 cm for the zenith-looking antenna with correlations of 97.63, 95.02, 95.35 percent, respectively. Our analysis shows that the roughness can introduce a bias to the measurements.

Index Terms — Global Navigation Satellite Systems-Reflectometry (GNSS-R), Costal Altimetry, Singular Spectrum Analysis (SSA)

1. INTRODUCTION

The characterization and accurate estimation of coastal waters can contribute to understanding the climate and environmental changes. This is also essential since a large population live in coastal areas and can be affected by associated natural disasters. Moreover, these areas are involved in substantial economic and trading activities. The sea level also is a key parameter for defining vertical datum in geodesy.

Spaceborne Radar Altimeters (RA) and traditional Tide Gauges (TG) are the common instruments for sea-level monitoring. There are limitations associated with these techniques. The TG is pointwise and can be affected by vertical motions. The RA is restricted by its spatiotemporal resolution and lower performance over coastal areas [1].

Besides positioning, navigation and timing, the Global Navigation Satellite System (GNSS) has been used for plenty of other applications including monitoring of the environment. GNSS-Reflectometry as a novel remote sensing technique utilizes GNSS reflected signals from the earth surface to study various parameters and phenomena, e.g. sea-level [1], sea surface roughness [2], soil moisture [3], flood [4], sea ice [5], ocean eddies [6], precipitation [7], wind speed [8], and several other applications.

The potential of ground-based GNSS-R for the sea-level altimetry has been investigated by several studies using zenith-looking Right-Handed Circular Polarization (RHCP) antennas with geodetic receivers. These studies are mainly considered the observations from low elevation angles. Investigating the performance of GNSS-R technique based on different polarizations and orientations of the antennas is desirable.

We designed three scenarios based on zenith- and sea-looking orientations as well as Left- and Right-Handed Circular Polarization (LHCP and RHCP). Besides, the effect of different wind speeds on the quality of the results is evaluated.

Among several spectral analysis methods, e.g. Lomb-Scargle periodogram [9], Least Squares Harmonic Estimation (LSHE) [10], we utilize Singular Spectrum Analysis (SSA) [11, 12] as a nonparametric and well-elaborated method for the times series analysis. The SSA is an effective method for retrieving different components of a signal. Here, SSA is used to extract the interferometric frequency, generated from the interference of the direct and reflected GNSS signals.

2. DATA AND METHODOLOGY

The dataset used in this study is the correlation sums at In-phase and Quadrature (I/Q) levels produced by the dedicated GNSS Occultation, Reflectometry, and Scatterometry (GORS) receiver [2, 5] from three antennas: a zenith-looking and two sea-looking antennas with a 98° tilt with respect to zenith. The antennas are installed at about 3 meters above the sea surface level. We collocate two ancillary datasets from the nearest meteorological station and a tide gauge located about 300 meters away from the GNSS-R station.

The methodology of this study is focused on estimating sea levels during different wind speeds. The frequency of interferometric oscillations in the I/Q time series is related to sea level as follow [2]:

$$\delta\rho = 2\,\delta H\,sin(e)\,, \delta f = \frac{2\,\delta H\,cos(e)}{\lambda}\cdot\frac{de}{dt} \qquad (1)$$

where $\delta\rho$ is the path difference between the direct and reflected signals, e is elevation angle of the tracked satellite, δH is the height between the antenna and sea surface, λ is the signal wavelength and δf is the interferometric frequency which is retrieved using SSA.

Briefly, the methodology contains three main steps illustrated in Figure 1. The first step includes the data preparation described by [2]. The second or key step focuses on applying SSA to the time-series of each PRN over reflection events. For detailed Information about SSA, readers could refer to [11].The retrieved interferometric signal is then inverted to the sea level estimate. We finish this step by outlier removal and finding the median of the sea surface height in the step of 5 min with a temporal window of 3 hours. In the final step, we evaluate the estimated sea surface heights with respect to the tide gauge observations and different wind speeds.
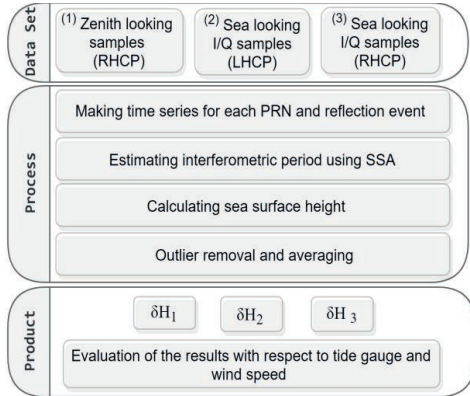
Fig. 1 Methodology flowchart based on the Singular Spectrum Analysis (SSA).

3. RESULTS AND DISCUSSION

The results of the SSA-based sea level retrievals from the GNSS-R dataset are presented and discussed in this section. Figure 2 shows an example of applying SSA to I/Q time series to extract the interferometric fringes. The method can simultaneously mitigate other irrelevant components. As seen in the figure, the applied method can effectively reveal the amplitude variations of the interferometric signal. The detected peaks in the bottom panel of Fig. 1 is used to estimate the period of interest for the calculation of height according to (1).
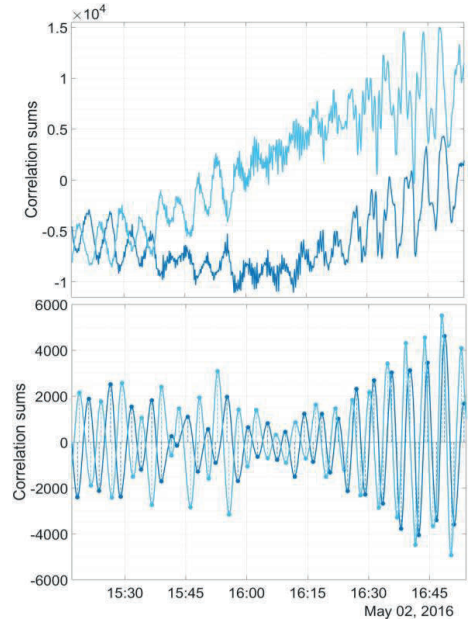
Fig. 2 - Top panel: an example of the in-phase / quadrature (I/Q) time series from GPS PRN 12 on May 02, 2016. Bottom panel: the result of retrieving interferometric fringes from the I/Q correlation sums using Singular Spectrum Analysis (SSA). The dark and light blue separate the in-phase and quadrature samples, respectively. The dots in the bottom panel show the detected peaks after applying SSA. The dashed lines illustrate the estimated amplitude.

Figure 3 shows the distribution of sea level anomalies from GNSS-R against tide gauge observations. The measurements from the sea-looking LHCP antenna shown on the right panel represent the best performance compared to both zenith-looking and sea-looking RHCP antennas. The larger errors from the zenith-looking antenna in the left panel compared to the midel panel shows that the change of the antenna orientation towards the sea improves the accuracy of the GNSS-R sea level measurements.
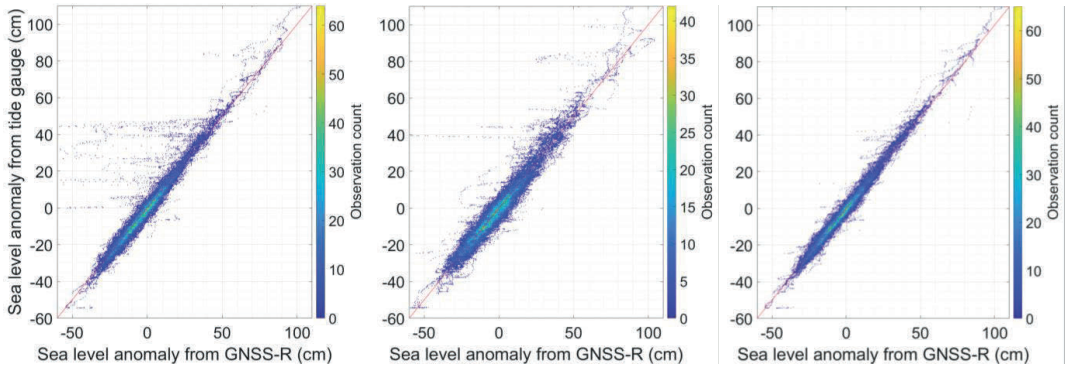
Fig. 3 – Comparisons of GNSS-R sea level measurements with respect to tide gauge data. The GNSS-R measurements are based on the application of Singular Spectrum Analysis (SSA) to the observations from the antennas in different polarizations, i.e. Right- and Left-Handed Circular Polarization (RHCP and LHCP), and two orientations, i.e. zenith-looking and sea-looking. The left panel shows the results of the zenith-looking RHCP antenna, the middle panel is associated with the sea-looking RHCP antenna, and the right panel depicts the measurements from the sea-looking LHCP antenna. The red lines overlaid on the plots show the one to one relationship.

To evaluate the possible impact of sea surface roughness on the sea level measurement, we use the collocated wind measurements. Figure 4 gives an overview of the impact of different states on the accuracy of the measurements. The figure shows that as the wind speed increases, the accuracy of the retrieved sea level degrades for all the antenna configurations. The investigation also reveals that the wind speeds can impose a bias in the measurements. The bias, in turn, has a contribution to the accuracy.

It should be noted that the limited fetch at a coastal GNSS-R experiments can partially shield the nearby sea surface against some wind directions. As reported by [2], this can result in different sea surface roughness for wind speeds from different directions. The roughness estimates from the latter study based on the same dataset is used here to evaluate possible dependency between the roughness and the GNSS-R sea level retrievals. The top panel in Fig. 5 provides an overview of roughness estimates against different wind speeds and directions. A delicate dependency between the height measurement errors and the roughness estimates can be seen in the bottom panel of Fig. 5.
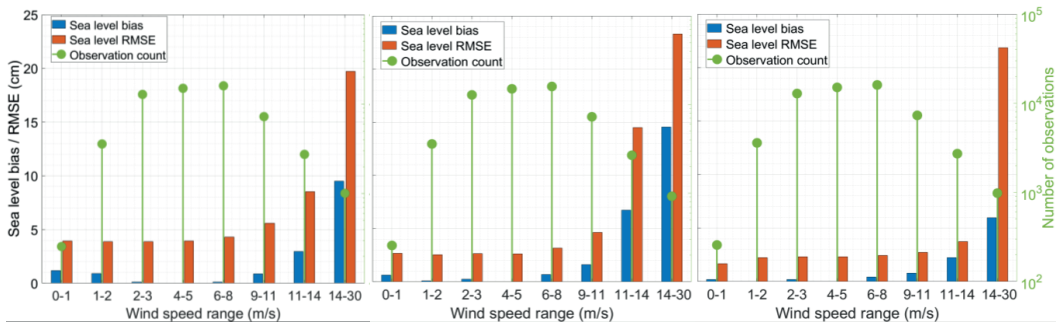
Fig. 4 - A performance assessment of GNSS-R sea level measurements at different ranges of wind speed. The sea level measurements are based on the application of Singular Spectrum Analysis (SSA) to the observations from the antennas in different polarizations, i.e. Right and Left Handed Circular Polarization (RHCP and LHCP), and two orientations, i.e. zenith-looking and sea-looking. The left, middle, and right panels show the results from a zenith-looking RHCP antenna, a sea-looking RHCP antenna, and a sea-looking LHCP antenna, respectively. The blue bars show the bias of the two datasets, i.e. the GNSS-R and tide gauge data, over each wind speed range. The red bars depict the Root Mean Squared Errors (RMSE) of the GNSS-R sea level measurements with respect to the tide gauge observations. The number of observations over each wind speed range is shown by green lines.
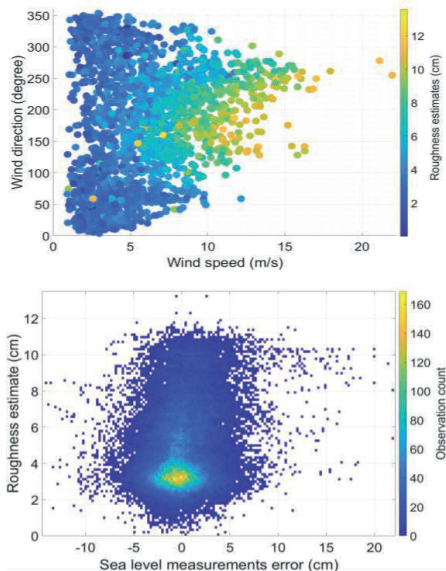
Fig. 5 - Top panel: the estimates of sea surface roughness in terms of standard deviation of height. The estimates are obtained from [2]. Bottom panel: the distribution of GNSS-R sea level measurement errors with respect to the sea surface roughness.

4. CONCLUSION

The results of sea level measurements from GNSS-Reflectometry observations in a coastal experiment are presented in this study. To retrieve these measurements, we applied Singular Spectrum Analysis (SSA) to the in-phase and quadrature observations from three antennas with different polarizations and orientations. Comparison of collocated tide gauge observations with the GNSS-R sea level retrievals from different antenna polarizations and orientations reports an overall Root Mean Square Error (RMSE) ranging from 2.8 to 4.7 cm for a period of one year, i.e. from January to December 2016. The measurements from a seaward-tilted Left-Handed Circulation Polarization (LHCP) antenna showed the best performance for sea level monitoring. The presence of measurement biases during different wind speeds were detected in the analysis. However, the reported biases could be different for other GNSS-R experiments since the location of our setup is surrounded by complex coastlines. These coastlines can minimize the impact of winds for some of the directions.

5. ACKNOWLEDGMENT

6.REFERENCES

[1]   F. Geremia-Nievinski *et al.*, "SNR-based GNSS reflectometry for coastal sea-level altimetry: results from the first IAG inter-comparison campaign," *Journal of Geodesy,* vol. 94, no. 8, pp. 1-15, 2020.

[2]   M. Hoseini *et al.*, "On the Response of Polarimetric GNSS-Reflectometry to Sea Surface Roughness," *IEEE Transactions on Geoscience and Remote Sensing,* 2020.

[3]   C. Chew and E. Small, "Soil moisture sensing using spaceborne GNSS reflections: Comparison of CYGNSS reflectivity to SMAP soil moisture," *Geophysical Research Letters,* vol. 45, no. 9, pp. 4049-4057, 2018.

[4]   M. Rajabi, H. Nahavandchi, and M. Hoseini, "Evaluation of CYGNSS Observations for Flood Detection and Mapping during Sistan and Baluchestan Torrential Rain in 2020," *Water,* vol. 12, no. 7, p. 2047, 2020.

[5]   A. M. Semmling *et al.*, "Sea-Ice Concentration Derived From GNSS Reflection Measurements in Fram Strait," *IEEE Transactions on Geoscience and Remote Sensing,* vol. 57, no. 12, pp. 10350-10361, 2019.

[6]   M. Hoseini, M. Asgarimehr, V. Zavorotny, H. Nahavandchi, C. Ruf, and J. Wickert, "First evidence of mesoscale ocean eddies signature in GNSS reflectometry measurements," *Remote Sensing,* vol. 12, no. 3, p. 542, 2020.

[7]   M. Asgarimehr, V. Zavorotny, J. Wickert, and S. Reich, "Can GNSS reflectometry detect precipitation over oceans?," *Geophysical Research Letters,* vol. 45, no. 22, pp. 12,585-12,592, 2018.

[8]   G. Foti, C. Gommenginger, and M. Srokosz, "First Spaceborne GNSS-Reflectometry Observations of Hurricanes From the UK TechDemoSat-1 Mission," *Geophysical Research Letters,* vol. 44, no. 24, pp. 12,358-12,366, 2017.

[9]   K. M. Larson, J. S. Löfgren, and R. Haas, "Coastal sea level measurements using a single geodetic GPS receiver," *Advances in Space Research,* vol. 51, no. 8, pp. 1301-1310, 2013.

[10]   M. Rajabi, A. Amiri-Simkooei, H. Nahavandchi, and V. Nafisi, "Modeling and Prediction of Regular Ionospheric Variations and Deterministic Anomalies," *Remote Sensing,* vol. 12, no. 6, p. 936, 2020.

[11]   M. Hoseini, F. Alshawaf, H. Nahavandchi, G. Dick, and J. Wickert, "Towards a zero-difference approach for homogenizing gnss tropospheric products," *GPS Solutions,* vol. 24, no. 1, p. 8, 2020.

[12]   M. Rajabi, A. Amiri-Simkooei, J. Asgari, V. Nafisi, and S. Kiaei, "Analysis of TEC time series obtained from global ionospheric maps," *Journal of Geomatics Science and Technology,* vol. 4, no. 3, pp. 213-224, 2015.

Paper V

Polarimetric GNSS-R Sea Level Monitoring using I/Q Interference Patterns at Different Antenna Configurations and Carrier Frequencies

Mahmoud Rajabi, Mostafa Hoseini, Hossein Nahavandchi, Maximilian Semmling, Markus Ramatschi, Mehdi Goli, Rüdiger Haas, Jens Wickert

Abstract—Coastal sea level variation as an indicator of climate change is extremely important due to its large socio-economic and environmental impact. The ground-based Global Navigation Satellite System (GNSS) reflectometry (GNSS-R) is becoming a reliable alternative for sea surface altimetry. We investigate the impact of antenna polarization and orientation on GNSS-R altimetric performance at different carrier frequencies. A one-year dataset of ground-based observations at Onsala Space Observatory using a dedicated reflectometry receiver is used. Interferometric patterns produced by the superposition of direct and reflected signals are analyzed using the Least-Squares Harmonic Estimation (LS-HE) method to retrieve sea surface height. The results suggest that the observations from GPS L1 and L2 frequencies provide similar levels of accuracy. However, the overall performance of the height products from the GPS L1 show slightly better performance owing to more observations. The combination of L1 and L2 observations (L12) improves the accuracy up to 25% and 40% compared to the L1 and L2 heights. The impacts of antenna orientation and polarization are also evaluated. A sea-looking Left-Handed Circular Polarization (LHCP) antenna shows the best performance compared to both zenith- and sea-looking Right-Handed Circular Polarization (RHCP) antennas. The results are presented using different averaging windows ranging from 15-minute to 6-hour. Based on a 6-hour window, the yearly Root Mean Square Error (RMSE) between GNSS-R L12 sea surface heights with collocated tide gauge observations are 2.4, 3.1, and 4.1 cm with the correlation of 0.990, 0.982, and 0.969 for LHCP sea-looking, RHCP sea-looking, and RHCP up-looking antennas, respectively.

Index Terms—Global Navigation Satellite Systems-Reflectometry (GNSS-R), Coastal Sea Level Monitoring, Polarimetric GNSS-R, Altimetry, GPS, GNSS, L-Band Remote Sensing, Least-Squares Harmonic Estimation (LS-HE)

I. INTRODUCTION

S EA surface level is a key parameter in many scientific disciplines, including geology, geodesy, oceanography and archaeology which could contribute to recognizing climate and environmental variation. Modern civilization could be affected by major and minor changes in sea surface level due to global warming and natural causes such as floods, tsunami and volcanoes [1]. The information about sea surface level is also vital due to the large population, economic and commercial activities in coastal areas. In addition, sea surface level is essential to defining vertical datum (geoid) and consequently, measuring and understanding Earth's geometric shape. Therefore, it is essential to monitor sea surface level using accurate and reliable methods.

Two prevalent methods have been used for sea level monitoring, traditional tide gauges, and spaceborne radar altimeters. These methods have some limitations. The tide gauge measurements are point-wise and also affected by subsidence, tectonics and human activities [1]. Close to the coastal area, data accuracy of the radar altimeters is degraded due to the effect of the land on its large footprint, and the corrections which are applied for geophysical effects. Consequently, we do not have reliable and accurate spaceborne radar observations in the coastal area besides the limitation on the spatiotemporal resolution of this method [2].

Global Navigation Satellite Systems (GNSS) were designed primarily for providing positioning, navigation, and timing services. The GNSS signals are also being used for numerous remote sensing applications of the Earth's surface and atmosphere, in addition to its primary aim. GNSS-Reflectometry (GNSS-R) as a state-of-the-art remote sensing technique, uses reflected GNSS signals to retrieve and investigate numerous geophysical parameters and phenomena over the Earth's surface (land, ocean, and ice). GNSS-R is a multi-static radar technique in the L-band range of the electromagnetic signals, which works in all weather conditions, day and night, and is ideal for measuring or detecting many variables and natural events, such as sea level [3], sea surface roughness [4], ocean eddies [5], sea ice and snow depth [6], flood [7], precipitation [8], wind speed [9] .

Ground-based GNSS-R can act as a multi-purpose sensor, which has drawn attention over the past decades. The method is an alternative option for traditional tide gauges for monitoring sea surface level in coastal areas. A GNSS-R sensor can cover a wider area of the sea surface and collect additional useful data from the reflecting surface, e.g. sea surface roughness and ice coverage. Tide-gauges measurements can be affected by local vertical displacements and require extra procedures to

M. Rajabi, M. Hoseini and H. Nahavandchi are with the Department of Civil and Environmental Engineering, Norwegian University of Science and Technology, 7491 Trondheim, Norway (e-mail: mahmoud.rajabi@ntnu.no).

M. Semmling is with the German Aerospace Center DLR, Institute for Solar-Terrestrial Physics, Neustrelitz, Germany.

M. Ramatschi is with the Department of Geodesy, German Research Center for Geosciences (GFZ), 14473 Potsdam, Germany.

M. Goli is with Faculty of Civil and Architectural Engineering, Shahrood University of Technology, Iran.

R. Haas is with the Department of Space, Earth and Environment, Chalmers University of Technology, Gothenburg, Sweden

J. Wickert is with the Department of Geodesy, German Research Centre for Geosciences (GFZ), 14473 Potsdam, Germany, and also with the Institute of Geodesy and Geoinformation Science, Technische Universität Berlin, Germany

connect the measured relative sea level to the global reference frame. In contrast, coastal GNSS-R stations can monitor and correct the local vertical displacements and provide sea level measurements in the global reference frame. The concept of sea surface level monitoring using GNSS-R was conceived in 1993 [3] and applied for ground-based GNSS-R stations signals in 2000 [10]. Afterward, the performance and reliability of the method have been studied in several cases, e.g. [11, 12, 13, 14, 15, 16, 17].

Most of the ground-based GNSS-R altimetry experiments have used an up-looking geodetic antenna and ordinary surveying receiver based on the Signal to Noise Ratio (SNR) observations of the Global Positioning System (GPS). In addition, various configurations have been considered in different studies in terms of antenna orientation, polarization, and receiver type. For example, Santamaria-Gomez and Watson [18] used three weeks of SNR data in Spring Bay, Australia, from a side-looking GNSS Right-Handed Circular Polarization (RHCP) antenna to improve the SNR altimetry performance compared to a zenith-looking antenna. Padokhin et al. [19] used a four-day dataset obtained from a side-looking and a zenith-looking geodetic antenna to investigate the influence of the antenna layout and the impact of wind waves on GNSS-R altimetry. Alonso-Arroyo et al. [20] utilized three-month data based on a tilted antenna to see how the reflected GNSS signals were affected by coastal sea state. Rodriguez-Alvarez et al. [21] and Hongguang et al. [22] also used a single side-looking antenna for sea level altimetry.

A few studies have utilized dedicated reflectometry receivers with tilted antennas. For example, Semmling et al. [23] use an Occultation, Reflectometry, and Scatterometry (GORS) receiver. Liu et al. [24] reports a monthly RMSE of 4.37 cm with respect to tide gauge observations using GPS L1 and a tilted Left-Handed Circular Polarization (LHCP) antenna [24]. The latter study uses phase observations during coherent reflection events which limits the measurements to the reflection at low elevation angles or during lower sea states. Fran Fabra et al. [25] used coherent differential phase between direct and both LHCP and RHCP reflected signals for the retrieval of absolute ellipsoidal heights over sea ice. Lifeng Bao et al. [26] to improve precision and spatial resolution of GNSS-R altimetry used one up-looking geodetic GNSS receiver, one downward LHCP antenna, and an atomic clock.

This study aims to give an inter-comparison overview of GNSS-R altimetry observations recorded using different antenna designs and carrier frequencies. Compared to the typical geodetic installations, the tilted antenna orientation coupled with different polarizations strengthens the power of captured interferometric patterns. This can prolong the detectability of these patterns at higher elevation angles. A multivariate spectral analysis method is used here to take the advantage of available concurrent observations. Moreover, the quality of the observations made by each satellite Pseudo Random Noise (PRN) is assessed.

We design different scenarios for the investigation using a dedicated reflectometry receiver under similar conditions, i.e. the same processing method, antenna model, location and weather conditions. The variable parameters in the scenarios are antenna polarizations and orientations, as well as carrier frequency of the signal. The analysis includes the impact of different wind speeds and averaging windows. A relatively long-term dataset from a coastal GNSS-R station with special design and unique features, which is established by the German research center for geosciences (GFZ) is used. The Least-Squares Harmonic Estimation (LS-HE) method is used for spectral analysis and finding the frequency of interferometric signals. The interferometric or compound signal is generated as a result of interference of direct and reflected signals. The frequency observations of the interferometric signals are used to calculate sea surface height. The LS-HE method has the capacity of multivariate formulation and is not limited to integer frequencies and evenly spaced data [27]. The rest of this paper is organized as follows. The study area and dataset are presented in Section 2. The methodology and mathematical concepts are described in Section 3. The discussion of data processing and the results are explained in Section 4. Finally, the paper is finalized by a conclusion in Section 5.

II. DATA AND SITE

We use a one-year dataset from January to December 2016 obtained from a dedicated GNSS-R site installed and operated by GFZ. This is one of the two GNSS-R stations at Onsala Space Observatory in Sweden ($57.393°N$, $11.914°E$). The observations with elevation angles between 5 and 40 degrees are selected for the investigation. Besides the GNSS-R observations, we use two ancillary datasets including the wind and sea level measurements from a close by meteorological station and a traditional tide gauge. Both are operated by the Onsala Space Observatory and located at about 300 m distance from the GNSS-R station. Figure 1 shows the study area, reflection points for different PRNs, and a picture of the station antennas and their orientations. A schematic view of the experiment setup and an example of the receiver outputs for satellite PRN 3 during a reflection event is shown in Figure 2.

The station antennas are installed on a concrete foundation with an approximate height of 3 meters from the sea surface. Three types of antennas are installed at the station, one is up-looking and the two others are sea-looking. The up-looking antenna is RHCP and assigns higher gain values to direct GPS signals for acquisition and tracking purposes. The sea-looking antennas with RHCP and LHCP designs are considered for tracking sea reflected GPS signals at two different polarizations. The tilt angle between the up-looking and sea-looking antennas is $98°$. Usage of a single side-looking antenna would cause difficulty to continuously track the direct signals due to significant contributions from the reflected signals. Therefore, an upright antenna needs to be used as the master link for the tracking. It should be noted that the side-looking antennas can partially block the reception of reflections in the up-looking antenna. Therefore, the up-looking antenna used at Onsala station might not provide exactly equivalent configuration compared to a single isolated upright antenna.

A GORS receiver [28] with four antenna inputs is utilized in the experiment. The first input is dedicated to the master channel of the receiver and is connected to the up-looking
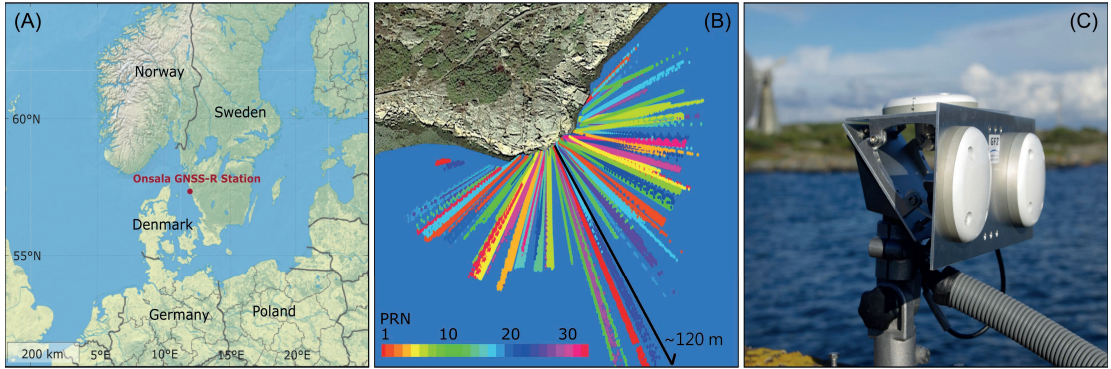
Fig. 1. (A) The red point on the map shows the Onsala GNSS-R station in the southwest of Sweden which the experiment setup is installed there. (B) The scatter plot of the reflection points over the sea surface. The colors show the GPS PRN numbers related to the reflection tracks. (C) The experiment setup and antenna orientations (up- and sea-looking).
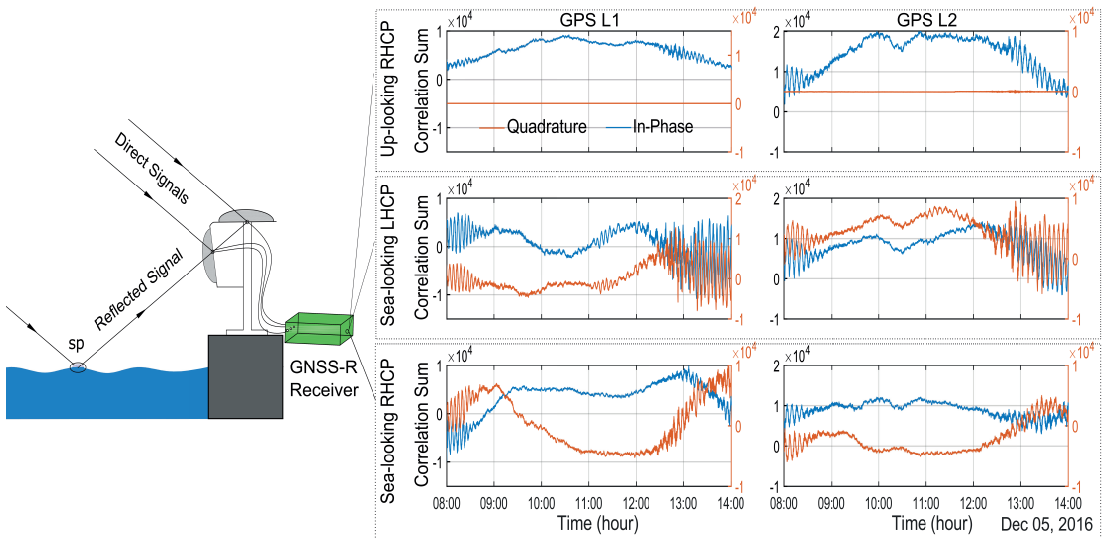
Fig. 2. A schematic view of the GNSS-R experiment setup on the left. The right graphs illustrate example time series of the in-phase and quadrature correlation sums from each antenna in GPS L1 and L2 bands. The graphs are related to a reflection event on December 5, 2016 from the GPS PRN 3. The specular point is denoted by "sp".

antenna. The second and third inputs are used for the slave channels and are connected to the sea-looking antennas.

According to [29] the signal processing flow in the dedicated reflectometry receiver can be briefly described as follows (See Figure 3 for a schematic representation of the receiver architecture). The received signal, i.e. $E_d + E_r$ in Figure 3, after digitization in the receiver can be written as:

$$s(t) = A\, D(t - \tau)\, C(t - \tau)\, cos(2\pi(f_{IF} + f_D)t + \varphi) \quad (1)$$

with $s(t)$ being the received signal, A the amplitude, D and C respectively the modulated navigation data and the PRN code,

t the time, τ the code delay, f_{IF} an intermediate frequency, f_D the Doppler frequency shift, and φ is an initial phase. The receiver generates the following models of the carrier signal at In-phase and Quadrature (I/Q) levels in the master channels:

$$
\begin{aligned}
\text{in-phase}: &\quad \cos(2\pi(f_{IF} + \tilde{f}_D)t + \tilde{\varphi}) \\
\text{quadrature}: &\quad \sin(2\pi(f_{IF} + \tilde{f}_D)t + \tilde{\varphi}) \quad (2)
\end{aligned}
$$

where $\tilde{f}_D$ and $\tilde{\varphi}$ are estimated Doppler frequency and initial phase which are produced by a closed-loop tracking process in the receiver. After multiplying the received signal by the two models and applying a low pass filter, the results are correlated
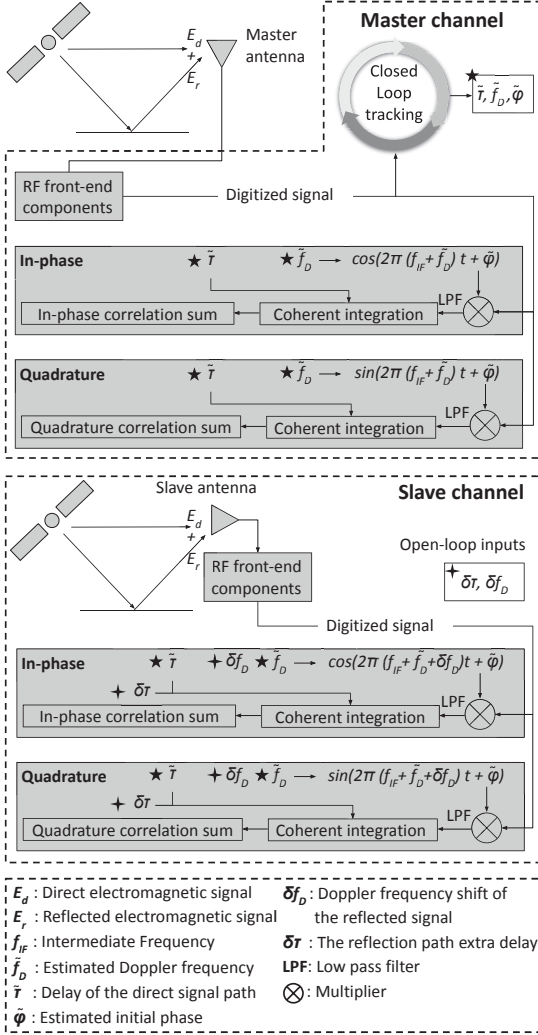
Fig. 3. A schematic diagram of the dedicated GNSS-Reflectometry receiver architecture used in this study.

with the PRN code of the satellite. The navigation data is then demodulated to yield a phasor (γ_m) as the output of the master channel [23]:

$$\gamma_m(\tilde{\tau}) = e^{-j\delta\varphi}[A_d + A_r e^{jk\delta\rho}\Lambda(\Delta\tau)] \quad (3)$$

where $\tilde{\tau}$ is the delay of direct signal which is estimated within the closed-loop tracking process, j is the imaginary unit ($j^2 = -1$), $\delta\varphi$ is the phase difference between the compound and direct signals, the amplitudes of the direct and reflected signals are A_d and A_r, respectively, and $k = 2\pi/\lambda$ is the carrier wavenumber with λ being the carrier wavelength. Figure 4 shows phasor representations of the direct, reflected, and compound signals with the reflectometry relative phase

$\psi = k\,\delta\rho$. The parameter $\Delta\tau$ denotes the time delay due to the excess path ($\delta\rho$) traveled by the reflected signal compared to the direct path. The function $\Lambda(\Delta\tau)$ is triangular auto-correlation function with the properties: $\Lambda(0) = 1$ and $\Lambda(\tau) = \Lambda(-\tau)$. Under successful operation of the phase lock-loop (Fig. 4-B), the amplitude of the signal is completely tracked in the in-phase component of the master channel, I_m [29]. Therefore, the quadrature component of the master channel, Q_m, vanishes and the signal SNR can be calculated by squaring I_m, expressed by:

$$A_c^2 = I_m^2 = A_d^2 + A_r^2 + 2A_dA_r\cos(k\delta\rho) \quad (4)$$

where A_c is the amplitude of the compound signal. The SNR value expressed in (4) is similar to the SNR observations from geodetic receivers described in [30]. The parameter $\delta\rho$ will be later used for the sea level retrieval (see section III).

For the slave channels, the receiver can be steered through an open-loop scheme using external inputs for tracking the signals intercepted by the slave antennas. The external inputs, δf_D and $\delta\tau$, are relative values with respect to the reference values $\tilde{\tau}$ and $\tilde{f}_D$. The parameter δf_D is used during carrier wipeoff and $\delta\tau$ for the code correlation in the slave channel. The slave channel output can be expressed by:

$$\gamma_s(\tilde{\tau} + \delta\tau) = e^{-j\,\delta\varphi}[A_d'\,\Lambda(\delta\tau) +$$
$$A_r'\,e^{j\,k\,\delta\rho}\,\Lambda(\delta\tau - \Delta\tau)] \quad (5)$$

where subscript s refers to the slave channels. A_d' and A_r' are respectively the amplitudes of direct and reflected signals in the slave channel. The amplitudes of direct and reflected signals are different in the master and slave channels, mainly because of the different antenna gains. Figure 4-C shows a simplified phasor representation of direct, reflected, and compound signals in the slave channel.

The low reflector height at the Onsala GNSS-R station with respect to the sea surface results in $\delta f_D \approx 0$ and $\delta\tau \approx \Delta\tau \approx 0$. Therefore, the receiver outputs for the slave channels at I/Q levels can be simplified to:

$$\gamma_s = A_c'\,e^{j\Delta\varphi} = I_s + jQ_s$$
$$= e^{-j\delta\varphi}[A_d' + A_r'\,e^{j\,k\,\delta\rho}] \quad (6)$$

where $\Delta\varphi$ is the slave-master phase difference and A_c' is the amplitude of the compound signal in the slave channel. The I/Q components of the slave channel output can be written as:

$$I_s = A_d'\cos(\delta\varphi) + A_r'\cos(k\,\delta\rho - \delta\varphi)$$
$$Q_s = -A_d'\sin(\delta\varphi) + A_r'\sin(k\,\delta\rho - \delta\varphi) \quad (7)$$

The first terms of (7) are related to the contribution of the direct signal while the second terms comprise the effect of the reflected signal:

$$I_s = I_d + I_r$$
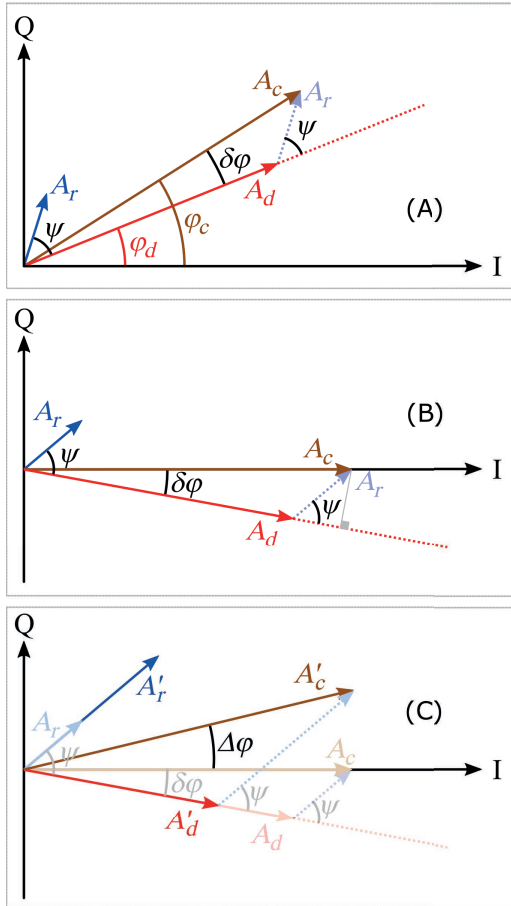$$Q_s = Q_d + Q_r \quad (8)$$

Fig. 4. The phasor diagrams of direct, reflected, and compound signals respectively denoted by subscript d, r, and c in the in-phase/quadrature (I/Q) axes: (A) before and (B) after tracking the phase of the compound signal in the master channel. The phasor diagram shown in (C) is related to the slave channel. The angle ψ is the reflectometry-relevant phase, $\delta\varphi$ is the phase difference between the compound and direct signals, and $\Delta\varphi$ is the phase of the compound signal in the slave channel. The phase shifts due to baseline between the master and slave antennas and different carrier phase wind-up effects for the up-looking and side-looking antennas are not included in the figure.

The direct signal terms, i.e. I_d and Q_d, can be extracted e.g. by fitting a low-order polynomial. The amplitude and frequency of the interferometric patterns in the reflected signal terms, i.e. I_r and Q_r, can be determined through different spectral analysis or modeling methods. The LS-HE method, which is further described in the next section, can simultaneously model the direct signal effects and retrieve period of the interferometric oscillations from the I/Q samples. The amplitude of the direct,

reflected, and compound signals in the slave channels can be respectively calculated by:

$$
\begin{aligned}
A_d'^{\,2} &= I_d^2 + Q_d^2 \\
A_r'^{\,2} &= I_r^2 + Q_r^2 \\
A_c'^{\,2} &= I_s^2 + Q_s^2 \\
&= A_d'^{\,2} + A_r'^{\,2} + 2A_d' A_r' \cos(k\delta\rho + \phi_0) \quad (9)
\end{aligned}
$$

where ϕ_0 is an initial phase shift. The original output of the GORS receiver is based on 5-millisecond coherent integration, i.e. 200 Hz sampling rate. In this study, the 200 Hz correlation sums are down-sampled using a 10-second (0.1 Hz) integration at I/Q levels for each of the antennas.

In general, having access to the I/Q outputs gives the opportunity of looking at the signal in a 3D sense and retrieving the phase of interferometric signal and the coherence state [24]. In this study, we directly utilize the I/Q outputs. Both of the components encompass the oscillating interferometric patterns regardless of the coherency of the reflection. This feature in both of the I/Q components is used here to detect the corresponding Doppler residual in a multivariate approach as described below.

III. METHOD

The methodology of this study contains three main stages (Fig. 5). The first stage is the data preparation through which the time series associated with each reflection event are created. In the second stage, we focus on finding the interferometric frequency using multivariate LS-HE in different scenarios. The frequency (L1/L2) and polarization (RHCP/LHCP) of the reflected signals as well as the orientation of the antenna (up-/sea-looking) are variable factors in these scenarios.

Four main scenarios for the estimation of the sea surface heights are designed as follow, each one using L1 and L2 separately: (A) using the I components of the up-looking RHCP antenna (one time series), (B) using the I/Q components of the sea-looking RHCP antenna (two time series), (C) using the I/Q components of the sea-looking LHCP antenna (two time series), (D) using the I/Q components of the both sea-looking antennas (four time series). In addition, the sea surface heights are estimated by combining the retrieved heights from L1 and L2 for each main scenario for possible improvement. Consequently, the sea surface heights are retrieved in 12 different solutions. These products make it possible for us to assess the performance of polarimetric GNSS-R in different antenna's angle plus the performance of L1, L2, and combination of them (L12). The parameter of interest in the LS-HE analysis is the period of the interferometric signals.

The time series of the reflection events are divided into smaller segments by considering a time window. The time window for retrieving this periodic pattern is set to a minimum of 15 min but it is flexibly extended to 30 min until it includes at least two interferometric periods. It is worth mentioning that higher antenna height with respect to the sea surface could have reduce this window size resulting in a better temporal
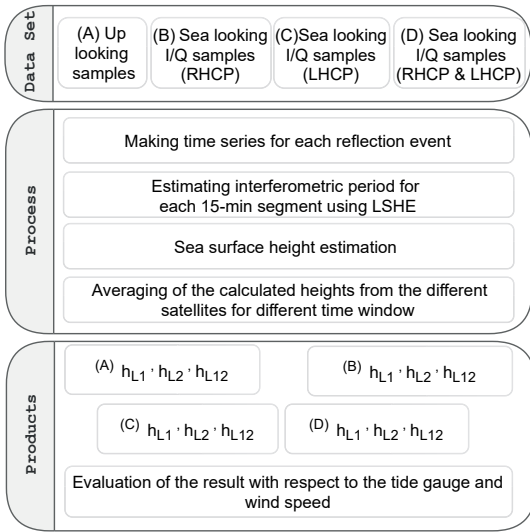
publication. Citation information: DOI 10.1109/TGRS.2021.3123146, IEEE

6

Fig. 5. Methodology flowchart based on the Least Squares Harmonic Estimation (LS-HE).

Fig. 6. Schematic geometry of the ground-based GNSS-R altimetry based on the path difference between the direct and reflected satellite signals. ρ_{sat-sp} is the distance between the satellite and specular point, $\rho_{sat-rec}$ is the distance between the satellite and receiver antenna, ρ_{sp-rec} is the distance between the specular point and receiver antenna, e is the satellite elevation angle, $\delta\rho$ is the extra path of the reflected signal compared to the direct signal, and h is the height difference between the phase center of the antenna and sea surface.

resolution. We move the overlapping window and analyze the segment with a time step of 1-min to cover the whole time series. The sea surface height is estimated from each segment.

To combine the estimated heights from different satellites we use an averaging window. For outlier detection, we use a native MATLAB function that utilizes the median absolute deviation (MAD) values. All the values beyond three scaled MAD with respect to the median are considered as outliers. After outlier elimination, the median value of the estimates within the averaging window is considered as the final height estimate. The final estimates are calculated every 5 minutes with different averaging windows ranging from 15 minutes to 6 hours (6-hours, 3-hours, 1-hours, and 15 minutes). The last stage of the methodology is the validation of the GNSS-R height estimates with the collocated tide gauge observations at different wind speeds.

A. Least-Squares Harmonic Estimation (LS-HE)

The LS-HE is one of the frequency analysis methods from the generation of the Fourier spectral analysis. The method is restricted to neither integer frequencies nor evenly-spaced time series and can be applied to datasets with gaps. The LS-HE method can efficiently include a linear trend as a deterministic part of the model and the covariance matrix as the stochastic part of the model [31]. One important feature of the method compared to the least squares spectral analyses described by earlier studies e.g. [32, 33, 34] is the multivariate formulation to identify common-mode signals of multiple time series. This feature has been utilized in scenarios B, C, and D to enhance retrieval of the common interferometric signal. For scenario A which includes only one time series, the analysis becomes univariate. The LS-HE method was presented and

utilized by [27] for the GPS position time series, then applied by [35] for the estimation of GNSS-R lake ice thickness and here is introduced for GNSS-R altimetry. For more information about the theory of LS-HE, we may refer to [36, 27, 31].

B. Sea surface height calculation

The superposition of direct and reflected signals constructs compound signals. The concept of calculating the sea surface height from the GNSS-R observations is based on the retrieval of the interferometric patterns in the compound signal. The LS-HE method used in this study includes individual linear terms for each of the I/Q components of the master or slave samples. These linear terms can absorb the effect of direct signal variations (see (7)). Therefore, the effect of direct signal and interferometric oscillations can be effectively separated within the LS-HE analysis. The estimated interferometric period by LS-HE can then be related to the geometry of the reflection as described below.

The difference between the direct and reflected signals paths creates a Doppler shift which is in fact the frequency of the interferometric fringes [28]:

$$\delta f = \frac{1}{\lambda}\frac{d(\delta\rho)}{dt} \tag{10}$$
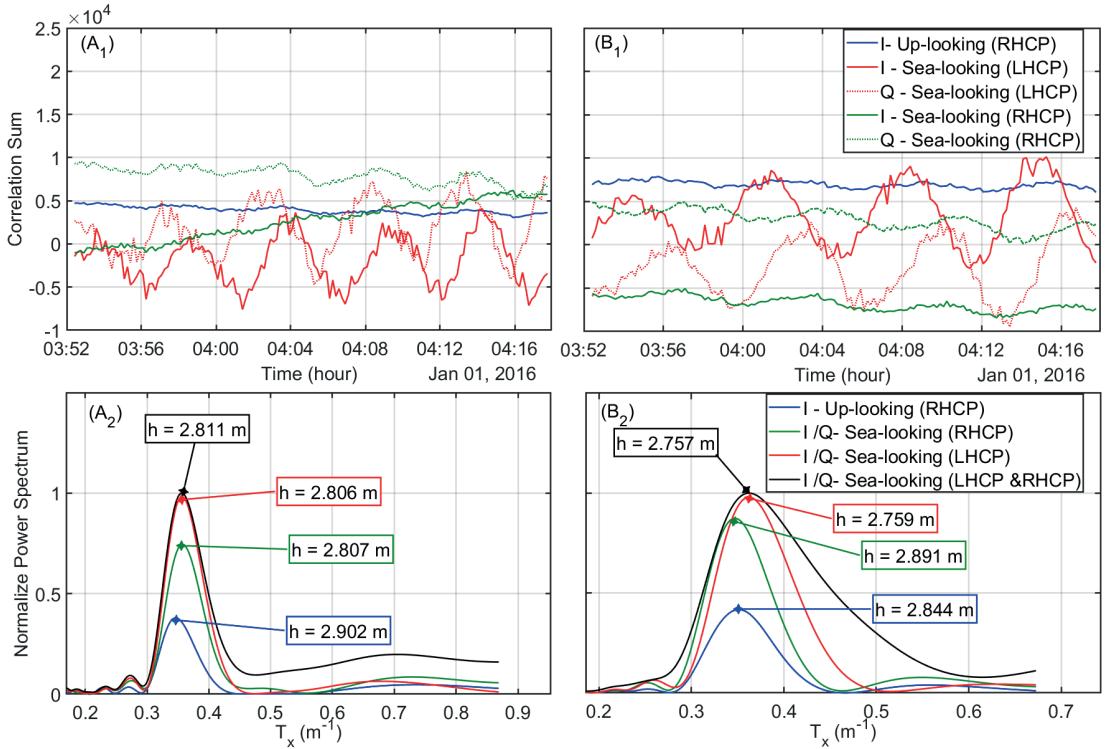$$\delta\rho = \rho_{ref} - \rho_{dir}, \tag{11}$$

Fig. 7. Examples of observation time series of PRN 26 for one segment which are used to retrieve interferometric period (T_{int}) using multivariate LS-HE formulation. (A_1) and (B_1) show the In-phase and Quadrature components for GPS L1 and L2, respectively. (A_2) and (B_2) illustrate the dominant interferometric period retrieved by LS-HE based on different combinations of the time series.

where ρ_{dir} and ρ_{ref} are the distance between the satellite and the antenna for direct and reflected signals, respectively, δf is the Doppler shift, and λ is the wavelength of the signal carrier. As shown in Figure 6, $\delta \rho$ can be estimated by:

$$\delta \rho = 2\,h\,sin(e) \qquad (12)$$

where e is the satellite elevation angle, h is the height difference between the phase center of the antennas and sea surface. Let us introduce the variable $x = 2\sin(e)/\lambda$. The interferometric frequency with respect to x denoted by δf_x can be retrieved by:

$$\delta \rho = \lambda\,h\,x$$
$$\delta f_x = \frac{1}{\lambda}\frac{d(\delta\rho)}{dx} = h + x\frac{dh}{dx} = h + x\,\dot{h}\frac{dt}{dx} \qquad (13)$$

with $\dot{h} = dh/dt$ being the height rate. To account for the height rate in the height retrieval process, we first calculate a sea level estimate using the detected interferometric period (T_{int}) in the LS-HE analysis:

$$P(T_x) = LSHE(x, Y)$$

$$\{P_{max}, T_{int}\} = max[P(T_x)]$$
$$h \approx \delta f_x = \frac{1}{T_{int}} \qquad (14)$$

where $P(T_x)$ is the power spectrum, Y is the matrix of observations, P_{max} is the detected maximum power using the max function. The columns of Y for each scenario include the following time series:

Solution A: $\quad Y = [I_m^2]$

Solution B: $\quad Y = [I_s^R, Q_s^R]$

Solution C: $\quad Y = [I_s^L, Q_s^L]$

Solution D: $\quad Y = [I_s^R, Q_s^R, I_s^L, Q_s^L] \qquad (15)$

with superscript R and L denoting the RHCP and LHCP sea-looking antennas. Having the sea level estimate h from the LS-HE analysis and $\dot{h} = 0$ as the initial value, we find final values of h and $\dot{h}$ through iterative minimization of the following cost function:

$$\min_{h,\dot{h}} \sum_{i}^{N} \|\hat{Y}_i - a_i \sin(\frac{4\pi[h + \delta h]\sin(e)}{\lambda} + \phi_i)\| \qquad (16)$$

$$\delta h = \frac{\dot{h}\tan(e)}{\dot{e}} \qquad (17)$$

where δh is a correction term to compensate the height rate effect, $\dot{e}$ is the elevation angle rate, $\hat{Y}_i$ is the i-th observation time series after removing the linear trend, N is the number of observations processed by LS-HE which is 1 in scenario A, 2 in scenarios B and C, and 4 in scenario D, a_i and ϕ_i are the amplitude and phase offset of the interferometric signal in the i-th observation time series that are estimated by least squares analysis.

It should be noted that the side-looking outputs might be contaminated by small phase differences. Two possible causes can be antenna phase center variations [24] and the offset vectors between the master and slave antennas shown in Fig. 6. These effects can introduce low-frequency components to the I/Q outputs. However, at this station these components have much lower frequency compared to the prominent interferometric fringes [37] and would not significantly affect our sea level measurements.

IV. RESULTS AND DISCUSSION

A. Data preparation

The data preparation starts with selecting valid observations which include reflected signals from the sea surface. For this purpose, the precise location of the specular points is estimated within a ray tracing algorithm described by [38] which considers earth surface curvature. A spatial mask using a polygon is then created and applied to the observations to keep the specular points on the sea surface and filter out the reflections from land. To decrease atmospheric effect observations with elevation angles below 5 degrees are excluded. The remaining atmospheric effect is neglected due to the low reflector height. The receiver position is calculated by precise analysis of the direct signals using broadcast ephemerides for the satellite position. The Earth Gravitational Model (EGM96) is used as a reference height. For more information we may refer to [23]. Figure 1-B illustrates the sea-reflected specular points for different GPS satellites used in this study.

B. Applying the LS-HE

For utilizing the LS-HE method, we use a numerical search to catch the dominant interferometric signals in each segment. The step size for searching the interferometric periods is small for the lower periods and gets larger at higher periods using the following recursive formula:

$$T_i = T_{i-1}(1 + \alpha \frac{T_{i-1}}{T_{max}}) , \ \alpha = 0.01 , \ i = 1, 2, ..., T_i \le T_{max},$$
$$(18)$$

where T_i are the trial periods, T_0 and T_{max} are the minimum and maximum detectable periods in the time window of the segments based on the Nyquist's theorem and the α coefficient allows us to make the initial step bigger and smaller for frequency searching. We assume the covariance matrix is the Identity matrix $Q_y = I$ for each time series.

Figure 7 shows an example outcome of the LS-HE on the time series which is generated from a segment of one

event for satellite PRN 26 in L1 and L2 bands. Figure 7-A_1 and B_1 show the I and Q components from each antenna and frequency. Figure 7-A_2 and B_2 depict the results of frequency analysis based on the four scenarios for L1 and L2. As can be recognized from the frequency analysis results in the figure, the highest power of the interferometric period belongs to multivariate analysis of time series of both sea-looking antennas. Slightly lower power can be seen for the time series of the LHCP sea-looking antenna.

C. GNSS-R height retrieval and evaluation

The RMSE values of GNSS-R height estimates from the time series of 31 GPS satellites based on different antenna configurations are summarized in Fig. 8. The heights are estimated using the median of each PRN's observations over a 6-hour window and are compared to tide gauge measurements. The RMSE values shown in this figure are related to individual performance assessments of each satellite. The analysis shows that changing the orientation of the antenna towards the reflecting surface can improve Accuracy. This can be recognized by relatively smaller errors in the estimated heights from the sea-looking RHCP antenna (Fig. 8-A) compared to the up-looking RHCP antenna (Fig. 8-B). The sea-looking LHCP antenna (Fig. 8-C), however, shows a better accuracy compared to the sea-looking RHCP antenna. The fully polarimetric solution, i.e. by the combination of the LHCP and RHCP sea-looking antennas, exhibits the best performance with more consistency between the L1 and L2 measurements and over all the PRNs. Discrepancies in the performance of different PRNs shown in Fig. 8 might be related to various factors including the performance of the antennas in different azimuth angles in terms of phase center variations and antenna gain, as well as satellites Equivalent Isotropically Radiated Power (EIRP) variations. In the next step, we retrieve the final sea level products by combining the observations from all the satellites.

The polarization of the antenna can also affect the GNSS-R height estimation. This can originate from the strength of the reflected signals in different polarizations. The direct GNSS signals with RHCP design will have both RHCP and LHCP components after reflection. The strength of these components can be calculated from Fresnel equations and are functions of the elevation angle of satellites and permittivity of the reflecting surface. The power loss due to reflectivity of seawater at Onsala station [37] suggests that the RHCP component is the dominant component at very low elevation angles. The strengths of the RHCP and LHCP components are almost the same at the elevation angle of about 7 degrees. For higher elevation angles the LHCP component is the predominant part of the signal. Therefore, the LHCP antenna can capture stronger reflections at higher elevation angles. This provides improved performance for retrieving interferometric periods from the LHCP time series (Fig. 8-C). The combination of retrievals from the RHCP and LHCP antennas provide the best performance as can be seen from Fig. 8-D.

Figure 9 presents estimated sea surface height anomalies, using the described method based on the scenarios A, B, C, D. The anomalies are the sea surface heights minus their mean
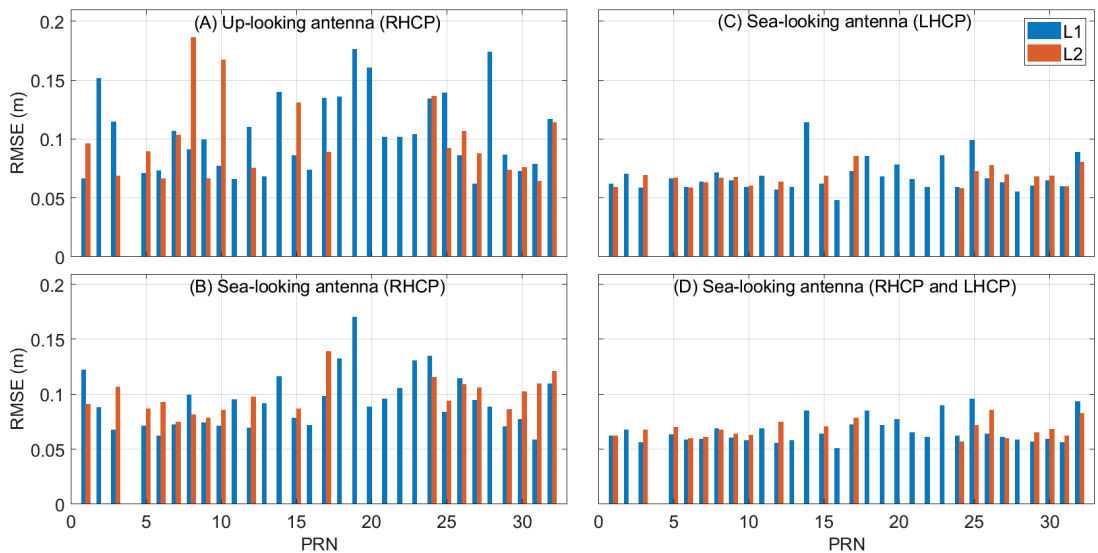
Fig. 8. The Root Mean Squared Error (RMSE) values based on the comparison of GNSS-R sea surface heights with the tide gauge measurements for each GPS Pseudo Random Noise (PRN) numbers from A) up-looking antenna with Right-Handed Circular Polarization (RHCP), B) sea-looking RHCP antenna, C) sea-looking Left-Handed Circular Polarization (LHCP) antenna, and D) combined sea-looking RHCP and LHCP antennas. The red bars are RMSE values of the L2 retrieved heights and the blue bars belong to the L1 retrieved heights. The empty L2 bars are related to the GPS IIR satellites block which do not transmit the L2C signal. The time step and the averaging window for calculating the heights are 5-min and 6-h.

value calculated separately for each solution. The collocated tide gauge measurements are overlaid for comparison. The left panels show the results for the whole dataset (one year) and the right panels illustrate a closer look over a time span of 2 days. As shown in the figure, in all of the four scenarios, the height estimates from the combination of L1 and L2 observations (L12), closely follow the tide gauge measurements. The height retrievals from the L1 observations show almost similar performance compared to L12, although the L1 results from both of the sea-looking antennas show noticeable improvements with respect to the up-looking antenna. The quality of the height measurements from the L2 observations are slightly degraded compared to the L1 and L12 measurements, especially for the RHCP antennas. Considering the fact that not all GPS satellites transmit L2C signal, the lower quality of L2 observations in RHCP antennas can adversely impact the final height retrievals.

We evaluate the final height results using the RMSE values of the GNSS-R measurements with respect to the collocated tide gauge. The correlation values of the GNSS-R and tide gauge measurements are also calculated. Table I shows the RMSE and correlation values based on the described scenarios and four different time windows. The height estimates from the combination of the L1 and L2 observations (L12) provide the best accuracy and robustness. The L12 solution can improve the results up to 25% and 40% compared to the L1 and L2, respectively. The results from L1 observations provide the

closest accuracy with respect to the L12 results. Figure 10 is a visualization of Table I . As seen in the table and figure the best accuracy is achieved with the 6-hour window in the mode of L12 using either LHCP antenna or the combination of the two sea-looking antennas. The results for the combination of the sea-looking antennas in L12 mode is 2.3, 3.0, 4.5, and 5.6 cm for the window size of 6, 3, 1 hour, and 15 minutes.

The overall improvement of the RHCP sea-looking antenna compared to the RHCP up-looking antenna in L2 observations is smaller compared to the L1 results. Despite the fact that the combination of sea-looking RHCP and LHCP antennas for each GPS PRN improves the corresponding accuracy (Fig. 8), the final sea level products from the sea-looking LHCP antenna (Fig. 10-C) shows almost the same performance compared to the combined solution (Fig. 10-D). The earlier inter-comparison study conducted by [16] at another GNSS-R station at Onsala has reported to have an RMSE range of 2.6 to 8.1 cm based on four different SNR-based methods and the window size of 6 to 8 hours. Compared to our study,¨the second GNSS-R station uses a geodetic receiver and an up-looking antenna with approximate height of 4 meters from the sea surface.

Wind speed is one of the parameters which affects the accuracy of the sea surface altimetry due to the change of the sea surface roughness. To assess the impact of wind on the accuracy of the estimated sea surface heights, the data are divided based on the Beaufort wind force scale, which
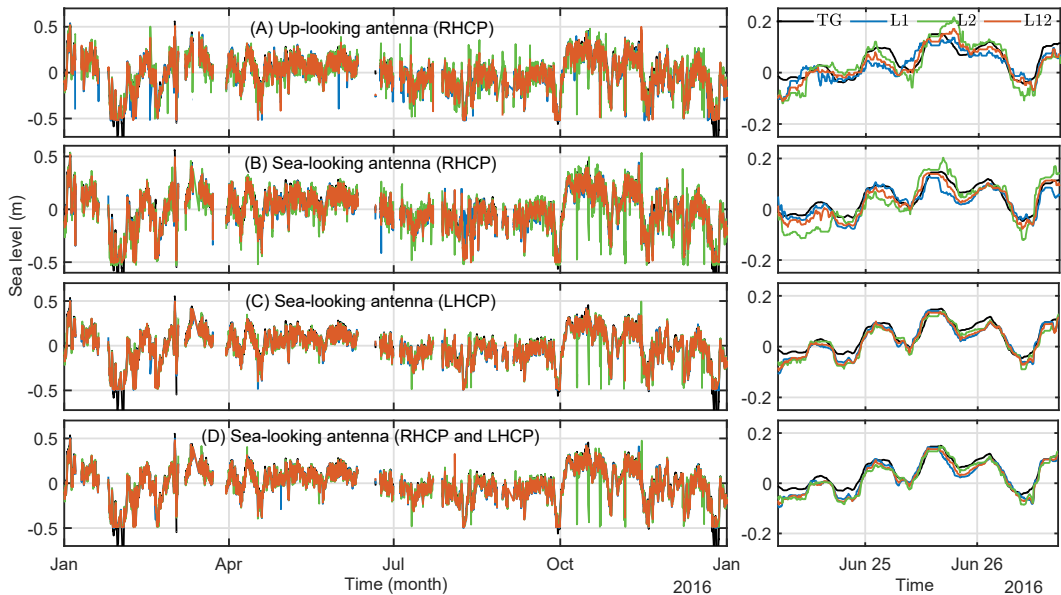
Fig. 9. Time series of sea surface height anomalies derived from GNSS-R observations at Onsala station for the year 2016 (left panels), and closer looks over a period of 2 days (right panels), overlaid on the collocated tide gauge measurements. The height measurements are estimated based on the GNSS-R observations from (A) the up-looking RHCP antenna, (B) the sea-looking RHCP antenna, (C) the sea-looking LHCP antenna, and (D) both sea-looking antennas. The black graph shows the tide gauge measurements, the blue, green, and red colors are the GNSS-R height estimates from the L1, L2, and combined L1 and L2 (L12) sea surface heights. The time step and the averaging window for calculating the heights are 5-min and 6-h.

is an empirical scale related to wind speed and observed conditions at sea or land. The right panels of Fig. 11 show the yearly RMSE values of the retrieved sea surface heights compared with tide gauge in different Beaufort wind force scale for solution C and D. The heights are estimated in 5-min time step and 6-h averaging window. As seen in the figure with the increase of the wind speed the accuracy degrades. This effect is more pronounced in the products related to L2 signals. Overall, the fully-polarimetric solution (D) shows slightly better performance compared to solution C. The left and middle panels of the figure also present the scatter plots of the GNSS-R sea surface height changes compared to the tide gauge sea level variations. As seen in the figure the distribution of the data in L1 and L12 height measurements are better than L2. The L2 sea level results are more sensitive to possible low-quality measurements due to fewer observations from the satellites transmitting L2C signal compared to L1. Generally, the results show excellent agreement with the tide gauge measurements in terms of the correlation and distribution. The solid red and dashed black lines respectively show the fitted linear line and 1:1 ideal correlation. The best agreement is related to L12 retrieved heights.

V. SUMMARY AND CONCLUSION

The study presents the results of sea level measurements using the reflected signals of the Global Navigation Satellite Systems (GNSS) from a coastal experiment at the Onsala Space Observatory in Sweden. The GNSS-Reflectometry (GNSS-R) experiment is equipped with three antennas with different polarizations and orientations. The measurements are calculated based on the application of the Least-Squares Harmonic Estimation method to a dataset of one year over 2016. Based on the flexible configuration of the experiment setup, the effects of polarization, antenna orientation, and the frequency of the GNSS signals are investigated and discussed. The dataset is accompanied by two collocated datasets from the nearest meteorological and tide gauge stations.

Our analysis shows that the best performance can be achieved by a combination of observations from L1 and L2 frequencies (L12) recorded by a sea-looking Left-Handed Circular Polarization (LHCP) antenna. Turning the antenna orientation towards the sea, i.e. a tilt angle of about 90 degrees with respect to the zenith, maximizes the gain of the antenna for capturing the reflections and thus stronger interferometric patterns. The seaward orientation can improve the accuracy of RHCP sea level results up to 20%, 13%, and 25% respectively for L1, L2, and L12. This improvement can reach about 48%, 50% and 47% for L1, L2, and L12 if the tilted antenna

TABLE I: The yearly Root Mean Squared Error (R) and the correlation (C) values of GNSS-R sea surface heights with tide gauge measurements based on four averaging windows, two antenna orientations (up-looking and sea-looking), and two polarizations, i.e. Right- and Left-Handed Circular Polarization (RHCP and LHCP). Subscript A, B, C, and D indicate the results from the up-looking RHCP antenna, sea-looking RHCP antenna, sea-looking LHCP antenna, and combination of both sea-looking antennas, respectively. $L1$, $L2$, and $L12$ respectively represent the sea level results of $L1$, $L2$, and combination of $L1$ and $L2$ height measurements (in the averaging step).

Win = 6 h	L1	L2	L12
R_A (cm)	4.6	5.7	4.1
C_A	0.963	0.943	0.969
R_B (cm)	4.2	5.7	3.1
C_B	0.968	0.948	0.982
R_C (cm)	2.4	3.6	2.4
C_C	0.990	0.977	0.990
R_D (cm)	2.4	3.8	2.3
C_D	0.990	0.973	0.990
Win = 3 h			
R_A (cm)	6.1	7.8	5.7
C_A	0.940	0.901	0.946
R_B (cm)	5.3	7.1	4.4
C_B	0.951	0.923	0.967
R_C (cm)	3.2	4.0	3.0
C_C	0.982	0.972	0.984
R_D (cm)	3.1	4.2	3.0
C_D	0.983	0.970	0.984
Win = 1 h			
R_A (cm)	8.6	10.4	8.14
C_A	0.893	0.847	0.901
R_B (cm)	7.4	9.1	6.6
C_B	0.912	0.884	0.930
R_C (cm)	4.7	5.3	4.5
C_C	0.964	0.954	0.967
R_D (cm)	4.6	5.4	4.5
C_D	0.965	0.952	0.967
Win = 15 min			
R_A (cm)	11.7	12.1	10.3
C_A	0.827	0.811	0.854
R_B (cm)	9.3	10.9	8.7
C_B	0.870	0.846	0.886
R_C (cm)	5.8	6.4	5.6
C_C	0.946	0.935	0.949
R_D (cm)	5.6	6.3	5.6
C_D	0.948	0.837	0.949
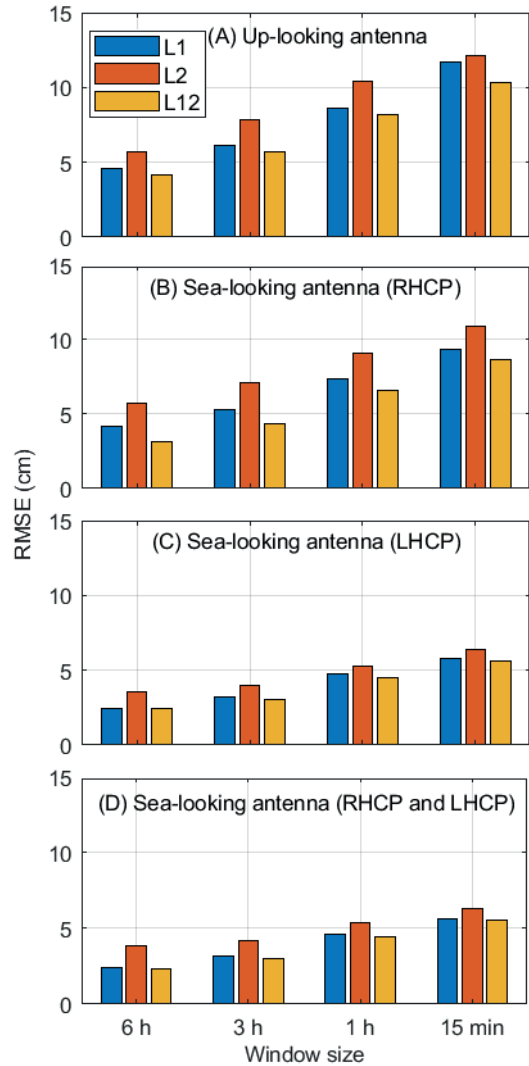
Fig. 10. The annual RMSE values of the GNSS-R sea surface height with respect to the tide gauge measurements for up-looking and sea-looking antennas in four types of window size to average sea surface heights.

is LHCP. The accuracy supremacy of LHCP measurements compared to the RHCP measurements can be attributed to the stronger reflections from the seawater at LHCP. Except for very low elevation angles, the LHCP component of the reflected signals is the dominant part. Therefore, while the RHCP antenna is an appropriate option for grazing angles

Fig. 11. The left and middle panels illustrate the scatter plots of the GNSS-R height anomalies and tide gauge height anomalies with respect to the wind speed. The graphs are related to the solutions C and D for L1, L2, and the combination of them (L12). The time step and the averaging window for calculating the heights are 5-min and 6-h. The fitted line and 1:1 ideal co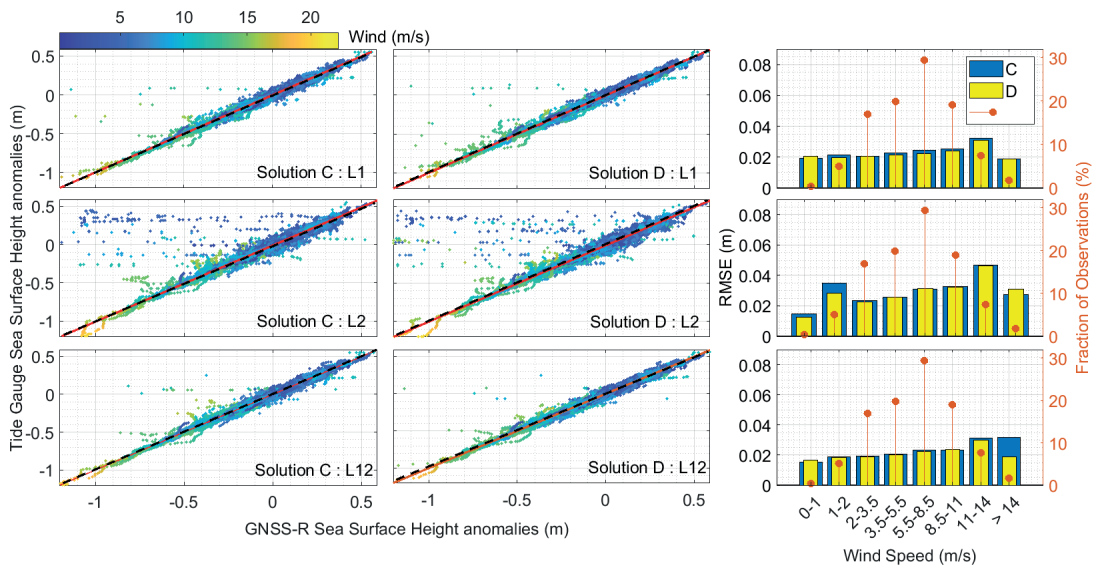rrelation are shown by the solid red line and dashed black line, respectively. The right panels show the RMSE values between the obtained GNSS-R heights and tide gauge measurements overlaid by the fraction of the data in red bars.

altimetry, using a LHCP antenna would be inevitable for higher elevation angles.

The effects of using L1 or L2 carrier frequencies are also investigated. The results from L2 frequency generally show a lower degree of accuracy most likely because of fewer observations (as not all satellites transmit L2C). We combined the L2 sea level products with the L1 products to form L12 measurements for robustness and enhancement. The size of the averaging window also is one of the parameters that affect the accuracy of final products. Longer averaging window improves the quality of the results. The Root Mean Square Error (RMSE) between GNSS-R sea surface heights for LHCP sea-looking antenna with respect to collocated tide gauge measurements are 2.4, 3.0, 4.5, and 5.6 cm for 6, 3, 1, and 0.25-hour window size, respectively.

The investigation of wind effect on the accuracy of GNSS-R sea level measurements reports a lower degree of accuracy during higher wind speeds. The RMSE value of the products can be two times larger in wind speeds above 11 m/s compared to calm sea surface during wind speeds below 2 m/s. However, the final L12 sea level estimates show a remarkable tolerance against high wind speeds, especially for the combined fully-polarimetric solution. The multivariate formulation of the method used in this study shows to be a promising tool for multi-frequency multi-constellation GNSS-R altimetry.

REFERENCES

[1] K. O. Emery and D. G. Aubrey, *Sea levels, land levels, and tide gauges*. Springer Science & Business Media, 2012, ISBN: 978-1-4613-9101-2.

[2] M. Fernandes, L. Bastos, and M. Antunes, "Coastal satellite altimetry–methods for data recovery and validation," in *3rd meeting of the international gravity and geoid commission "Gravity and Geoid*. Citeseer, 2002, pp. 26–30.

[3] Martin-Neira, "A passive reflectometry and interferometry system (PARIS): Application to ocean altimetry," *ESA journal*, vol. 17, no. 4, pp. 331–355, 1993.

[4] O. Germain, G. Ruffini, F. Soulat, M. Caparrini, B. Chapron, and P. Silvestrin, "The eddy experiment: Gnss-r speculometry for directional sea-roughness retrieval from low altitude aircraft," *Geophysical research letters*, vol. 31, no. 21, 2004.

[5] M. Hoseini, M. Asgarimehr, V. Zavorotny, H. Nahavandchi, C. Ruf, and J. Wickert, "First evidence of mesoscale ocean eddies signature in GNSS reflectometry measurements," *Remote Sensing*, vol. 12, no. 3, p. 542, 2020.

[6] F. Fabra, E. Cardellach, O. Nogués-Correig, S. Oliveras, S. Ribo, A. Rius, M. Belmonte-Rivas, M. Semmling, G. Macelloni, S. Pettinato *et al.*, "Monitoring sea-ice and dry snow with GNSS reflections," in *2010 IEEE international geoscience and remote sensing symposium*. IEEE, 2010, pp. 3837–3840.

[7] M. Rajabi, H. Nahavandchi, and M. Hoseini, "Evaluation of CYGNSS Observations for Flood Detection and Mapping during Sistan and Baluchestan Torrential Rain in 2020," *Water*, vol. 12, no. 7, p. 2047, 2020.

[8] M. Asgarimehr, M. Hoseini, M. Semmling, M. Ramatschi, A. Camps, H. Nahavandchi, R. Haas, and J. Wickert, "Remote Sensing of Precipitation Using Reflected GNSS Signals: Response Analysis of Polarimetric Observations," *IEEE Transactions on Geoscience and Remote Sensing*, pp. 1–12, 2021.

[9] G. Foti, C. Gommenginger, and M. Srokosz, "First Spaceborne GNSS-Reflectometry Observations of Hurricanes From the UK TechDemoSat-1 mission," *Geophysical Research Letters*, vol. 44, no. 24, pp. 12–358, 2017.

[10] K. D. Anderson, "Determination of water level and tides using interferometric observations of GPS signals,"

Journal of Atmospheric and Oceanic Technology, vol. 17, no. 8, pp. 1118–1127, 2000.

[11] F. Soulat, M. Caparrini, O. Germain, P. Lopez-Dekker, M. Taani, and G. Ruffini, "Sea state monitoring using coastal GNSS-R," *Geophysical Research Letters*, vol. 31, no. 21, 2004.

[12] J. Löfgren, R. Haas, H.-G. Scherneck, and M. Bos, "Three months of local sea level derived from reflected GNSS signals," *Radio Science*, vol. 46, no. 6, 2011.

[13] J. S. Löfgren and R. Haas, "Sea level measurements using multi-frequency GPS and GLONASS observations," *EURASIP Journal on Advances in Signal Processing*, vol. 2014, no. 1, pp. 1–13, 2014.

[14] J. Strandberg, T. Hobiger, and R. Haas, "Improving GNSS-R sea level determination through inverse modeling of SNR data," *Radio Science*, vol. 51, no. 8, pp. 1286–1296, 2016.

[15] K. M. Larson, R. D. Ray, and S. D. Williams, "A 10-year comparison of water levels measured with a geodetic GPS receiver versus a conventional tide gauge," *Journal of Atmospheric and Oceanic Technology*, vol. 34, no. 2, pp. 295–307, 2017.

[16] F. Geremia-Nievinski, T. Hobiger, R. Haas, W. Liu, J. Strandberg, S. Tabibi, S. Vey, J. Wickert, and S. Williams, "SNR-based GNSS reflectometry for coastal sea-level altimetry: results from the first IAG intercomparison campaign," *Journal of Geodesy*, vol. 94, no. 8, pp. 1–15, 2020.

[17] S. Tabibi, F. Geremia-Nievinski, O. Francis, and T. van Dam, "Tidal analysis of GNSS reflectometry applied for coastal sea level sensing in antarctica and greenland," *Remote Sensing of Environment*, vol. 248, p. 111959, 2020.

[18] A. Santamaría-Gómez and C. Watson, "Remote leveling of tide gauges using GNSS reflectometry: case study at

Spring Bay, Australia," *GPS solutions*, vol. 21, no. 2, pp. 451–459, 2017.

[19] A. Padokhin, G. Kurbatov, M. Nazarenko, and V. Smolov, "GNSS Reflectometry of the Black Sea level in the experiments at the Stationary Oceanographic Platform," *Moscow University Physics Bulletin*, vol. 73, no. 4, pp. 422–427, 2018.

[20] A. Alonso-Arroyo, A. Camps, H. Park, D. Pascual, R. Onrubia, and F. Martín, "Retrieval of significant wave height and mean sea surface level using the GNSS-R interference pattern technique: Results from a three-month field campaign," *IEEE Transactions on Geoscience and Remote Sensing*, vol. 53, no. 6, pp. 3198–3209, 2014.

[21] N. Rodriguez-Alvarez, X. Bosch-Lluis, A. Camps, I. Ramos-Perez, E. Valencia, H. Park, and M. Vall-Llossera, "Water level monitoring using the interference pattern GNSS-R technique," in *2011 IEEE International Geoscience and Remote Sensing Symposium*. IEEE, 2011, pp. 2334–2337.

[22] W. Hongguang, K. Shifeng, and Z. Qinglin, "A model for remote sensing sea level with GPS interferometric signals using RHCP antenna," in *ISAPE2012*. IEEE, 2012, pp. 624–626.

[23] A. M. Semmling, G. Beyerle, R. Stosius, G. Dick, J. Wickert, F. Fabra, E. Cardellach, S. Ribó, A. Rius, A. Helm *et al.*, "Detection of Arctic ocean tides using interferometric GNSS-R signals," *Geophysical Research Letters*, vol. 38, no. 4, 2011.

[24] W. Liu, J. Beckheinrich, M. Semmling, M. Ramatschi, S. Vey, J. Wickert, T. Hobiger, and R. Haas, "Coastal sea-level measurements based on GNSS-R phase altimetry: A case study at the Onsala Space Observatory, Sweden," *IEEE Transactions on Geoscience and Remote Sensing*, vol. 55, no. 10, pp. 5625–5636, 2017.

[25] F. Fabra, E. Cardellach, A. Rius, S. Ribó, S. Oliveras, O. Nogués-Correig, M. B. Rivas, M. Semmling, and S. D'Addio, "Phase altimetry with dual polarization GNSS-R over sea ice," *IEEE Transactions on Geoscience and Remote Sensing*, vol. 50, no. 6, pp. 2112–2121, 2011.

[26] L. Bao, N. Wang, and F. Gao, "Improvement of Data Precision and Spatial Resolution of cGNSS-R Altimetry Using Improved Device With External Atomic Clock," *IEEE Geoscience and Remote Sensing Letters*, vol. 13, no. 2, pp. 207–211, 2015.

[27] A. R. Amiri-Simkooei, C. C. Tiberius, and P. J. Teunissen, "Assessment of noise in GPS coordinate time series: methodology and results," *Journal of Geophysical Research: Solid Earth*, vol. 112, no. B7, 2007.

[28] A. M. Semmling, A. Rösel, D. V. Divine, S. Gerland, G. Stienne, S. Reboul, M. Ludwig, J. Wickert, and H. Schuh, "Sea-ice concentration derived from GNSS reflection measurements in Fram Strait," *IEEE Transactions on Geoscience and Remote Sensing*, vol. 57, no. 12, pp. 10 350–10 361, 2019.

[29] M. Semmling, "Altimetric monitoring of Disko Bay using interferometric GNSS observations on L1 and L2," Ph.D. dissertation, Deutsches GeoForschungsZentrum GFZ Potsdam, 2012.

[30] K. M. Larson, E. E. Small, E. Gutmann, A. Bilich, P. Axelrad, and J. Braun, "Using GPS multipath to measure soil moisture fluctuations: initial results," *GPS solutions*, vol. 12, no. 3, pp. 173–177, 2008.

[31] M. Rajabi, A. Amiri-Simkooei, H. Nahavandchi, and V. Nafisi, "Modeling and prediction of regular ionospheric variations and deterministic anomalies," *Remote Sensing*, vol. 12, no. 6, p. 936, 2020.

[32] P. Vaníček, "Further development and properties of the spectral analysis by least-squares," *Astrophysics and Space Science*, vol. 12, no. 1, pp. 10–33, 1971.

[33] N. R. Lomb, "Least-squares frequency analysis of un-

equally spaced data," *Astrophysics and space science*, vol. 39, no. 2, pp. 447–462, 1976.

[34] J. D. Scargle, "Studies in astronomical time series analysis. II-Statistical aspects of spectral analysis of unevenly spaced data," *The Astrophysical Journal*, vol. 263, pp. 835–853, 1982.

[35] Y. Ghiasi, C. R. Duguay, J. Murfitt, J. J. van der Sanden, A. Thompson, H. Drouin, and C. Prévost, "Application of gnss interferometric reflectometry for the estimation of lake ice thickness," *Remote Sensing*, vol. 12, no. 17, p. 2721, 2020.

[36] A. Amiri-Simkooei, "On the nature of GPS draconitic year periodic pattern in multivariate position time series," *Journal of Geophysical Research: Solid Earth*, vol. 118, no. 5, pp. 2500–2511, 2013.

[37] M. Hoseini, M. Semmling, H. Nahavandchi, E. Rennspiess, M. Ramatschi, R. Haas, J. Strandberg, and J. Wickert, "On the Response of Polarimetric GNSS-Reflectometry to Sea Surface Roughness," *IEEE Transactions on Geoscience and Remote Sensing*, 2020.

[38] A. M. Semmling, V. Leister, J. Saynisch, F. Zus, S. Heise, and J. Wickert, "A phase-altimetric simulator: Studying the sensitivity of Earth-reflected GNSS signals to ocean topography," *IEEE Transactions on Geoscience and Remote Sensing*, vol. 54, no. 11, pp. 6791–6802, 2016.

Mahmoud Rajabi graduated in Geodesy and geomatics from the University of Isfahan, Iran. He is currently PhD student at the Norwegian University of Science and Technology (NTNU). His research interests include atmospheric, ocean and land Remote Sensing using Mono- and Bi-static radar systems. His current research focuses on the monitoring of the ocean and land using both ground-based and space-borne GNSS-Reflectometry .

Markus Ramatschi received the Dipl.-rer. nat. in geophysics and the Ph.D. degree in geophysics from the Technical University of Clausthal, Clausthal-Zellerfeld, Germany, in 1992 and 1998, respectively. He is currently a Senior Scientist at the German Research Centre for Geosciences (GFZ), Potsdam, Germany. His research interests include the operation of a global GNSS sensor station network.

Mostafa Hoseini Mostafa Hoseini graduated in geodesy from the University of Tehran, Tehran, Iran. He has worked for several institutions as a GNSS Engineer in the field of positioning and navigation. Before starting his Ph.D. studies in 2018 at the Norwegian University of Science and Technology (NTNU), Trondheim, Norway, he worked on the analysis of GNSS atmospheric products at the German Research Centre for Geosciences (GFZ), Potsdam, Germany. His research interest includes GNSS-based sensors and techniques for remote sensing applications. His research interest also includes the monitoring of the ocean and Arctic using GNSS-Reflectometry onboard CubeSats. .

Mehdi Goli is an assistant professor of geodesy at the Faculty of Civil and Architectural Engineering, Shahrood University of Technology, Iran. He received his PhD degrees in geodesy from K. N. Toosi University of Technology, Iran. His research interests focus on space geodesy and geoid determination methods.

Hossein Nahavandchi received the Ph.D. degree from the Royal Institute of Technology (KTH), Stockholm, Sweden in 1998. He is currently a Professor of Geodesy and Geophysics with the Norwegian University of Science and Technology (NTNU), Trondheim, Norway. His research interests involve Global Geodetic Observations System (GGOS) including satellite gravimetry, satellite altimetry, satellite radar interferometry and GNSS to understand the dynamic Earth system by quantifying Earth's change in space and time.

Rüdiger Haas is a full professor for space geodesy at the Department of Space, Earth and Environment at Chalmers University of Technology, Sweden. He received his MSc and his PhD degrees in geodesy from Bonn University, Germany. He is the head of the research group for space geodesy at Chalmers and responsible for the geoscience activities at the Onsala Space Observatory. His research interests focus primarily on space geodetic techniques, such as Global Navigation Satellite Systems (GNSS), including GNSS reflectometry, and Very Long Basline Interferometry (VLBI).

Maximilian Semmling graduated in physics from Leipzig University, Leipzig, Germany, in 2007. He received the Ph.D. degree from Technische Universität Berlin, Berlin, Germany, in 2012. For his doctoral and post-doctoral studies, he was with the German Research Centre for Geosciences (GFZ), Potsdam, Germany, the Institute for Space Studies of Catalonia (IEEC), Barcelona, Spain, and the University of the Littoral Opal Coast (ULCO), Dunkirk, France. In 2020, he joined the Observation Department, German Aerospace Center (DLR), Institute for Solar-Terrestrial Physics, Neustrelitz, Germany. He is experienced in GNSS for Earth observation with a research focus on ocean altimetry and sea ice remote sensing. His work concentrates on the influence of atmosphere and space weather. Corresponding methods cover a wide range from ground-based measurements over maritime, and airborne to satellite platforms..

Jens Wickert received the graduate degree in physics from the Technical University Dresden, Germany, in 1989, and the Ph.D.degree in geophysics/meteorology from the Karl-Franzens-University Graz, Austria, in 2002. He currently holds a joint professorship of GFZ with the Technical University of Berlin on GNSS remote sensing, navigation and positioning. He is also the Deputy GFZ Section Head Space Geodetic Techniques and the GFZ Research Topic Director "The Atmosphere in Global Change". He has authored/co-authored around 250 ISI listed publications on GNSS Earth observation. He was Principal Investigator of the pioneering GPS radio occultation experiment aboard the German CHAMP satellite and coordinates numerous research projects on GNSS remote sensing.

Paper VI

Paper VII

First Evidence of Mesoscale Ocean Eddies Signature in GNSS Reflectometry Measurements

Mostafa Hoseini [1,2,*], Milad Asgarimehr [2,3], Valery Zavorotny [4], Hossein Nahavandchi [1], Chris Ruf [5] and Jens Wickert [2,3]

1   Department of Civil and Environmental Engineering, Norwegian University of Science and Technology NTNU, 7491 Trondheim, Norway
2   German Research Centre for Geosciences GFZ, 14473 Potsdam, Germany
3   Technische Universität Berlin, 10623 Berlin, Germany
4   Cooperative Institute for Research in Environmental Sciences, University of Colorado Boulder, Boulder, CO 80309, USA
5   Climate and Space Department, University of Michigan, Ann Arbor, MI 48109, USA
*   Correspondence: mostafa.hoseini@ntnu.no

Abstract: Feasibility of sensing mesoscale ocean eddies using spaceborne Global Navigation Satellite Systems-Reflectometry (GNSS-R) measurements is demonstrated for the first time. Measurements of Cyclone GNSS (CYGNSS) satellite missions over the eddies, documented in the Aviso eddy trajectory atlas, are studied. The investigation reports on the evidence of normalized bistatic radar cross section (σ^0) responses over the center or the edges of the eddies. A statistical analysis using profiles over eddies in 2017 is carried out. The potential contributing factors leaving the signature in the measurements are discussed. The analysis of GNSS-R observations collocated with ancillary data from the European Centre for Medium-Range Weather Forecasts (ECMWF) Reanalysis-5 (ERA-5) shows strong inverse correlations of σ^0 with the sensible heat flux and surface stress in certain conditions.

Keywords: GNSS Reflectometry; Mesoscale ocean eddies; Bistatic Radar Cross Section; CYGNSS

1. Introduction

Mesoscale ocean eddies can drive atmosphere response at mesoscales mainly through heat fluxes [1] and they have a local influence on near-surface wind, cloud properties, and rainfall [2]. Analysis of mesoscale eddy-atmosphere interactions from general circulation models suggests significant intermodel differences mainly stemming from two factors: surface wind strength and marine atmospheric boundary layer adjustments to mesoscale heat flux anomalies [3]. Several Earth-observing satellites have been aiding these models for decades with their data products.

Global Navigation Satellite System Reflectometry (GNSS-R) is a relatively new Earth observation technique for monitoring a large variety of geophysical parameters (see [4,5] for a review). This technique exploits the GNSS signals of opportunity after being reflected from the Earth's surface, both over lands and oceans. The signals are intercepted by low-cost, low-power and low-mass GNSS-R receivers and are processed to extract geophysical information. These receivers onboard small low Earth-orbiting satellites offer cost-effective Earth observations with high coverage and unprecedented sampling rate. Cyclone GNSS (CYGNSS) is the satellite constellation consisting of eight microsatellites with the main science objective of ocean wind speed monitoring especially during hurricane events, launched in December 2016 [6].

Ocean monitoring is one of the most mature spaceborne GNSS-R applications, with a proven capability of surface wind measurement [7–9]. Insignificant level of sensitivity to rain attenuation [10]

and cost-effective observation frequency are the main advantageous characteristics motivating researchers to develop new ideas for additional applications over oceans [11–13], and for the development of future novel GNSS-R missions [14,15].

Remote sensing of oceanic features, e.g., eddies, based on high precision GNSS-R altimetric measurements, are being pursued. For instance, [16] deduced sea surface topography observations from the GNSS-R phase measurements onboard the German High Altitude Long Range (HALO) research aircraft. In an air-borne GNSS-R study, the so-called "Eddy Experiment", the capabilities of the technique for ocean altimetry [17] and scatterometry [18] were additionally demonstrated. Nevertheless, the response of the measurements over mesoscale eddies is not yet characterized and documented, despite the available large datasets from recent GNSS-R satellite missions.

A high number of observations are provided by CYGNSS offering a possibility to study the feasibility of observing ocean eddies using GNSS-R measurements. This research focuses on the GNSS-R scatterometric observations (rather than in an altimetry configuration) and tries to characterize eddy signatures in those measurements for the first time. The data are empirically analyzed and the signatures and physical explanations are discussed. Following this introduction, Section 2 describes the datasets and the method. The results are reported and discussed in Section 3. Finally, concluding remarks are given in Section 4.

2. Data and Method

Four datasets are used for the analysis covering the period from March to December 2017. The main dataset consists of the CYGNSS GNSS-R measurements. The eight CYGNSS microsatellites are dispersed in $35°$ inclined orbits with an altitude of $\approx$520 km. The onboard GNSS-R receivers are equipped with distinct channels measuring up to four simultaneous GPS signals after reflection from the ocean surface [19]. The corresponding data are available at different processing levels. Level 1 (L1) provides a variety of parameters including the calibrated measurements of bistatic radar cross section (BRCS) as well as the Normalized BRCS (NBRCS) σ^0. The L1 data are further processed into the 10 m referenced wind speed above the ocean surface at Level 2 (L2). For the analysis in this study, σ^0 product is extracted from the Version 2.1 (v2.1) dataset [20,21].

CYGNSS measurements over the documented mesoscale eddies in Aviso's trajectory atlas version 2.0 are extracted. The atlas is a multi-mission altimetry-derived product with a daily temporal resolution [22]. Eddy characteristics, including the position and radius, spinning speed, and the type (cyclonic/anticyclonic) are extracted from the atlas.

Near-surface ocean current estimates from the Ocean Surface Current Analysis Real-time dataset (OSCAR) are also used in this study [23]. The ocean current data are provided with a spatial resolution of one-third degree. Nevertheless, they are spatially interpolated along the CYGNSS tracks. Due to the five-day temporal resolution of the OSCAR dataset, the tracks on those days, on which OSCAR current estimates are available, are collected for the analysis.

The analysis also uses ancillary data retrieved from the European Centre for Medium-Range Weather Forecasts (ECMWF) Reanalysis-5 (ERA-5) product. The ERA5 is a global atmospheric reanalysis based on an ECMWF model assimilating observations from various sources including satellite and ground-based measurements [24]. The retrieved parameters include surface wind-field, Sea Surface Temperature (SST), Sensible Heat Flux (SHF), and turbulent surface stress field. These data products offer a possibility to discuss potential interactions of the geophysical parameters with the GNSS-R σ^0. The reanalysis measurements are provided hourly with a spatial resolution of $0.25°$. The estimates are spatiotemporally interpolated along with the CYGNSS tacks being used in the study.

The eddy trajectory atlas detects an eddy as the outermost closed-contour of Sea Level Anomaly (SLA) encompassing a single extremum [22]. The area enclosed by the contour of maximum circum-average speed is considered as the eddy radius R. The CYGNSS tracks overpassing the eddy with a maximum distance of $2R$ from the eddy center are collected and transformed into a local coordinate system (Figure 1). The local coordinate system has the origin at the center of the moving

eddy with x- and y-axes oriented toward geographical east and north, respectively. Observations marked with a poor quality flag in the CYGNSS dataset (L1, v2.1) and tracks with more than 10% data loss are excluded from the collocated dataset.

The methodology of this study is based on the following steps. First, the signatures in the CYGNSS σ^0 are visually sought. The observed behavior in several cases can be the first evidence on the possibility of an eddy-left signature in the GNSS-R measurements. This examination is followed by statistical analyses to quantitatively characterize the signatures. We investigate the collocated dataset consisting of more than 2.7×10^5 NBRCS profiles over ≈ 6000 mesoscale eddies. The profiles in the along-track coordinate system are normalized using the radius of each eddy and gridded between $-1.1 \times R$ to $+1.1 \times R$ (Figure 1).
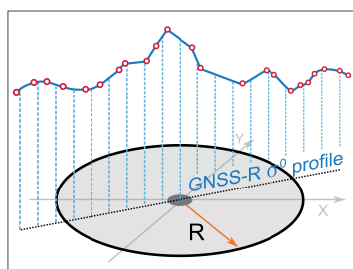

Figure 1. A sketch of the gridded GNSS-Reflectometry profile of Cyclone GNSS (CYGNSS) over an eddy and the local coordinate system with x- and y-axes oriented toward east and north, respectively.

The visually observed behaviors of the σ^0 profiles show noticeable changes over the central region or the edges of the eddies. These patterns are along with some linear and nonlinear changes in different scales. To extract the main nonlinear anomalies over the center or at the edges of eddies within the profiles, linear and small scales fluctuations of σ^0 should be filtered out. We apply Principal Component Analysis (PCA) [25] to reduce the dimensionality of the dataset while preserving most of the information within the σ^0 profiles. To this end, a data matrix $\mathbf{X_{m \times n}}$ is formed using n profiles, each of which with m gridded observation points. The profiles are centered by subtracting the mean values. Using Singular Value Decomposition (SVD), the data matrix X can be written as:

$$\mathbf{X} = \mathbf{U L V^T} \tag{1}$$

where the columns of $\mathbf{U}$ and $\mathbf{V}$ are the left and right singular vectors, respectively. $\mathbf{L}$ is a diagonal matrix with non-negative elements, the singular values λ. A proper group of singular values and corresponding singular vectors is selected to reconstruct the data matrix. Columns of the reconstructed matrix contain the filtered σ^0 profiles. Assuming the set $I = \{i, i+1, ..., k\}$ whose elements are the indices of the selected group, the reconstructed data matrix, $\hat{\mathbf{X}}$ is:

$$\hat{\mathbf{X}} = \mathbf{X_i} + \mathbf{X_{i+1}} + ... + \mathbf{X_k} , \quad \mathbf{X_i} = \lambda_i \mathbf{U_i V_i^T} \tag{2}$$

where $\mathbf{U_i}$ and $\mathbf{V_i}$ are the left and right singular vectors associated with the singular value λ_i. Columns of the matrices $\mathbf{X_i}$ represent uncorrelated features of the σ^0 profiles. The quality of each principal component (PC) can be measured by:

$$\Lambda_i = \frac{\lambda_i}{\sum_{l=1}^{d} \lambda_l} \tag{3}$$

where Λ_i represents the proportion of total variance explained by the principal component i. The parameter d ($d \leq min\{m, n\}$) is the number of non-zero singular values.

The investigation is followed seeking the conditions, in which the σ^0 response is more pronounced. To this end, the correlation coefficient between σ^0 and surface sensible heat flux is calculated at different wind speeds. Similarly, the correlation coefficient between σ^0 and the mean turbulent surface stress is obtained in a range of angular differences between the CYGNSS observational track and the turbulent surface stress. The results are presented in the following section.

3. Results and Discussion

Generally, two prominent anomalies are observed in our investigation as responses of σ^0 to the presence of the eddies: one jump at the eddy center (single-jump behavior) or two jumps at the eddy edges with a lower value at the center (double-jump behavior). Figure 2 demonstrates the double- (a–c) and single-jump (d–f) behaviors in different exemplary cases. The sudden increase in σ^0 is significant enough to be easily discerned in the measurements.
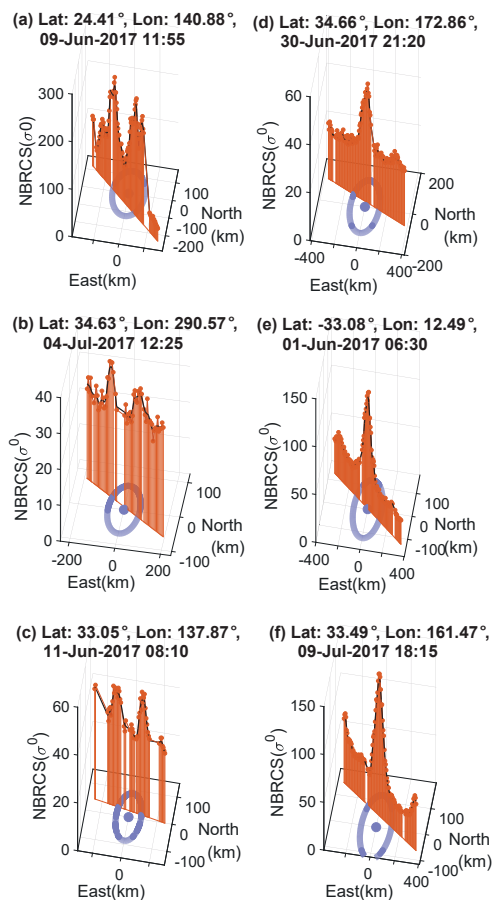

Figure 2. Exemplary cases of GNSS-Reflectometry σ^0 double-jump (**a–c**) and single-jump (**d–f**) behaviors observed in Cyclone GNSS (CYGNSS) tracks.

Additional exemplary cases are shown along with the collocated ancillary data in Figures 3–5. In Figure 3, clear fluctuations are repeatedly demonstrated over the eddy edges (similar to Figure 2a–c). Once the track enters the eddy-affected area, σ^0 increases significantly and then drops quickly at the center followed by another jump once the track leaves the eddy.
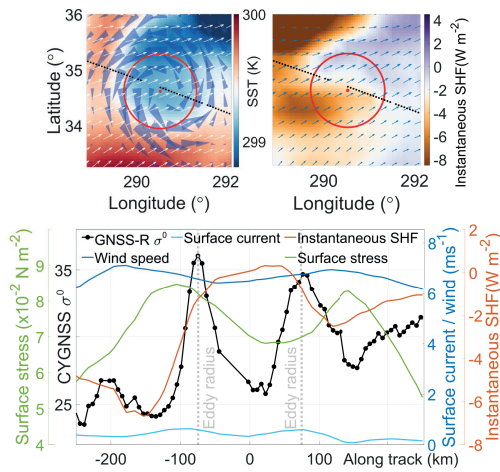
Figure 3. A track of Cyclone GNSS (CYGNSS) overpassing an eddy on 4 July 2017, 12:24. The top-left panel displays sea surface temperature, surface wind (white arrows) and current (blue cones). On the top-right, instantaneous surface sensible heat flux (SHF) as well as surface stress (blue arrows) are visualized. The bottom panel profiles CYGNSS σ^0 along with the wind and current velocity, instantaneous SHF and surface stress magnitudes.

Figure 4. A track of Cyclone GNSS (CYGNSS) overpassing three eddies on 4 June 2017, 08:11. The top panel displays sea surface temperature, surface wind (white arrows) and current (blue cones). In the middle, instantaneous surface sensible heat flux (SHF) as well as surface stress (blue arrows) are visualized. The bottom panel profiles CYGNSS σ^0 along with the wind and current velocity, instantaneous SHF and surface stress magnitudes, referenced at the center of the middle eddy.

Figure 4 shows a CYGNSS track which is long enough to overpass three cyclonic eddies. The σ^0 behaves similarly to Figures 2a–c and 3. The track does not cross the first eddy center. This causes an increase in the value of σ^0 when it passes the eddy outer lying area. A remarkable fact is that σ^0 remains almost at the same level moving over the eddy edges and again drops to lower values once it leaves the affected region. Reaching the second eddy, the track sweeps also the areas close to the eddy center and σ^0 responds with a lower value at the center and two considerable increases at the edges. The behavior of σ^0 is similar over the third eddy, however, the peaks stand at lower values.

Figure 5 shows another CYGNSS track overpassing three eddies. Similar to Figure 2d–f, σ^0 shows a single peak at the center. The track enters the core region with a sudden increase in σ^0 which again drops to its initial level once the track moves off the center. Similar behavior of σ^0 is observed reaching the central region of the second and third eddies.
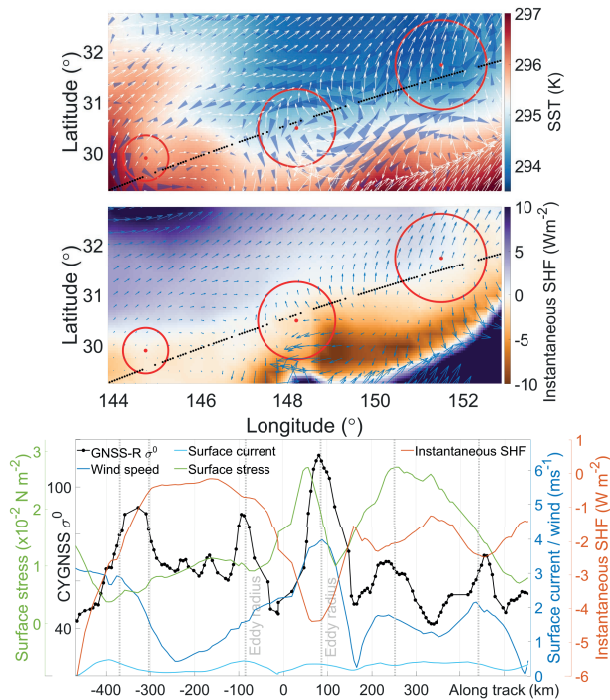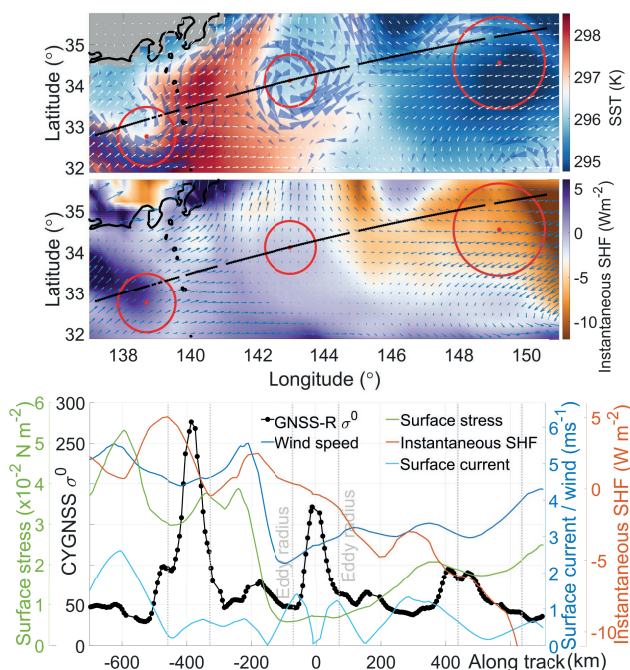

Figure 5. A track of Cyclone GNSS (CYGNSS) overpassing three eddies on 29 June 2017, 20:45. The top panel displays sea surface temperature, surface wind (white arrows) and current (blue cones). In the middle, instantaneous surface sensible heat flux (SHF) as well as surface stress (blue arrows) are visualized. The bottom panel profiles CYGNSS σ^0 along with the wind and current velocity, instantaneous SHF and surface stress magnitudes, referenced at the center of the second eddy.

Figure 6 shows the PCA results where the first nine principal components of the dataset preserve more than 95% of the statistical information in the dataset. The PCs represent low to high-fluctuating patterns within the profiles. The first PC mainly reflects the overall linear trend of the σ^0 profile. The other PCs capture the remaining non-linear variations of the profiles over the eddies. We reconstruct the profiles using the eight components PC2-PC9 and calculate the correlation coefficient of each reconstructed profile with synthetic templates of the two observed patterns. Since the peaks over the edges or at the center of the eddies could be slightly displaced from the exact expected location, we consider up to $\pm 0.1 \times R$ lag for the calculation of the correlation.

The analysis reveals that about 12.7% (15.9%) of profiles demonstrate a correlation coefficient of 0.7 or more with the single (double) peak template. We also carried out the same statistical analysis

over a new set of profiles collected regardless of the presence of eddies. In a reverse approach, the profiles demonstrating a high correlation with the templates (≥ 0.7) are investigated. About 45% of these profiles are either located on the eddies (according to the Aviso's trajectory atlas) or show a high correlation (≥ 0.7) with the surface current.
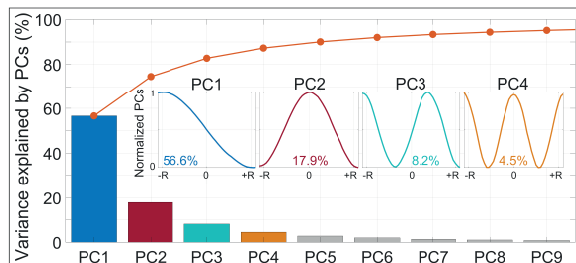

Figure 6. Principal components of the profiles and the total variance of the data explained by each principal component.

Results of the next statistical analysis over the collocated dataset reveal a strong negative correlation of CYGNSS σ^0 observations with both SHF and surface stress under certain conditions. Figure 7 provides insights into the favorable conditions, in which CYGNSS is more likely to sense surface stress and SHF over the eddies.
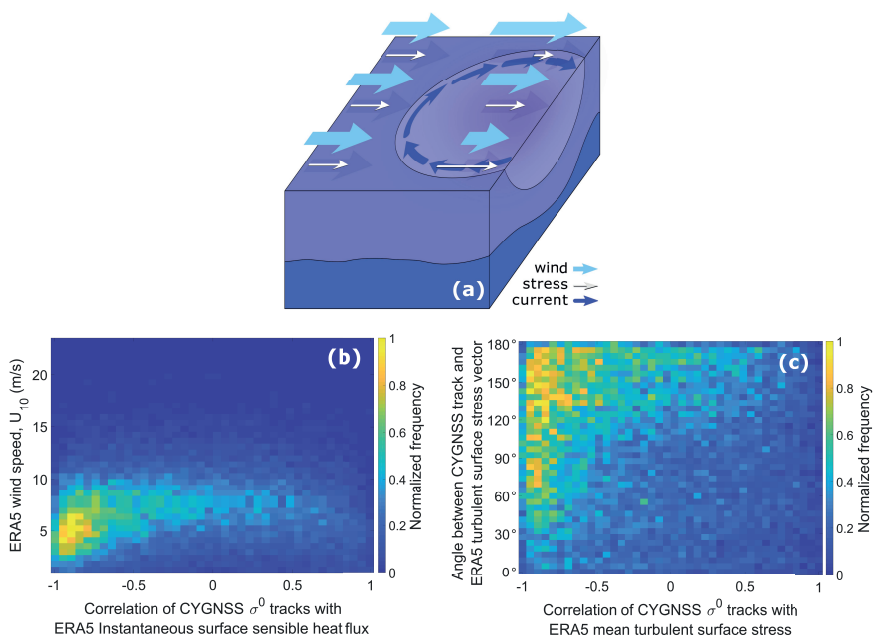
Figure 7. Schematic representation of surface stress change due to the interaction of an eastward uniform wind with the surface current associated with an anticyclonic eddy (**a**), Correlation of the σ^0 profiles of Cyclone GNSS (CYGNSS) with anomalies of instantaneous surface sensible heat flux at different wind speeds (**b**), the impact of different angular distances of the CYGNSS tracks with surface stress vector on the correlation between the σ^0 profiles and mean turbulent surface stress (**c**).

Figure 7a illustrates a simplified model of changing surface stress due to the interaction between the eddy surface current and wind speed. In Figure 7b, the behavior of σ^0 is highly correlated with SHF over the eddies at wind speeds between $\approx$3 m/s and 7 m/s, where the values of the correlation coefficients are mainly between -0.8 to -0.95. According to the theory, at high enough wind speed ($\approx> 5$ m/s), the surface parameter that controls the intensity of GNSS reflections from the ocean surface, or σ^0, is the low-pass mean square slope, MSS_{LP}, of the ocean surface [26]. It is determined by the part of the wave slope spectrum that resides at wavenumbers smaller than $k_* = k\ cos\theta_{inc}/3$ where θ_{inc} is an incidence angle and k is the wavenumber $(2\pi/\lambda)$ of the L-band GNSS signal [27]. The σ^0 is inversely proportional to MSS_{LP}. The largest contribution to the MSS_{LP} originates from the short-wave portion of the spectrum near k_*. From classic works of [28,29], it is known that there are two main mechanisms affecting that part of the wave spectrum: the varying wind surface stress and interaction of short waves with the current gradients. At low enough wind speed, the scattering of GNSS signals does not follow a pure quasi-specular scattering and there is a coherent scattering component that tends the mechanism to a higher-order Bragg scattering, driven by Rayleigh parameter [30]. Rayleigh parameter is proportional to waves at any wavenumbers. So, at this regime of wind speed, GNSS-R measurements could be more sensitive to surface state, even to small-scale roughness modifications [12]. Figure 7c shows the impact associated with the angular difference of CYGNSS tracks and surface stress field direction. The direction of the CYGNSS track with respect to the surface stress vector can increase the sensitivity of σ^0 to surface stress anomalies within the eddies. This means the GNSS-R measurements are highly likely to sense the stress field with a direction against the moving GNSS-R specular points. It can be also seen that for the absolute angular distances in the range of about 60 to 180 degrees the wind stress would be more pronounced in the CYGNSS measurements.

Atmospheric boundary layer change associated with the eddy-induced SST anomalies results in a varying wind field [31]. The modified local surface wind influenced by marine boundary layer dynamics [32,33] can partially explain the GNSS-R σ^0 patterns. The enhanced local wind over the warm core of the eddy can lead to the abrupt change in the GNSS-R σ^0 values. Since the improvement in the weather and climate projections require detailed observations and understanding of warm eddy-atmosphere interactions [34], this possible promising contribution by the GNSS-R technique should be investigated.

The first cold-core eddy shown in Figure 5 can cause a strong dampening of wind intensity due to downward transport of wind momentum, decelerating local surface wind. The sharp peak of GNSS-R σ^0 resides at the core region of the eddy where the SST has a lower value. This deceleration could also happen when a tropical cyclone reaches a strong cold-core eddy. Such eddies can broaden the eye size of the storm during its passage and reduce its intensity [35]. For instance, an unforeseen rapid weakening was demonstrated when the category 4 hurricane Kenneth passed over a cold-core eddy on 19–20 September 2005 [36].

The discussed air-sea interactions over the eddies could explain the response of GNSS-R observations to SHF at the ocean-atmosphere interface through the modified surface stress. In Figure 3, a local minimum of ERA5 surface stress values takes place almost over the core region of the eddy. The peaks of the stress values approximately reside over the rotating current of the eddy. The impact of the surface stress on the profile of CYGNSS σ^0 is evident where sudden fluctuations are seen over the edges and in the core. Larger SHF values with negative sign, i.e. upward direction of the flux, are well synchronized with two σ^0 minima at -150 and 150 km along with track coordinates.

In Figure 4, the most prominent change in the σ^0 profile can be seen over the middle eddy. The possible signature of this eddy could be explained by a high value of stress approximately at the eddy center where an increment of upward SHF is observed. The ERA5 could be subjected to deficiencies in resolving local sudden changes and It seems that it does not reveal the same level of details over the left eddy as those provided by the CYGNSS measurements. The behavior of σ^0 over the right eddy in this figure can be described by the expected behavior of σ^0 at very low wind speeds.

According to [37], at very low wind speeds (< 2.5 m/s), the bistatic radar cross section is directly proportional to the roughness (unlike the inverse correlation at higher wind speeds). Therefore, the clear correspondence between the magnitude of upward SHF and wind speed over this eddy closely matches the similar pattern in σ^0 while the wind speed values are mainly below 2 m/s.

The surface current associated with eddies is another factor that can affect surface stress. Considering surface stress as a function of wind and ignoring the surface current in the oceanic numerical modeling, can result in the overestimation of the total energy input of wind to the ocean [38]. Wind stress (τ) can be calculated as [39]:

$$\tau = \rho_a C_D \left(W - U \right) \left| W - U \right| \tag{4}$$

where ρ_a is the density of the air, C_D is the drag coefficient, and W and U are the wind and surface current, respectively.

The behavior of σ^0 in Figure 5 can be partially attributed to the modified surface stress at the eddy currents. Eddy-induced current can amplify or decrease the wind stress (Figure 7a) or alter its direction which can in turn change the level of σ^0 sensitivity to surface stress. Over the left eddy in Figure 5, the similar directional orientation of the CYGNSS track with respect to the surface stress field can lead to the weaker impact of stress on the σ^0 values (see Figure 7c). Interaction of eddy-induced current with surface stress can increase the σ^0 sensitivity over the edges resulting in lower σ^0 values. Therefore, the vanishing current at the core region would lead to the less pronounced impact of stress on σ^0. Although the stress field over the middle eddy is not as strong, the angular difference of the CYGNSS track with the stress field intensifies the impact. The strong current velocity on the edges enhances the stress on the left side and decreases the stress on the right side of the eddy (see Figure 7a), resulting slightly higher σ^0 values on the right edge compared to the left edge. The low magnitude of SHF over this cold-core eddy together with almost zero current velocity at the center cause a sudden peak in the σ^0 value. The higher SHF magnitudes and stress values between the two eddies keep the σ^0 values at a lower level.

It is worth mentioning that concentrated biogenic films from natural life in the ocean can potentially play a role in the power of reflected GNSS-R signals. The turbulence associated with the eddies brings the natural biogenic surfactants released from plankton and fishes to the surface, where the concentration of the surfactant molecules can generate a surface tension. This phenomenon could inhibit the development of Bragg waves [40]. Such areas are discerned as dark regions in the synthetic aperture radar images since the signal is mainly forward scattered rather than being backscattered. In a bistatic forward scattering configuration, the wide-enough smoothed regions can increase the power of GNSS signals after reflection from the ocean. Therefore, a dramatic increase in σ^0 over these regions can be expected. The characterization of biogenic surfactants' role in the signal forward scattering is recommended for future studies.

4. Conclusions

In this study, it is shown that spaceborne GNSS-R measurements can respond to the existence of eddies. Different characteristics of eddies can impact the local wind as well as surface stress which can, in turn, affect GNSS-R measurements. The normalized bistatic radar cross section (NBRCS) exhibits a clear inverse correlation with surface heat flux and surface stress under certain conditions. Nevertheless, characterization of the observed signatures requires further study considering other potential factors such as the effect of biogenic surfactants and the eddy-induced currents in the surface stress and ocean state. Many factors produce NBRCS changes. The complexity of oceanic and atmospheric mechanisms controlling the GNSS scattering demands further sophisticated analyses in future studies. There are still open questions such as the conditions of occurrences or the measurements specific behaviors over cyclonic or anticyclonic eddies. This study initiates the development of the novel GNSS-R technique for studying ocean mesoscale eddies, the feasibility of which has been demonstrated for the first time.

Conflicts of Interest: The authors declare no conflict of interest.

References

1. Small, R.D.; DeSzoeke, S.; Xie, S.; O'Neill, L.; Seo, H.; Song, Q.; Cornillon, P.; Spall, M.; Minobe, S. Air–sea interaction over ocean fronts and eddies. *Dyn. Atmos. Ocean.* **2008**, *45*, 274–319. [CrossRef]

2. Frenger, I.; Gruber, N.; Knutti, R.; Münnich, M. Imprint of Southern Ocean eddies on winds, clouds and rainfall. *Nat. Geosci.* **2013**, *6*, 608. [CrossRef]

3. Yang, P.; Jing, Z.; Wu, L. An Assessment of Representation of Oceanic Mesoscale Eddy-Atmosphere Interaction in the Current Generation of General Circulation Models and Reanalyses. *Geophys. Res. Lett.* **2018**, *45*, 11–856. [CrossRef]

4. Jin, S.; Cardellach, E.; Xie, F. *GNSS Remote Sensing*; Springer: Berlin/Heidelberg, Germany, 2014.

5. Zavorotny, V.U.; Gleason, S.; Cardellach, E.; Camps, A. Tutorial on remote sensing using GNSS bistatic radar of opportunity. *IEEE Geosci. Remote. Sens. Mag.* **2014**, *2*, 8–45. [CrossRef]

6. Ruf, C.S.; Atlas, R.; Chang, P.S.; Clarizia, M.P.; Garrison, J.L.; Gleason, S.; Katzberg, S.J.; Jelenak, Z.; Johnson, J.T.; Majumdar, S.J.; et al. New ocean winds satellite mission to probe hurricanes and tropical convection. *Bull. Am. Meteorol. Soc.* **2016**, *97*, 385–395. [CrossRef]

7. Foti, G.; Gommenginger, C.; Jales, P.; Unwin, M.; Shaw, A.; Robertson, C.; Rosello, J. Spaceborne GNSS reflectometry for ocean winds: First results from the UK TechDemoSat-1 mission. *Geophys. Res. Lett.* **2015**, *42*, 5435–5441. [CrossRef]

8. Ruf, C.S.; Gleason, S.; McKague, D.S. Assessment of CYGNSS wind speed retrieval uncertainty. *IEEE J. Sel. Top. Appl. Earth Obs. Remote. Sens.* **2018**, *12*, 87–97. [CrossRef]

9. Asgarimehr, M.; Wickert, J.; Reich, S. TDS-1 GNSS Reflectometry: Development and Validation of Forward Scattering Winds. *IEEE J. Sel. Top. Appl. Earth Obs. Remote. Sens.* **2018**, *11*, 4534–4541. [CrossRef]

10. Asgarimehr, M.; Wickert, J.; Reich, S. Evaluating Impact of Rain Attenuation on Space-borne GNSS Reflectometry Wind Speeds. *Remote. Sens.* **2019**, *11*, 1048. [CrossRef]

11. Alonso-Arroyo, A.; Zavorotny, V.U.; Camps, A. Sea ice detection using UK TDS-1 GNSS-R data. *IEEE Trans. Geosci. Remote. Sens.* **2017**, *55*, 4989–5001. [CrossRef]

12. Asgarimehr, M.; Zavorotny, V.; Wickert, J.; Reich, S. Can GNSS Reflectometry Detect Precipitation Over Oceans? *Geophys. Res. Lett.* **2018**, *45*, 12–585. [CrossRef]

13. Clarizia, M.P.; Ruf, C.; Cipollini, P.; Zuffada, C. First spaceborne observation of sea surface height using GPS-Reflectometry. *Geophys. Res. Lett.* **2016**, *43*, 767–774. [CrossRef]

14. Wickert, J.; Cardellach, E.; Martín-Neira, M.; Bandeiras, J.; Bertino, L.; Andersen, O.B.; Camps, A.; Catarino, N.; Chapron, B.; Fabra, F.; et al. GEROS-ISS: GNSS reflectometry, radio occultation, and scatterometry onboard the international space station. *IEEE J. Sel. Top. Appl. Earth Obs. Remote. Sens.* **2016**, *9*, 4552–4581. [CrossRef]

15. Cardellach, E.; Wickert, J.; Baggen, R.; Benito, J.; Camps, A.; Catarino, N.; Chapron, B.; Dielacher, A.; Fabra, F.; Flato, G.; et al. GNSS Transpolar Earth Reflectometry exploriNg System (G-TERN): Mission Concept. *IEEE Access* **2018**, *6*, 13980–14018. [CrossRef]

16. Semmling, A.; Beckheinrich, J.; Wickert, J.; Beyerle, G.; Schön, S.; Fabra, F.; Pflug, H.; He, K.; Schwabe, J.; Scheinert, M. Sea surface topography retrieved from GNSS reflectometry phase data of the GEOHALO flight mission. *Geophys. Res. Lett.* **2014**, *41*, 954–960. [CrossRef]

17. Ruffini, G.; Soulat, F.; Caparrini, M.; Germain, O.; Martín-Neira, M. The Eddy Experiment: Accurate GNSS-R ocean altimetry from low altitude aircraft. *Geophys. Res. Lett.* **2004**, *31*. [CrossRef]

18. Germain, O.; Ruffini, G.; Soulat, F.; Caparrini, M.; Chapron, B.; Silvestrin, P. The Eddy Experiment: GNSS-R speculometry for directional sea-roughness retrieval from low altitude aircraft. *Geophys. Res. Lett.* **2004**, *31*. [CrossRef]

19. Ruf, C.S.; Chew, C.; Lang, T.; Morris, M.G.; Nave, K.; Ridley, A.; Balasubramaniam, R. A new paradigm in earth environmental monitoring with the CYGNSS small satellite constellation. *Sci. Rep.* **2018**, *8*, 8782. [CrossRef]

20. Gleason, S.; Ruf, C.S.; O'Brien, A.J.; McKague, D.S. The CYGNSS Level 1 calibration algorithm and error analysis based on on-orbit measurements. *IEEE J. Sel. Top. Appl. Earth Obs. Remote. Sens.* **2018**, *12*, 37–49. [CrossRef]

21. Ruf, C.; Asharaf, S.; Balasubramaniam, R.; Gleason, S.; Lang, T.; McKague, D.; Twigg, D.; Waliser, D. In-Orbit Performance of the Constellation of CYGNSS Hurricane Satellites. *Bull. Am. Meteorol. Soc.* **2019**, *100*, 2009–2023. [CrossRef]

22. Faghmous, J.H.; Frenger, I.; Yao, Y.; Warmka, R.; Lindell, A.; Kumar, V. A daily global mesoscale ocean eddy dataset from satellite altimetry. *Sci. Data* **2015**, *2*, 150028. [CrossRef] [PubMed]

23. Bonjean, F.; Lagerloef, G.S. Diagnostic model and analysis of the surface currents in the tropical Pacific Ocean. *J. Phys. Oceanogr.* **2002**, *32*, 2938–2954. [CrossRef]

24. Hersbach, H.; Dee, D. ERA5 reanalysis is in production. *ECMWF Newsl.* **2016**, *147*, 5–6.

25. Jolliffe, I.T.; Cadima, J. Principal component analysis: A review and recent developments. *Philos. Trans. R. Soc. Math. Phys. Eng. Sci.* **2016**, *374*, 20150202. [CrossRef]

26. Zavorotny, V.U.; Voronovich, A.G. Scattering of GPS signals from the ocean with wind remote sensing application. *IEEE Trans. Geosci. Remote. Sens.* **2000**, *38*, 951–964. [CrossRef]

27. Zavorotny, V.U.; Voronovich, A.G. Validity of the Kirchhoff-Geometric Optics Approach for Modeling of Ocean Bistatic Radar Scattering. In Proceedings of the IGARSS 2019–2019 IEEE International Geoscience and Remote Sensing Symposium, Yokohama, Japan, 28 July–2 August 2019; pp. 668–671. [CrossRef]

28. Plant, W.J. A relationship between wind stress and wave slope. *J. Geophys. Res. Ocean.* **1982**, *87*, 1961–1967. [CrossRef]

29. Phillips, O. On the response of short ocean wave components at a fixed wavenumber to ocean current variations. *J. Phys. Oceanogr.* **1984**, *14*, 1425–1433. [CrossRef]

30. Voronovich, A.G.; Zavorotny, V.U. Bistatic radar equation for signals of opportunity revisited. *IEEE Trans. Geosci. Remote. Sens.* **2017**, *56*, 1959–1968. [CrossRef]

31. Johannessen, J.A.; Kudryavtsev, V.; Akimov, D.; Eldevik, T.; Winther, N.; Chapron, B. On radar imaging of current features: 2. Mesoscale eddy and current front detection. *J. Geophys. Res. Ocean.* **2005**, *110*. [CrossRef]

32. Wallace, J.M.; Mitchell, T.; Deser, C. The influence of sea-surface temperature on surface wind in the eastern equatorial Pacific: Seasonal and interannual variability. *J. Clim.* **1989**, *2*, 1492–1499. [CrossRef]

33. Samelson, R.; Skyllingstad, E.; Chelton, D.; Esbensen, S.; O'Neill, L.; Thum, N. On the coupling of wind stress and sea surface temperature. *J. Clim.* **2006**, *19*, 1557–1566. [CrossRef]

34. Sugimoto, S.; Aono, K.; Fukui, S. Local atmospheric response to warm mesoscale ocean eddies in the Kuroshio-Oyashio Confluence region. *Sci. Rep.* **2017**, *7*, 11871. [CrossRef]

35. Ma, Z.; Fei, J.; Liu, L.; Huang, X.; Cheng, X. Effects of the Cold Core Eddy on Tropical Cyclone Intensity and Structure under Idealized Air–Sea Interaction Conditions. *Mon. Weather. Rev.* **2013**, *141*, 1285–1303. [CrossRef]

36. Walker, N.D.; Leben, R.R.; Pilley, C.T.; Shannon, M.; Herndon, D.C.; Pun, I.F.; Lin, I.I.; Gentemann, C.L. Slow translation speed causes rapid collapse of northeast Pacific Hurricane Kenneth over cold core eddy. *Geophys. Res. Lett.* **2014**, *41*, 7595–7601. [CrossRef]

37. Voronovich, A.G.; Zavorotny, V.U. The transition from weak to strong diffuse radar bistatic scattering from rough ocean surface. *IEEE Trans. Antennas Propag.* **2017**, *65*, 6029–6034. [CrossRef]

38. Renault, L.; Molemaker, M.J.; McWilliams, J.C.; Shchepetkin, A.F.; Lemarié, F.; Chelton, D.; Illig, S.; Hall, A. Modulation of Wind Work by Oceanic Current Interaction with the Atmosphere. *J. Phys. Oceanogr.* **2016**, *46*, 1685–1704. [CrossRef]

39. Seo, H.; Miller, A.J.; Norris, J.R. Eddy–Wind Interaction in the California Current System: Dynamics and Impacts. *J. Phys. Oceanogr.* **2016**, *46*, 439–459. [CrossRef]

40. Gagliardini, D.A., Medium Resolution Microwave, Thermal and Optical Satellite Sensors: Characterizing Coastal Environments Through the Observation of Dynamical Processes. In *Remote Sensing of the Changing Oceans*; Tang, D., Ed.; Springer: Berlin/Heidelberg, Germany, 2011; pp. 251–277. [CrossRef]

Article

Evaluation of CYGNSS Observations for Flood Detection and Mapping during Sistan and Baluchestan Torrential Rain in 2020

Mahmoud Rajabi *, Hossein Nahavandchi and Mostafa Hoseini

Department of Civil and Environmental Engineering, Norwegian University of Science and Technology NTNU, 7491 Trondheim, Norway; hossein.nahavandchi@ntnu.no (H.N.); mostafa.hoseini@ntnu.no (M.H.)

* Correspondence: mahmoud.rajabi@ntnu.no; Tel.: +47-92332254

check for
updates

Abstract: Flood detection and produced maps play essential roles in policymaking, planning, and implementing flood management options. Remote sensing is commonly accepted as a maximum cost-effective technology to obtain detailed information over large areas of lands and oceans. We used remote sensing observations from Global Navigation Satellite System-Reflectometry (GNSS-R) to study the potential of this technique for the retrieval of flood maps over the regions affected by the recent flood in the southeastern part of Iran. The evaluation was made using spaceborne GNSS-R measurements over the Sistan and Baluchestan provinces during torrential rain in January 2020. This area has been at a high risk of flood in recent years and needs to be continuously monitored by means of timely observations. The main dataset was acquired from the level-1 data product of the Cyclone Global Navigation Satellite System (CYGNSS) spaceborne mission. The mission consisted of a constellation of eight microsatellites with GNSS-R sensors onboard to receive forward-scattered GNSS signals from the ocean and land. We first focused on data preparation and eliminating the outliers. Afterward, the reflectivity of the surface was calculated using the bistatic radar equations formula. The flooded areas were then detected based on the analysis of the derived reflectivity. Images from Moderate-Resolution Imaging Spectroradiometer (MODIS) were used for evaluation of the results. The analysis estimated the inundated area of approximately 19,644 km^2 (including Jaz-Murian depression) to be affected by the flood in the south and middle parts of the Sistan and Baluchestan province. Although the main mission of CYGNSS was to measure the ocean wind speed in hurricanes and tropical cyclones, we showed the capability of detecting floods in the study area. The sensitivity of the spaceborne GNSS-R observations, together with the relatively short revisit time, highlight the potential of this technique to be used in flood detection. Future GNSS-R missions capable of collecting the reflected signals from all available multi-GNSS constellations would offer even more detailed information from the flood-affected areas.

Keywords: CYGNSS; flood detection; Sistan and Baluchestan; flood mapping; GNSS-R

1. Introduction

Natural disasters are the reason for many serious disturbances to communities and the environment. There have been many human, environmental, social, and economic losses, which are beyond the power of the community to tolerate [1]. Floods have been considered as one of the most catastrophic events, causing extensive damage to the artificial and natural environment and devastation to human settlements [2]. Economic losses due to the effects of damaging floods have increased significantly around the world [3]. Flooding happens when water bodies overflow riversides, lakes, dams, or dikes in low-lying lands during heavy rainfall [4]. The higher temperature at the Earth's surface leads to

increased evaporation and greater overall precipitation [5]. Increased precipitation, although associated with inland flooding, can also increase the risk of coastal flooding [6].

Flood detection, and subsequently, produced maps, are beneficial in two important phases: During the flood, when we need emergency management planning, and after the flood, for land use planning, defining construction standards, and damage assessment [7]. Heavy precipitation has led floods to occur more frequently in different countries, which have drawn considerable attention over the past years. There are many regions of Iran affected by floods, for instance, heavy rainfall from mid-March to April 2019 led to flooding in 28 of 31 provinces, with the most severe flooding occurring in Golestan, Fars, Khuzestan, and Lorestan [8]. The recent torrential rain in mid-January 2020 in the southeastern region of Iran caused a devastating flood in the Sistan and Baluchestan province. We investigated the latter case in this study.

Land surveying and airborne observations are the traditional methods for flood detection, but when when flood detection is conducted on a large scale, these methods are costly and slow. Space-based Remote Sensing (RS) can be considered as a practical alternative that provides up-to-date information from various sensors that have been onboard different satellites. However, there are some limitations in using RS data products for the study of flooding. For instance, optical RS can have its limitations during severe weather conditions and during night. Therefore, in some cases before and after a flood event, the optical RS imagery does not provide the required information [7]. Radar RS in the microwave spectrum can surpass these restrictions because the wave can penetrate clouds and vegetation and can effectively work at night. Among the several radars RS sensors currently in operation, Synthetic Aperture Radar (SAR) imagery provides high spatial resolution data which is typically based on a monostatic configuration. However, the revisit time of satellites with the configuration of the monostatic radar (single satellites), like SAR, is long (more than one week) and cannot offer the desirable continuous high temporal resolution for flood detection purposes. Accordingly, owing to the highly dynamic nature of the flood, SAR images are not used operationally during floods [9–11].

The primary services of the Global Navigation Satellite System (GNSS) are positioning, navigation, and timing. Besides, many other applications, including GNSS RS, have been introduced in recent decades. Measurements made by GNSS RS techniques provide valuable information about different components of the Earth system. Observations of the GNSS signals passing through the atmosphere have been employed to study the atmospheric layers and their variabilities [12,13]. GNSS signals after reflection from the Earth's surface can also provide information about the reflecting surface. These reflections have been used to study various parameters of the Earth's surface and water cycles, such as snow depth [14], ice height and sea level [15], soil moisture [16], vegetation [17], flood [11,18], ocean eddies [19], wind speed [20], salinity [21], etc.

Global Navigation Satellite System Reflectometry (GNSS-R) is an innovative technique aimed at deriving geophysical parameters by analyzing GNSS signals reflected off the Earth's surface in a bistatic geometry. This technique is an efficient microwave remote sensing approach that utilizes transmitted navigation signals as sources of opportunity. Numerous GNSS satellites, including GPS, Galileo, GLONASS, and Bei-Dou/Compass, are currently transmitting navigation signals based on spread-spectrum technology. Thus, a constellation of GNSS-R small satellites, at a lower cost compared to ordinary RS satellites, can provide a much shorter revisit time using low-cost, low-power passive sensors. Many earlier studies have introduced the applications of GNSS-R on the oceans, land, and ice [22–24].

The soil moisture, surface roughness, vegetation, and topography are parameters which affect microwave signals. GNSS-R signals as a bistatic radar are also affected by those parameters [25]. However, GNSS signals are at the L-band, which is ideal for soil moisture and surface water remote sensing due to the higher capacity to penetrate vegetation compared to shorter wavelengths [16]. In addition, this technique uses the bistatic configuration, which has a lower sensitivity to surface roughness relative to monostatic [26]. The signals reflected off the surface have a direct relation with

surface water and moisture content [11]. For example, the rise of soil moisture leads to increase the signal strength. Using this mechanism could contribute to detecting soil saturation, flooded area, and inland water.

The Cyclone Global Navigation Satellite System (CYGNSS) mission is a constellation of eight microsatellites, each with a GNSS-R receiver onboard. The receiver can track and process four GPS signals simultaneously. The tracked GPS L1 C/A signals after reflection from the Earth's surface are used to produce Delay Doppler Maps (DDMs). The overall median revisit time is 2.8 h, and the mean revisit time is 7.2 h [27]. Theoretically, the footprint of reflection received by CYGNSS is nearly 0.5 km × 0.5 km. For the ocean, which has a very rough surface, the spatial resolution is approximately 25 km × 25 km [28,29]. Table 1 shows CYGNSS microsatellite parameters retrieved from [16,23]. The main mission of CYGNSS is to measure the ocean surface wind speed in hurricanes and tropical cyclones, so a relatively low orbital inclination was designed for the satellites. CYGNSS continuously makes measurements over the oceans and provides useful information over the land [29]. CYGNSS offers distinct features compared to other remote sensing techniques such as optical and active monostatic radar. It uses a passive sensor at the L-band frequency wave, which works in all weather conditions regardless of the time of the day, i.e., it can penetrate clouds, fog, rain, storms, and vegetation, and works at night, unlike optical sensors. The CYGNSS constellation of eight microsatellites provides a relatively short revisit time with global coverage over equatorial regions. The products of CYGNSS are publicly available over the oceans and land.

Table 1. The Cyclone Global Navigation Satellite System (CYGNSS) satellite parameters.

Parameters	Description
Orbit	LEO, ~520 km, Nonsynchronous
Period	95.1 min
Spatial Resolution	~25 km × 25 km (incoherent), ~0.5 km × 5 km (coherent, theoretical)
Revisit Times	2.8 h median, 7.2 h mean
Polarization of the reflectometry antennas	LHCP
Coverage	−38 < Latitude < 38 & −180 < Longitude < 180
Type of Data which is relevant	Observe GPS L1 C/A signals and Delay Doppler Maps

Radar remote sensing for soil moisture retrieval and surface water detection is common using both monostatic [7,30] and bistatic geometry. The sensitivity of spaceborne GNSS-R (as a bistatic radar) to surface water and soil moisture has been widely studied [11,16,18,23,31–33]. Most of the studies have used observations from ground-based or space-based receivers, e.g., CYGNSS or Technology Demonstration Satellite-1 (TDS-1). Observational evidence demonstrates that GNSS-R is highly sensitive to inland surface waters, e.g., lakes and rivers [34].

Sistan and Baluchestan is one of the driest regions of Iran, with a slight increase in rainfall from east to west, and is a province at a high risk of flooding. The aim of this study was to indicate the capability of spaceborne GNSS-R for detecting and mapping of flood in the south part of Iran. The methodology for preparing and processing data is the same as those used described by the authors of [16,18].

2. Study Area

The Sistan and Baluchestan province is located in the east and southeast of Iran (58°55′–63°20′ E longitude and 25°04′–31°25′ N latitude), bordering Pakistan and Afghanistan, and its capital is Zahedan. This province is the second largest province in Iran with an area of 180,726 km^2 and a population of about 2.5 million. Figure 1A shows the location of this province on the Maphill Earth map. There is a depression in the study area known as the Hamun-Jaz-Murian basin, which is part of the central plateau basin. This basin is located in the southeast of Iran between 56°17′ and 61°25′ E longitude and 26°32′ and 29°35′ N latitude (Figure 1B). Its total area is about 69,390 km^2, of which 44% is mountains. The depression belongs to Kerman and Sistan-Baluchistan provinces [35]. Figure 1C shows a flooded region in IranShahr, which is one of the cities in this province.
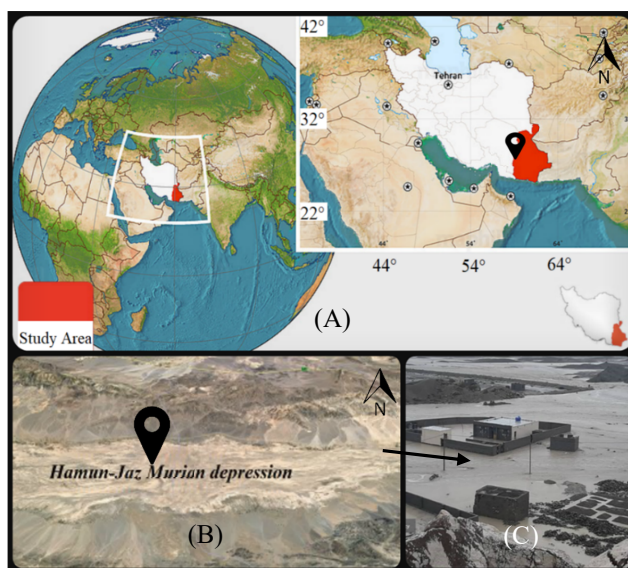
Figure 1. (**A**) The red region shows the location of the Sistan and Baluchestan province in the southeast of Iran, which is our study area. (**B**) The Hamun Jaz-Murian depression, which is located between the Kerman and Sistan and Baluchestan provinces. (**C**) IranShahr, one of the flooded cities in the study area.

Sistan and Baluchestan is one of the warmest regions in Iran, with a desert climate and an average daily temperature of 29 degrees centigrade. For several months of the year, it is warm at temperatures continuously above 25 degrees centigrade, and temperatures sometimes exceed above 40 degrees centigrade. Figure 2 illustrates the average precipitation per day over 20 years. As can be seen, 0.40 mm/day rainfall is normal during January in the province, but between 10 January and 12 January 2020, this amount is over 100 mm. Figure 3 shows the precipitation rate from 8 January to 13 January 2020.
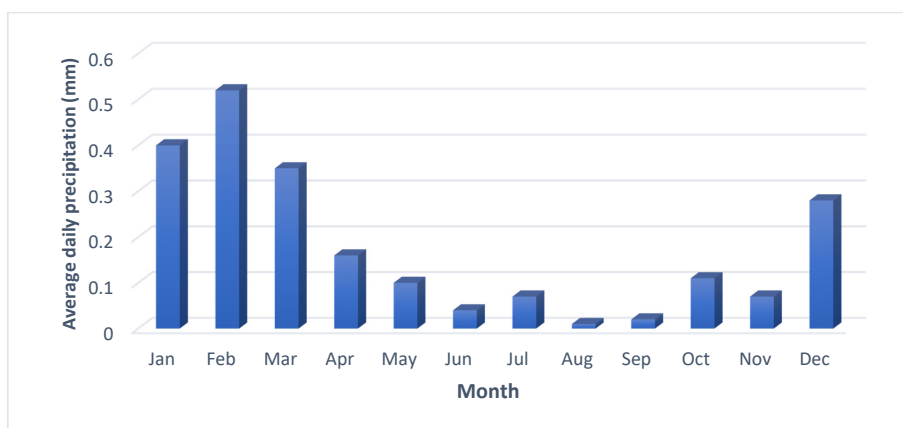

Figure 2. Average daily precipitation data collected from three meteorological stations in the Sistan and Baluchestan province based on the average values of the last 20 years [36].
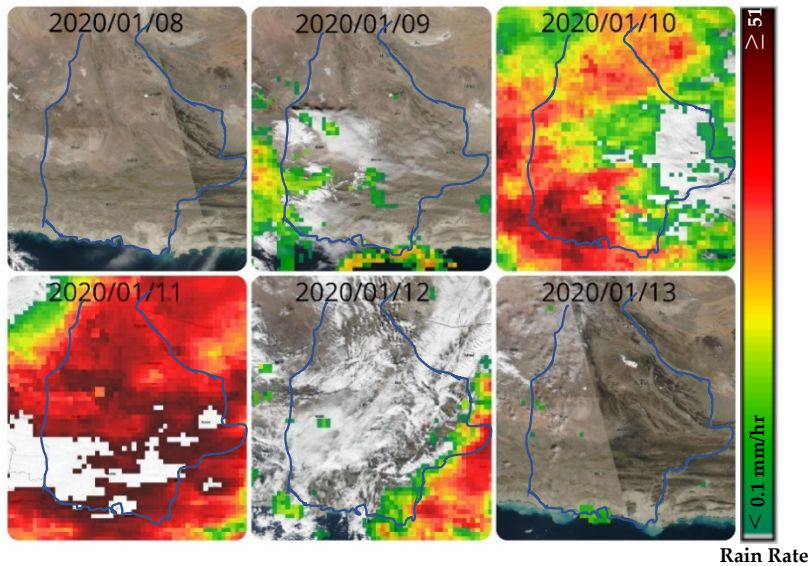
Figure 3. Rate of torrential precipitation in the Sistan and Baluchestan province over the period of six days from 8 January to 13 January, 2020. The maps were generated using the data provided by the authors of [37].

3. Data Set Description

3.1. CYGNSS data

There are three levels of CYGNSS data products in version 2.1, which represent the second post-provisional based on calibrated and validated level 1 algorithms. The level 1 (L1) dataset contains the measurement of surface Normalized Bistatic Radar Cross Section (NBRCS). The level 2 (L2) dataset includes derived ocean surface wind speed and Mean Square Slope (MSS). The level 3 (L3) dataset delivers hourly averaged wind speed and MSS on a 0.2 degree × 0.2 degree grid.

We used CYGNSS L1 data as the lowest level of the available data products. The format of the data is NetCDF (Network Common Data Form). Daily observations of each of the eight CYGNSS satellites are included in a NetCDF file. Accordingly, there are up to eight files for every Day Of a Year (DOY). The daily base data is available free of charge on the website of Physical Oceanography Distributed Active Archive Center (PO. DAAC) of NASA's Jet Propulsion Laboratory (JPL) at https://podaac.jpl.nasa.gov. Table 2 shows the main variables of the L1 data [24] which were used in this study.

Table 2. The Cyclone Global Navigation Satellite System (CYGNSS) data source parameters.

Parameters	Description
ddm_snr	Delay Doppler Map (DDM) signal-to-noise ratio, in dB
gps_tx_power_db_w	GPS transmit power, in dB.
rx_to_sp_range	Distance between the CYGNSS spacecraft and the specular point, in meters.
tx_to_sp_range	Distance between the GPS spacecraft and the specular point, in meters.
gps_ant_gain_db_i	GPS transmit antenna gain. Antenna gain in the direction of the specular point, in dBi
sp_rx_gain	Specular point Rx antenna gain. The receive antenna gains in the direction of the specular point, in decibel isotropic (dBi).
quality_flags	Per-DDM quality flags
sp_lat	Specular point latitude, in degrees North
sp_lon	Specular point longitude, in degrees East
sp_inc_angle	The specular point incidence angle, in degrees

3.2. Satellite Image

Moderate-Resolution Imaging Spectroradiometer (MODIS) is an advanced sensor on the Terra and Aqua Spacecraft for gathering data through a broad spectrum of electromagnetic waves. Terra was the first satellite of the Earth Observing System (EOS) program and was launched on 18 December, 1999. It passes north to south over the equator in the morning. Aqua is the second EOS satellite which carries a MODIS sensor and passes south to north across the equator in the afternoon. Terra and Aqua MODIS cover the Earth's surface every one to two days. The sensors onboard these satellites measure 36 spectral bands from 0.405 μm to 14.385 μm. The data is released by different resolutions, i.e., 250 m (bands 1–2), 500 m (bands 3–7), and 1000 m (bands 8–36). The MODIS data is accessible at https://modis.gsfc.nasa.gov and can be used for a significant number of applications in the land, atmosphere, and, ocean [38]. Figure 4 shows the false-color images of the Sistan and Baluchestan province (also regions of the Kerman and Hormozgan provinces) before the flood (A) and during the flood (B). The images were acquired by MODIS (bands 7–2–1) on 8 January and 13 January 2020. These images were used here for validation purposes.
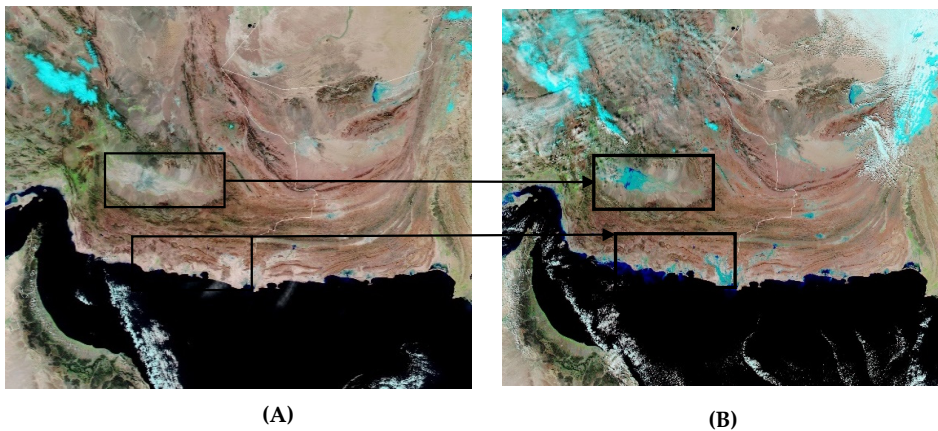

(A)   **(B)**

Figure 4. Moderate-Resolution Imaging Spectroradiometer (MODIS) images of the study area (**A**) before the flooding on 8 January 2020, and (**B**) during the flood on 13 January 2020. The dark blue regions are the inundated areas. The clouds in the image are shown with light blue which can be distinguished from the inundated areas [39].

4. Method and Discussion

The methodology in the current paper includes five main steps, as illustrated in Figure 5. The steps are: (1) Data collection, (2) data preparation, (3) calculating the surface reflectivity, (4) data calibration, and (5) flood detection and validation. Each step is described as follows.

4.1. The Bistatic Radar Equations

Radar is a system for detecting targets and deriving information such as position, velocity, and reflectivity signature from the detected objects [40]. It transmits a signal and receives the echo after it is reflected by a target. The types of radar systems based on the location of the transmitter (TX) and the receiver (RX) can be divided into colocated or monostatic radars, which measure backscattered signals, and separated or bistatic radars, which measure forward-scattered signals. The main difference between monostatic and bistatic radars is the separation of the transmitter and receiver [41]. Figure 6 shows monostatic and bistatic constellation for satellites.
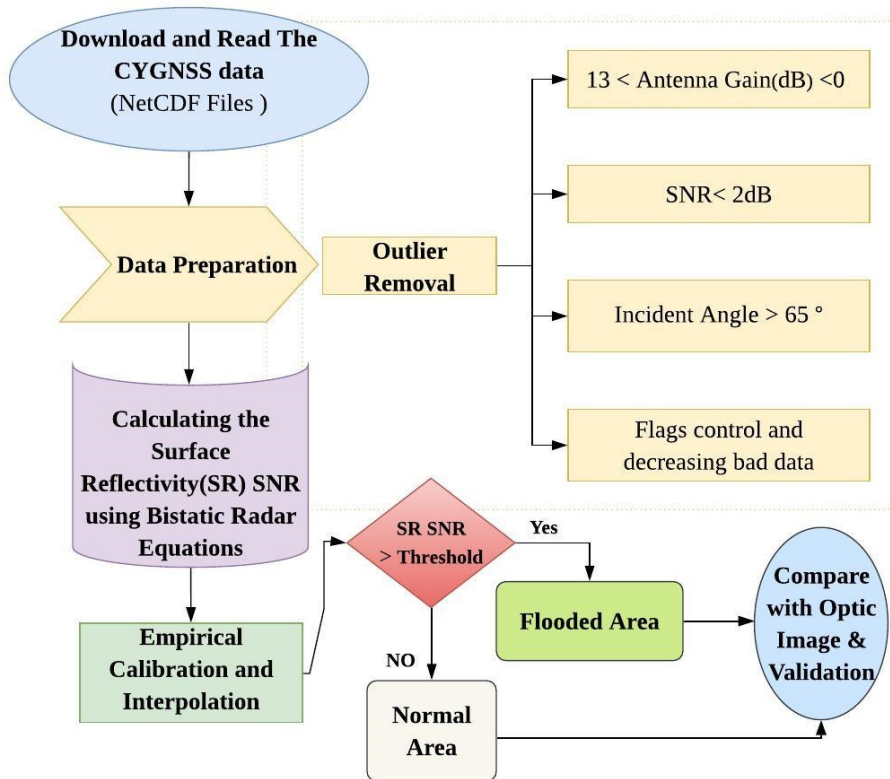
Figure 5. Methodology flowchart based on the bistatic radar concept and using CYGNSS data.
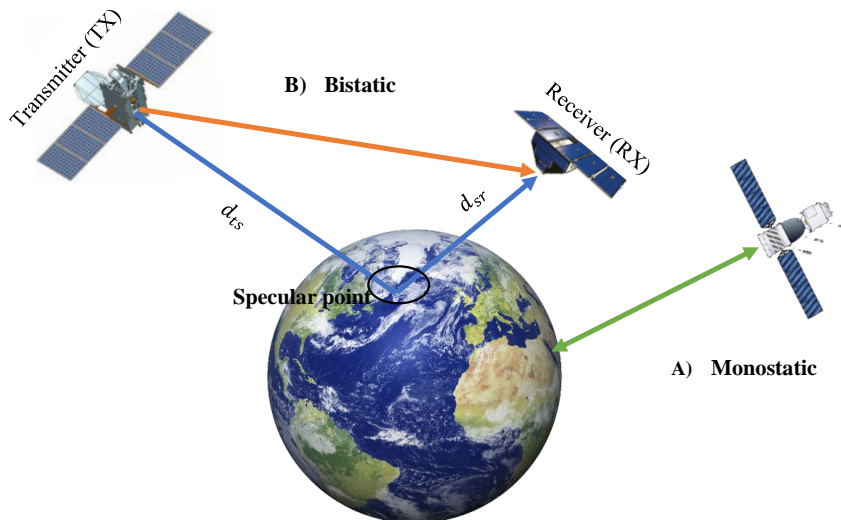

Figure 6. Simple schematic view of mono (**A**) and bistatic (**B**) radars constellation for satellite remote sensing.

The CYGNSS and GPS constellations form a bistatic radar system. The GPS satellites transmit circularly polarized microwave signals which are collected by the CYGNSS reflectometry receivers after forward-scattering from the Earth's surface. The scattered signals contain valuable information about the physical properties of the reflecting surface. Inland waters can be detected by CYGNSS, assuming a coherent forward-scattering mechanism [33,34,42]. The peak value of coherent scattered power is defined as [22,23,43]:

$$P_{RL}^{coh} = \frac{P_R^t \, G^t \, G^r}{(d_{ts} + d_{sr})^2} \left(\frac{\lambda}{4\pi}\right)^2 \Gamma_{RL} \tag{1}$$

where P_{RL}^{coh} is the peak value of coherently received power, R denotes the right-handed circular polarization (RHCP) GPS transmit antenna, and L is related to the left-handed circular polarization (LHCP) of forward-scattered signals collected by the downward-looking antenna. P_R^t is the transmitted power, G^t is the gain of the transmitter antenna, G^r is the gain of the receiver antenna, λ is the GPS L1 wavelength (~0.19 m), and d_{ts} is the distance between the specular reflection point and the GPS transmitter, while d_{sr} is the distance between the specular reflection point and the GNSS-R receiver and Γ_{RL} is the surface reflectivity along with the incidence angle. In addition to the mentioned parameters P_{RL}^{coh} is affected by system noise. Therefore, signal-to-noise ratio (SNR) could be defined as:

$$SNR = \frac{P_{RL}^{coh}}{N} = \frac{P_R^t \, G^t \, G^r}{(d_{ts} + d_{sr})^2} \left(\frac{\lambda}{4\pi}\right)^2 \frac{\Gamma_{RL}}{N} \tag{2}$$

where N is the noise value. Since the magnitude of the SNR is not equal to the reflected power, the surface reflectivity or corrected SNR along with the incidence angle could be computed using:

$$SNR_c = \frac{\Gamma_{RL}}{N} = SNR \frac{(d_{ts} + d_{sr})^2}{P_R^t G^t G^r} \left(\frac{4\pi}{\lambda}\right)^2 \tag{3}$$

Finally, the SNR_c in decibel (dB) is:

$$SNR_{c \, dB} = SNR_{dB} + 10 \log\left(\frac{(d_{ts} + d_{sr})^2}{P_R^t G^t G^r} \left(\frac{4\pi}{\lambda}\right)^2\right) \tag{4}$$

This parameter ($SNR_{c \, dB}$) is strongly related to the hydrological conditions of the land surface [18,34]. In this study, the following CYGNSS L1 variables were used for the calculation of the surface reflectivity:

- ddm_snr ($SNR_{dB} = 10 \log(S_{max}/N_{avg})$ with S_{max} being the maximum value in a single DDM bin and N_{avg} is the average raw noise counts per-bin
- gps_tx_power_db_w (P_R^t)
- gps_ant_gain_db_i (G^t)
- sp_rx_gain (G^r)
- rx_to_sp_range (d_{sr})
- tx_to_sp_range (d_{ts})

The parameter λ is the wavelength of the GPS L1 carrier (~0.19 m). We converted all the values to the dB scale (some of them were already in dB within the CYGNSS files).

4.2. Data Preparation and Calibration

Before and after using Equation (4), we employed several corrections and data editions and outlier identification as follows:

- GPS transmitter bias: GPS transmit powers are approximate estimates with some biases which should be considered. The main sources of these biases could be unknown transmitting powers of GPS satellites and the biases in P_R^t associated with GPS pseudorandom noise (PRN) codes [16,44]. We used empirical calibration developed by Chew et al. (2018) for CYGNSS products. Table 3 shows the magnitude of the biases which should be corrected during the estimation of $SNR_{c\ dB}$ [15].
- Incidence angle: This parameter also affects a coherent reflection when the incidence angles are above 40 degrees or 50 degrees and was negligible for our purpose [34], but we deleted data with an incidence angle of more than 65 degrees.
- Quality Control Flags: The Level 1A data product used in this study was refined by applying a set of quality control flags designed and included in the data to indicate potential problems [27,45]. The specific flags we used were 2, 4, 5, 8, 16, and 17, which were related to S-band transmitter powered up, spacecraft attitude error, black body DDM, DDM is a test pattern, the direct signal in DDM, and low confidence in the GPS EIR estimate, respectively. Based on the work by Chew et al. (2018) on soil moisture, we removed data with those quality flags in this study.
- Additional correction and removal: We removed data with SNR_{dB} less than 2dB and CYGNSS antenna gain of less than 0 dB or more than 13 dB. These corrections were empirical and are not standardized, but have been shown to be beneficial [16].

Table 3. Empirical biases in $SNR_{c\ dB}$ according to pseudorandom noise (PRN).

PRN	Bias (dB)	PRN	Bias (dB)	PRN	Bias (dB)	PRN	Bias (dB)
1	1.017	9	1.498	17	0.256	25	0.880
2	0.004	10	−0.783	18	−0.206	26	0.163
3	1.636	11	−0.230	19	−0.206	27	0.409
4	-	12	−1.021	20	0.345	28	−0.712
5	−0.610	13	0.007	21	−0.909	29	−1.032
6	0.24	14	−0.730	22	−0.838	30	0.877
7	−0.709	15	−0.376	23	−0.858	31	−0.562
8	0.605	16	−0.481	24	1.140	32	−0.819

Figure 7 shows the statistical information for corrected SNR using three days of CYGNSS data during the flood time. Figure 7A shows the calculated surface reflectivity SNR of CYGNSS tracks before (left side) and after (right side) the data preparation. As can be seen in the middle part of the figure, some of the measurements that may be misleading were removed. Figure 7B,C show the distribution of the measurements with respect to the incidence angle and antenna gain. Despite the fact that the data rectification procedure discarded about 48% of the observations, CYGNSS still provided enough data to detect the flood. The flooding period continued until 17 January 2020. We analyzed a dataset consisting of three days of CYGNSS observations to reduce the effect of losing a significant portion of the data.

4.3. Interpolation

An interpolation process was used here to retrieve a representative grid from the CYGNSS observation points. As shown in Figure 7A, the data derived from CYGNSS have irregular structures based on the satellite along-tracks. We used the natural neighbor interpolation method for gridding. The method was developed by Sibson [46] and is a multivariate interpolation according to Voronoi tessellation [47]. The principal formula is [48]:

$$G(x, y) = \sum_{i=1}^{N} w_i\, f(x_i, y_i) \tag{5}$$

where G is the estimated value at (x, y), $w_i = Q_k/R_k$ is the weights, and $f(x_i, y_i)$ is the known data at (x_i, y_i), R_k is the area of the initial Voronoi diagram element for point $P_k = (x_i, y_i)$. Q_k is the intersection

area of R_k and newly constructed element for the point (x, y). Therefore, the method algorithm is the algorithm to insert an additional point into the existing Voronoi diagram. Figure 8 illustrates the visual view of the natural neighbor interpolation method.
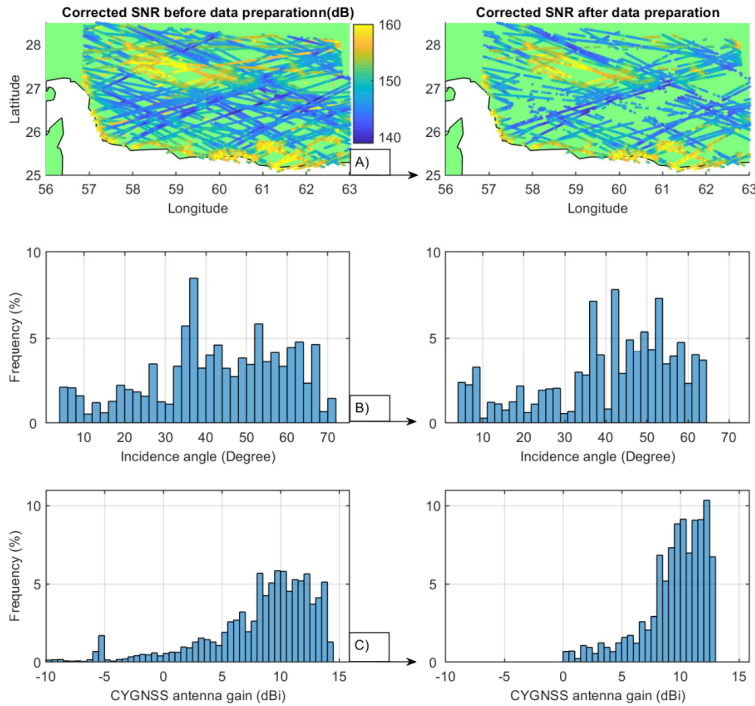

Figure 7. Statistical information of the data preparation step for the CYGNSS observations over a period of three days (13 January to 15 January 2020). (**A**) Corrected signal-to-noise ratio (SNR) before and after the preprocessing step. (**B**,**C**) The distribution of data according to incidence angle and antenna gain before and after data preparation.
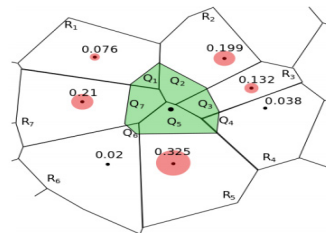
Figure 8. The natural neighbor interpolation method. The area of the colored circles are the interpolating weights. The shaded area is a new Voronoi element for the point to be interpolated [48].

For CYGNSS data interpolation over our region of interest, we generated a grid with the resolution of 0.1° along the geodetic longitude and latitude and applied the mentioned interpolation method. Figure 9 shows the data before and after gridding. As can be seen from the figure, the gridded data is more sensible compared to the satellite tracks representation. Since SNR was not equal in magnitude to the $SNR_{c\ dB}$, the observations and corrections made in Equation (4) resulted in magnitudes greater than 140 dB (Figure 7A). To see the anomalies of the corrected $SNR_{c\ dB}$ in a visually reasonable range [11], 140 dB was subtracted from the original $SNR_{c\ dB}$ values.
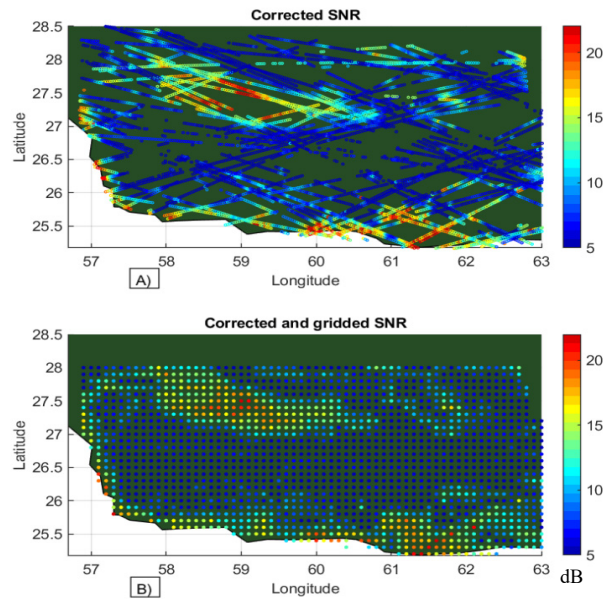
Figure 9. The outcome of the interpolation process for the corrected SNR ($SNR_{c\ dB}$) over the period of three days from 13 January to 15 January 2020. (**A**) Representation of the CYGNSS measurements along the satellite tracks, (**B**) the interpolated data at $0.1° \times 0.1°$ grid points using the natural neighbor interpolation method.

4.4. Evaluation and Mapping

As can be seen in Figure 4B, the flood happened in the south and middle part of the Sistan and Baluchestan province in Iran. Figure 10 shows the flooded regions which were detected by CYGNSS observations overlaid on the MODIS image (Figure 4B) for verification. The figure contains three regions with significant SNR anomalies. The regions are labeled A, B, and C.

Region A in Figure 10 belongs to the Hamun-Jaz Murian depression in the southeast of Iran, placed between the Kerman province and Sistan and Baluchestan province. The shape of the depression or basin is oblong and enclosed by the mountains. There is a seasonal lake, Hamun, in the middle of the basin, which has been dry through the recent dry years. Although the Halil and Bampur rivers are the main sources of feeding for the basin, neither of both bring significant water to the basin to fill this lake, because the water is used for agricultural purposes on the way [49,50]. Moreover, the recent flood in January 2020 was unique in terms of flood volume over the last decade. The previous flood in this region happened in June 2007. Figure 11 demonstrates the capability of CYGNSS measurements in the detection and mapping of the flood over this depression.

To calculate the flooded areas using corrected SNR, a threshold was used to distinguish inundated from noninundated areas. A simple threshold method has been used in previous studies with monostatic and bistatic radars [11,18]. As is seen in Figures 10–13, observations with the values greater than 11 dB corresponded to the flooded areas. This threshold was used for the detection of inundation in this study. This value could be different in other regions. The roughness and vegetation could weaken the signals and change the threshold. The threshold used by [11] was 12dB for the medium-vegetation density and typical roughness.

As can be distinguished from flooded areas in Figures 11 and 12, the values of corrected SNR more than 11 dB have a high correlation with the satellite image in the inundated region. However, minor discrepancies could be related to georeferencing or interpolation errors. The overall evaluation of the results using the three days of CYGNSS data reports an acceptable performance for flood detection.
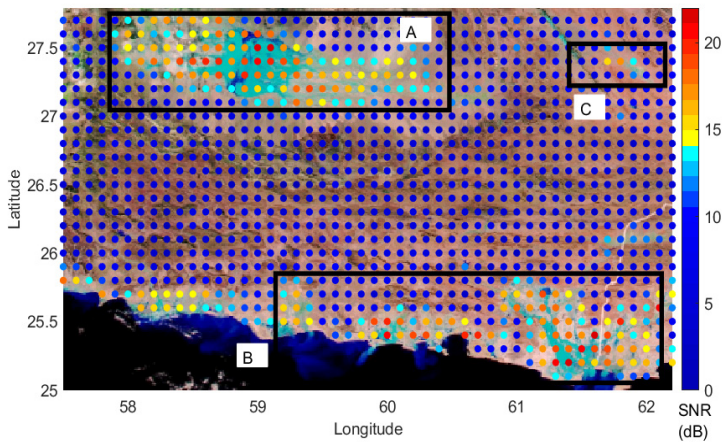
Figure 10. The georeferenced optical satellite imagery of the flood from MODIS (13 January 2020) overlaid by the corrected signal to noise ratio derived from CYGNSS observations (13 January to 15 January 2020). The regions labeled A, B, and C show significant SNR anomalies.
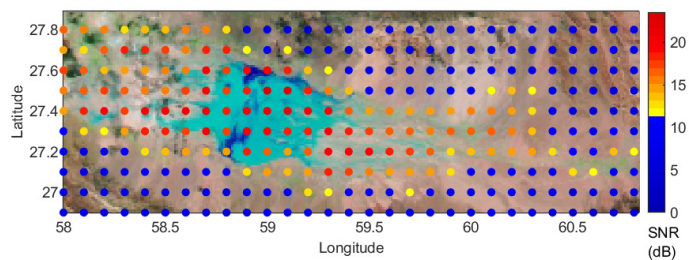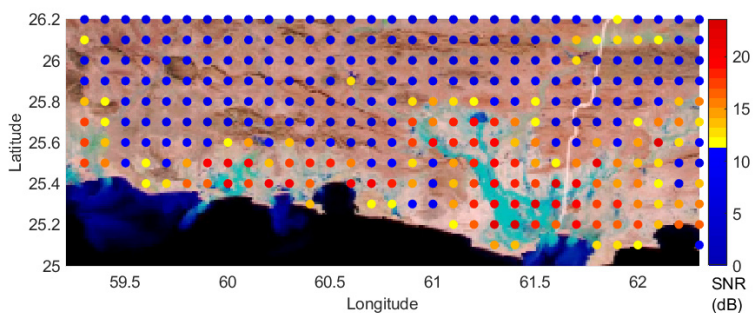

Figure 11. The georeferenced optical satellite imagery of the flood over the Hamun-Jaz Murian basin (region A in Figure 10) from MODIS (13 January 2020) overlaid by the corrected SNR derived from CYGNSS observations (13 January to 15 January 2020).

Figure 12. The georeferenced optical satellite imagery of the flood over coastlines and inundation of the nearby rivers (region B in Figure 10) from MODIS (13 January 2020) overlaid by the corrected SNR derived from CYGNSS observations (13 January to 15 January 2020).

Governments could use flood maps to establish the risk regions, safe evacuation options, and update the reaction plan. In the absence of promising and accurate flood maps, the development processes in or nearby the risk area are affected. The community lacks a tool to guide development to be more secure and to reduce future risks.
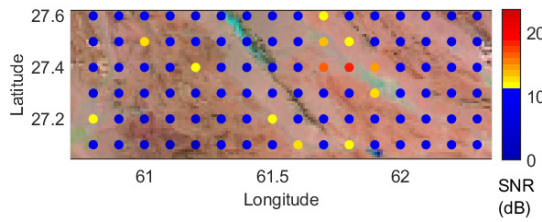
Figure 13. The georeferenced optical satellite imagery of the flood over the cities of Zaboli and Suran (region C in Figure 10) from MODIS (13 January 2020) overlaid by the corrected SNR derived from CYGNSS observations (13 January to 15 January 2020). The region includes a river and an inland water body.

We proceeded to map the detected inundation area. Google Maps was used here as an infrastructure which provides information about roads, cities, villages, etc. The derived data which shows flooded regions (data over 11 dB) was mapped on Google Maps. Figure 14 illustrates the three major regions of flood in Sistan and Baluchestan. Due to the flood in region A, corresponding to the Hamun-Jaz-Murian basin, the cities close to the basin, i.e., IranShahr, Eslam Abad, and Golmorti, and the roads between them, were affected. The area of this region is about 8706 square kilometers. Region B, which is close to the coastline and encompasses a few rivers, many cities, villages, farmlands, and roads, was also hit by the flood. The area of this region is about 9742 square kilometers. Region C, in close proximity to the region A, includes a river, an inland lake, and the cities Zaboli and Suran, which were affected. The area of this flooded region is about 1196 square kilometers. Therefore, based on the estimates from the CYGNSS observations, about 19644 square kilometers were affected by the flood in the south and middle parts of the Sistan and Baluchestan province. More severe impacts were seen in the regions close to the coastlines and nearby rivers.
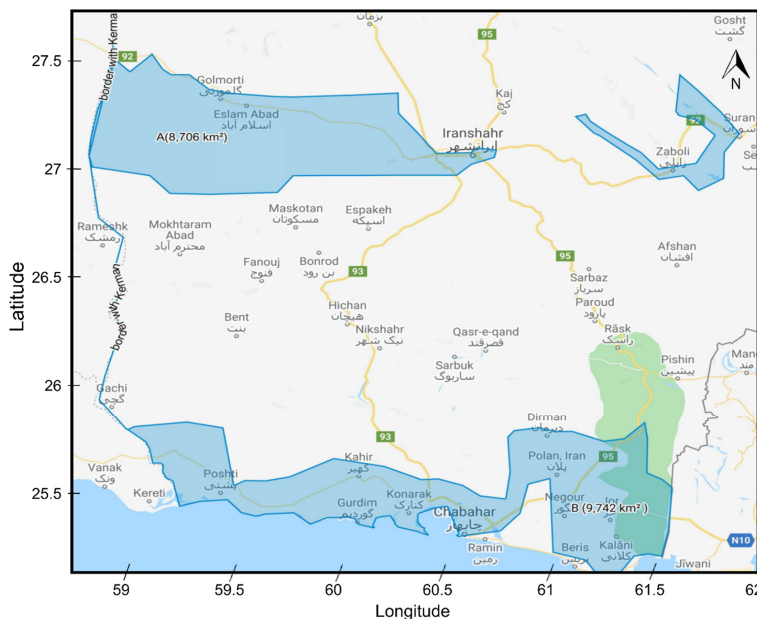

Figure 14. Map of the flooded regions laid over Google Maps. The blue-colored polygons show the boundary of the flooded areas, yellow lines are roads, and names of the cities are written on the map.

5. Summary and Conclusions

We applied the GNSS-R remote sensing technique based on a dataset of spaceborne observations of reflected GPS signals over the land to detect and map the recent flood in the southeastern part of Iran. The flood occurred in the Sistan and Baluchestan province after the heavy rain in mid-January 2020. The dataset used was acquired from the data products of the NASA CYGNSS mission. The main parameter of interest used in the analysis was the delay doppler map SNR, which was retrieved from the level-1 data product. First, a data preparation procedure was applied to remove outliers and discard low-quality data. In the next step, inverse bistatic radar formula was used to calculate the corrected SNR, which was closely related to surface reflectivity and hydrological conditions. The corrected SNR values were calibrated and interpolated to a regular grid over the study area. After calibration and gridding, the corrected SNR was verified with the MODIS optical image. A threshold of about 11 dB or more could be distinguished between the inundated and noninundated areas in the regions of interest. Finally, the flood-affected areas were mapped on Google Maps. The area of the flooded regions was estimated to be about 19,644 km^2 or 10.8% of the province. Many cities, roads, and other infrastructures were affected by the flood in these regions. The results indicate the regions close to depression, lakes, and coastal areas are at a high risk of flooding in this province. This study confirms that CYGNSS data is of value for hydrological investigations, particularly flood detection in the Sistan and Baluchestan province. Despite a relatively short revisit time of CYGNSS observations, the spatial resolution of the data products needs to be improved for mapping purposes. This issue could be addressed in future missions by, e.g., increasing the number of onboard processing channels, as well as by processing the reflected signals from other GNSS constellations such as GLONASS, Galileo, and BeiDou.

References

1. Van Westen, C. Remote sensing for natural disaster management. *Int. Arch. Photogramm. Remote Sens.* **2000**, *33*, 1609–1617.
2. Salami, R.O.; von Meding, J.K.; Giggins, H. Vulnerability of Human Settlements to Flood Risk in the Core Area of Ibadan Metropolis, Nigeria. *Jàmbá J. Disaster Risk Stud.* **2017**, *9*, 1–14. [CrossRef] [PubMed]
3. ADPC; UNDP. *Integrated Flood Risk Management in Asia*; A Primer ADPC: Bangkok, Thailand, 2005.
4. Abidin, H.Z.; Andreas, H.; Gumiar, I.; Sidiq, T.P.; Gamal, M. Environmental impacts of land subsidence in urban areas of Indonesia. In *FIG Working Week*; TS 3—Positioning and Measurement: Sofia, Bulgaria, 2015.
5. Nash, L.L. *The Colorado River Basin and Climatic Change: The Sensitivity of Streamflow and Water Supply to Variations in Temperature and Precipitation*; US Environmental Protection Agency, Office of Policy, Planning, and Evaluation: Washington, DC, USA, 1993.
6. Houston, J. Variability of precipitation in the Atacama Desert: Its causes and hydrological impact. *Int. J. Clim. J. R. Meteorol. Soc.* **2006**, *26*, 2181–2198. [CrossRef]
7. Brivio, P.A.; Colombo, R.; Maggi, M.; Tomasoni, R. Integration of remote sensing data and GIS for accurate mapping of flooded areas. *Int. J. Remote Sens.* **2002**, *23*, 429–441. [CrossRef]
8. CNN. Available online: https://edition.cnn.com/2019/04/07/middleeast/iran-flood-fatalities/index.html. (accessed on 7 April 2019).

9. Oberstadler, R.; Hönsch, H.; Huth, D. Assessment of the mapping capabilities of ERS-1 SAR data for flood mapping: A case study in Germany. *Hydrol. Process.* **1997**, *11*, 1415–1425. [CrossRef]

10. Kuenzer, C.; Guo, H.; Huth, J.; Leinenkugel, P.; Li, X.; Dech, S. Flood mapping and flood dynamics of the Mekong Delta: ENVISAT-ASAR-WSM based time series analyses. *Remote Sens.* **2013**, *5*, 687–715. [CrossRef]

11. Chew, C.; Reager, J.T.; Small, E. CYGNSS data map flood inundation during the 2017 Atlantic hurricane season. *Sci. Rep.* **2018**, *8*, 1–8. [CrossRef]

12. Rajabi, M.; Amiri-Simkooei, A.R.; Asgari, J.; Nafisi, V.; Kiaei, S. Analysis of TEC time series obtained from global ionospheric maps. *J. Geomat. Sci. Technol.* **2015**, *4*, 213–224.

13. Rajabi, M.; Amiri-Simkooei, A.R.; Nahavandchi, H.; Nafisi, V. Modeling and Prediction of Regular Ionospheric Variations and Deterministic Anomalies. *Remote Sens.* **2020**, *12*, 936. [CrossRef]

14. Tabibi, S. Snow Depth and Soil Moisture Retrieval Using SNR-Based GPS and GLONASS Multipath Reflectometry. Ph.D. Thesis, University of Luxembourg, Luxembourg, 2016.

15. Li, W.; Cardellach, E.; Fabar, F.; Rius, A.; Ribó, S.; Martín-Neira, M. First spaceborne phase altimetry over sea ice using TechDemoSat-1 GNSS-R signals. *Geophys. Res. Lett.* **2017**, *44*, 8369–8376. [CrossRef]

16. Chew, C.; Small, E. Soil moisture sensing using spaceborne GNSS reflections: Comparison of CYGNSS reflectivity to SMAP soil moisture. *Geophys. Res. Lett.* **2018**, *45*, 4049–4057. [CrossRef]

17. Wu, X.; Li, Y.; Xu, J. Theoretical study on GNSS-R vegetation biomass. In Proceedings of the 2012 IEEE International Geoscience and Remote Sensing Symposium, Munich, Germany, 12 November 2012.

18. Wan, W.; Liu, B.; Zeng, Z.; Chen, X. Using CYGNSS data to monitor China's flood inundation during typhoon and extreme precipitation events in 2017. *Remote Sens.* **2019**, *11*, 854. [CrossRef]

19. Hoseini, M.; Asgarimehr, M.; Zavorotny, V.; Nahavandchi, H.; Ruf, C.; Wickert, J. First evidence of mesoscale ocean eddies signature in GNSS reflectometry measurements. *Remote Sens.* **2020**, *12*, 542. [CrossRef]

20. Clarizia, M.P.; Ruf, C.S. Wind speed retrieval algorithm for the Cyclone Global Navigation Satellite System (CYGNSS) mission. *IEEE Trans. Geosci. Remote Sens.* **2016**, *54*, 4419–4432. [CrossRef]

21. Liu, B.; Wan, W.; Hong, Y. Can the Accuracy of Sea Surface Salinity Measurement Be Improved by Incorporating Spaceborne GNSS-Reflectometry? *IEEE Geosci. Remote Sens. Lett.* **2020**. [CrossRef]

22. Zavorotny, V.U.; Gleason, S.; Cardellach, E.; Camps, A. Tutorial on remote sensing using GNSS bistatic radar of opportunity. *IEEE Geosci. Remote Sens. Mag.* **2014**, *2*, 8–45. [CrossRef]

23. Eroglu, O.; Kurum, M.; Boyd, D.; Gurbuz, A.C. High Spatio-Temporal Resolution CYGNSS Soil Moisture Estimates Using Artificial Neural Networks. *Remote Sens.* **2019**, *11*, 2272. [CrossRef]

24. Teunissen, P.; Montenbruck, O. *Springer Handbook of Global Navigation Satellite Systems*; Springer: Cham, Switzerland, 2017.

25. Guerriero, L.; Pierdicca, N.; Egido, A.; Caparrini, M.; Paloscia, S.; Santi, E.; Floury, N. Modeling of the GNSS-R signal as a function of soil moisture and vegetation biomass. In Proceedings of the 2013 IEEE International Geoscience and Remote Sensing Symposium-IGARSS, Melbourne, VIC, Australia, 21–26 July 2013.

26. Masters, D.; Axelrad, P.; Katzberg, S. Initial results of land-reflected GPS bistatic radar measurements in SMEX02. *Remote Sens. Environ.* **2004**, *92*, 507–520. [CrossRef]

27. Ruf, C.; Chang, P.S.; Clarizia, M.P.; Gleason, S.; Jelenak, Z. *CYGNSS Handbook*; Michigan Pub: Ann Arbor, MI, USA, 2016; p. 154.

28. Ruf, C.S.; Atlas, R.; Chang, P.S.; Clarizia, M.P.; Garrison, J.; Gleason, S.; Katzberg, S.; Jelenak, Z.; Johnson, J.; Sharanya, J.; et al. New ocean winds satellite mission to probe hurricanes and tropical convection. *Bull. Am. Meteorol. Soc.* **2016**, *97*, 385–395. [CrossRef]

29. Ruf, C.S.; Chew, C.; Lang, T.; Morris, M.; Nave, K.; Ridley, A.; Balasubramaniam, R. A new paradigm in earth environmental monitoring with the CYGNSS small satellite constellation. *Sci. Rep.* **2018**, *8*, 1–13. [CrossRef]

30. Zribi, M.; Gorrab, A.; Baghdadi, N.; Lili-Chabaane, Z.; Mougenot, B. Influence of radar frequency on the relationship between bare surface soil moisture vertical profile and radar backscatter. *IEEE Geosci. Remote Sens. Lett.* **2013**, *11*, 848–852. [CrossRef]

31. Camps, A.; Park, H.; Pablos, M.; Foti, G.; Gommenginger, C.; Liu, P.W.; Jugge, J. Sensitivity of GNSS-R spaceborne observations to soil moisture and vegetation. *IEEE J. Sel. Top. Appl. Earth Obs. Remote Sens.* **2016**, *9*, 4730–4742. [CrossRef]

32. Chew, C.; Shah, R.; Zuffada, Z.; Hajj, G.; Masters, D.; Mannuci, A. Demonstrating soil moisture remote sensing with observations from the UK TechDemoSat-1 satellite mission. *Geophys. Res. Lett.* **2016**, *43*, 3317–3324. [CrossRef]

33. Gerlein-Safdi, C.; Ruf, C.S. A CYGNSS-based algorithm for the detection of inland waterbodies. *Geophys. Res. Lett.* **2019**, *46*, 12065–12072. [CrossRef]

34. Morris, M.; Chew, C.; Reager, J.; Shah, R.; Zuffada, C. A novel approach to monitoring wetland dynamics using CYGNSS: Everglades case study. *Remote Sens. Environ.* **2019**, *233*, 111417. [CrossRef]

35. Amineh, Z.B.A.; Hashemian, S.J.A.-D.; Magholi, A. Integrating Spatial Multi Criteria Decision Making (SMCDM) with Geographic Information Systems (GIS) for delineation of the most suitable areas for aquifer storage and recovery (ASR). *J. Hydrol.* **2017**, *551*, 577–595. [CrossRef]

36. World Data. Available online: https://www.worlddata.info (accessed on 1 February 2020).

37. Huffman, G.J.; Bolvin, D.T.; Nelkin, E.J. Integrated Multi-satellitE Retrievals for GPM (IMERG) technical documentation. *NASA/GSFC Code* **2015**, *612*, 47.

38. Lindsey, R.; Herring, D.; Abbott, M.; Conboy, B.; Esaias, W. *MODIS Brochure*; Goddard Space Flight Center: Greenbelt, MD, USA, 2013.

39. Flash Flooding in Iran. 2020. Available online: https://earthobservatory.nasa.gov/images/146150/flash-flooding-in-iran (accessed on 1 February 2020).

40. Eaves, J.L. Introduction to radar. In *Principles of Modern Radar*; Van Nostrand Reinhold; Springer: New York, NY, USA, 1987; pp. 1–27.

41. Bruder, J.A. IEEE Radar standards and the radar systems panel. *IEEE Aerosp. Electron. Syst. Mag.* **2013**, *28*, 19–22. [CrossRef]

42. Nghiem, S.V.; Zuffada, C.; Shah, R.; Chew, C.; Lowe, S.T.; Mannucci, A.J.; Cardellach, E.; Brakenridge, G.R.; Geller, G.; Rosenqvist, A. Wetland monitoring with global navigation satellite system reflectometry. *Earth Space Sci.* **2017**, *4*, 16–39. [CrossRef]

43. Masters, D. Surface Remote Sensing Applications of GNSS Bistatic Radar: Soil Moisture and Aircraft Altimetry. Ph.D. Thesis, University of Colorado, Boulder, CO, USA, 2004.

44. Wang, T.; Ruf, C.S.; Block, B.; McKague, D.; Gleason., S. Characterization of GPS L1 EIRP: Transmit power and antenna gain pattern. In Proceedings of the 31st ION GNSS, Miami, FL, USA, 24–28 September 2018.

45. Basis, A.T. Cyclone Global Navigation Satellite System (CYGNSS). Prepared by: Maria Paola Clarizia, University of Michigan, Valery Zavorotny, NOAA. 2015.

46. Sibson, R. *A Brief Description of Natural Neighbor Interpolation (Chapter 2)*; Barnett, V., Ed.; Interpolating Multivariate Data; John Wiley: Chichester, UK, 1981; pp. 21–36.

47. Voronoi, G. Nouvelles applications des paramètres continus à la théorie des formes quadratiques. Deuxième mémoire. Recherches sur les parallélloèdres primitifs. *J. für die reine und angewandte Mathematik (Crelles J.)* **1908**, *1908*, 198–287. [CrossRef]

48. Tsidaev, A. Parallel algorithm for natural neighbor interpolation. In Proceedings of the 2nd Ural Workshop on Parallel, Distributed, and Cloud Computing for Young Scientists, Yekaterinburg, Russia, 6 October 2016.

49. Harrison, J. The Jaz Murian depression, Persian Baluchistan. *Geogr. J.* **1943**, *101*, 206–225. [CrossRef]

50. Frs, N.F. From Musandam to the Iranian Makran. *Geogr. J.* **1975**, *141*, 55–58. [CrossRef]

NTNU
Norwegian University of
Science and Technology